First tau neutrino appearance, non-unitary mixing and absolute orientation measurements in KM3NeT

L Cerisy

To cite this version:

L Cerisy. First tau neutrino appearance, non-unitary mixing and absolute orientation measurements in KM3NeT. Physics [physics]. Aix-Marseile Université, 2024. English. ⟨NNT : 2024AIXM0001⟩. ⟨tel-04989662⟩

HAL Id: tel-04989662

https://hal.science/tel-04989662v1

Submitted on 13 Mar 2025

NNT : 2024AIXM0001

THÈSE DE DOCTORAT

Soutenue à AMU — Aix-Marseille Université
le 25 novembre 2024 par

Luc CERISY

First tau neutrino appearance, non-unitary mixing and absolute orientation measurements in KM3NeT

Discipline
Physique et Sciences de la Matière

Spécialité
Physique des Particules et Astroparticules

École doctorale
ED352

Laboratoire/Partenaires de recherche
Centre de Physique des Particules de Marseille (CPPM)

Composition du jury

Corinne GOY LPSC, Grenoble	Rapporteure
Sebastian BÖSER JGU, Mainz, Allemagne	Rapporteur
Ana TEIXEIRA LPC, Clermont	Examinatrice
Anca TUREANU Univ. of Helsinki, Finlande	Examinatrice
Cristinel DIACONU CPPM, Marseille	Président du jury
Jürgen BRUNNER CPPM, Marseille	Directeur de thèse
Vincent BERTIN CPPM, Marseille	Co-directeur de thèse

Affidavit

I, undersigned, Luc Cerisy, hereby declare that the work presented in this manuscript is my own work, carried out under the scientific supervision of Jürgen Brunner and Vincent Bertin in accordance with the principles of honesty, integrity and responsibility inherent to the research mission. The research work and the writing of this manuscript have been carried out in compliance with both the french national charter for Research Integrity and AMU charter on the fight against plagiarism.

This work has not been submitted previously either in this country or in another country in the same or in a similar version to any other examination body.

Marseille, 30/09/2024

List of publications and conferences

List of publications:

1. L. Cerisy et al. [KM3NeT collaboration], Undersea measurements of neutrino oscillations, NOW 2024 Proceedings, 010, 2024 : cette publication contient une partie des analyses et résultats décrits dans le Chapitre 6 et 7
2. L. Cerisy et al. [KM3NeT collaboration], Non unitary neutrino mixing with KM3NeT/ ORCA, XXXI International Conference on Neutrino Physics and Astrophysics, Poster, 2024 : cette publication contient une partie des analyses et résultats décrits dans le Chapitre 7
3. S. Aiello et al. [KM3NeT collaboration], Study of tau neutrinos and non-unitary neutrino mixing with the first 6 detection units of KM3NeT/ORCA, accepted by KM3NeT PC, 2024 : cette publication contient les analyses et résultats décrits dans le Chapitre 6
4. L. Cerisy et al. [KM3NeT collaboration], Particle identification in KM3NeT/ORCA, Proceedings of 38th International Cosmic Ray Conference 444, 1191, 2023 10.22323/1.444.1191 : cette publication contient une partie des analyses et résultats décrits dans le Chapitre 5
5. S. Aiello et al. [KM3NeT collaboration], First observation of the cosmic ray shadow of the Moon and the Sun with KM3NeT/ORCA, Eur. Phys. J. C 83, 344 (2023), 10.1140/epjc/s10052-023-11401-5 : cette publication contient une partie des analyses et résultats décrits dans le Chapitre 3

Conferences and schools:

1. 2024, Neutrino Oscillation Workshop 2024, Otranto, Italie
2. 2024, XXXI International Conference on Neutrino Physics and Astrophysics, Milan, Italie
3. 2023, IRN Neutrino, Karlsruhe, Germany
4. 2023, Antares exposition, La-Seyne-Sur-Mer, France
5. 2023, 38th International Cosmic Ray Conference, Nagoya, Japan
6. 2022, IRN Neutrino, Orsay, France
7. 2022, Ecole de Gif 2022: La Physique des Neutrinos, Paris, France
8. 2022, Introduction to the Physics of Neutrinos, Helsinki, Finland

Abstract

This thesis presents advancements in the calibration of KM3NeT/ORCA, and demonstrates the capabilities of the detector with only 6 detection units (DUs) to observe tau neutrinos and test models that go beyond 3-flavour neutrino oscillations. Using KM3NeT/ORCA data from February 2020 to August 2023, the cosmic ray shadows of the Moon and Sun were observed with high significance. The signals were used to further constrain the detector absolute orientation to the level of $[-0.15°, +0.55°]$ at 3σ. In addition the sun shadow signal was found to be anti-correlated with its activity, the latter reflected in the number of sunspots. To complement the results of the Moon/Sun shadow calibration, an innovative acoustic positioning technique, based on the beamforming principle was developed and successfully used during a dedicated sea campaign. The calibration consist of sending acoustic signals from a boat, and reconstruct the source position in the detector frame. This promises further improvements to the detector pointing accuracy at the level of $\approx 0.1°$. The analysis of the data is ongoing. The first observation of the tau neutrino appearance in KM3NeT/ORCA is reported, based on 433 kt-years of data taken with six DUs. The tau neutrino normalisation was measured as $0.48^{+0.49}_{-0.33}$, and the charged-current cross section was found to be $\sigma_\tau^{\text{meas}} = (2.5^{+2.6}_{-1.8}) \times 10^{-38}$ cm^2 for a median neutrino energy of 20.3 GeV including Feldman Cousin corrections. This result provides a foundation for future cross-section measurements from KM3NeT/ORCA in this energy range. Furthermore, the thesis introduces an analysis of the non-unitary neutrino mixing (NUNM) using the same KM3NeT/ORCA 433 kt-years atmospheric neutrino data . The limits on the NUNM parameters were improved, particularly for α_{33}, which was constrained to -0.05 at 2σ, a two-fold improvement over previous bounds, mainly from light sterile neutrino search of atmospheric neutrino experiments. Pairs of NUNM parameters were also tested and a small deviation was observed for the sum of α_{22} and α_{33}. The study represents the first direct search for low-scale non-unitary mixing using atmospheric neutrinos. This work underscores the improvements in the KM3NeT's pointing accuracy contributing to the advancement of neutrino astronomy. The detector was also demonstrated to be a powerful instrument for probing fundamental neutrino properties.

Summary

This thesis presents advancements in the calibration of KM3NeT/ORCA, and demonstrates the capabilities of the detector with only 6 detection units (DUs) to observe the tau neutrino appearance and test models that go beyond 3-flavour neutrino oscillations.

With up to 18 DUs of KM3NeT/ORCA, 1.4 Mt-years of data were taken from February 2020 to August 2023. This data was used to observe the cosmic ray shadows of the Moon and Sun with high significance. The signals were used to further constrain the detector absolute orientation to the level of $[-0.15°, +0.55°]$ at 3σ. In addition, using the same data, the sun shadow signal was found to be anti-correlated with its activity, the latter reflected in the number of sunspots. When incorporating the new set of data taken after August 2023 the parameters describing the correlation will be measured.

To complement the results of the Moon/Sun shadow calibration, an innovative acoustic positioning technique, based on the beamforming principle was developed and successfully used during a dedicated sea campaign in July 2024. The calibration consist of sending acoustic signals from a boat, and reconstruct the source position in the detector frame. The source position is determined with an ≈ 50 cm precision thanks to the positioning system using the boat GPS. The time stability of the pulse emission is ensured thanks to the GPS pulse-per-second at the μs level. The analysis of the data was consistent with the expected pulse time stability of ≈ 100 μs. The analysis of the pointing accuracy is currently ongoing. The goal is to reach a further improvement of the knowledge on the detector pointing accuracy at the level of $\approx 0.1°$.

The thesis presents a first observation of the tau neutrino appearance with KM3NeT/ORCA based on 433 kt-years of data taken with six DUs. The amount of tau neutrinos produced in the atmosphere is negligible compared to muon and electron neutrinos. However the detection of tau neutrino by atmospheric neutrino experiments is a direct evidence for the neutrino oscillation. The ratio of observed and expected tau neutrinos called *tau normalisation*, can be translated into a measurement of the tau neutrino cross-section. The tau normalisation was measured as $0.48^{+0.49}_{-0.33}$, and the charged-current cross section was

found to be $\sigma_{\tau}^{\text{meas}} = (2.5^{+2.6}_{-1.8}) \times 10^{-38}$ cm^2 for a median neutrino energy of 20.3 GeV including Feldman Cousin corrections. This result provides a foundation for future cross-section measurements from KM3NeT/ORCA in this energy range. It is already competitive with the most precise measurements. In the future, additional data points will allow to probe the structure of the tau neutrino cross-section.

Furthermore, the thesis introduces an analysis of the non-unitary neutrino mixing (NUNM) using the same KM3NeT/ORCA 433 kt-years atmospheric neutrino data. The limits on the NUNM parameters were improved, particularly for α_{33}, which was constrained to -0.05 at 2σ, a two-fold improvement over previous bounds. The previous bound were mainly from light sterile neutrino search of atmospheric neutrino experiments as Super-Kamiokande and IceCube. Pairs of NUNM parameters were also tested and a small deviation was observed for the sum of α_{22} and α_{33} with a p-value of 0.9% calculated based on the Feldman Cousin approach. The study represents the first search for low-scale non-unitary mixing using atmospheric neutrinos. The sensitivity of KM3NeT/ORCA to the NUNM parameters is largely enhanced by the strong earth matter effects. In the future, additional systematics study will evaluate the effect of the correlation between the NUNM parameters and the parameters accounting for the uncertainties on the flux.

This work underscores the improvement of our knowledge of the absolute orientation of KM3NeT. Better constraining the pointing accuracy will help to reach the angular precision potential of KM3NeT/ARCA, which will contribute to the advancement of neutrino astronomy. The KM3NeT/ORCA detector was also demonstrated to be a powerful particle physics instrument for probing fundamental neutrino properties, including the neutrino oscillation, the neutrino mass and testing extensions of the standard model.

Résumé

Cette thèse présente des avancées dans la calibration absolue de KM3NeT/ORCA et démontre les capacités du détecteur avec seulement 6 DUs à observer des neutrinos tau et à tester des modèles qui vont au-delà des oscillations des neutrinos avec 3 saveurs. À partir des données de KM3NeT/ORCA collectées entre Février 2020 et Novembre 2021, les ombres en rayons cosmiques de la Lune et du Soleil ont été observées avec une haute significativité statistique. Ces signaux ont permis de contraindre davantage l'orientation absolue du détecteur à $[-0.15°, +0.55°]$ à 3σ. De plus, le signal de l'ombre du Soleil a montré une anti-corrélation avec l'activité solaire. Pour compléter ces résultats de calibration, une technique innovante de positionnement acoustique, basée sur le principe de *beamforming*, a été développée et utilisée lors d'une campagne en mer dédiée. Cette méthode permet d'améliorer la précision de pointage du détecteur à un niveau de $\approx 0.1°$. L'analyse des résultats est en cours. La première observation de l'apparition des neutrinos tau dans KM3NeT/ORCA est décrite, basée sur 433 *kt-years* de données enregistrées avec six DUs. Le paramètre de normalisation des neutrinos tau a été mesuré à $0.48^{+0.49}_{-0.33}$, et la section efficace du courant chargé pour les neutrinos tau a été trouvée égale à $\sigma_\tau^{\text{meas}} = (2.5^{+2.6}_{-1.8}) \times 10^{-38}$ cm^2 pour une énergie médiane des neutrinos tau de 20.3 GeV, incluant les corrections Feldman Cousin. Ce résultat fournit une base pour les futures mesures de sections efficaces des neutrinos tau par KM3NeT/ORCA dans cette gamme d'énergie. En outre, la thèse présente une analyse du mélange non-unitaire des neutrinos (NUNM) utilisant les mêmes données atmosphériques de 433 *kt-years* de KM3NeT/ORCA. Les limites sur les paramètres NUNM ont été améliorées, en particulier pour α_{33}, qui a été contraint à -0.05 à 2σ. Soit une amélioration d'un facteur deux par rapport aux contraintes précédentes. Des paires de paramètres NUNM ont également été testées et une légère déviation a été observée pour la somme de α_{22} et α_{33}. Cette étude représente la première recherche de mélange non-unitaire des neutrinos dans une gamme d'energie basse à l'aide de neutrinos atmosphériques. Ce travail souligne les améliorations de la précision de pointage de KM3NeT, contribuant au progrès de l'astronomie avec les neutrinos. Il a également été démontré que ce détecteur est capable de sonder les propriétés fondamentales des neutrinos.

Résumé étendu

Cette thèse, intitulée *First tau neutrino appearance, non unitary mixing and absolute orientation measurements in KM3NeT*, présente trois axes principaux de recherche dans le cadre de l'expérience KM3NeT montrée dans la Figure 1 : l'observation des neutrinos tau, l'étude de modèles de mélange non unitaire des neutrinos (NUNM), et l'amélioration de la calibration du détecteur. Ces travaux contribuent à améliorer la connaissance de l'orientation absolue du télescope, ainsi qu'à explorer au-delà des oscillations des neutrinos à trois saveurs.

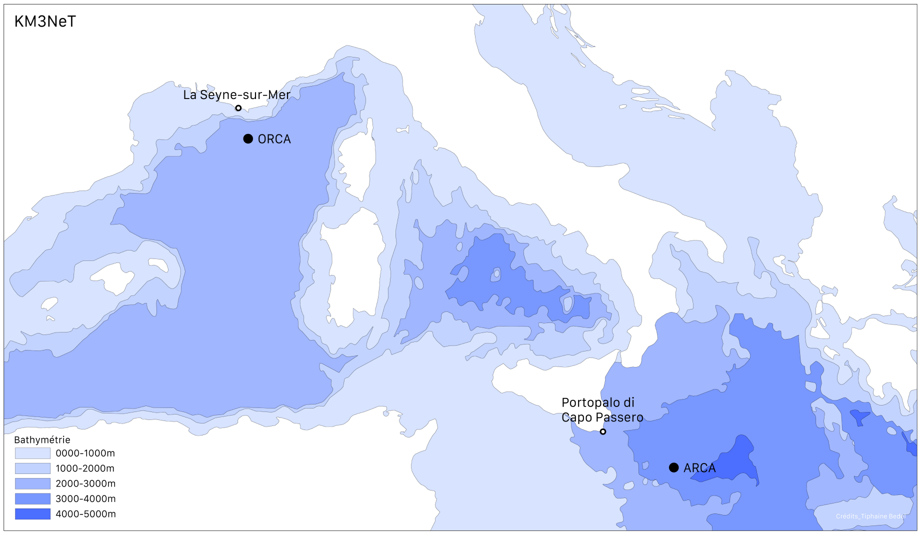

Figure 1: Profondeur des sites de KM3NeT.

Calibration de l'orientation absolue de KM3NeT

Un des résultats principaux de cette thèse est l'amélioration de la calibration de l'orientation absolue du détecteur à travers deux méthodes distinctes. Ces calibrations sont essentielles pour assurer une connaissance approfondie de la résolution angulaire du télescope à neutrinos KM3NeT.

Mesure de l'ombre de la Lune et du Soleil en rayons cosmiques

La première méthode de calibration repose sur l'observation des ombres produites par les rayons cosmiques lorsqu'ils sont occultés par la Lune et le Soleil. L'analyse des données des rayons cosmiques, collectées entre février 2020 et novembre 2021, avec 6 unités de détection (DUs), a permis de réaliser une mesure statistiquement significative de ces ombres, illustrée dans la Figure 2.

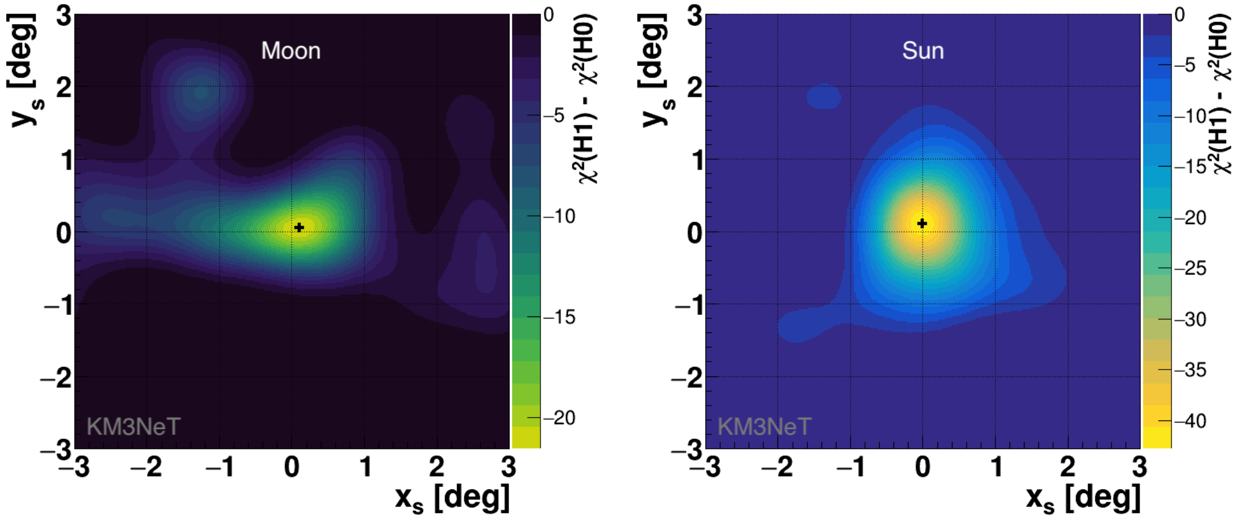

Figure 2: Le $\Delta\chi^2_{H1/H0}$ en fonction de x_s et y_s est montré pour la Lune à gauche, et le Soleil à droite. La croix noire indique le minimum du fit.

Cette technique offre une méthode alternative à la calibration sur les sources lumineuses de référence, absentes pour les neutrinos, pour la mesure de l'orientation absolue du détecteur. Cette mesure a atteint une précision inédite avec l'échantillon de données de février 2020 à août 2023, prises avec entre 6 et 18 DUs, de l'ordre de $[-0.15°, +0.55°]$ à 3 σ en rotation azimutale. La performance de pointage de KM3NeT/ORCA est illustrée dans la Figure 3.14. Le résultat de cette étude est compatible avec l'orientation absolue nominale du détecteur.

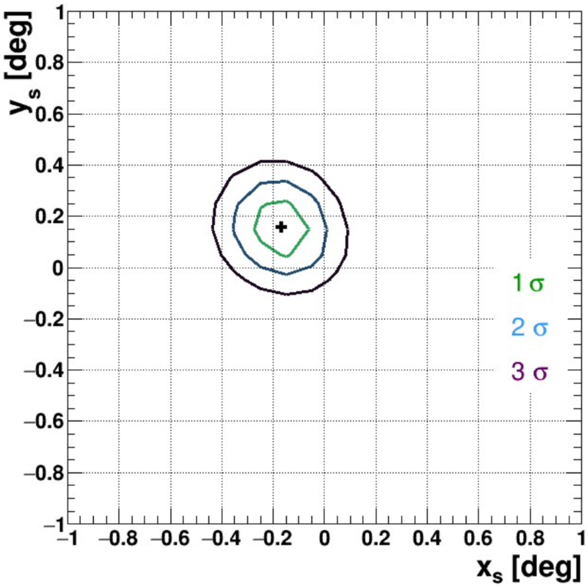

Figure 3: Intervalles de confiance pour la Lune et le Soleil combinés, pour les données prises avec entre 6 et 18 DUs. La croix noire indique le minimum du fit.

De plus, une étude de l'ombre du Soleil en fonction du temps a permis d'observer la corrélation entre la variation de l'amplitude de l'ombre du Soleil et son activité. L'activité du Soleil est mesurée à travers le nombre de taches solaires présentes à sa surface. L'amplitude de l'ombre est mesurée à la position nominale (0,0). La Figure 4 illustre cette corrélation pour le Soleil, absente pour la Lune. Cette corrélation peut être interprétée grâce à la structure du champ magnétique Solaire qui évolue avec son activité. En période de forte activité, la disposition chaotique des lignes de champ engendre des déviations aléatoires des rayons cosmiques, ce qui tend à réduire et changer la forme de l'ombre du Soleil. Au contraire en période de basse activité, les lignes de champ suivent une structure sous forme de dipôle avec comme conséquence une augmentation de l'amplitude et la taille de l'ombre du Soleil.

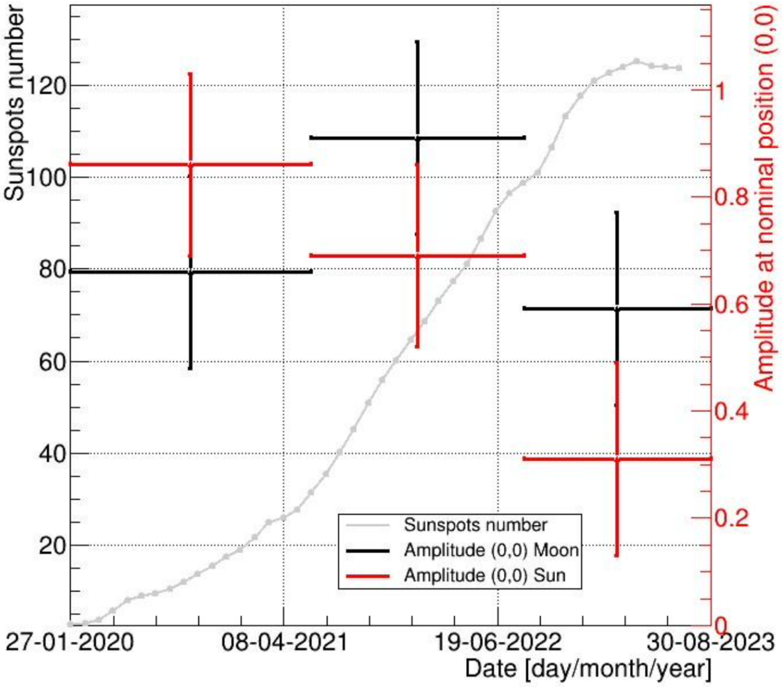

Figure 4: Le nombre de taches solaires est montré sur l'axe Y gauche et l'amplitude sur l'axe Y droit pour trois périodes de temps de durée égale. Les amplitudes des ombres de la Lune et celle du Soleil sont montrées avec des croix noires et rouges, respectivement.

Mesure du pointage absolu du télescope avec des signaux acoustiques

L’étude acoustique présentée dans cette thèse propose une technique alternative pour améliorer la précision de l’orientation absolue du détecteur avec un objectif de moins de 0.1°. La technique de calibration acoustique repose sur la diffusion de signaux acoustiques depuis une balise située sur un bateau. Ces signaux sont détectés par les hydrophones situés sur les ancres des unités de détection (DUs). En utilisant la technique de filtrage spatial, la position de la source est reconstruite dans le référentiel du détecteur, puis comparée à la position absolue de la balise calibrée par GPS, afin de contraindre l’orientation absolue et d’améliorer ainsi la précision de pointage du détecteur.

Le filtrage spatial consiste à rechercher un point dans l’espace où la somme des signaux reçus par les hydrophones, après avoir compensé les délais de propagation, présente des interférences constructives. Cette analyse est effectuée sur une grille de points autour de la position GPS de la source. Les signaux de tous les récepteurs sont ensuite corrélés avec le modèle d’émission, et le point de corrélation maximale fournit la meilleure estimation de la position de la balise.

La preuve de concept pour KM3NeT/ORCA a été décrite dans une étude précédente où le système a été simulé [1]. Cependant, des instabilités dans la synchronisation des impulsions acoustiques lors de la précédente campagne en mer en 2020 ont empêché de mener à terme l’étude de l’orientation absolue. Le travail présenté dans cette thèse a permis de résoudre les instabilités temporelles, et de réaliser une nouvelle opération en mer en juillet 2024 qui a donné lieu à une nouvelle analyse de l’orientation absolue encore en cours.

Algorithme d’identification des particules

L’identification des particules est un aspect essentiel de l’analyse des données de neutrinos dans KM3NeT. L’algorithme de reconstruction développé par KM3NeT utilise les signaux de lumière générés par les particules chargées lorsqu’elles traversent l’eau de mer. Les particules chargées, comme les muons et les électrons, produisent de la lumière Cherenkov, qui est détectée par les DOMs. La topologie du signal de lumière peut être utilisée pour identifier la saveur du neutrino qui a interagi.

L’algorithme nommé Random Grid Search (RGS) est une méthode transparente et rapide qui utilise une combinaison de coupures en une ou deux dimensions pour distinguer différentes populations d'événements. Il s'appuie sur seulement quelques paramètres (4 ou 5) issus de la reconstruction et facilite la comparaison entre les données expérimentales et les simulations. Initialement introduit en 1995 lors de la recherche du quark top à Fermilab, il est encore utilisé aujourd'hui, notamment dans les recherches de super-symétrie au LHC.

L'algorithme consiste à rechercher les meilleures coupures possibles, spécifiquement dans les régions où le signal est attendu. Des combinaisons de coupures en 1D ou 2D sont utilisées pour séparer des événements, et les performances du modèle sont évaluées sur la base des taux de vrais positifs et de faux positifs associés aux différentes coupures.

L'efficacité du RGS est comparée à celle d'un algorithme utilisant des Boosted Decision Trees (BDTs) pour isoler les topologies de type trace des topologies de type cascade comme illustré dans la Figure 5. La performance du BDT est meilleure d'environ 5%, mais la réorganisation et l'optimisation des coupures ont permis d'obtenir une sensibilité similaire à la mesure de l'apparition des neutrino tau entre les deux algorithmes d'identification de particules.

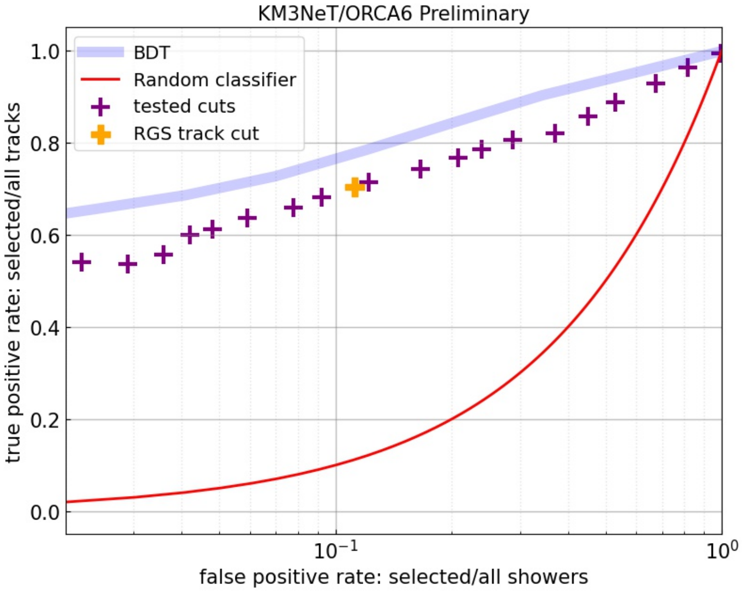

Figure 5: L'efficacité du RGS pour isoler les topologies de type trace est comparée à l'efficacité du BDT en bleu.

Observation des neutrinos tau

L'observation des neutrinos tau est l'un des résultats majeurs de cette thèse. Des neutrinos tau ont été détectés dans KM3NeT/ORCA permettant de réaliser une mesure de leurs propriétés dans une gamme d'énergie presque inexplorée. Cette observation constitue une avancée importante dans l'étude des oscillations des neutrinos atmosphériques, dont sont issus l'ensemble des neutrinos tau observés dans KM3NeT/ORCA. Le nombre d'interactions par courant chargé de neutrinos tau observées, comparé à la prédiction donnée par le paramètre $S_\tau = 0.48^{+0.49}_{-0.33}$, est illustré dans la Figure 6.

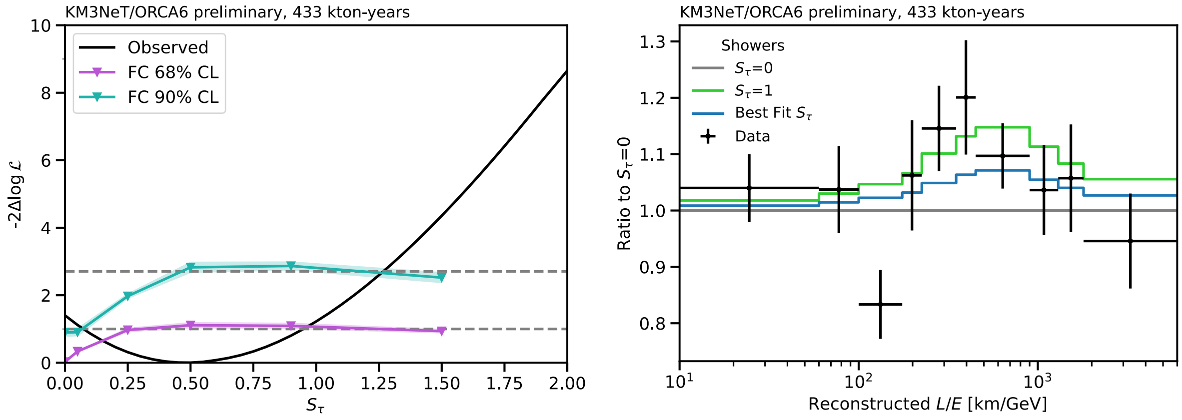

Figure 6: **Gauche:** Profil de likelihood mesuré pour les interactions par courant chargé de neutrino tau. **Droite:** Mesure de la distribution en L/E dans la classe des cascades. Le modèle du meilleur fit est comparé au modèle avec une normalisation nominale et à celui avec une apparition des neutrinos tau nulle.

L'observation de l'apparition des neutrinos tau peut être traduite en une mesure de la section efficace d'interaction à courant chargé du neutrino tau avec une valeur de :

$$\sigma_\tau^{\mathrm{meas}}(E_{\nu_\tau}) = (2.5^{+2,6}_{-1.8}) \times 10^{-38}\,\mathrm{cm}^2$$

pour une énergie médiane des neutrinos tau E_{ν_τ} de 20.3 GeV comme illustrée dans la Figure 7. Cette mesure marque une avancée dans la connaissance des interactions des neutrinos tau, dans cette gamme d'énergie, largement influencé par la masse du lepton chargé tau.

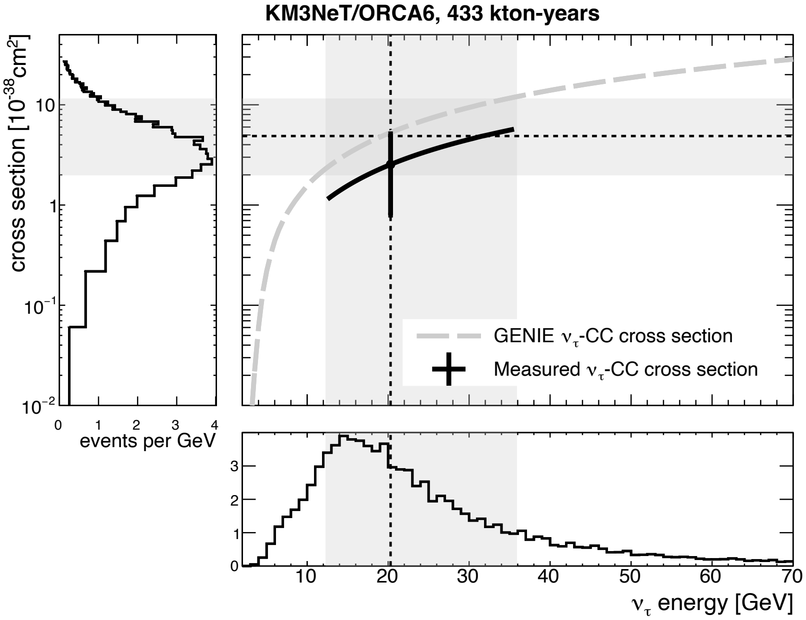

Figure 7: Mesure de la section efficace d'interaction du neutrino tau par courant chargé en noir, comparé à la prédiction théorique moyennée par rapport à $\nu_\tau/\bar{\nu_\tau}$ en gris en fonction de l'énergie.

Étude des modèles de mélange non unitaire des neutrinos

Un autre volet de cette thèse concerne l'exploration des modèles de mélange non unitaire des neutrinos (NUNM). Cette non-unitarité peut être liée à l'existence de nouvelles particules, proposées dans le modèle *seesaw* pour expliquer les faibles masses des neutrinos. Cette étude considère le régime de masse en dessous de 15 MeV pour que les états de masse des neutrinos soient accessibles lors de la désintégration des pions, qui constituent la principales source de neutrinos dits atmosphériques. De plus, pour être dans un régime de masse où les oscillations entre nouveaux états de masses sont moyennées, la masse doit être supérieur à 10 eV. En utilisant les données correspondant à un temps d'exposition de 433 kt-yr, prises avec 6 unités de détections, des contraintes ont été ajoutées sur les paramètres de ces modèles de non-unitarité, en particulier sur le paramètre α_{33}, qui a été restreint à -0.05 à 2 σ, améliorant ainsi la limite précédente par un facteur de 2, comme illustré dans la Figure 8. Des corrections Feldman Cousin ont été appliquées aux limites calculées.

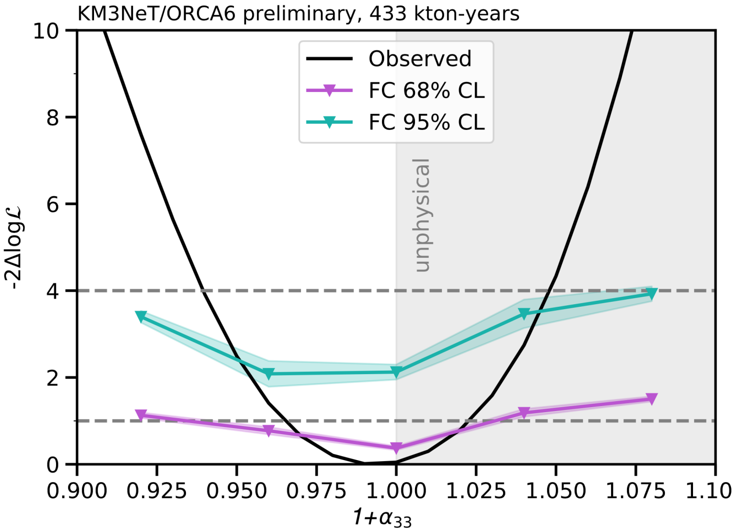

Figure 8: Mesure du profil de likelihood pour le modèle de non-unitarité avec α_{33} libre.

L'influence de la prise en compte du potentiel V_{NC} dans le calcul des effets de matière dans le cas d'un mélange non-unitaire à été décrite. Les effets de matière augmentent largement la sensibilité de KM3NeT/ORCA aux paramètres NUNM.

De plus, l'analyse des paires de paramètres NUNM a révélé une déviation peu significative pour la somme des paramètres α_{22} et α_{33}, offrant ainsi des pistes pour une exploration plus approfondie des combinaisons entre paramètres de la matrice de mélange non unitaire dans cette gamme d'énergie. La déviation est illustrée dans la Figure 9. Une étude Feldman Cousin a été effectuée pour vérifier l'applicabilité du théorème de Wilks dans l'espace des paramètres α_{22} et α_{33}. Cette étude a démontré que le $\Delta\chi^2$ obtenu avec les données correspond à une valeur de p de 0.9% compatible avec la prédiction donnée par le théorème de Wilks.

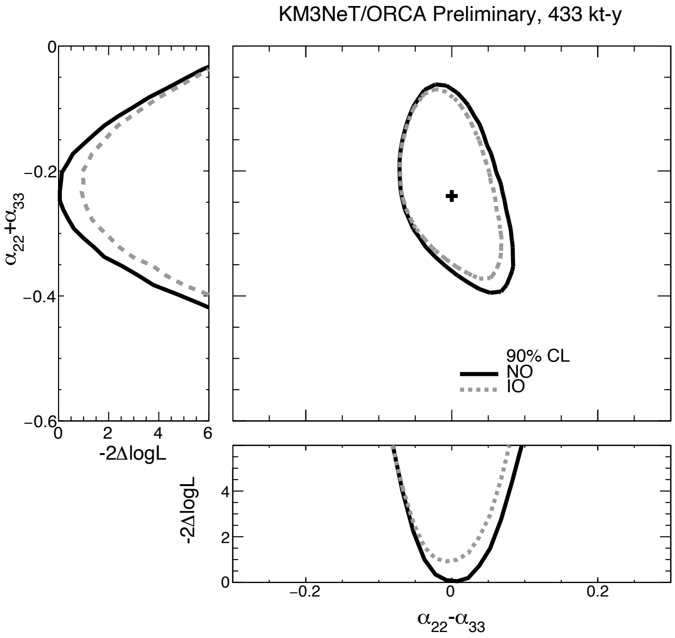

Figure 9: Le contour pour un intervalle de confiance à 90% pour les deux hiérarchies de masses, normale et inversée en noir et en gris pointillé, respectivement.

C'est jusqu'alors la seule mesure de la non-unitarité à basse masse avec plus d'un paramètre libre, utilisant des neutrinos produits dans l'atmosphère et traversant la Terre. L'étude des modèles NUNM ouvre des perspectives pour la recherche de physique allant au-delà du Modèle Standard.

Conclusion

En conclusion, cette thèse a contribué à l'amélioration de systèmes de calibration du détecteur KM3NeT. Des contraintes plus fortes sur son orientation absolue ont été fixées, élargissant ainsi la connaissance sur la précision de pointage du télescope. Grâce à une étude de l'ombre en rayons cosmiques, une corrélation entre l'activité du Soleil et l'ombre du Soleil a été mesurée.

D'autre part, une alternative simple et efficace fondée sur des combinaisons de coupures a été décrite pour discriminer les topologies de type traces des topologies de type cascades. Sa performance a été mesuré légèrement en dessous d'un algorithme de type BDT.

L'observation des interactions par courants chargés des neutrinos tau permet d'établir une mesure du paramètre de normalisation associé à l'apparition des neutrino tau. Cette observation permet aussi une mesure de la section efficace de l'interaction du neutrino tau par courant chargé, dans une région d'énergie encore relativement inexplorée.

Les résultats obtenus dans cette thèse ajoutent des contraintes sur les modèles de mélange non unitaires des neutrinos, dans un régime de masse basse, en considérant les paramètres individuellement ou par paires. L'étude révèle l'importance des effets de matière pour le calcul des probabilités d'oscillation dans le cas non unitaire.

Ainsi l'expérience KM3NeT se positionne comme un instrument de premier plan pour approfondir notre connaissance de la matière à travers l'étude des oscillations des neutrinos.

Remerciements

This thesis has been a long and difficult journey. However it was foremost an incredible opportunity. An opportunity to learn, more than I could dream of, a unique opportunity to contribute to the current knowledge in our field, and an opportunity to meet beautiful people.

First I would like to thank the jury for making this efforts of coming down to Marseille, and for asking me things to verify I deserve such a jury. Thanks to Anca that I met in Helsinki when I started the PhD and that did not forget me.

In particular I would like to deeply thank Sebastian Boser and Corinne Goy for reading in details and provide me your suggestions for the manuscript.

Now I will switch to German. Although I don't speak German I will make this effort once, forgive me for the wrong pronunciation.

Jurgen, vielen Dank, dass du mir nicht nur umfangreiches Wissen in der Physik vermittelt hast, sondern auch gezeigt hast, dass es möglich ist, den Everest zu bezwingen, wenn man mit Aufrichtigkeit und Hingabe arbeitet. Du hast mir beigebracht – ohne es jemals auszusprechen –, dass ich zu viel fähig bin, und dafür danke ich dir von Herzen für das Vertrauen, das du mir seit unserer ersten Begegnung entgegengebracht hast.

Ich habe meinen Vater verloren, als ich noch klein war, und ich denke, er wäre glücklich zu sehen, dass ich Menschen wie dich gefunden habe, um meinen Weg mit ihnen zu teilen. Ebenfalls danke, Alex, für deine Hilfe.

Vincent, merci pour ton accompagnement constant, et la confiance que tu m'as accordé. On a été en mer ensemble envoyer des sons vers le fond pour discuter avec ORCA, de l'extérieur on doit nous prendre pour des fous, mais je suis heureux qu'on y soit arrivé, même s'il reste encore du travail. Et merci de m'avoir permis d'aller vendre nos neutrinos jusqu'au Japon !

Merci à Damien, Mathieu, Manu, Paschal pour votre aide, et vos conseils.

Une fois vous m'avez dit en réunion que j'étais en retard sur l'analyse 'tau appearance', et qu'il est très rare qu'une experience rattrape son retard. Je tenais à vous dire que j'ai tout donné et que je l'ai rattrapé.

Merci à Jerome, Evelyne, Catherine, Sylvain, Pierre, Julian pour votre acceuil au CPPM, ansi qu'Eric bien sur et Mathieu et JP.

Merci à Stefano Panebianco pour m'avoir transmis un gout prononcé pour la recherche experimentale, on a passé que deux mois à travailler ensemble mais ce fut pour moi une découverte précieuse.

Merci au père Camille d'inspirer partout autour de vous la force, la joie et la paix comme vous me l'avez toujours donné.

Merci à ma mère, qui m'a fait confiance, et m'a toujours aimée, même quand je suis lent à répondre. Si on en est arrivé la, c'est avant tout grâce à elle, merci pour tout maman.

Merci à mes frères et soeur, Marie, Thomas et Jennifer (et son fils Paul dans mon coeur), je suis heureux de partager cette thèse avec vous.

Merci à mes amis, d'enfance, Harold, Luis, Nino, Maxime, Ilyes, Rodi de m'avoir suivi toute ma vie, mes amis de KM3NeT, de Marseille, de Genève, de St Martin de la Brasse, d'être venu à la soutenance ca me fait énormément plaisir, et en même temps c'est normal.

Merci à toute ma famille pour votre amour et votre soutien indéfectible, et en particulier ma grand mère qui à fait le trajet jusqu'à Marsielle pour la soutenance.

Merci à Jean le Graet, Etienne, Grod, Tur-tur, Vanuf, Gaya, Hich et Max d'être qui ils sont, continuez comme ça, tout en gardant à l'esprit que ce n'est pas en tapant sur ceux qui nous tappe dessus qu'on rétablie l'équilibre.

Godefroy, malgré le fait qu'on ai des discussions ardentes, je voulais te dire que tu m'as appris beaucoup, et que tu m'as ouvert les yeux sur des choses, merci pour ça. Tu es quelqu'un qui compte beaucoup pour moi , tu m'as parfois aidé quand tu étais toi même en difficulté, c'est une vrai qualité que tu as. Au moment ou j'écris ces mots, depuis la Guinée Forestière, dans le parc nationale du Haut Niger, je t'envoi mes meilleures pensées pour que tu viennes à bout de ton manuscrit de thèse. Je n'ai pas de doute que tu vas finir en beauté, et on se reverra à l'occasion de ta soutenance comme promis !

Merci à la personne qui m'a donné la main pendant toute la durée de ce périple. J'ai hate qu'on continue le chemin ensemble. Et comme j'ai rarement l'occasion de te le dire devant un tel public: je t'aime Tiphaine.

Contents


ORCA
ARCA

Introduction

The main objectives of this thesis are reported as follows. First of all, to improve the knowledge on the absolute orientation of the KM3NeT detectors in order to establish a robust and competitive pointing accuracy. This will indirectly help in the search for new point-like sources of neutrinos. To achieve that purpose different calibration techniques and results are reported.

In addition this thesis aims at improving the knowledge on the charged current tau neutrino interaction cross section by observing ν_τ appearance with data coming from an early stage of the KM3NeT/ORCA detector with only six detection units.

Last but foremost, a key objective of this thesis is to test with the same data, non-unitarity neutrino mixing models in the accessible energy region where they are the least constrained. Those models that describe the generation of the neutrino masses typically involve new massive particles.

Chapter 1 describes neutrinos in the Standard Model and possible extensions to explain the observed oscillations and the neutrino masses.

Chapter 2 explains the detector design and construction. The event reconstruction and simulations are also described. Finally the different calibrations are reported with a particular focus on the positioning system.

Chapter 3 describes the first Moon and Sun cosmic ray shadow measurement with KM3NeT/ORCA6. Constraints on the absolute orientation are discussed together with an exploration of a possible cosmic ray physics signal from the Sun.

Chapter 4 discusses the preparations for a measurement of the absolute orientation using a dedicated acoustic sea campaign.

Chapter 5 explains the technical details of the analysis including the description of an alternative particle identification technique. In addition the fit likelihood and the systematics used in the analysis are introduced.

Chapter 6 presents the observation of the tau neutrino appearance used to measure the charged current ν_τ cross section.

Chapter 7 presents the results on the measurement of the non-unitary neutrino mixing parameters α_{22}, α_{33} and $|\alpha_{32}|$ fitted individually or as pairs.

The contributions of the author of this thesis include:

- The participation to the construction of KM3NeT and the dismantling of ANTARES. The help during deployment campaign as part of the onshore or offshore team.
- The implementation of the Moon/Sun analysis framework used in **Chapter 3**.
- The implementation of the Matlab routine to emit the pulses, control and communicate with all equipments in the acoustic emission system used in **Chapter 4**.
- The preparation and realisation of a successful sea campaign during which the acoustic data used in **Chapter 4** was taken.
- The implementation of the non-unitary neutrino mixing model used in **Chapter 7** in the public software OscProb.
- The implementation of the non-unitary neutrino mixing analysis framework used in **Chapter 7** in the KM3NeT software for oscillation studies.

Chapter 1

Physics context

1.1 History

The story of the neutrino begins in the late XIX$^{\text{th}}$ century when Becquerel discovered radioactivity. Unlike other types of radioactivity Chadwick observed in 1914 that the energy spectrum of the emitted electron in the β-decay was continuous. This led Pauli to the idea, in 1930, that the emission of a new invisible particle could explain the β-decay spectrum while preserving the energy conservation. The new particle should have a mass below 1% of the proton mass, have a spin 1/2 and be neutral therefore he proposed to name it 'neutron'. However Chadwick discovered the neutron in 1932, therefore Fermi proposed in 1933 in the 4-fermion interaction theory - the first weak interaction theory - to name it 'neutrino' (the little neutron in Italian). Although it was thought to be undetectable because of its very small cross section, it was observed, after several attempts, by Reines and Cowan in the Savannah river experiment with a 3/1 signal over background ratio. They have announced their discovery in a letter to Pauli on the 15th of June 1956 [2]. This started a long experimental journey to search for the shy particle's properties.

1.2 Neutrinos and the Standard Model

1.2.1 Electroweak theory

The Standard Model (SM) was born in the end of the sixties as an attempt to build a renormalizable theory for the weak interaction e.g. which ensures finite predictions of physical observables. The Glashow-Weinberg-Salam theory unifying weak and electromagnetic interaction was awarded the Nobel prize in 1979. Since then, the SM predicted the existence of several particles including the $W^{\pm}$, Z and Higgs boson, the latter discovered in 2012 at the Large Hadron Collider (LHC) by the ATLAS and CMS experiments. The SM remains today a common ground in particle physics.

The electroweak theory [3] is a quantum field theory (QFT) that describes particles as quantized excitations of underlying fields. The particles transform under the rules of Lie groups. Those groups named G are defined as a set of elements $\{a, b, \dots\}$ with a multiplication law

$$(a, b) : G \times G \to G$$
$$(a, b) \mapsto ab$$

satisfying closure, associativity, existence of unit element and existence of an inverse element. The group operations as multiplication and inversion, are smooth e.g. infinitely differentiable.

The Lagrangian of the SM describes the evolution of the fields involved in a physical system with respect to the space and time. The SM was constructed by searching for the transformations of the fields that leave the Lagrangian invariant. They represent local gauge symmetries and the groups that contain those transformations are referred to as gauge groups. The gauge group SU(2) contains all transformations that can be represented with a 2×2 unitary matrix of determinant equal to 1. SU(2) doublets are two-field-component vectors written as

$$\psi_l : \quad \begin{pmatrix} \nu_e(x) \\ e(x) \end{pmatrix}, \quad \begin{pmatrix} \nu_\mu(x) \\ \mu(x) \end{pmatrix}, \quad \begin{pmatrix} \nu_\tau(x) \\ \tau(x) \end{pmatrix} \tag{1.1}$$

that transforms under the SU(2) group with $l = e, \mu, \tau$. The chiral projections of ψ are defined as

$$\psi_{lL} = \frac{1-\gamma^5}{2}\psi, \quad \psi_{lR} = \frac{1+\gamma^5}{2}\psi \tag{1.2}$$

with $\gamma^5 = i\gamma^0\gamma^1\gamma^2\gamma^3$ built with the Dirac gamma matrices from the Dirac equation. The $\mathrm{SU}(2)_L$ gauge transformations are represented by 2×2 unitary matrices that act on the weak isospin doublets ψ_l and leave the Lagrangian invariant. They are defined as

$$\psi_{lL}(x) \to \psi'_{lL}(x) = \exp\left(-\frac{\mathrm{i}}{2}\mathrm{g}\alpha^a(x)\sigma^a\right)\psi_{lL}(x) \tag{1.3}$$

$$\psi_{lR}(x) \to \psi'_{lR}(x) = \psi_{lR}(x) \tag{1.4}$$

with $a = 1, 2, 3$ the parameter of transformation, σ^a are the Pauli matrices and g the gauge coupling constant associated to the weak force. In this description of the SM the right-handed component of the field ψ_{lR} transforms as a singlet under $\mathrm{SU}(2)_L$ meaning the gauge transformation leaves unchanged the right-component of the field (index 'L' after 'SU(2)'). This choice is based on the empirical evidence for maximal parity violation in weak interaction. It was discovered by Wu in 1957 [4] via the observation of the rates of emissions of gamma rays and electrons from cobalt-60 radioactive decay in two opposite direction. This observation was theorised in the 2-component neutrino theory by Landau, Lee, Yang and Salam awarded the Nobel prize the same year where the neutrino is described as a massless left or right-handed particle. Still in 1957 Goldhaber experiment probed the helicity of the neutrino and concluded that neutrinos are left-handed. From those experimental evidences the SM was constructed with a massless left-chirality neutrino field ν_L. Thus ν_R does not appear in the SM which assumes massless neutrinos although there is no theoretical motivation not to include it, given the existence of the e_R - or any other fermion - field.

The electromagnetic interaction provides the electroweak theory with a gauge transformation from the gauge group $\mathrm{U}(1)_Y$. The group, unitary of degree 1 and abelian, is associated to the weak hypercharge operator Y defined by $Q = I_3 + \frac{1}{2}Y_W$ where Q is the electric charge and $I_3 = \frac{1}{2}\sigma_3$ is the weak isospin operator. The $\mathrm{U}(1)_Y$ gauge transformations are represented by complex numbers with absolute value 1 representing rotations that act on the ψ_l field and leave the Lagrangian invariant. They are defined as

$$\psi(x) \to \psi'_{lL}(x) = \exp\left(-\frac{\mathrm{i}}{2}\mathrm{g'}Y_L\beta\right)\psi_{lL}(x) \tag{1.5}$$

$$\psi(x) \to \psi'_{lR}(x) = \exp\left(-\frac{\mathrm{i}}{2}\mathrm{g'}Y_R\beta\right)\psi_{lR}(x) \tag{1.6}$$

with β the parameter of transformation, Y the weak hypercharge operator and g' the gauge coupling constant associated to the electromagnetic force.

In order to build a theory that preserve gauge invariance a covariant derivative is used. It involves gauge fields to ensure that the derivative of a field transforms in the same way as the field itself. The required gauge fields are $W^a_\mu, a = 1, 2, 3$ the three from $\mathrm{SU}(2)_L$ group and one field, B_μ, from the $U(1)_Y$ group. They are involved in the description of the field strengths as follows

$$F^a_{\mu\nu} = \partial_\mu A^a_\nu - \partial_\nu W^a_\mu - \frac{g}{2}\epsilon_{abc}\left(W^b_\mu W^c_\nu - W^b_\nu W^c_\mu\right) \tag{1.7}$$

$$G_{\mu\nu} = \partial_\mu B_\nu - \partial_\nu B_\mu. \tag{1.8}$$

Due to the violation of parity in the SM, the mass term $m\bar{\psi}\psi = m\left(\bar{\psi}_L\psi_R + \bar{\psi}_R\psi_L\right)$ does not leave the Lagrangian invariant under $\mathrm{SU}(2)_L$ gauge transformation. Therefore to preserve the symmetries of the SM the fermionic fields are considered to be massless. However in 1964, Brout, Englert, and Higgs found a mechanism [5] giving rise to the mass. In this mechanism an energy potential $\mathrm{V}(\phi)$ function of the Higgs field doublet $\Phi(x)$ is involved in the Lagrangian. The potential finds its minimum for an infinity of non-zero values of the Higgs field that forms the vaccum manifold (the space of all possible vacuum states). The Higgs field acquires a vacuum expectation value (vev) by fixing the arbitrary phase of the field. The $\mathrm{SU}(2)_L \times \mathrm{U}(1)_Y$ symmetry of the SM is then spontaneously broken down to $\mathrm{U}(1)_{em}$. The zero phase convention is the unitarity gauge defined as

$$\Phi(x) \longrightarrow \phi(x) = \begin{pmatrix} 0 \\ \frac{v+\varphi(x)}{\sqrt{2}} \end{pmatrix} \tag{1.9}$$

with v the vev of the Higgs field and $\varphi(x)$ a real function describing the excitation around the vev of the Higgs field: the Higgs boson.

From the covariant derivatives in the kinetic term of the Higgs Lagrangian that involves the gauge fields W_μ^a and B_μ the bosons mediating electroweak and electromagnetic interaction naturally arise:

$$W_\mu = \frac{1}{\sqrt{2}}\left(W_\mu^1 - iW_\mu^2\right) \tag{1.10}$$

$$Z_\mu = \cos\theta_W W_\mu^3 - \sin\theta_W B_\mu \tag{1.11}$$

$$A_\mu = \sin\theta_W W_\mu^3 + \cos\theta_W B_\mu. \tag{1.12}$$

with W_μ and Z_μ for the weak interaction bosons, the massless photon field A_μ resulting from the unbroken $\mathrm{U}(1)_{em}$ symmetry and the Weinberg's angle θ_W defined as

$$\cos\theta_W = \frac{g}{\sqrt{g^2+g'^2}}, \qquad \sin\theta_W = \frac{g'}{\sqrt{g^2+g'^2}}. \tag{1.13}$$

From the spontaneous symmetry breaking (SSB) the masses of the W^+, W^+, Z^0 and H (for Higgs) bosons are generated as

$$m_W^2 = \frac{1}{4}g^2v^2 \tag{1.14}$$

$$m_Z^2 = \frac{1}{4}(g^2+g'^2)v^2 \tag{1.15}$$

$$m_H^2 = 2\lambda v^2 \tag{1.16}$$

with $v = 246$ GeV and λ the self-coupling constant of the Higgs field. The mass term resulting from the SSB are not invariant under the SM symmetries.

1.2.2 Lepton masses

In order to generate the mass of the fermions that do not naturally arise from the Higgs mechanism the symmetries of the SM must be preserved. From the Yukawa term the masses of the fermions upon the SSB are generated while preserving the symmetry. The Yukawa term in the Lagrangian is defined as

$$\mathcal{L}_{\text{Yukawa}} = -\sqrt{2}y_\ell\overline{\psi}_{\ell L}\Phi\psi_{\ell R} + h.c. \tag{1.17}$$

where the Higgs field Φ become ϕ after the SSB and y_ℓ is the Yukawa coupling constant a free dimensionless parameter associated to the lepton ℓ. From this term arise the lepton masses, which gives for the electron

$$\mathcal{L}_{\text{Yukawa}} = -y_e v\,\overline{e}_L(x)e_R(x) - y_e\overline{e}_L(x)e_R(x)\varphi(x) + h.c. \tag{1.18}$$

where $m_e = y_e v$. As described above the Yukawa term is constructed for quarks and leptons from the left and right-handed components of the fields coupling to the Higgs field. However by construction (from empirical evidence) in the SM only the left-handed component of the neutrino field is included, therefore the neutrino mass term can't be generated within the SM.

1.2.3 Neutrino interaction

As part of the left-handed component of the lepton doublet $\psi_{\ell L} = \begin{pmatrix} \nu_{\ell L} \\ \ell_L \end{pmatrix}$ the neutrino participate in the weak interaction. The interactions with the weak bosons upon SSB are found by writing the covariant derivatives of the left and right-handed leptonic fields involving the gauge fields W^a_μ and B_μ. The Lagrangian for the CC interaction is defined as

$$L^{CC}_{int} = -\frac{g}{2\sqrt{2}}j^{CC}_\mu W^\mu + \text{h.c.} \tag{1.19}$$

with W^μ the weak boson field and the charged current j^{CC}_μ for the three generation of leptons written as

$$j^{CC}_\mu = 2\left[\bar{\nu}_{eL}\gamma^\mu e_L + \bar{\nu}_{\mu L}\gamma^\mu \mu_L + \bar{\nu}_{\tau L}\gamma^\mu \tau_L\right]. \tag{1.20}$$

Only the left-handed projection of the leptonic fields take part in the weak interaction. Weak charged currents have a Vector-Axial structure that implies parity violation. This gives rise to the charged current interaction involving charged leptons and neutrinos as shown in Figure 1.1 with the exchange of a $W^{+/-}$ boson. The Lagrangian for the NC interaction is defined as

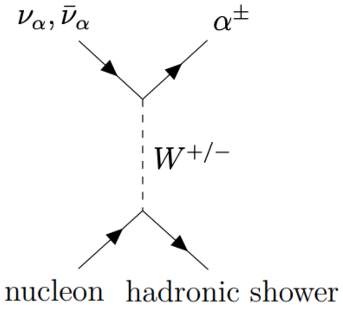

Figure 1.1: Feynman diagram for charged current (CC) interaction involving a lepton α and a neutrino ν_α.

$$\mathcal{L}_{\text{int}}^{NC} = -\frac{g}{2\cos\theta_W} j_\mu^{NC} Z^\mu \tag{1.21}$$

with Z^μ the Z^0 boson field and the neutral current j_μ^{NC} for the electron that includes a weak and electromagnetic part written as

$$j_\mu^{NC} = 2g_L^\nu \bar{\nu}_{eL}\gamma_\mu \nu_{eL} + 2g_L^e \bar{e}_L \gamma_\mu e_L + 2g_R^e \bar{e}_R \gamma_\mu e_R \tag{1.22}$$

The coefficients g_L^f, g_L^e, g_R^e are defined as

$$g_L^f = I_3^f - q_f \sin^2\theta_W \tag{1.23}$$

$$g_R^f = -q_f \sin^2\theta_W \tag{1.24}$$

where I_3^f is the third component of weak isospin and q_f is the electric charge of the corresponding fermionic particle f. The electromagnetic coupling constant $g_{em} = g\sin\theta_W$ corresponds to the charge of the electron e. The neutral-current interaction converts neutrinos in themselves as shown in Figure 1.2 with the exchange of a Z^0 boson.

1.2.4 Neutrino cross section

In most charged current interaction at the GeV scale, the nucleon is disrupted and hadronic final states are produced. This hadronisation process occurs as a consequence of the confinement in the strong interaction. As shown in Figure 1.3 above 10 GeV the deep inelastic

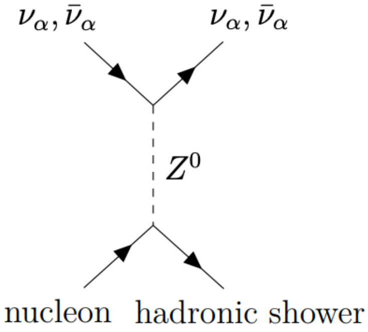

Figure 1.2: Feynman diagram for neutral current (NC) interaction involving a neutrino ν_α with flavour α.

scattering (DIS) prevails. An isoscalar target has a balanced number of protons and neutrons. The total neutrino-nucleon cross section is of the order $\sigma_\nu/E \approx 10^{-38}\text{cm}^2/\text{GeV}$. In the region between 2 and 10 GeV also relevant for KM3NeT/ORCA the resonant scattering occurs where the nucleon is converted to a resonant state. The resonance then produces a set of one or several π or K during decay. In addition the cross section at first order increases linearly with E_ν. Due to the helicity of the relativistic neutrino there is a smaller

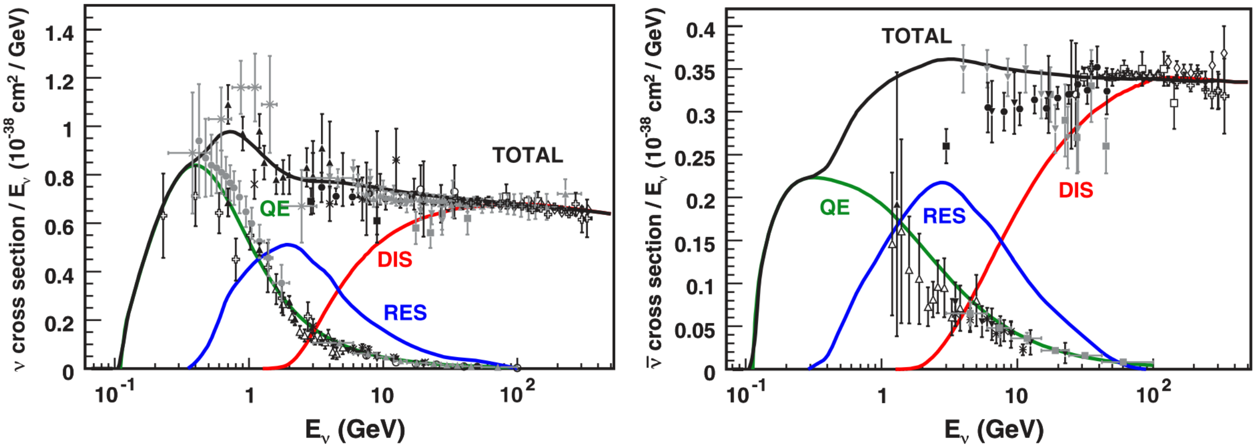

Figure 1.3: The total muon neutrino and anti-neutrino charged-current cross section per nucleon divided by the neutrino energy, as a function of energy, for an isoscalar target. The different processes which contribute to the total cross section are shown as quasi-elastic scattering (QE), deep inelastic scattering (DIS) and resonance production (RES). Taken from [6].

scattering angle between the neutrino and the outgoing lepton and a higher energy transfer to the outgoing lepton (smaller bjorken-y) for anti-neutrinos compared to neutrinos. This results in the ratio of neutrino anti-neutrino cross sections ratio as $\sigma_{\nu}^{CC}/\sigma_{\bar{\nu}}^{CC} \approx 2$. The NC cross section is about three times smaller than for CC interaction.

The products of the charged current interaction can be defined as $\bar{\nu}_{\ell}$ + nucleon $\rightarrow$ $\ell^{-} + H$ or ν_{ℓ} + nucleon $\rightarrow \ell^{+} + H$ with ℓ the lepton and H the hadronic shower.

The different topologies and event signature that are observed from DIS interaction in the sea water are described in Figure 1.4. They constitute the signal events that water Cherenkov detectors search for. For all neutrino interactions a hadronic shower is produced carrying a fraction y of the neutrino energy. The longitudinal extension of the shower is expected to be small (below 10 metres) due to the short interaction length in water therefore resembling a single point emission. Depending on the outgoing lepton flavour the event signature is considered to be track-like or shower-like. If it is track-like the light pattern from the outgoing lepton is expected to match the hypothesis of a Cherenkov light emitting muon. Below 100 GeV the muon is expected to be a minimum ionizing particle with a constant energy loss (dE/dx) producing a long and straight track. The atmospheric muons and the CC muon neutrino events appear predominantly track-like.

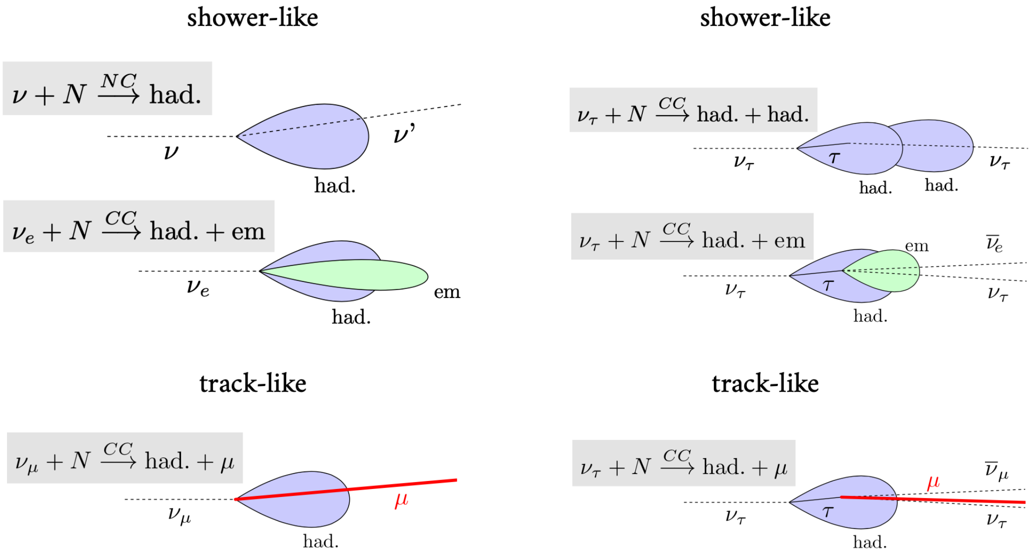

Figure 1.4: Schematic of the topologies of the neutrino interaction for ν^{NC}, ν_e^{CC} and ν_μ^{CC} on the left side and ν_τ^{CC} on the right side from [7].

In addition due to the short radiation length of few tens of cm of the outgoing electron, the electron neutrino interaction is considered shower-like. It propagates in water before an electromagnetic shower is produced involving the emission of photons and $e^{+/-}$ pairs until the energy falls below the threshold of pair production and bremsstrahlung. Electromagnetic showers only have an extension of few metres with a ≈ 20% larger light yield than hadronic showers produced in NC interaction.

The tau neutrino-nucleon scattering has a minimum energy threshold of

$$E_{\text{thres}} = m_\tau \left(1 + \frac{m_\tau}{2 \cdot m_N}\right) = 3.46\,\text{GeV} \tag{1.25}$$

with the outgoing tau lepton $\tau^\pm$ and the tau lepton mass $m_\tau = 1.777\,\text{GeV}/c^2$.

The CC tau neutrino interaction cross section is described in Figure 1.5. For anti-neutrino with ≈ 20 GeV the DIS is 2/3 of the total cross section while in the neutrino case DIS contributes to the vast majority of the interactions. Due to the heavy tau lepton mass the CC tau neutrino cross section is suppressed to the level of half the other flavour cross sections at around 25 GeV as shown in Figure 1.6 obtained with [8]. Only few measurements of the CC tau neutrino cross section exist. From the theoretical side, the relative contribution of the different scattering differs compared to the electron and muon neutrino cross section. Additional form factors in the cross section have a sizeable impact. The theoretical uncertainty on the muon to tau neutrino cross-section ratio above 10 GeV are estimated to be below 1% (2% for anti-neutrino) in the DIS regime [9]. In the lower energy region where the nucleus and the tau polarisation impact have not been studied extensively the uncertainties are larger. Due to the mass of the tau lepton and its effect

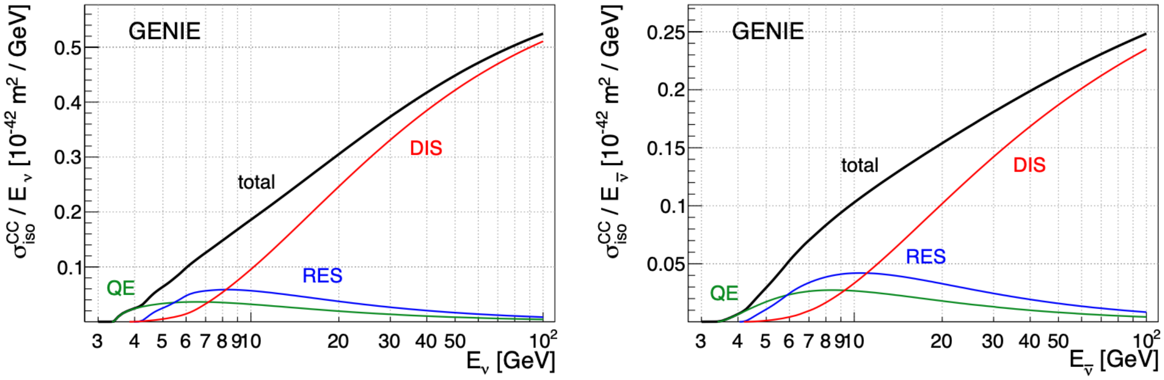

Figure 1.5: The total tau neutrino and anti-neutrino per nucleon charged-current cross sections divided by neutrino energy, as a function of energy, for an isoscalar target.

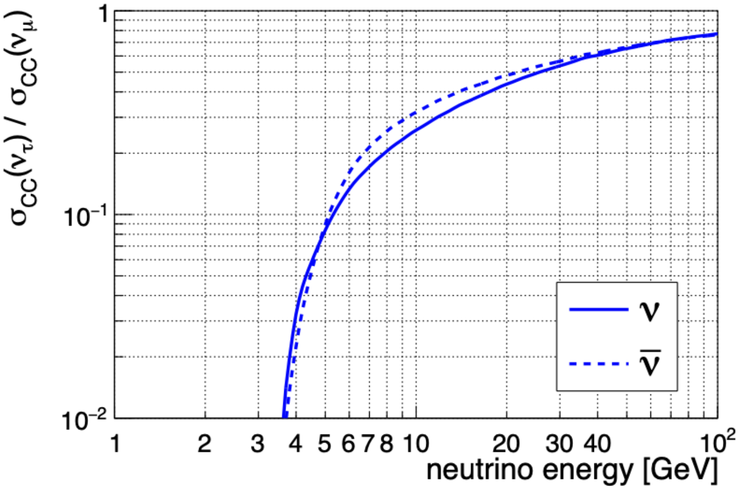

Figure 1.6: The ratio of the total tau neutrino and anti-neutrino to muon neutrino and anti-neutrino respectively charged-current cross sections per nucleon as a function of energy.

on the maximum inelasticity y the neutrino is closer to the anti-neutrino cross section compared to the case of the muon neutrino.

In all CC ν_τ interaction a tau lepton is produced with a decay livetime of 2.9×10^{-13} seconds. The decay livetime converts in a track of a few millimetres in the relevant few GeVs energy range therefore negligible when compared to the precision on the vertex (shower origin) position. Although at higher energies in the hundreds of TeV to PeV range the tau lepton is relativistic enough for the tau npoeutrinos to produce a double shower signature. The tau decay is illustrated in Figure 1.7. The CC tau neutrino interaction

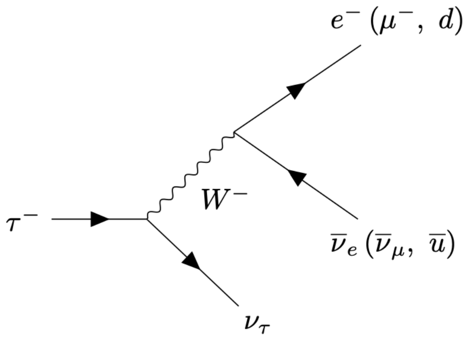

Figure 1.7: Feynman diagram for the tau lepton decay.

appears predominantly in the shower-like channel due to the hadronic or electromagnetic showers produced after the decay. However when the tau decays into a muon, a track-like event signature is expected. A tau neutrino is always produced in the final states for lepton number conservation. If leptonic, the decay will produce a second neutrino alongside the charged lepton. On the other hand the hadronic final state (65% BR) typically involves the production of pions. The branching ratios of the tau decay are provided in Figure 1.8. Where 17.4% of the decays will leave a track-like signature and 82.6% are expected shower-like. Due to the invisible outgoing tau neutrino produced in the interaction the overall light yield is lower, compared to other CC interactions

$$\left.\begin{array}{lll} \tau^- & \rightarrow e^- \, \overline{\nu}_e \, \nu_\tau & (17.8\%) \\ \tau^- & \rightarrow \mu^- \, \overline{\nu}_\mu \, \nu_\tau & (17.4\%) \end{array}\right\} \quad \textbf{leptonic} \quad \textbf{(35.2\%)}$$

$$\left.\begin{array}{lll} \tau^- & \rightarrow \pi^- \, \pi^0 \, \nu_\tau & (25.5\%) \\ \tau^- & \rightarrow \pi^- \, \nu_\tau & (10.8\%) \\ \tau^- & \rightarrow \pi^- \, \pi^0 \, \pi^0 \, \nu_\tau & (9.3\%) \\ \tau^- & \rightarrow \pi^- \, \pi^- \, \pi^+ \, \nu_\tau & (9.0\%) \\ \tau^- & \rightarrow \pi^- \, (> 2\pi) \, \nu_\tau & (9.0\%) \end{array}\right\} \quad \textbf{hadronic} \quad \textbf{(64.8\%)}$$

Figure 1.8: Tau decay branching ratios.

1.3 Neutrino masses

Constructed on robust experimental evidence, including the discovery of maximal parity violation and the measurement of the Z decay width [10], the minimal SM involves only three left-handed massless neutrino fields transforming as doublets under the fundamental representations of the gauge group $SU(2)_L \times U(1)_Y$. The discovery of neutrino oscillations [11] predicted by Pontecorvo in 1957 [12] paved the way to non-zero neutrino mass. Since then, neutrino oscillations were measured with a high precision by numerous neutrino experiments described in Section 1.4. However in its current form the SM does not allow for the generation of the neutrino mass, which typically for the fermions involves left and right chiralities. Therefore the SM must be extended with at least a right-handed chirality component of the neutrino field.

1.3.1 Present constraints

Neutrino oscillations, described in Section 1.4, are driven by the mass square difference Δm^2 between neutrino mass eigenstates ν_1, ν_2, ν_3 with masses m_1, m_2, m_3. The measured Δm^2_{31} Δm^2_{21} can be translated in a lower limit on the highest neutrino mass and m_2 as

$$\begin{aligned} &m_\nu^{\text{high}} = \max\{m_2, m_3\} > 50 \text{ meV}. \\ &m_2 > 8 \text{ meV}. \end{aligned}$$

In addition other experiments probe directly the neutrino mass via the measurement of the shape of the electron energy spectrum originating from tritium beta decay. A different shape of the spectrum is expected around the end point for a non-zero neutrino mass. The KATRIN experiment has reported the current best limit on the effective electron neutrino mass [13]

$$m_\beta = \sqrt{\sum_i |U_{ei}|^2 m_i^2} < 450 \text{ meV} \tag{1.26}$$

which is $\approx 10^{-6}$ order of magnitude below the electron mass. Therefore placing a limit of < 500 meV on m_ν^{high}. In addition the field of cosmology based on the Planck, ACT and DESI BAO data [14] has recently placed stringent bounds on the sum of the neutrino masses as

$$\sum m_\nu \equiv \sum_{i=1}^{3} m_i < 72 \text{ meV}. \tag{1.27}$$

However, due to a best fit in the negative nonphysical region the constraints are so strict that they are in tension with the extensively measured neutrino oscillation, therefore suggesting physics beyond the standard model of cosmology which is based on the cosmological constant λ_{CDM} [15].

1.3.2 Dirac mass term

The simplest extension of the SM in order to write the neutrino mass does not require any new mechanism nor particles in the SM [3]. It is refereed to as the Dirac mass term. In analogy to the leptons and quarks it involves a right-handed neutrino field $\nu_R(x)$ independent from $\nu_L(x)$ for each of the three generations. The Yukawa term corresponding to the Dirac neutrino is defined as

$$\mathcal{L}_{\text{Yukawa}} = -\sqrt{2} y_{\nu_l} \overline{\psi}_{lL} \tilde{\Phi} \nu_{lR} + \text{h.c.} \tag{1.28}$$

with y_{ν_l} the Yukawa constant coupling associated to ν_l ($l = e, \mu, \tau$), $\tilde{\Phi}$ the conjugated Higgs doublet also involved in the quark mass term and ψ_{lL} the lepton doublet. The mass term appears after SSB as

$$\mathcal{L}^D_{\text{mass}} = -\overline{\nu_R} M^D \nu_L + \text{h.c.} = -\sum_{\ell,\ell'} \overline{\nu}_{\ell L}(x) M^D_{\ell'\ell} \nu_{\ell' R}(x) + \text{h.c.} \tag{1.29}$$

with M^D a 3×3 complex non-diagonal matrix.

In order to find the physical fields of the theory that satisfy the free Dirac equation uncoupled, M^D must be diagonalized as $M^D = U^\dagger m V$ with U, V unitary matrices. Therefore revealing the physical fields ν_1, ν_2, ν_3 that are associated to the masses m_1, m_2, m_3 and satisfy the Dirac equation. The fields involved in the weak interaction $\nu_{\ell L}$ are mixed with a linear superposition of the mass fields defined as

$$\nu_{\ell L}(x) = \sum_{i=1,2,3} U_{\ell i} \nu_{iL}(x) \tag{1.30}$$

$$\nu_{\ell R}(x) = \sum_{i=1,2,3} U_{\ell i} \nu_{iR}(x). \tag{1.31}$$

with $U_{\ell i}$ the lepton mixing matrix. In the Dirac scenario the family lepton number is not conserved, due to the mixing, however the total lepton number is conserved.

The Yukawa coupling constant y_f describing the coupling of the fermions with the Higgs boson increases with increasing mass of the fermion [16] as

$$y_\nu \simeq 3 \times 10^{-13}, \quad y_e \simeq 3 \times 10^{-6}, \quad y_t \simeq 1. \tag{1.32}$$

when considering a neutrino mass of ≈ 50 meV, t the top quark. The hierarchy of the fermion mass spectrum represents a fundamental problem in elementary particle physics and can't be solved within the framework of the Standard Model. However, despite neutrino mass, the large separation between the electron and the t-quark mass scale in the SM already suggest a more fundamental theory. A new theory involving a mass scale Λ different from the electroweak scale v was proposed by Weinberg in 1979 [17] called the effective field theory (EFT). It extends the SM by introducing higher mass dimension operators ($dim > 4$) dynamically giving rise to the neutrino mass. In this theory the total lepton number is violated by two units and the theory is non-renormalizable.

1.3.3 Dirac and Majorana mass terms

A Majorana field describes a particle that is its own anti-particle therefore satisfying the equation $\psi(x) = \psi_L + (\psi_L)^c = \psi^c(x)$ with $\psi^c(x)$ the charged-conjugated field and C the charge-conjugated matrix. As mentioned in the previous section, the mass term in the Lagrangian involves a left and right chirality component. To build it it is possible to conjugate the left-handed component ψ_L which transforms it into a right-handed field $(\psi_L)^c$ not independent from ψ_L (as in the Dirac case). Therefore in that case the field $\nu = \nu_L + (\nu_L)^c$ and the Majorana mass term is defined as

$$\mathcal{L}^M_{mass} = -\frac{1}{2}\overline{\nu^C_L} M \nu_L + \text{h.c.} \tag{1.33}$$

with M the non-diagonal Majorana mass matrix. This mass term could rise from a dimension > 5 operator within the EFT, therefore violating the total lepton number.

The most general mass term involving both Dirac and Majorana mass term is written as a combination of all the chiral fields as

$$\mathcal{L}^{D+M}_{mass} = -\frac{1}{2}\overline{(\nu_L)^c} M^L \nu_L - \overline{\nu_R} M^D \nu_L - \frac{1}{2}\overline{(\nu_R)^c} M^R \nu_R + \text{h.c.} \tag{1.34}$$

with M^L, M^D, M^R non-diagonal 3×3 matrices. They are associated to the left-handed Majorana, the Dirac and the right-handed Majorana mass term, respectively. However at this stage the field are not the physical fields as the mass matrix is not diagonal. The Lagrangian can be written in a larger matrix form as

$$\mathcal{L}^{D+M}_{mass} = -\frac{1}{2}\overline{(n_L)^c} M n_L + \text{h.c.}, \tag{1.35}$$

with the neutrino field as

$$n_L = \begin{pmatrix} \nu_L \\ (\nu_R)^c \end{pmatrix} \tag{1.36}$$

and

$$M = \begin{pmatrix} M^L & (M^D)^T \\ M^D & M^R \end{pmatrix}. \tag{1.37}$$

The matrix M is 6×6 symmetrical. In order to simplify the discussion the case of a single generation among e, μ, τ is considered. In that case M is defined as

$$M = \begin{pmatrix} m_L & m_D \\ m_D & m_R \end{pmatrix}. \tag{1.38}$$

As in the Dirac case M has to be diagonalised following $M = (U^\dagger)^T m U^\dagger$ with m the neutrino mass matrix. The mixing matrix $U = \mathcal{O}\eta^{1/2}$ with η a diagonal matrix with entries ± 1 and

$$\mathcal{O} = \begin{pmatrix} \cos\theta & \sin\theta \\ -\sin\theta & \cos\theta \end{pmatrix} \tag{1.39}$$

with $\tan 2\theta = \frac{2m_D}{m_R - m_L}$. The mixing angle θ describes the mixing of the neutrino mass states within a single generation. The masses involved in $m = \mathrm{diag}\{m_{1a}, m_{1b}\}$ are defined as

$$m_{1a,1b} = |\ \frac{1}{2}(m_L + m_R) \pm \frac{1}{2}\sqrt{(m_R - m_L)^2 + 4m_D^2}\ |. \tag{1.40}$$

If $m_L = m_R = 0$ the scenario falls back to the Dirac mass term with $m_\nu = m_D$. When $m_L \approx m_R << m_D$ neutrinos are Pseudo-Dirac e.g they behave as Dirac particles with almost degenerate mass $m_\nu \approx m_D$ and mass states that involve a small Majorana mixing. In the general case the diagonalised mass term can be written as

$$\mathcal{L}_{mass}^{D+M} = -\frac{1}{2}\overline{\nu^M} m \nu^M \tag{1.41}$$

with

$$\nu^M = U^\dagger n_L + (U^\dagger n_L)^c = \begin{pmatrix} \nu_{1a} \\ \nu_{1b} \end{pmatrix}. \tag{1.42}$$

In that description the ν^M that diagonalize the mass matrix are composed of two massive Majorana ($\nu^M = (\nu^M)^c$) fields, ν_{1a} and ν_{1b}, associated to m_{1a} and m_{1b}. The two left-handed component of the neutrino field n_L can be decomposed as

$$\nu_{1L} = \cos\theta\sqrt{\eta_1}\nu_{1aL} + \sin\theta\sqrt{\eta_2}\nu_{1bL} \tag{1.43}$$

$$(\nu_{1R})^c = -\sin\theta\sqrt{\eta_1}\nu_{1aL} + \cos\theta\sqrt{\eta_2}\nu_{1bL}. \tag{1.44}$$

Therefore described as mixed stated involving the left-handed ν_{1L} and ν_{2L} mass states.

The minimal Dirac and Majorana scenario in the three generation framework involves 6 neutrino mass states as illustrated in Figure 1.9 where the quarks and leptons are presented with their masses and electric charge. The neutrino oscillation measurement are consistent with at least 2 massive neutrino states, therefore if neutrinos are Majorana particles there exist at least two additional unobserved neutrino states.

In general, the mass and mixing matrix could be of dimension $n = 3 + n_u$ where n_u is the number of unobserved neutrino states and ℓ is e, μ or τ therefore weak defining the interaction fields as

$$\nu_{\ell L} = \sum_{i=1}^{n} U_{\ell i}\nu_{iL} \tag{1.45}$$

$$(\nu_{uR})^c = \sum_{i=1}^{n} U_{ui}\nu_{iL}. \tag{1.46}$$

The new mass states can be produced in any interaction where kinematically allowed. In the case of $n = 3$ the three generation structure of the SM is preserved.

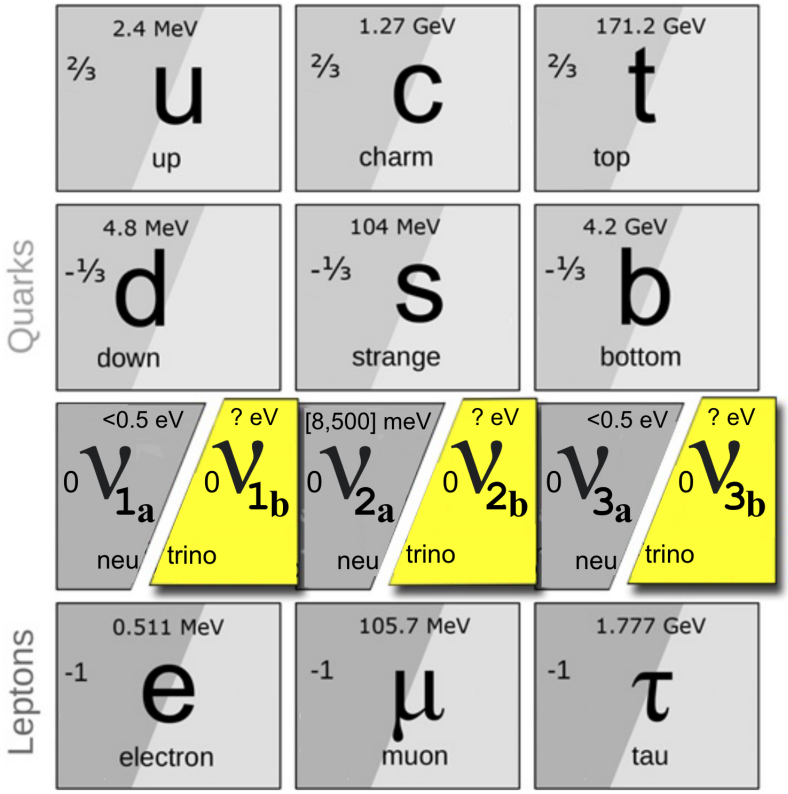

Figure 1.9: The three generations of fermions of the Standard Model and beyond. There are 3 neutrino mass states: ν_1, ν_2, ν_3. Each generation of neutrino is composed of two mass states, identical in the Dirac scenario and with distinct masses in the Dirac+Majorana scenario.

1.3.4 Seesaw mechanism

The seesaw mechanism resembles the Dirac+Majorana scenario. It restricts $M^L = 0$ and assumes the Dirac mass is generated from the Higgs mechanism after SSB and the Yukawa coupling is unknown, it is assumed to be of the order of 1. The mass matrix elements associated to the right-handed Majorana mass term in the minimal seesaw must be higher than $v = 246$ GeV. In that case for a single generation ℓ with the mass states ν_{1a} and ν_{1b}, the masses $m_{1a} \approx m_D^2/m_R << m_R$ and $m_{1b} \approx m_R$. The neutrino fields are defined as

$$\nu_{\ell L} \simeq i\nu_{1aL} + \frac{m_D}{m_R}\nu_{1bL} \tag{1.47}$$

$$(\nu_{\ell R})^c \simeq -i\frac{m_D}{m_R}\nu_{1aL} + \nu_{1bL}. \tag{1.48}$$

In that scenario the m_{ia} masses are suppressed thanks to the high mass scale m_{ib} of the heavy neutrino counterpart ν_{ib} (with $i = 1, 2, 3$) at the order of the grand unified theory (GUT) scale.

Only three neutrino flavours were observed, suggesting that the new neutrino states are either very massive (canonical type-I seesaw) therefore difficult to produce, either accessible but with small couplings to the favour neutrino fields. Other seesaw mechanism exist involving a Higgs triplet (type-II seesaw) or three heavy triplet fermion (type-III seesaw) to generate the small neutrino masses. Depending on the value for the neutrino Yukawa coupling constant, and relying on new parameters in the the D+M mass matrix, the new neutrino states can be observed at intermediate masses (as in the linear and inverse Type-I seesaw). However the constraints from the weak interaction involving the electroweak lepton doublets and neutrino oscillation constraints on the neutrino mixing matrix unitarity suggest very small $U_{\ell i}$ $(i > 3)$ couplings making them currently unobserved.

In this dissertation the presence of new states in the intermediate mass scale is later studied as a deviation of the neutrino mixing matrix from unitarity producing slight changes in the oscillation probabilities.

1.4 Neutrino oscillations

1.4.1 Theory of neutrino oscillation

In the SM neutrinos are produced from charged current interaction as

$$\mathcal{J}_\mu^{CC} = \sum_{\alpha=e,\mu,\tau} \bar{\nu}_{\alpha L}\gamma_\mu \alpha_L \tag{1.49}$$

with $\nu_{\alpha L}$ the left-handed projection of neutrino field. Assuming Dirac or Majorana neutrinos mass states the Lagrangian is diagonalized by the fields ν_i, $i = 1, 2, ...3 + n_u$ with n_u unobserved possible neutrinos fields. In the standard oscillation framework, $n_u = 0$ is assumed. The ν_i fields are well-defined since they admit creation and annihilation operators. On the other hand the flavour fields do not admit creation and annihilation operators, since they do not have a definite mass, therefore $|\nu_\alpha\rangle$ states are strictly defined as a coherent superposition of the mass states as

$$|\nu_\alpha\rangle = \sum_{i=1}^{3} U^*_{\alpha i} |\nu_i\rangle \tag{1.50}$$

with $U = U_{\mathrm{PMNS}}$ the lepton mixing matrix. The mixing matrix U is assumed to be 3×3 unitary thus $UU^\dagger = I$ therefore

$$\sum_i |U_{\alpha i}|^2 \equiv 1 \quad \alpha = \{e, \mu, \tau\} \quad \text{and} \quad \sum_\alpha |U_{\alpha i}|^2 \equiv 1 \quad i = \{1, 2, 3\}. \tag{1.51}$$

U_{PMNS} rotates the mass basis onto the flavour basis as

$$\begin{pmatrix} \nu_e \\ \nu_\mu \\ \nu_\tau \end{pmatrix} = U_{\mathrm{PMNS}}(\theta_{12}, \theta_{13}, \theta_{23}, \delta_{\mathrm{CP}}, \alpha_1, \alpha_2) \begin{pmatrix} \nu_1 \\ \nu_2 \\ \nu_3 \end{pmatrix}. \tag{1.52}$$

with three mixing angles $\theta_{12}, \theta_{13}, \theta_{23}$, one charge parity violating phase δ_{CP} and two additional phases α_1, α_2 if neutrinos are Majorana. The matrix elements are expressed as

$$U_{\mathrm{PMNS}} = \begin{pmatrix} c_{12}c_{13} & s_{12}c_{13} & s_{13}e^{-i\delta_{\mathrm{CP}}} \\ -c_{23}s_{12} - s_{23}c_{12}s_{13}e^{i\delta_{\mathrm{CP}}} & c_{23}c_{12} - s_{23}s_{12}s_{13}e^{i\delta} & s_{23}c_{13} \\ s_{23}s_{12} - c_{23}c_{12}s_{13}e^{i\delta_{\mathrm{CP}}} & -s_{23}c_{12} - c_{23}s_{12}s_{13}e^{i\delta_{\mathrm{CP}}} & c_{23}c_{13} \end{pmatrix} \begin{pmatrix} 1 & 0 & 0 \\ 0 & e^{i\alpha_1} & 0 \\ 0 & 0 & e^{i\alpha_2} \end{pmatrix} \tag{1.53}$$

with $s_{ij} \equiv \sin(\theta_{ij})$.

The oscillation probabilities in this dissertation are calculated using the OscProb software [18] in KM3NeT. The complete matter potential V and the mass splitting matrix Δ are defined in Eq. 7.7 with $V_{CC} = \sqrt{2}G_F n_e$ and $V_{NC} = -\frac{1}{\sqrt{2}}G_F n_n$, where n_e and n_n are the electron and neutron number density, respectively.

$$\Delta = \frac{1}{2E}\begin{bmatrix} 0 & 0 & 0 \\ 0 & \Delta m^2_{21} & 0 \\ 0 & 0 & \Delta m^2_{31} \end{bmatrix} \qquad V = \begin{bmatrix} V_{CC} + V_{NC} & 0 & 0 \\ 0 & V_{NC} & 0 \\ 0 & 0 & V_{NC} \end{bmatrix} \tag{1.54}$$

However when assuming a unitary neutrino mixing, as the NC interaction identically couples to all flavours, it introduces an overall phase shift which does not affect the oscillation probabilities therefore the V_{NC} term can be set to zero. In the non-unitary case studied in the Chapter 7 this effect must be included as it deeply modifies the oscillation pattern.

The Hamiltonian in matter H_m in the mass basis that characterise the evolution of the neutrino state is defined as

$$H_m = \Delta + U^{\dagger} V U \tag{1.55}$$

Eq. 7.10 describes the oscillation probability to observe flavour γ from initial flavour β after propagation of a distance L in a fixed density medium.

$$P^{\alpha}_{\gamma\beta} = S^2_{\beta\gamma} = \left| \left(U e^{-iH_m L} U^{\dagger} \right)_{\beta\gamma} \right|^2 = \left| \sum_{i=1}^{3} U_{\gamma i} e^{-i(E_i - E_j)L} U^*_{\beta i} \right|^2 \tag{1.56}$$

with $H_m|\nu_i\rangle = E_i|\nu_i\rangle$, and for ultra-relativistic neutrinos the energy difference is written as

$$E_i = \sqrt{m_i^2 + p^2} \tag{1.57}$$

$$E_i - E_j \simeq \frac{\Delta m^2_{ij}}{2E} \tag{1.58}$$

$$\Delta m^2_{ij} = m_i^2 - m_j^2. \tag{1.59}$$

The amplitude S is multiplied for every density layers considered, as described in Chapter 7, the Preliminary Reference Earth Model (PREM) model [19] is used to account for the earth density layers. The term $\frac{\Delta m^2_{ij}}{2E}$ enters the exponential, providing neutrino oscillation experiment sensitivity to the observable mass square differences. To explain oscillation measurements at least two of the three neutrino masses must be non-zero.

The sign of Δm^2 allows to measure the hierarchy of the neutrino mass states, the neutrino mass ordering (NMO). The sign of Δm^2_{21} has been measured by solar neutrino experiments to be positive therefore $m_2 > m_1$. However the sign of Δm^2_{31} remains unknown, thus several atmospheric neutrino experiments and long-baseline neutrino experiments are currently working on establishing it. The sensitivity of KM3NeT/ORCA to discriminate the NMO comes from the $\nu/\bar{\nu}$ asymmetry in the earth matter effects, which is inverted when the mass ordering is flipped. The effect is most visible in the electron neutrino appearance channel at the energy close to the matter resonance. The global significance for the NMO is currently below 3 σ, it is expected to be known before 2030.

In order to observe the oscillations the neutrino must satisfy several conditions that help understand the reasons why neutrino oscillate and charged leptons don't [20]. The neutrino oscillation involves the intrinsic quantum-mechanical uncertainties σ_E and σ_p on the energy and momentum of the particle, respectively. The particle can be described as a wave packet of the spatial size $\sigma_x \approx 1/\sigma_p$ instead of a plane wave as shown in Figure 1.10. From the particle's energy and momentum and their uncertainties it is possible to determine the squared mass of the particle with an uncertainty σ_{m^2} as

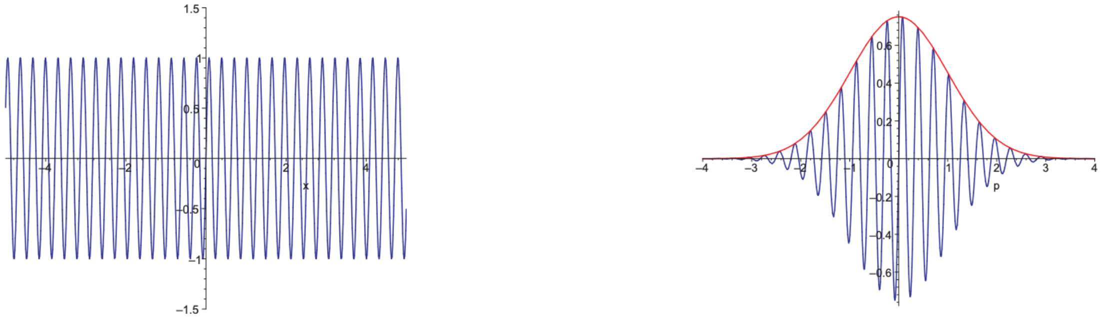

Figure 1.10: A plane wave is shown on the left and a wave packet on the right.

$$\sigma_{m^2} = \left[(2E\sigma_E)^2 + (2p\sigma_p)^2\right]^{1/2} \tag{1.60}$$

As $\sigma_{m^2} \gg |\Delta m^2|$ for the neutrino it is not possible to resolve which neutrino mass eigenstate was produced. The mass eigenstates are therefore said to be emitted coherently, forming a mixed flavour state. It is not the case for charged leptons that do not satisfy this condition in most interactions, due to their large squared mass difference. Therefore charged leptons are emitted as incoherent flavour states which are not mixed and thus equivalent to their mass states. In addition to the condition on the coherence at production the neutrinos must conserve their coherence during propagation in order for the mass states to interfere and oscillation to occur. The length l_{coh} depends on the energy of the neutrinos as

$$l_{\text{coh}} \simeq \frac{2E^2}{|\Delta m^2|}\sigma_x. \tag{1.61}$$

Eventually the neutrino looses its coherence during propagation due to the wave packet separation that occurs because the mass states have different group velocities. The coherence condition is largely satisfied in the case of earth-crossing atmospheric neutrinos.

1.4.2 Current experimental constraints

The NuFIT is an analysis project that provides up-to-date global fits of neutrino oscillation parameters. It compiles data from various neutrino experiments to determine the best-fit values, confidence intervals, and constraints for parameters such as mixing angles (θ_{12}, θ_{13}, θ_{23}), mass-squared splittings (Δm^2_{21}, Δm^2_{31}), and the CP-violating phase. The combined fit results from 2021 are shown in Figure 1.11 from [21].

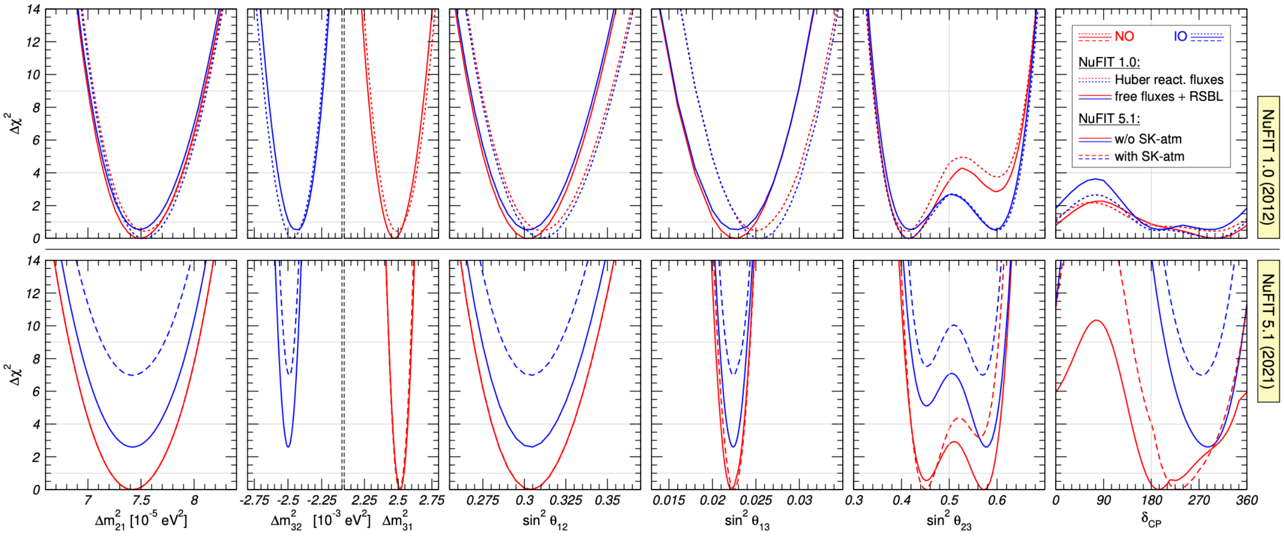

Figure 1.11: NuFIT 5.1 likelihood profiles from the combined fit for all standard oscillation parameters with and without SK atmospheric neutrino data.

The Table 1.12 from [21] provides the current best knowledge on the mixing angles mass splittings and CP-phase. The ordering remains unknown therefore results are shown for both cases. Results with and without SK atmospheric neutrino data are shown.

The knowledge on the θ_{23} octant will provide an answer on the possible symmetry between ν_μ and ν_τ. A maximal mixing angle for θ_{23} could make them interchangeable, with a mixing for both neutrino flavours in the ν_3 state. The crucial parameter that remain to be measured are the neutrino mass ordering (Δm^2_{31} sign), the CP violating phase and the θ_{23} octant.

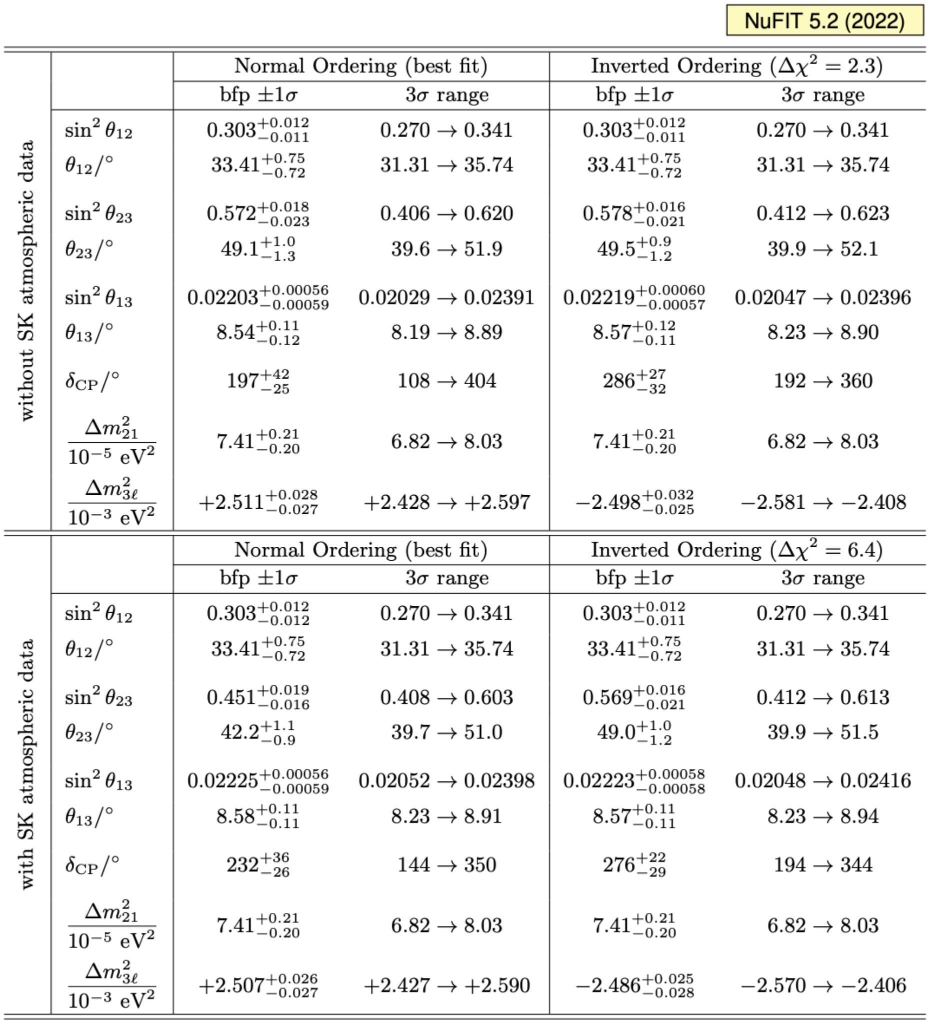

NuFIT 5.2 (2022)

		Normal Ordering (best fit)		Inverted Ordering ($\Delta\chi^2 = 2.3$)	
		bfp $\pm 1\sigma$	3σ range	bfp $\pm 1\sigma$	3σ range
without SK atmospheric data	$\sin^2\theta_{12}$	$0.303^{+0.012}_{-0.011}$	$0.270 \to 0.341$	$0.303^{+0.012}_{-0.011}$	$0.270 \to 0.341$
	$\theta_{12}/^\circ$	$33.41^{+0.75}_{-0.72}$	$31.31 \to 35.74$	$33.41^{+0.75}_{-0.72}$	$31.31 \to 35.74$
	$\sin^2\theta_{23}$	$0.572^{+0.018}_{-0.023}$	$0.406 \to 0.620$	$0.578^{+0.016}_{-0.021}$	$0.412 \to 0.623$
	$\theta_{23}/^\circ$	$49.1^{+1.0}_{-1.3}$	$39.6 \to 51.9$	$49.5^{+0.9}_{-1.2}$	$39.9 \to 52.1$
	$\sin^2\theta_{13}$	$0.02203^{+0.00056}_{-0.00059}$	$0.02029 \to 0.02391$	$0.02219^{+0.00060}_{-0.00057}$	$0.02047 \to 0.02396$
	$\theta_{13}/^\circ$	$8.54^{+0.11}_{-0.12}$	$8.19 \to 8.89$	$8.57^{+0.12}_{-0.11}$	$8.23 \to 8.90$
	$\delta_{\mathrm{CP}}/^\circ$	197^{+42}_{-25}	$108 \to 404$	286^{+27}_{-32}	$192 \to 360$
	$\frac{\Delta m^2_{21}}{10^{-5}\ \mathrm{eV}^2}$	$7.41^{+0.21}_{-0.20}$	$6.82 \to 8.03$	$7.41^{+0.21}_{-0.20}$	$6.82 \to 8.03$
	$\frac{\Delta m^2_{3\ell}}{10^{-3}\ \mathrm{eV}^2}$	$+2.511^{+0.028}_{-0.027}$	$+2.428 \to +2.597$	$-2.498^{+0.032}_{-0.025}$	$-2.581 \to -2.408$
		Normal Ordering (best fit)		Inverted Ordering ($\Delta\chi^2 = 6.4$)	
		bfp $\pm 1\sigma$	3σ range	bfp $\pm 1\sigma$	3σ range
with SK atmospheric data	$\sin^2\theta_{12}$	$0.303^{+0.012}_{-0.012}$	$0.270 \to 0.341$	$0.303^{+0.012}_{-0.011}$	$0.270 \to 0.341$
	$\theta_{12}/^\circ$	$33.41^{+0.75}_{-0.72}$	$31.31 \to 35.74$	$33.41^{+0.75}_{-0.72}$	$31.31 \to 35.74$
	$\sin^2\theta_{23}$	$0.451^{+0.019}_{-0.016}$	$0.408 \to 0.603$	$0.569^{+0.016}_{-0.021}$	$0.412 \to 0.613$
	$\theta_{23}/^\circ$	$42.2^{+1.1}_{-0.9}$	$39.7 \to 51.0$	$49.0^{+1.0}_{-1.2}$	$39.9 \to 51.5$
	$\sin^2\theta_{13}$	$0.02225^{+0.00056}_{-0.00059}$	$0.02052 \to 0.02398$	$0.02223^{+0.00058}_{-0.00058}$	$0.02048 \to 0.02416$
	$\theta_{13}/^\circ$	$8.58^{+0.11}_{-0.11}$	$8.23 \to 8.91$	$8.57^{+0.11}_{-0.11}$	$8.23 \to 8.94$
	$\delta_{\mathrm{CP}}/^\circ$	232^{+36}_{-26}	$144 \to 350$	276^{+22}_{-29}	$194 \to 344$
	$\frac{\Delta m^2_{21}}{10^{-5}\ \mathrm{eV}^2}$	$7.41^{+0.21}_{-0.20}$	$6.82 \to 8.03$	$7.41^{+0.21}_{-0.20}$	$6.82 \to 8.03$
	$\frac{\Delta m^2_{3\ell}}{10^{-3}\ \mathrm{eV}^2}$	$+2.507^{+0.026}_{-0.027}$	$+2.427 \to +2.590$	$-2.486^{+0.025}_{-0.028}$	$-2.570 \to -2.406$

Figure 1.12: Three-flavour oscillation parameters from NuFit 5.2. The results shown in the upper (lower) section are obtained without (with) the inclusion of data from atmospheric neutrinos provided by the Super-Kamiokande Collaboration. The numbers in the 1st (2nd) column are obtained assuming NO (IO), i.e., relative to the respective local minimum.

1.5 Sources of neutrinos and muons

The overall flux of neutrinos can be separated into different energy components described in Figure 1.13 from [22]. The spectrum spans from the unobserved cosmological neutrinos that are relics from the freeze-out shortly after the Big Bang which could improve our understanding of the cosmological evolution of the universe, to the cosmogenic component generated in the interactions of ultra-high energy cosmic rays (described hereafter) with photons of the cosmic microwave background (CMB).

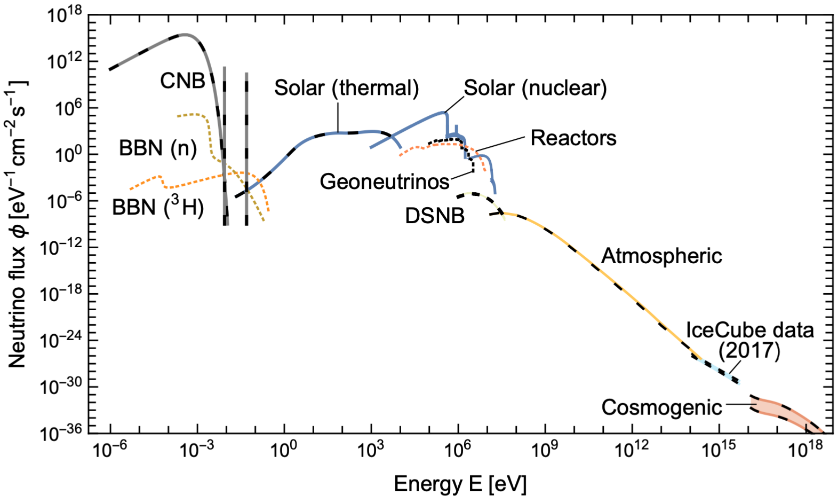

Figure 1.13: Neutrino flux component across energy scales from [22].

The size and sensitivity of recent neutrino telescope has increased to the point where a cosmogenic neutrino candidate was observed by KM3NeT/ARCA in Febuary 2023.

1.5.1 Atmospheric neutrinos

Cosmic rays (CR) are charged particles mainly composed of protons and light nuclei. Since they can be deflected by irregular Galactic magnetic fields, their arrival directions at the Earth are almost isotropic. Once a primary CR particle reaches the Earth's upper atmosphere and interacts with an air nucleus, it produces an air shower of secondary particles. At the energies relevant for KM3NeT ($> GeV$) the cosmic rays interaction is the most abundant source of neutrinos. The primary cosmic ray flux is composed of a majority of protons (95%), of helium (4%) and heavier nuclei (1%). The energy spectrum follows different power laws, depending on the energy. A common explanation for the entire spectrum of cosmic rays is still unresolved. Pions and kaons decays dominate the conventional component of the atmospheric neutrino flux. The decay of charged kaons involving neutrinos gives

$$\begin{aligned} K^+ &\longrightarrow \mu^+\nu_\mu \quad \text{(leptonic, 64\%)} \\ K^+ &\longrightarrow \pi^0 e^+\nu_e,\ \pi^0\mu^+\nu_\mu \quad \text{(semileptonic, 8\%)} \end{aligned}$$

and neutral kaon decays gives

$$\begin{aligned} K^0_L &\longrightarrow \pi^\pm e^\mp \nu_e \quad (41\%) \\ K^0_L &\longrightarrow \pi^\pm \mu^\mp \nu_\mu \quad (27\%). \end{aligned}$$

In addition the pion decay

$$\pi^+ \longrightarrow \nu_\mu\mu^+ \longrightarrow \nu_\mu\bar{\nu}_\mu\nu_e e^+$$

also provides a large contribution to the atmospheric neutrino flux. From the equation of the pion decay a flavour ratio of $1:2:0$ for $e:\mu:\tau$ is expected. This ratio changes with energy and towards the zenith as the fraction of muons (and at higher energies also pions) that travel up to the sea level before decaying increases. The atmospheric neutrino flavour repartition is illustrated in Figure 1.14 from [7]. The flux is essentially free of ν_τ below 10 TeV. An approximate isotropy is expected in azimuth. In addition the low energy neutrino flux is reduced at the solar activity maximum. Seasonal variation of the conditions in the atmosphere modify the rates of muons and neutrinos. This was measured to be around an $\approx 3\%$ effect in the muon rates for KM3NeT/ORCA [23], which is not simulated. The flux per flavour shown in Figure 1.14 is calculated from the HKKM group simulations [24]. They account for all mentioned effects in a 3D simulations of the flux. In this dissertation the flux tables are taken at the Frejus site. The larger flux close to the horizon is due to the larger distance the secondary particles from the shower can travel and decay before reaching the ground.

From the atmospheric neutrino sample detected by KM3NeT/ORCA, the overall flux of neutrinos shown in Figure 1.15 was measured in [25] and compared to the HKKM group estimation.

1.5.2 Atmospheric muons

The most penetrating component of the secondary particles emitted in the cosmic ray interactions in the atmosphere are muons, which can be detected at the surface of the

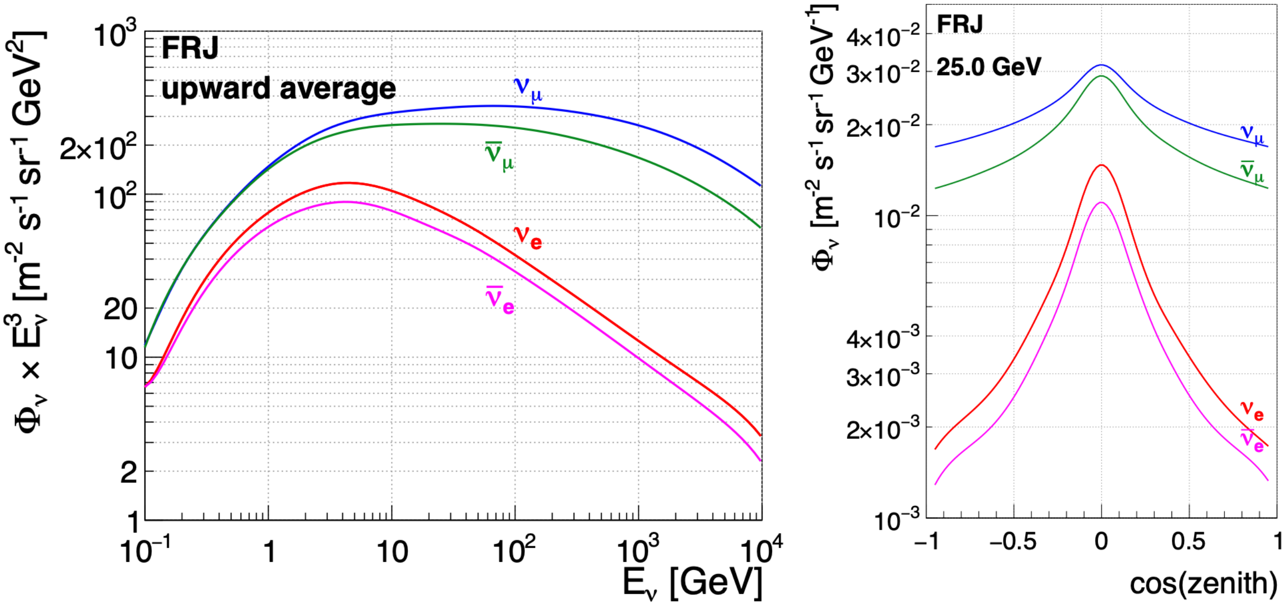

Figure 1.14: The flux distributions at Fréjus site as function of the energy and cosine of the zenith angle are shown.

Earth but also at underground or underwater detectors. In order to reach the KM3NeT/ ORCA detector [26] at a depth of 2500 metres below sea level [27], vertically down-going muons need a minimal energy of around 500 GeV at sea level and thus they must have originated from primary CRs of energies exceeding several TeV/nucleon as described in [28]. 90% of the CR particles yielding muons used in this analysis have energies between 3 and 330 TeV as illustrated in Figure 1.16. The angle between the primary CR and the secondary muon is on average within 0.1° at these energies [29] which is around 5 times lower than the expected angular resolution of the detector for muons. At the KM3NeT/ ORCA detector the muons are dominantly minimal-ionizing with energies ranging from few tens of GeV to few hundred GeV. The simulation of the atmospheric muon flux resulting from the kaons and pion decays is described in the next Chapter. The event rate of the atmospheric muon events reconstructed with the ORCA6 (6DUs configuration, left) and ARCA6 (6-DUs configuration, right) detectors as a function of the primary CR energy is shown in Figure 1.16 from [30].

Atmospheric muons represent a source of background for KM3NeT which searches for neutrino signals. Therefore muons are in most cases rejected by applying a cut on the zenith direction to select upward-going neutrinos, using the Earth as a filter. However, they

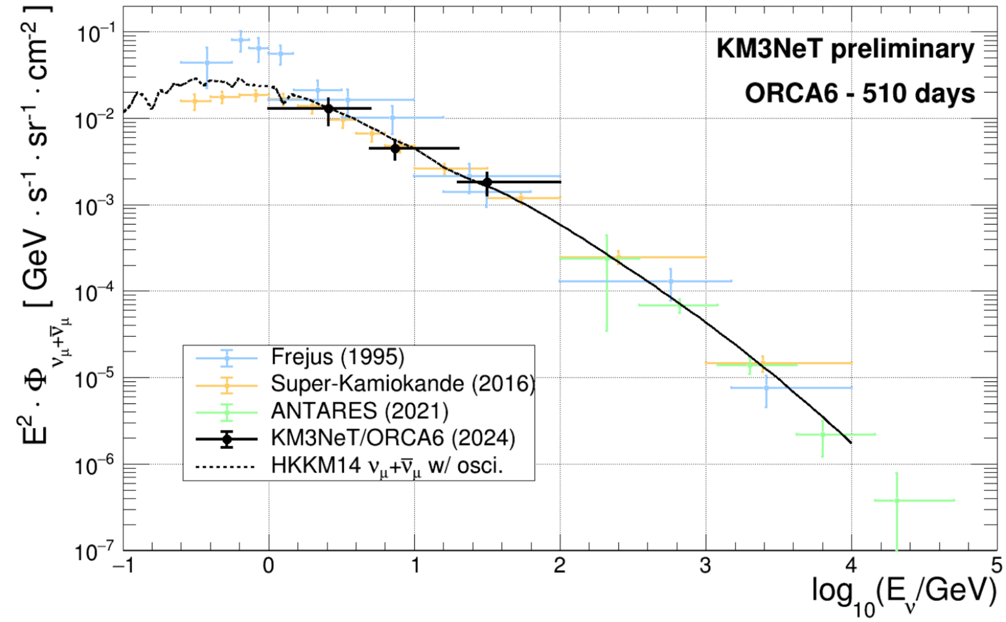

Figure 1.15: The overall flux of neutrinos measured in [25] and compared to the HKKM group estimation.

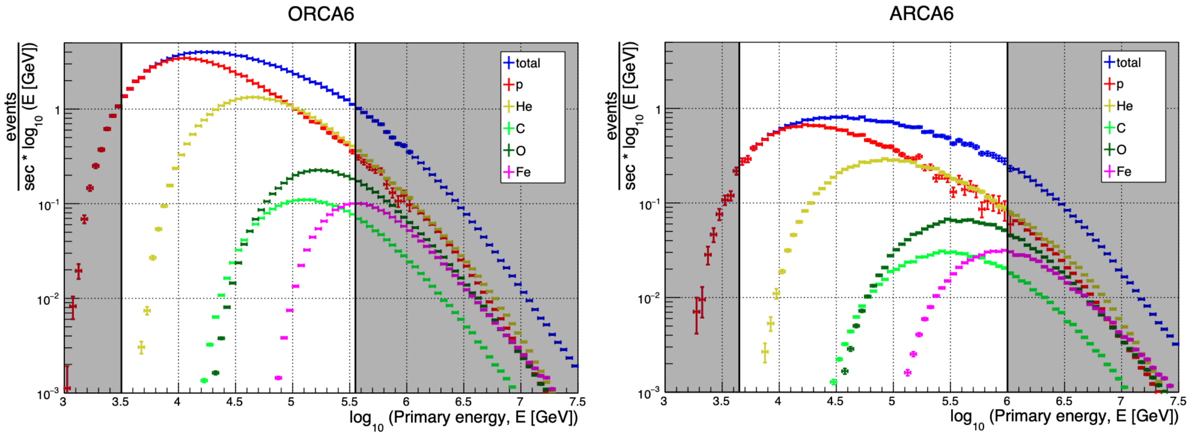

Figure 1.16: Event rate of the atmospheric muon events reconstructed with the ORCA6 (left) and ARCA6 (right) detectors as a function of the primary CR energy from [30]. The highlighted area corresponds to the 90% fraction of events.

are not always rejected, the muons are also crucial for the detector calibration, absolute orientation calibration (discussed in Chapter 3) and time synchronisation (discussed in the Chapter 2). They are also used for exploring the evolution of the CR sun shadow (discussed in Chapter 3), the CR anisotropy in right-ascension [31], the seasonal variation [23] and the primary cosmic ray spectrum and composition [32].

Chapter 2

KM3NeT

The Kilometer Cube Neutrino Telescope (KM3NeT) is a network of neutrino telescopes in the Mediterranean Sea. Its pioneering technical design is described in [26]. It is composed of two detectors KM3NeT/ORCA and KM3NeT/ARCA located near French and Italian coasts respectively, as shown in Figure 2.1. It involves a collaboration of more than 250 scientists from 70 institutes across 15 countries.

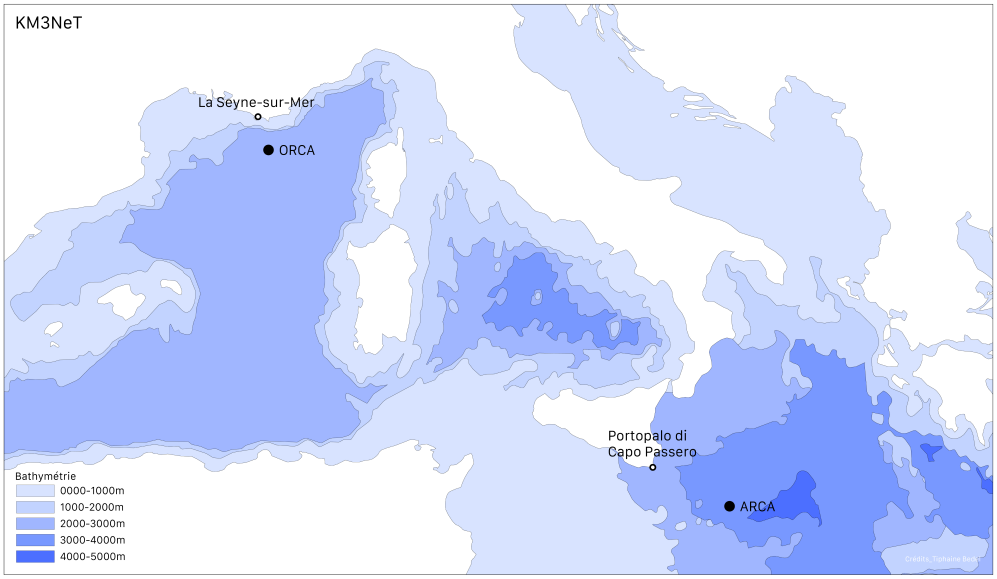

Figure 2.1: Depth of KM3NeT sites, credits to T. Bedel.

The main purpose of KM3NeT/ARCA (Astroparticle Research with Cosmics in the Abyss) is to find new astrophysical TeV to EeV neutrino sources. In a complementary way KM3NeT/ORCA (Oscillation Research with Cosmics in the Abyss) is designed to determine the neutrino mass ordering from the observation of GeV-scale atmospheric neutrino oscillations. In addition both detectors are currently used to search in real-time for low energy (MeV) neutrinos from supernovae [33].

2.1 Technical design

The geometry of KM3NeT/ARCA and KM3NeT/ORCA described in Table 2.1 was optimised to achieve their respective physics goal. However the technology and data acquisition system employed in both detectors is essentially identical.

	KM3NeT/ARCA	**KM3NeT/ORCA**
Building blocks	2	1
Number of DUs	230	115
DOM vertical spacing [m]	36	9
DU horizontal spacing [m]	95	20
Depth [m]	3450	2450
Instrumented volume [Mton]	1000	7

Table 2.1: Geometry of KM3NeT.

The following part will mainly concentrate on the KM3NeT/ORCA technical design. Optical sensors are used to detect the photons induced by the charged particles originating from the neutrino interaction with the sea water. The photons are detected as they impinge on a photocatode which leads to the extraction of an electron by photoelectric effect inside the photomultiplier tube (PMT). In order to host the PMTs, another fundamental element of KM3NeT innovative design is used: the Digital Optical Module (DOM) in Figure 2.2.

It is a 44-cm glass sphere that resist to high pressure and contains an electronic board used for the digitisation, readout and transmission of the signal impulsed by the detection of light. A single DOM houses thirty-one 3 inch Hamamatsu R14374 PMTs in order to obtain isotropic light coverage. The PMTs are arranged in 5 rings of 6 PMTs and a single PMT at the bottom pointing downwards. There are 12 PMTs in the upper hemisphere and 19 PMTs in the lower hemisphere due to the presence of a penetrator. The PMTs are held

Figure 2.2: Design of the DOM with the PMTs at its surface.

in place by a 3D printed support. A reflection ring around each PMT increases by 20–40% the sensitive area and a transitive gel fills the space from the inner surface of the glass to the PMT. In addition the DOM houses a variety of calibration tools such as a compass and an accelerometer, an acoustic piezo sensor for real time relative positioning, a gyroscope, a pressure gauge, a humidity sensor, and a flashable LED. As shown in Figure 2.3 (from [34]) 18 DOMs are arranged along a structure of two vertical thin 4 mm diameter polymer Dyneema ropes. The ropes are attached to the anchor lying on the seafloor thanks to a hand-made splice. A buoy attached at the top helps to increase the overall buoyancy in order to minimize the tilt of the string due to the sea current. The vertical electro-optical cable (VEOC) is an oil-filled plastic tube containing 18 optical fibres for data transfer, and two copper wires for the power supply distribution. The cable is connected to the DOMs via a pressure-resistant penetrator (below 1 bar inside) and runs along the vertical string down to the base module (BM). The BM protected by a titanium cylinder contains the power supply system, the control electronics and the optical network hardware. This component is responsible for powering and synchronising the DOMs, amplifying the optical signal, and interlacing the 18 DOM wavelengths from the connected DUs into a single fibre that is plugged to the node. All those elements together compose what is called a detection unit (DU). A building block (BB) contains 115 DUs. The DUs bases are inter connected with the electro optical interlink cable up to a node that provides power to 6 to 8 chain of four DUs for KM3NeT/ORCA as shown in Figure 2.4. The nodes are located on the periphery

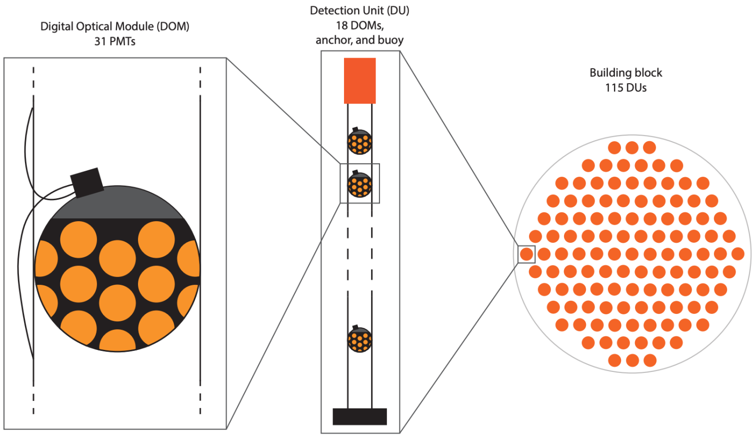

Figure 2.3: Design of the structure that host the KM3NeT's eyes.

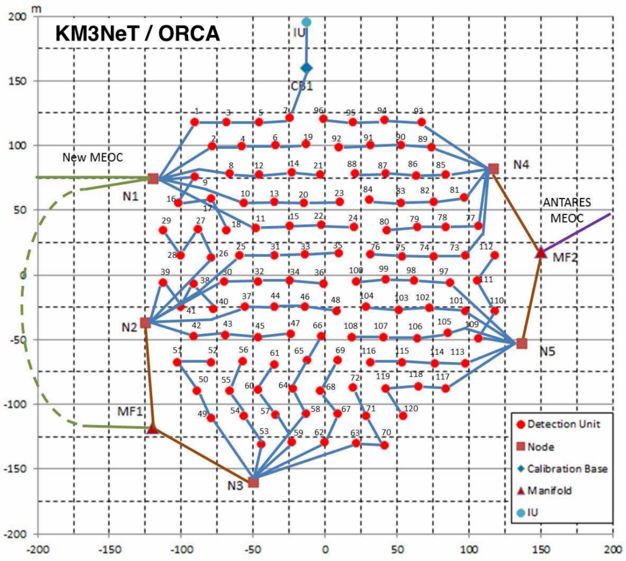

Figure 2.4: Footprint of KM3NeT/ORCA after completion.

of the array. As shown in Figure 2.5 each node has eight connectors, each of which can either power four DUs daisy chained, a calibration unit or an earth and sea science sensor. The main electro optical cable (MEOC) provides power supply with a conductor at 3.5 kV AC from the shore station to the node and transmit the data through optical fibres. The data path is defined as follows: the real-time data transit from the DOM through the VEOC down to the BM. Then the data transit through the interlink cable to the last BM of the chain of four which interlaces the 4×18 optical fibres and connects via the interlink cable to the junction box. A long MEOC section runs for several 10th of kms over the seafloor before reaching the beach *Les Sablettes* in La-Seyne-Sur-Mer (for KM3NeT/ ORCA). From the close-by *power hut* to the shore station the data transit through an optical cable below ground. The shore station recently (december 2023) moved from the historical Institut Michel Pacha to the Ifremer site take place. Real-time monitoring tools were built to continuously monitor the detector which includes verifying the PMT hit rates, trigger rates, data storage and acoustic data monitoring. Every member of KM3NeT is asked to contribute to the monitoring of the detector by making a week-duration shift every year for scrutinizing and quickly detect new malfunctioning elements.

Figure 2.5: Photograph of a KM3NeT/ORCA node and the eight user ports.

2.2 Construction

The first DUs of KM3NeT were deployed on the 21th of September 2017 and 3rd of December 2015 for ORCA and ARCA respectively. KM3NeT is build based on the feedback of ANTARES its predecessor. It was useful to lower the costs, improve the detection efficiency, the design and electronics of KM3NeT. When the sensitivity of KM3NeT to physics measurements surpassed ANTARES, the latter was dismantled in June 2022. The first deep-sea neutrino telescope ANTARES successfully operated from 2006 to 2022 during 16 years with 12 DUs each involving 25 storey composed of three Optical Modules (OMs). The storeys were vertically separated by 14.5 metres. It uses the pioneer concept of operating OMs in the Mediterranean sea water with PMTs facing 45° downwards. During the dismantling it was noted that the OMs were surprisingly well preserved. One ANTARES DU had been incorporated a KM3NeT DOM in order to test the new concept of multi-PMTs DOMs as shown in Figure 2.6. This makes the transition to KM3NeT.

Figure 2.6: A storey with the OMs from ANTARES during the dismantling is shown on the left. More storeys can be seen stretching to the horizon in the water. On the right side a KM3NeT DOM incorporated to an ANTARES DU for testing the multi-PMTs technical design.

The planning of the construction for KM3NeT/ORCA is currently (in summer 2024) foreseen completion in October 2028. Besides KM3NeT/ARCA is expected to be completed in June 2028.

The construction of KM3NeT can be divided in several steps, including the DOM assembly with the Hamamatsu PMTs and test [35], the DU integration and calibration, the Launcher of Optical Module (LOM) loading with the DU as shown in Figure 2.7 and the deployment. At CPPM the group participates in many steps of the construction including the test of the DUs before and during deployment. It also comprises the DU calibration in the dark room described in Section 2.7 and acoustics tests. Then occurs the loading of the LOM, a spherical structure that hosts the 18 DOMs of a DU until it is unfurled

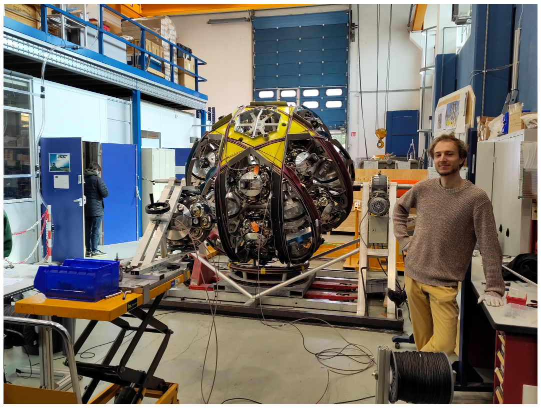

Figure 2.7: Loading of a LOM with a DU at CPPM.

from the bottom of the sea. A team of ≈ 5 technicians is required to perform the loading which lasts 2 days. During this process the Dyneema ropes are fixed to the DOMs and carefully enrolled together with the VEOC around the LOM. The DOMs are inserted one-by-one inside the LOM then the buoy is inserted in the centre. Spacers are fixed along the Dyneema ropes to maintain them separated. The procedure follows with the installation of the LOM and the BM as in Figure 2.8 on the anchor and the ropes are manually attached to the anchor with a splice.

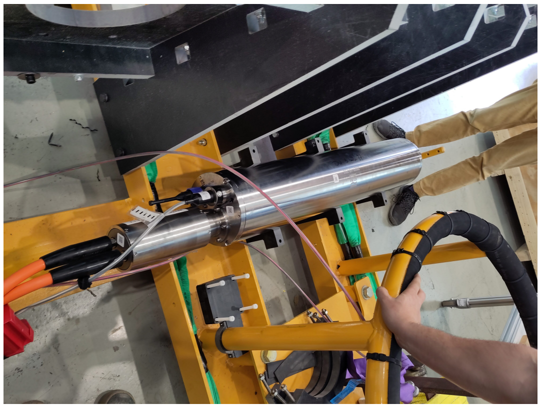

Figure 2.8: Base module installation on the anchor.

Once the LOM is furled and the anchor prepared, it can be loaded on a truck as in Figure 2.9 to ship it to the shore storage at the Foselev Marine dock in La Seyne-sur-Mer. At the storage the DU awaits until a propitious weather time window is found together with the availability of the teams and boats involved in the deployment and the authorization

Figure 2.9: Transport of a DU from CPPM after the LOM loading.

of the French marine authorities. The restrictive weather conditions are a swell below 1 metre for the DU deployment and down to 0.5 metres for operations on the DUs and a wind below 15 knots. When all those conditions are met and there are a sufficient number of DUs ready for deployment, ≈ 3 times a year, the DUs are tested again before being transferred on the Castor boat from the Foselev Marine company. The Castor boat shown in Figure 2.10 was chosen for its large deck to host the DUs (up to 7 DUs can be boarded),

Figure 2.10: Boat from the Foselev Marine company used to transport the DUs during the sea operation and deploy them.

its 3 km long winch cable and its Dynamic Positioning capabilities (that allows to stay at a given surface position within 1 metre despite wind and current). The boat was found to be compatible with the deployment requirements. At the start of the deployment sea operation, the boats navigates to the detector location: 42.8 deg latitude and 6.0 deg longitude 30 km from La-Seyne-Sur-Mer which takes almost 3 hours. The second boat, the Janus shown in Figure 2.11 hosts a remotely operated vehicle (ROV) that performs several underwater operations (DU connexions, LOM release and surveys). Once the Janus is on site the ROV is tested in water at a depth of 1 m, 10 m and 100 m. In addition the ROV shown in Figure 2.12 will watch with a camera the DUs during descent and help with the positioning and orientation of the DU on the seafloor described in Section 2.6.

Figure 2.11: Boat from the Ship As A Service (SAAS) marine company necessary to control the positions before the DU unfurling and connect it.

Eventually the ROV connects the DU to another DU or to the node which allows to run a first series of test at the shore station to verify the communication with the DU elements (BM and DOMs). If the test passes and a minimum of 15 DOMs are responding the ROV activates and watches the unfurling. About 45 minutes later the empty LOM structure is recovered at the sea surface. If the LOM release happens during the night flashers are installed on the LOM to help the recovery. The communication tools used by the pilots of the ROV to perform the deployment tasks are shown in Figure 2.13 it involves several cameras, a sonar, a display of the ROV, DU and boat positions.

This procedure is repeated for each KM3NeT DU to be deployed. Once the operation is finished the ROV enters back into its cage before it is being pulled up to the deck of the JANUS. Some mechanical parts of the ROV are can be damaged during the sea operation

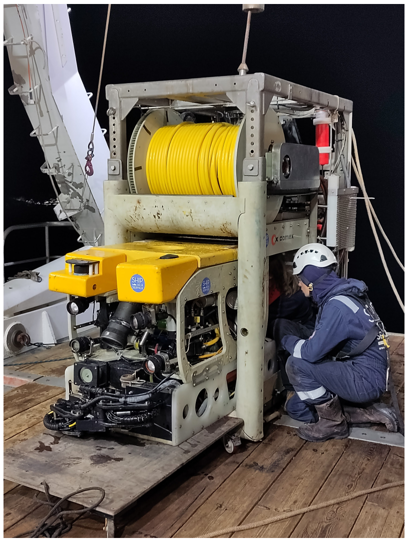

Figure 2.12: The ROV from SAAS equipped with mechanical arms qualified for deep sea environment. A pilot/technician is inspecting the cabling.

Figure 2.13: The pilots of the ROV with the camera, sonar and boat position.

due to the harsh environment at such depths. However the engineers on the boat have all pieces to repair it during the operation. If the offshore repair fails the boats are sent back to the shore for 1 or 2 days in order to find and fix the failure.

For a period of 510 out of 632 stable data taking days between the 26th of January 2020 and the 18th of November 2021 KM3NeT/ORCA was operated with 6 DUs. The detector configuration shown in Figure 2.14 is referred to as KM3NeT/ORCA6 and represents 5% of the nominal volume. This is the dataset used for most of the results presented in that dissertation.

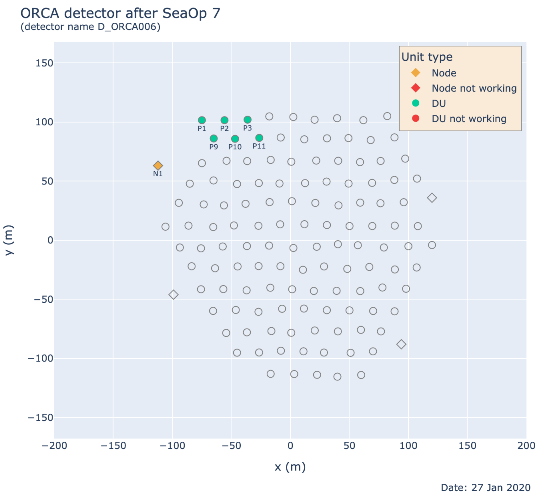
ORCA detector after SeaOp 7
(detector name D_ORCA006)

Date: 27 Jan 2020

Figure 2.14: The footprint of KM3NeT/ORCA6 showing the 6 working DUs in green and the node 1 in orange.

After several iterations in which I had the opportunity to participate either at the shore station or twice (05/12/22 and 18/11/23) in the offshore team on the Janus, the KM3NeT/ORCA detector eventually reached the 1st of May 2023 the 18 DUs configuration during a successful sea operation. As shown in Figure 2.15 left, two DUs are non-working, P30 was successfully replaced in June 2024 and P1 is foreseen to be replaced in October 2024. The data taken in this configuration of KM3NeT/ORCA is used in the study on the sun shadow evolution presented in Chapter 3. It is currently the measurement using the largest KM3NeT/ORCA dataset. In addition the Figure 2.15 right presents the 21 DUs configuration of KM3NeT/ARCA that was operated from the 22nd of September 2022 until the 11th of September 2023 for a livetime of 308 days used for studying the pointing capabilities of KM3NeT/ARCA that are presented in Chapter 3.

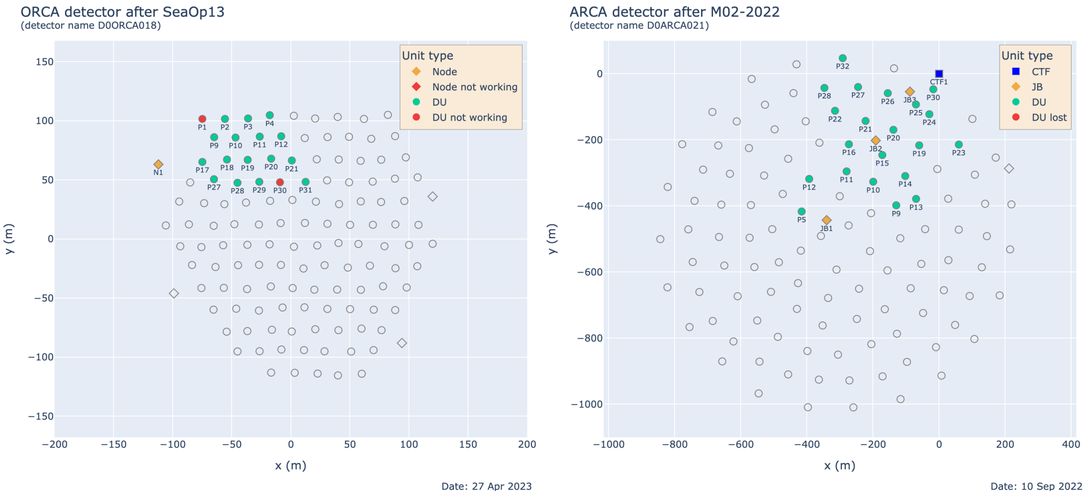

ORCA detector after SeaOp13
(detector name D0ORCA018)

ARCA detector after M02-2022
(detector name D0ARCA021)

Date: 27 Apr 2023

Date: 10 Sep 2022

Figure 2.15: The footprint of KM3NeT/ORCA and KM3NeT/ARCA showing the 18 and 21 installed DUs respectively, at the end of 2023.

The current status of the detector construction in August 2024 is illustrated in Figure 2.16. KM3NeT/ORCA with 23 DUs deployed reaches 20% of its nominal volume and KM3NeT/ARCA with 28 DUs reaches 12%.

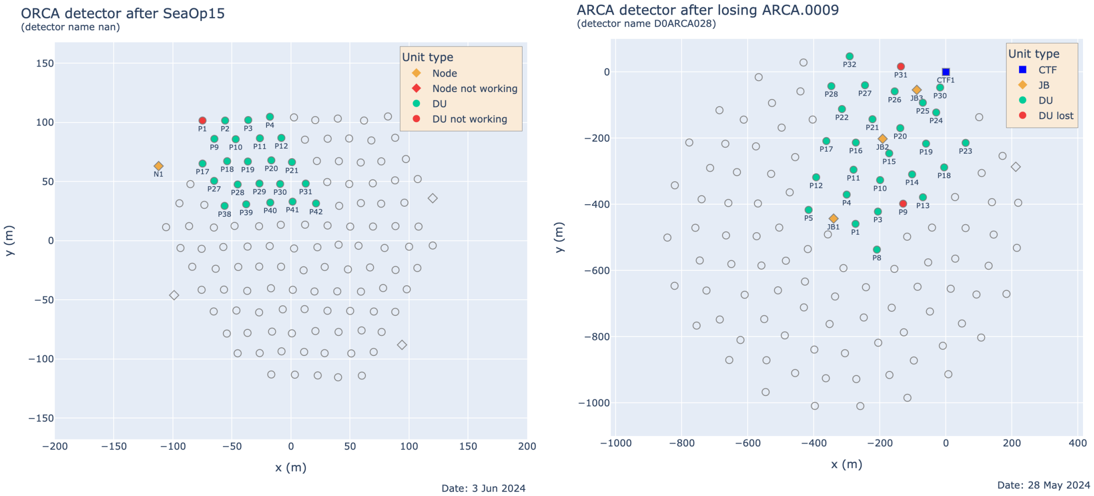

ORCA detector after SeaOp15
(detector name nan)

ARCA detector after losing ARCA.0009
(detector name D0ARCA028)

Date: 3 Jun 2024

Date: 28 May 2024

Figure 2.16: The current footprint of KM3NeT/ORCA and KM3NeT/ARCA with 23 and 28 DUs respectively.

2.3 Detection principle

2.3.1 Cherenkov light

Light from a radioactive source in water was already observed in 1910 by Marie Curie. It was believed at the time that fluorescence was responsible for this effect. However it was shown that the light spectrum was continuous and the effect independent of the medium composition by Pavel Cherenkov in 1937. This observation was in contradiction with the theory of fluorescent light emission. The same year Ilia Frank and Igor Tamm proposed the classical theory describing the radiation of an electron moving uniformly in a dielectric medium. The effect was also observed in the atmosphere in 1953 [36].

During its propagation across a dielectric medium, a charged particle induces a local polarisation. That is a displacement of the electrons of the nearby atoms according to the sign of the charge of the particle. If the particle is non-relativistic the polarisation field will be spherically symmetric and no radiation will be observed. However if the particle's speed approaches the phase velocity of light in the medium, the polarisation is no longer symmetric and a resultant dipole field will be apparent at large distances from the particle's track. Therefore at each position along its track the charged particle induces for a short duration a dipole field resulting in the subsequent emission of an electromagnetic pulse [37]. This electromagnetic pulse propagates as a spherical wave. However in order for the wavelet emissions to be coherent along the path, the particle's speed v_p must exceed the light's speed $v = c/n$ with n the refractive index of the medium. When this condition is met some points in space away from the track experience constructive interference as shown in Figure 2.17.

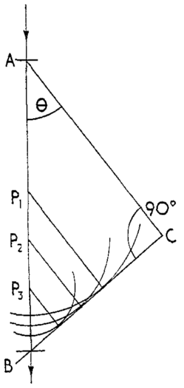

Figure 2.17: Huygens construction to illustrate the coherence of the wavelets.

The charged particle propagates from A to B during the time $\Delta\tau$. It passes through arbitrary points such as P_1, P_2 and P_3 on the path segment AB. The emissions from these points are coherent and interfere constructively to form a plane wave front BC. This takes place when the particle traverses AB in the same duration that the light travels the segment AC. In the duration $\Delta\tau$ the particle will travel a distance AB $= \Delta\tau\ v_p$, and the light a distance AC $= \Delta\tau\ (c/n)$. This yields the *Cherenkov relation*

$$\cos\theta = \frac{1}{\beta n} \tag{2.1}$$

where $\beta = v_p/c$. A maximum Cherenkov angle of emission is defined by $\theta_{max} = \cos^{-1}(1/n)$ when $\beta \to 1$. In the case of sea water $n = 1.35$, and $\theta_{max} = 42.2°$. The spectrum of Cherenkov emission follows

$$\frac{\mathrm{d}N_\gamma}{\mathrm{d}\lambda \mathrm{d}x} = \frac{\alpha 2\pi}{\lambda^2}\left(1 - \frac{1}{\beta^2 n^2}\right). \tag{2.2}$$

with the fine-structure constant $\alpha \approx 1/137$, the wavelength of light λ, and the path length x. For the case of a constant refractive $n \approx 1.35$ and ultra-relativistic particles ($\beta \to 1$), integrating Equation 2.2 within 300 nm to 700 nm gives around 400 photons/cm appropriate for the use of PMTs. In addition the energy of muons and electrons considered in this work are well above the energy threshold to radiate Cherenkov radiation.

2.3.2 Water properties

The blue light absorption coefficient in sea water is about 0.015 m^{-1} corresponding to an absorption length of 67 m close to the one of optically pure water around $\approx$ 70m [38]. This study was made near Capo Pasero (Sicily) in the Southern Ionian Sea in 2006. It also demonstrated that there is no seasonal variation to the absorption.

The scattering properties of the water for blue light ($\lambda = 473$ nm) and UV light ($\lambda =$ 375 nm) were studied by measuring the distribution of the arrival times of photons emitted by a pulsed LED source and collected several tens of metres away by a PMT. This study was performed by the ANTARES collaboration in 2004 [39] which also provide absorption length measurements. The extracted effective scattering length mainly from Mie scattering is defined as

$$\lambda_{\mathrm{sct}}^{\mathrm{eff}} = \frac{\lambda_{\mathrm{sct}}}{1 - \langle\cos\theta\rangle} \tag{2.3}$$

where $\langle\cos\theta\rangle$ is the average cosine of the scattering angle and λ_{sct} the scattering length. This yieds $\approx$ 260 m in blue and $\approx$ 120 m in UV. The various parameters describing the light transmission properties are subject to a 5-10 % uncertainty relevant for the KM3NeT/ ORCA measurements presented in this dissertation.

The optical properties of deep glacial ice at the South Pole were studied in 2006 [40]. They depend strongly on the depths and the purity of the ice. However it reveals a larger absorption length than sea water Cherenkov telescopes as lies between 50m and 200m depending on the depth. While the scattering length on the contrary is lower, between 50cm at low depths where bubbles in the ice affects the light transmission and 100m at higher depths.

2.4 Event reconstruction

2.4.1 Hit

The KM3NeT eyes i.e. the PMTs are used to extract information from the light pattern produced by the charged particles propagating in the sea water near the detector. The PMT allows to convert the photon's deposited energy into an electric signal. When the photon impinges on the photo-cathode a photo-electron is produced by photo-electric effect and it is accelerated thanks to an electric potential. As the electron reaches the first dynode it provokes the emission of secondary electrons which are accelerated in turn. This is repeated until the desired charge amplification is reached and the electrons are collected on the anode where an electric pulse is produced.

The final observable are the time, the energy, and the incoming direction of the particle. In order to approach those quantities a threshold in the amplitude of the PMT response must be set. The primary charge extracted for a single photo-electron (spe) is used as a reference. In that case the corresponding amplitude of the PMT response is set to 1. The threshold on the amplitude is fixed to 0.3 therefore allowing to define the Time-over-Threshold (ToT) of the pulse as shown in Figure 2.18.

The electric pulse produced in the anode is preamplified before reaching a discriminator in the PMT printed circuit board. The time-to-digital converter (TDC) implemented in the custom Field Programmable Gate Arrays (FPGA) Central Logic Board (CLB) inside the DOM records the time the leading edge crosses the threshold and the ToT. This defines a hit. It contains information on the PMT ID, the time with a nanosecond accuracy synchronised in the CLB via the White Rabbit system and the ToT which relates to the primary extracted charge on the photo-cathode that depends on the number of

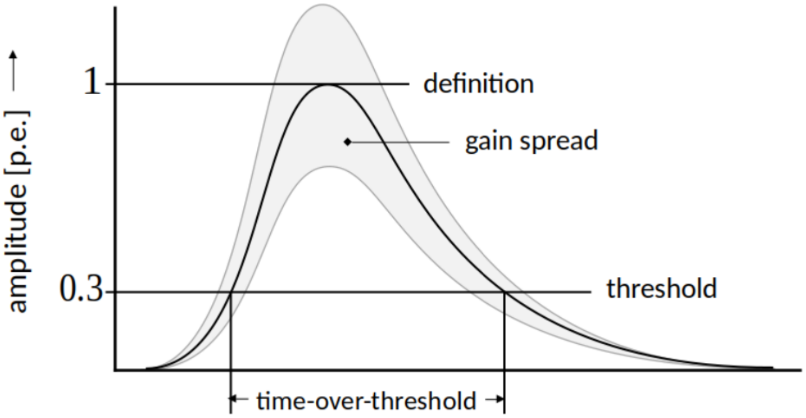

Figure 2.18: Amplitude of the response of a KM3NeT PMT to a single photo-electron event.

incident photons. The analog-to-digital conversion occurs inside the **Digital** Optical Module (DOM) in contrast with ANTARES the predecessor of KM3NeT which used Optical Modules (OMs).

The High Voltage (HV) of the PMT is tuned to reach an amplification gain of 3×10^6. In that configuration the distribution of the ToT for single photo-electrons peaks at 26.4 ns with 4.7 ns gaussian width. If the ToT of a hit is larger than 255 ns it is split in two consecutive hits to cope with the 8-bit storage. The Transit Time Spread (TTS) Full Width at Half Maximum (FWHM) is well below the 5 ns requirement and the Peak to Valley ratio useful to better discriminates spe from noise is at 2.7, comfortably above the required threshold specified by KM3NeT. The average number of emitted photo-electrons divided by the number of incident photons is referred to as the quantum efficiency (QE) of the PMT. The typical highest QE of $\approx 25\%$ at 350 nm is in the region where the wavelength from Cherenkov light is low enough to have high-intensity and high enough not to be absorbed by the medium. In addition the wavelength is beyond the transparency limit of the DOM glass at around 200 nm.

Hits are grouped in packets during a fixed time interval of 100 ms referred to as a frame and sent to the shore. The maximum expected duration of a neutrino event in the KM3NeT/ARCA detector is around 3 μs therefore unlikely to occur during two frames. The frames from all DOMs with the same UTC timestamp are called timeslices and are the basis for the onshore trigger and event builder farm.

A close to ≈ 7 kHz optical background hit rate is observed by the PMT in sea water due to the presence of radioactivity, mainly from ^{40}K beta decays. The bioluminescence can increase the rate of the optical background up to the MHz scale. A high-rate-veto HRV is set in order to disable the acquisition of the TDC of a PMT when the ≈ 20 kHz threshold is crossed. The rate of atmospheric muons is many orders of magnitude below at the level of tens of Hz in the entire detector. It is the dominant source of background once the optical noise is filtered out and it will be reduced by searching for up-going events and by using dedicated algorithms explained in Chapter 5.

Each DOMs produces on average ≈ 13 Mbps of optical data and an acoustic data rate of 586 kbps per DOM. Once digitised all hit data are sent to be processed at the shore station computing centre following the all-data-to-shore concept from ANTARES.

2.4.2 Trigger

A hit rate of half a GHz is expected for a single KM3NeT building block. Thus motivating the use of a filter and trigger system to reduce the data and extract physics events from the overwhelming background. The level 0 data refers to the optical data as they arrive on shore. The 100 ms data frames are gathered by the dataqueues in the data acquisition (DAQ) system and sent to the datafilters for application of the trigger algorithms to select the data to be saved on tape by the datawriters. The datafilters can discard data from specific PMTs if needed. The term "hit" is generalised in the following to describe a single hit or a set of hits matching a time condition:

- L0 hit: A hit that includes a hit time and ToT information.
- L1 hit: At least 2 L0 hits within a single DOM, occurring within a time window of 10 ns.
- L2 hit: A L1 hit that satisfies an additional criterion for the angular separation of the hit PMTs, with a minimum of 90°.
- SN hit: L1 hits on at least 4 PMTs within 10 ns or 15 ns and a minimum of 90° angular separation.

The trigger timeslice contains an array of a given triggered hit type in a 100 ms time interval. The L2 and L0 trigger timeslices are processed by the KM3NeT trigger algorithms. A minimum number of causally-connected hits across multiple DOMs that match a given event topology is searched for. The trigger algorithms are defined as follows:

- 3D muon: Designed to find track-like events defined in Section 2.4.3, it searches for causally connected L2 hits, on a minimum number of DOMs, in a cylinder of a given diameter and infinite length; the full solid angle is covered by testing hundreds of track

directions;
• 3D shower: Designed to find shower-like events defined in Section 2.4.4, it searches for causally connected L2 hits, within a spherical volume of given radius, with a minimum number of DOMs;
• MX shower: Designed to find low-energy shower-like events in KM3NeT/ORCA, it is similar to the 3D shower with the relaxed condition of having a single L2 hit the rest being L0 hits.

The triggers identifies all remaining clusters of causally-connected hits matching one of the criteria. Then a triggered event data structure is created to store the L0 hits which formed the trigger (triggered hits) plus a collection of the L0 hits (snapshot hits) occurring in a ± 1.3 μs enlarged time window with respect to the duration of the triggered hits for KM3NeT/ORCA. The general idea is to extend the range of the triggered hit times by the detector size divided by the speed of light in water. The triggered events are then store in root files.

2.4.3 Track reconstruction algorithm

When considering the hypothesis of light being produced by a muon track in the detector, the energy, the time and position (start position) at which the first detected light was emitted and the direction of the track are the key parameters to be reconstructed. The distance that separates the start and stop position (position of the emission of the last detected photon) is the track length, a useful estimate of the energy for minimum ionising particles. To evaluate those parameters a likelihood maximisation is used in the fit procedure.

For KM3NeT/ARCA, the track reconstruction chain is defined as
JMuonPrefit $\longrightarrow$ JMuonSimplex $\longrightarrow$ JMuonGandalf $\longrightarrow$ JMuonStart $\longrightarrow$ JMuonEnergy
For KM3NeT/ORCA, the track reconstruction chain is defined as
JMuonPrefit $\longrightarrow$ JMuonSimplex $\longrightarrow$ JMuonStart $\longrightarrow$ JMuonGandalf $\longrightarrow$ JMuonStart $\longrightarrow$ JMuonEnergy, with the description of the algorithms given in Table 2.2 from [41].

In order to reduce the complexity of the direction fit algorithm a **direction prefit** is performed scanning through a set of $\approx$ 1000 directions isotropically distributed. The χ^2 from the fit based on the the differences between the expected and measured time of arrival at the PMT is minimised. The expected times are estimated for a given track direction with a model of a Cherenkov-light emission from the muon track. A quality criteria of the track reconstruction is computed from the χ^2 to sort the track candidates.

Function	**Algorithm name**
Prefit direction estimate	JMuonPrefit
Intermediate direction fit	JMuonSimplex
Full direction fit	JMuonGandalf
Track length estimate	JMuonStart
Energy estimate	JMuonEnergy

Table 2.2: Stages of the track reconstruction chain and the corresponding program name from [41].

An **intermediate direction fit** is performed by repeating the fit with an additional condition on the distance from the track and a reduced time window. When several hits are recorded on the same PMT the first one is used.

In the **full direction fit** the position and direction of the track are estimated. The maximum likelihood method is used on the track candidates given by the previous steps. The tables of photo-electron distribution for muon light, given in [41], are used in that fit. The time residual used for the fit is the difference between the expected and measured hit time. At this stage all first hits within a cylinder of a given radius from the track and within a [-50,-450] ns time window are included. The track-length determines the height of the cylinder. After the maximisation of the likelihood to reject the background hypothesis a quality of the fit is measured together with the time, position and direction of the track. At this stage the angular error estimate *beta* on the track direction is determined.

The **track-length estimate** uses the back-projection of the hits contained in a cylinder with a given radius on the track assuming the Cherenkov hypothesis for the emission. This provides an estimate of the starting and stopping point of the track.

The **energy estimate** uses a likelihood function based on the probability to observe or not observe a hit on a PMT in a given time window. By considering the photo-electron distribution tables for the muon light the likelihood can be minimized and the energy estimated from a predefined allowed range.

2.4.4 Shower reconstruction algorithm

For KM3NeT/ORCA, the shower reconstruction chain is defined as JORCAShowerPrefit ⟶ JORCAShowerPositionFit ⟶ JORCAShowerFit ⟶ JMuon-Gandalf ⟶ JORCAShowerBjY, with the description of the algorithms given in Table 2.3 from [42].

Function	**Algorithm name**
Position prefit	JORCAShowerPrefit
Position fit	JORCAShowerPositionFit
Direction and energy fit	JORCAShowerFit
Bjorken Y fit	JORCAShowerBjY

Table 2.3: Stages of the shower reconstruction chain and the corresponding program name.

The energy, position, time and direction in KM3NeT/ORCA are also reconstructed with an algorithm dedicated to the shower events. It uses the electromagnetic shower photo-electron distribution as a function of PMT arrival times. The point of the shower maximum is defined in the prefit as the position where the shower radiates the most light, it is used as a starting value for the vertex position. Starting from a set of L0 and L2 hits that are causally connected the vertex position and time are estimated by minimising the time residuals.

Then the position and time of the vertex are estimated in the position fit based on the photo-electron distribution tables and assuming isotropic light emission. To achieve this a likelihood function involving the first hit probabilities is minimised. It also contains the information on the distance from the vertex to the PMT, the emission angle of the light, the time residual and the shower energy.

Once the position and time of the vertex are fixed, the direction and energy are estimated in the dedicated fit using a new likelihood function build with the photo-electron tables and the PMT hit and no-hit probabilities as in the Track reconstruction. Those tables provide the information on the expected number of hits on the PMTs depending on its orientation for a given energy in the hypothesis of a shower emission. From the likelihood maximisation process the energy is defined within a given energy range.

A fit for reconstructing the shower direction is then performed using the electromagnetic shower photo-electron distribution table. The full procedure is detailed in [42].

2.4.5 PID features

Features from the reconstruction algorithms will be used for the track shower discrimination described in Chapter 5. Here, a Cherenkov hit is defined as a hit which distance from the track is below 100 metres and the time of the hit is within ±15 ns range from the expected time of the hit based on the Cherenkov hypothesis for the light emission.

- f1 : The number of reconstructed track candidates within 1° from the best track given by the track direction fit from the reconstruction, which matches the triggered hits with the hypothesis of a cherenkov-light-emitting muon. For track-like events a higher number of track candidates falling within 1° is expected.
- f2 : The furthest Cherenkov hit distance to the start of the track in metres, and zero for the events that do not have any Cherenkov hits. For shower-like events a lower distance from the reconstructed start of the track is expected.
- f3 : The log of the distance between the shower pre-reconstructed vertex and the position of the brightest point of the shower after the position fit. For track-like events a higher distance from the brightest point of the shower to the reconstructed vertex is expected.
- f4: The distance between the shower reconstructed vertex and the position along the track from the track algorithm at the time of the shower vertex. For track-like events a higher distance from the shower reconstructed vertex to the position along the track is expected.
- f5 : The mean of the absolute value of the time residuals of the hits within 10° around the Cherenkov angle assuming the best direction from the shower reconstruction. For track-like events a higher time residuals for the shower reconstruction is expected.

2.5 MC simulation

Several backgrounds and neutrino signals are simulated in KM3NeT. The processing chain of the simulated Monte Carlo (MC) data must follow as closely as possible the conditions in which the real data is processed. This involves the generation and propagation of muons from the atmosphere to the detector as well as the run-by-run simulation of the pure optical noise, the neutrino propagation and interaction nearby the detector. The direct and scattered light propagation in the detector volume are also modeled. This simulated data is structured in the same way as real data and the same trigger and reconstruction algorithms are applied to it. As a final step machine learning algorithms are used for high level signal background discrimination and particle identification.

The detector coordinates system and the definition of the volumes used in the simulation are given in Figure 2.19 from [8].

The **instrumented volume** is the smallest volume that enclose all detector elements. It is encompassed in the active volume where Cherenkov light production is simulated referred to as the **detector can** a cylinder that extends the instrumented volume by three time the water absorption length. The **interaction volume** is defined by the volume

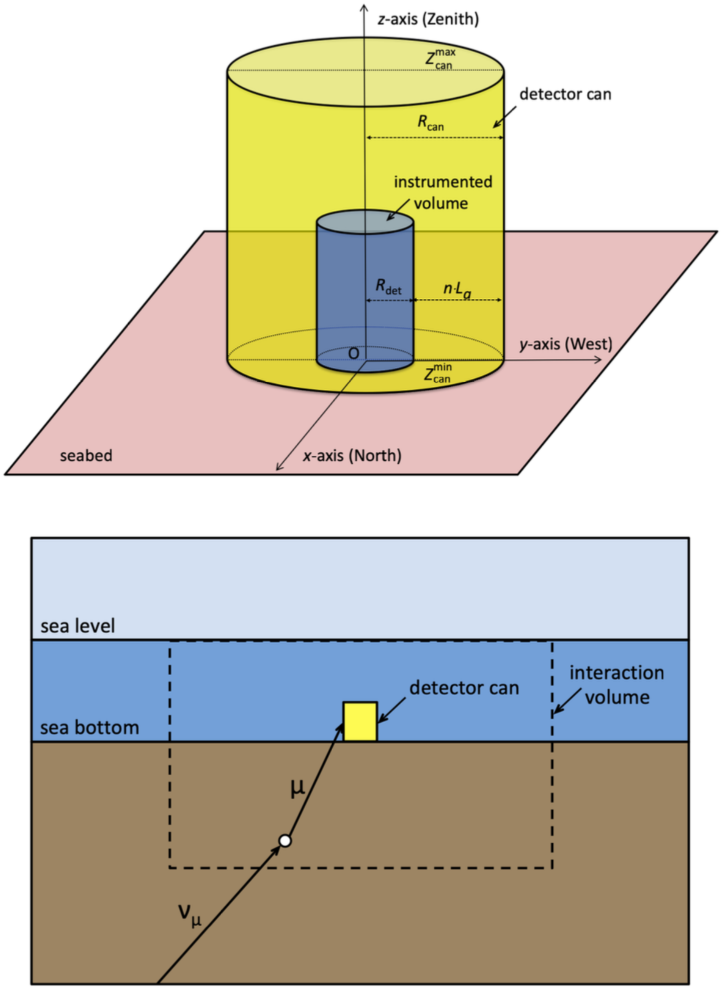

Figure 2.19: Representation of the instrumented volume, the detector can and the interaction volume of KM3NeT from [8].

where a neutrino interaction can possibly lead to detectable particles. Therefore its definition depends on the neutrino flavour. The events where the particles produced from the interaction reach the detector can are saved.

2.5.1 Atmospheric muons

The atmospheric muons are generated with the MUon GEnerator from PArametric formulas (MUPAGE) software [43]. It is used to quickly generate -thanks to parametric formulas - vast amount of muons at the surface of the can without simulating the primary CR interaction with atmospheric air nuclei that requires heavy computational resources. MUPAGE is compatible with detector depths from 1.5 to 5 km water equivalent and for a zenith angle from 0° (down-going atmospheric muons) to 85° (almost horizontal muons). It accounts for the multiplicity of the bundles, i.e. the number of muons in each bundle. The parametric formulas within MUPAGE describe the distribution of muons as function of the depth, the flux, the radial distance from the bundle axis (lateral spread), the single muon energy spectrum and the multiple muon energy spectrum. The flux is dominated by single muons. The parameters used in MUPAGE parametrisation for KM3NeT are tuned with an atmospheric muons flux from cosmic ray air shower simulation known as the Hadronic, Electromagnetic and Muonic components in Air Showers (HEMAS) simulation software [44] based on MACRO data [45].

2.5.2 Neutrino generation

KM3NeT uses a GENIE-based code gSeaGen [8] to simulate neutrino interactions and the subsequent produced particles. It accounts for the composition of the medium and the topology depending on the neutrino flavour. The four media SeaWater, Rock, Mantle, and Core are implemented in gSeaGen. The vertices for the generation of neutrinos are positioned outside the detector interaction volume. They lie on a disk perpendicular to a given neutrino direction pointing towards the can with a radius such that the shadow of the disk entirely covers the detector can. In order to address the issue of low statistics given the low neutrino interaction probabilities, they are scaled up to match the maximum possible total interaction probability, i.e. the probability at the maximum neutrino energy (corresponding to the maximum cross section) and for the maximum possible neutrino path length in the interaction volume. This allows to use the code for a large range of energies as required by neutrino telescopes and the information on the interaction probability is stored in the event weight. A weight denoted as w_{evt} is assigned to every event. It ensures the event generation is shaped in accordance with the anticipated neutrino flux

$$w_{\text{evt}} = w_{\text{gen}} \cdot \phi(E, \theta, \varphi).$$

The event weight is the product of the neutrino flux $\phi(E, \theta, \varphi)$ and the generation weight w_{gen}, where E represents the neutrino energy and θ and ϕ are the zenith and azimuth angles, respectively. The generation weight in [8] is defined as

$$w_{\text{gen}} = \frac{I_E \cdot I_\theta \cdot T_{\text{gen}} \cdot A_{\text{gen}} \cdot N_\nu \cdot E^X \cdot P_{\text{scale}} \cdot P_{\text{Earth}}(E, \theta)}{N_{\text{Tot}}}.$$

where

- I_E is the energy phase space factor, equivalent to the generation spectrum E^{-X} integrated over the whole simulated neutrino energy range.
- I_θ represents the angular phase space factor, which varies based on the nature of the neutrino source. For a diffuse flux, it is $2\pi(\cos\theta_{max} - \cos\theta_{min})$, measured in steradians (sr). For point-like or extended sources, it takes a dimensionless value of 1.
- T_{gen} denotes the simulated livetime, corresponding to one year and expressed in seconds.
- A_{gen} is the area of the generation surface and is measured in square metres. It depends on the neutrino direction and is computed on a per-event basis.
- N_ν is the count of generated neutrino types.
- N_{Tot} represents the total count of incoming neutrinos that have been simulated.
- E^X corresponds to the reciprocal of the generation spectrum evaluated at the energy of the generated neutrino.
- P_{scale} is the GENIE interaction probability scale.
- $P_{\text{Earth}}(E, \theta)$ stands for the transmission probability through the Earth, evaluated as

$$P_{\text{Earth}}(E, \theta) = e^{-N_A \sigma(E) \rho_l(\theta)}.$$

where

- $\sigma(E)$ represents the total CC cross section per nucleon, taking into account the various compositions of the Earth layers for the interaction of neutrinos with nucleons. The small effect of NC interaction is ignored as it would reduce the energy of the neutrinos without absorbing it.

- $\rho_l(\theta)$ is the column depth along the neutrino path inside the Earth up to the interaction vertex. It is determined through the line integral of the Earth density profile from the Preliminary Earth Model (PREM) [19] for a zenith angle θ.

Those event weights are mandatory for the user to be able to produce a fair comparison of the data versus MC event distributions.

2.5.3 Light propagator

The propagation of light is performed with KM3Sim for $<$ 500 GeV neutrinos. KM3Sim software based on Geant4 [46] is derived from the Hellenic Open University Reconstruction & Simulation (HOURS) software. It propagates each photons produced by the particles present after the event generation step separately. In addition it accounts for the PMT characteristics such as the PMT photocathode area, the quantum efficiency, the angular acceptance, and the transmission of light in the optical module glass sphere and in the optical gel. Although it is accurate in the description of the distribution of photons, the computing time increases with energy which forces to use another light propagator called JSirene for higher energies. This propagator uses an alternative strategy to find the detected number of photo-electrons per PMT which depends on precomputed tables of probability density functions (PDFs) of the direct and single-scattered light arrival time [47].

2.6 Position and orientation calibration

Due to the sea water properties and it's innovative multi-PMTs technology, KM3NeT/ARCA is expected to reach the unprecedented angular resolution for high energy muon neutrinos of 0.05°. In order to achieve this competitive pointing capability, the positions of the DOMs need to be resolved thanks to the Acoustic Positioning System (APS) with an accuracy of $\approx$ 10 cm, which corresponds to an uncertainty on the hit time of around 1 nanosecond in water. In addition the relative DOM orientations must be resolved to an accuracy of about 3 degrees [48]. The absolute orientation, driving the uncertainty on the pointing accuracy is discussed in the next Chapter.

2.6.1 Absolute acoustic positioning at deployment

During the sea operation on the KM3NeT/ORCA site, the position of the elements to be deployed are monitored in real-time based on the Navigation Absolute Acoustic Positioning System (NAAPS). To extract the absolute position the system measures the travel time of

10-20 kHz band acoustic pulses emitted from fixed or mobile transponders (acoustic beacons) to the ship's transducer (acoustic receiver). The concept of the system is schematised in Figure 4.2.

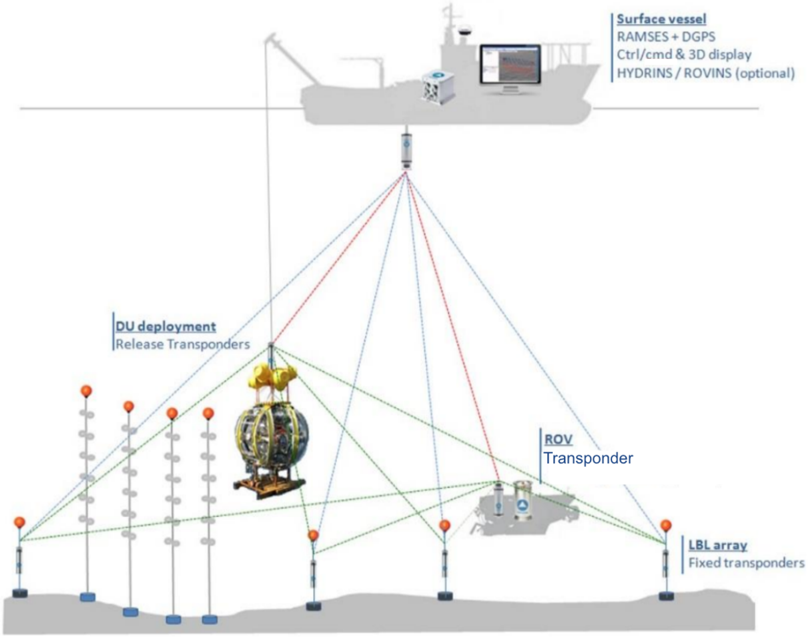

Figure 2.20: Navigation Absolute Acoustic Positioning System scheme for KM3NeT/ ORCA deployment.

In order to provide a unique sub-metre deployment positioning accuracy the system requires the presence on the sea floor of the acoustic long-baseline (LBL) battery-powered autonomous beacons from the RAMSES system provided by the Exail (former iXBlue) company. A LBL beacon is shown in Figure 2.21 before deployment. The sea operation to deploy and establish the position of the LBL beacons involves an Exail boat shown in

Figure 2.21: LBL beacon from RAMSES system.

Figure 2.22 with an acoustic transducer. The LBL beacon once deployed is interrogated every 6 seconds from the boat using the RAMSES system during a 600-metre-radius circular path shown in Figure 2.23. The positions are given in the absolute reference frame of the DGPS coupled to the inertial central Hydrins based on optical gyroscopes (heading, tilts, acceleration) in order to determine in real time the position of the transducer with respect to the DGPS antenna taking into account the movements of the ship. The GPS positions have an intrinsic error at the ≈ cm level. From these positions and accounting for the measured sound velocity profile with respect to the depth the calibrated fixed position of the LBL beacons are found by multilateration with an accuracy of ≈ 50cm thanks to the RAMSES Kalman filter [49]. The LBL positions on the sea floor are shown in Figure 2.24,

Figure 2.22: Exail GGIX boat for LBL deployment.

Figure 2.23: LBL positions calibrated with the RAMSES Kalman filter.

they are deployed far from the detector centre thus increasing the lever arm to better constrain its absolute positioning. This 50 cm uncertainty on the absolute positioning translates for a LBL device 1 km away from the detector centre to an ≈ 0.03° error on the absolute orientation of the detector.

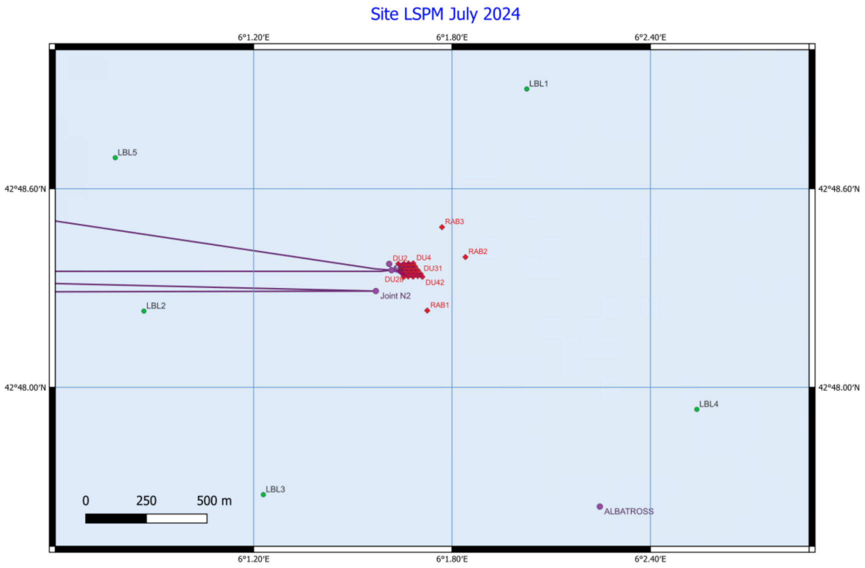

Figure 2.24: The LBL positions in the KM3NeT/ORCA network are shown in green. The ORCA DUs and RAB are shown in red. The nodes are shown in purple.

During the deployment of a DU onboard the Castor boat from Foselev Marine the acoustic transducer is located at a 6.3 metre depth at the edge of a mechanical arm shown in Figure 2.25. A beacon is placed on the winch cable attached to the DU as visible in Figure 2.26. The offsets for the arm geometry to calculate the real time position of the transducer with respect to the DGPS antenna on the ship thanks to the inertial central Hydrins are taken into account. Another beacon is also attached to the ROV, therefore the position of the two boats (Castor and Janus), the ROV and the DU are monitored in real-time with a sub-meter accuracy thanks to the NAAPS shown in Figure 2.27. The surface position of the ship is adjusted to land the DU within a 2 metre radius target. The ROV manually corrects the orientation of the DU anchor before landing. Once the DU is released from the winch deep sea cable of the boat, the anchor position on the seafloor is calculated with an accuracy of 50 cm relative to the LBL beacons and the anchor orientation is provided by the ROV compass with an uncertainty of 10°.

The 50 cm error on the DU position relative to the LBL beacons translates for a 100

Figure 2.25: Mechanical arm with the transducer on the Castor boat.

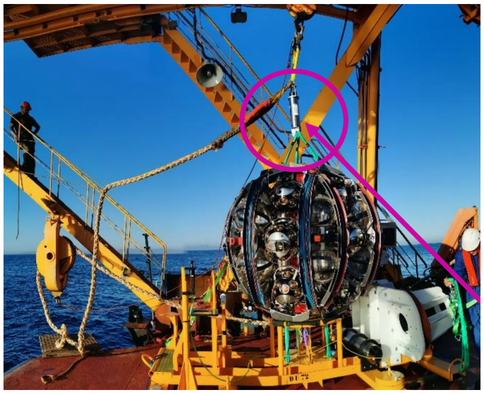

Figure 2.26: Autonomous beacon attached to the winch cable close to the DU.

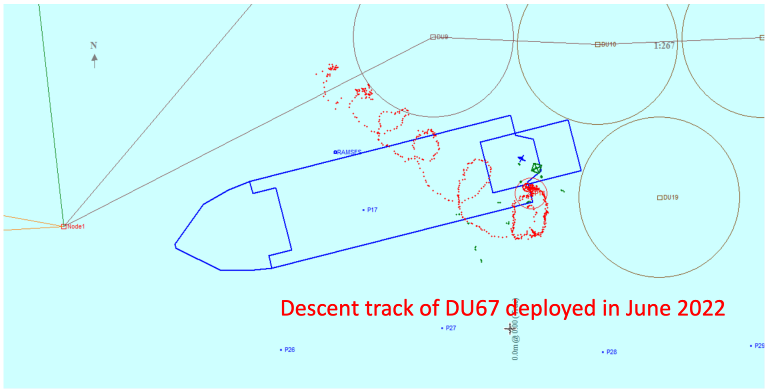

Figure 2.27: Monitored sub-metre calibrated positions of the boat and beacon during the DU descent.

metre wide (current) detector to a maximum ≈ 0.6° error on the absolute orientation. This gives an approximate order of magnitude of the expected error on the absolute pointing of KM3NeT/ORCA. Besides it is expected that when increasing its size during construction the detector will have a higher lever arm thus a lower contribution of the positioning error into the absolute orientation uncertainty. This can be compared to the KM3NeT/ARCA error on the absolute positions at the level of ≈10 m using an Ultra Short BaseLine (USBL) acoustic positioning system system during deployment which converts (for a currently 550m wide detector) into a maximum angular error of around 2.3°.

2.6.2 Acoustic positioning fit

The relative positions of the DOMs are found during a fitting procedure involving Piezo-electric acoustic sensors present in every DOM. They are cylindrical piezo ceramics with a diameter of 18 mm and a height of 11.5 mm as shown in Figure 2.31. Where they are located the pressure is slightly below the atmospheric value, and the cooling is achieved by the 13°C water temperature. Since all DOMs and BMs of the detector are synchronised and phased with respect to the GPS time signal transmitted from shore, the whole acoustic receivers array is synchronized to the GPS master clock. The time synchronisation from the GPS system on shore is based on the satellites multilateration system. Since the shore station relocation in January 2024 the GPS system was failing to find the satellites signals. However it was solved in August 2024. During that time the timing was provided instead by the NTP server.

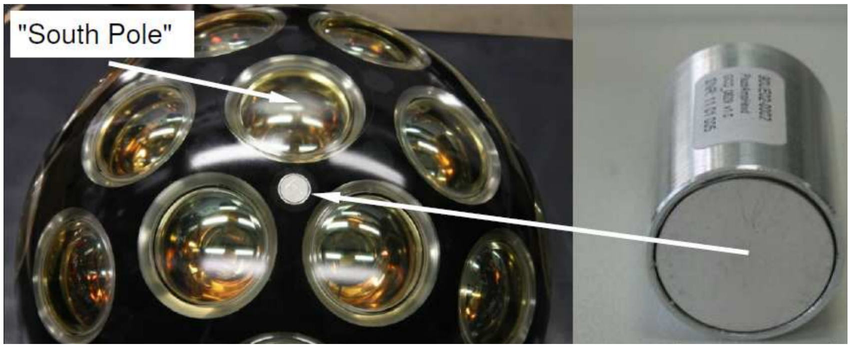

Figure 2.28: A piezo-electric digital acoustic sensor integrated in a KM3NeT DOM.

Currently only the internal to the DOM piezo sensors are used in the acoustic position fit. In addition external emitters, recoverable acoustic beacon (RAB) powered on battery are placed on tripods standing on the sea floor and some are directly attached to the DU base or node (node only for KM3NeT/ARCA) as shown in 2.29 from [48].

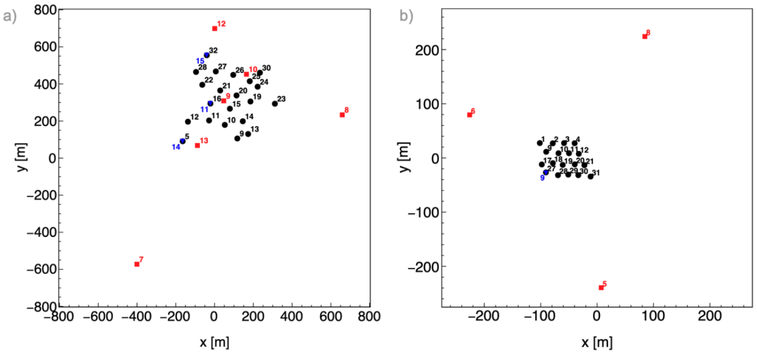

Figure 2.29: Footprint of the current (a) ARCA and (b) ORCA detector configurations. The x and y direction correspond to the easting and northing with respect the detectors reference frame. Detection units are represented with black dots, autonomous acoustic emitters with red squares and emitters on the base modules with blue triangles.

The RABs are distributed within or outside the detector footprint, in order to accurately compute the positions of the DOMs. The emission pattern of the emitters is 10 consecutive emissions or pings every 10 minutes. In addition the emitters which are connected to the base modules or junction boxes, emit continuously ≈ 1 ping every 30 seconds. Each of the emitters has a specific frequency, which is recognised by an acoustic data filter (ADF). The filter matches the possible waveform of the signal by searching in the acoustic raw data to identify the emitter. Its saves in its output a time-of-arrival and an emitter identifier.

The nominal position of the detector elements are extracted from the anchor position given after deployment and are used as the starting values for the fit. The estimated time-of-emission is computed from the knowledge on the nominal positions, the sound velocity at this depth, and the recorded time-of-arrival. An acoustics event is triggered when several piezos measure an emission in a given time window. The acoustic fit consist of fitting the detector geometrical model to a set of acoustic events that lasts 10 minutes. During this period the detector does not move significantly.

The geometrical model is parameterised by static (fixed) and dynamic (updated every 10 minutes) parameters. Included in the static parameters are the anchor position, the height of the DOMs, the external hydrophones position that depends of the anchor's orientation and the RAB positions. In addition two fixed mechanical parameters describing the DU shape are used and the sound velocity is also fixed to the measured value.

Concerning the dynamic parameters, two tilt angles, amplitude and orientation shown in Figure 2.30, are involved with their 2^{nd} order corrections, a parameter accounting for the overall stretching of the Dyneema rope holding the DU, and the time-of-emission of the acoustic signals. The acoustic fit minimises the χ^2 built as the sum of differences between the measured and estimated times of arrival normalised by an assumed resolution, chosen to be 50 microseconds corresponding to $\approx$ 7.5 cm.

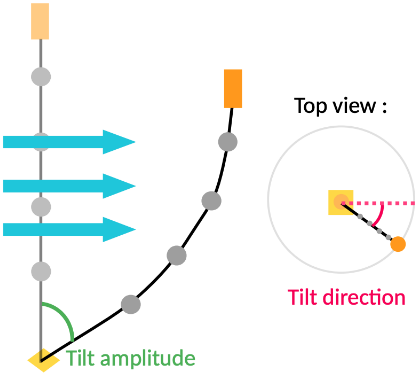

Figure 2.30: Scheme of the parameters involved in the dynamic geometrical model : tilt amplitude and orientation.

In addition to the position, the orientation of the DOMs and DU bases are calibrated separately thanks to magnetometer and accelerometer that are integrated in each DOM. These compasses helps contraining the twist of the DU as shown in Figure 2.30. The compasses are calibrated in the lab before deployment. Once the DU is deployed a static calibration is performed in-situ by correcting the optical module orientations to find the alignment of the modules for each DU using the compass data in a 10 minutes time window. It is based on the fitting of the data to a polynomial model of a continuous DU twist around the vertical axis.

The compass data is recorded every 10 seconds therefore allowing for a dynamic calibration of the orientations. Every 5 minutes the average DOM orientation are calculated and updated. Filters are applied to remove larger than 5° deviation from the local interpolation of the orientation. If the DOM is missing compass data, the orientation is interpolated from the neighbouring DOMs.

Figures 2.32 and 2.33 from [48] show the tilt and twist angles of several DUs in ORCA and ARCA over several days.

A coherent movement of the DUs correlated with sea current is observed. The sea current can lead to $> 6°$ tilt amplitude and 180° difference in tilt orientation in ARCA

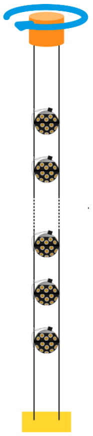

Figure 2.31: Scheme of the twist angle for dynamic orientation

due to the overall length of the DUs, 4x larger compared to ORCA (≈200m compared to ≈700m). Therefore the dynamic position calibration is mandatory to reach the ultimate angular resolution in particular for the ARCA detector.

Atmospheric muons can be used to complement the acoustic positioning calibration. During the reconstruction of an event the best track quality is found based on the triggered hit time residuals of that event. One might consider additional free parameters in the track fit, such as offsets on the positioning and orientation of a given DU. [50]. It is then used to verify the output of the acoustic fits as shown in Figure 2.34 and Figure 2.35 and to calibrate the inter-DUs time offsets as shown in the next Section. The dynamic orientations agree with the muon calibration by ±3° and the positions by ±10 cm, consistent with the specifications to reach the envisaged angular resolution of KM3NeT.

2.6.3 External piezo-sensors

The acoustic receivers hosted on the DU base are external piezo-sensors referred to as hydrophones, shown in Figure 2.36.

They will be used for the acoustic studies presented in Chapter 4. They are composed of a spherical piezo-ceramic element, read-out by an analogue board splitting the signal in two lines with different gains, +46 dB and +26 dB. This has been implemented to avoid signal saturation when the hydrophone is placed ≈ 1m close to the beacon. It also allows to use the high gain channel to analyze data received from up to a few km beacons and to study fainter acoustic signals like bio-acoustics environmental signals and possible acoustic

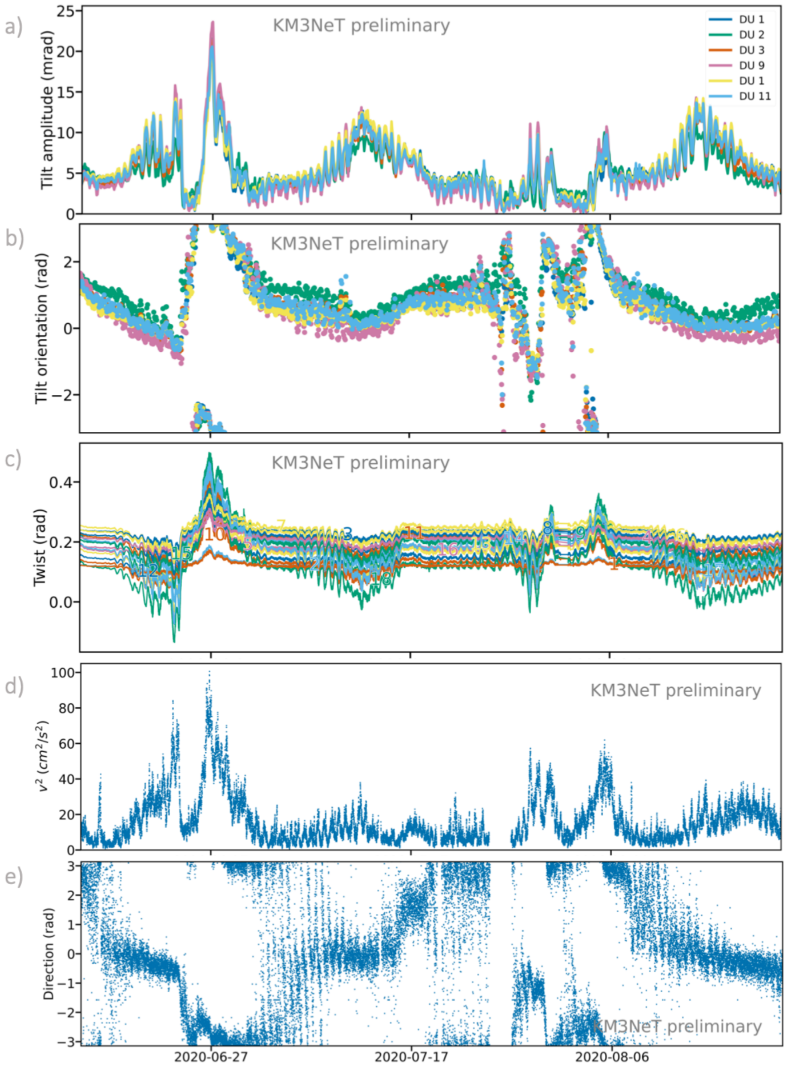

Figure 2.32: (a) Tilt amplitude for each detection unit. (b) Tilt orientation for each detection unit. (c) Twist of the optical modules from detection unit 11. The different modules are indicated by a number corresponding to their position along the DU; 1 for the lowest module, 18 for the top one. (d) Square of the measured sea current velocity. (e) Measured sea current direction. All plots are for the same period, which comprises four months of the KM3NeT/ORCA6 detector.

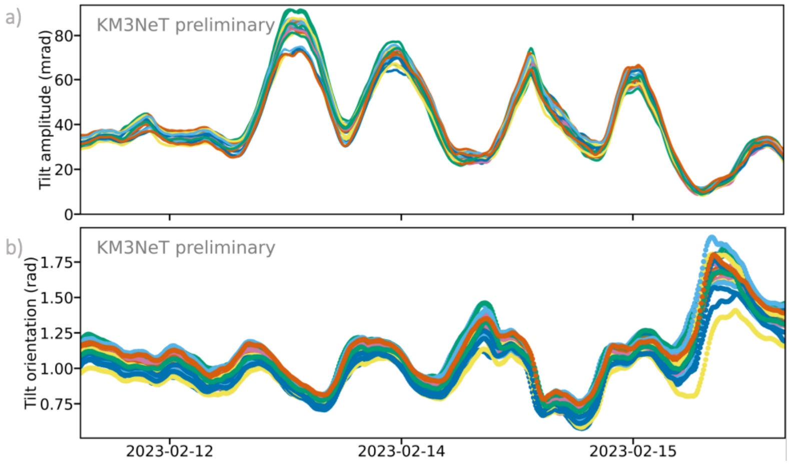

Figure 2.33: a) Tilt amplitude and b) tilt orientation, for a few days period of the current KM3NeT/ARCA detector, with a 21 detection units configuration. The different lines indicate different detection units.

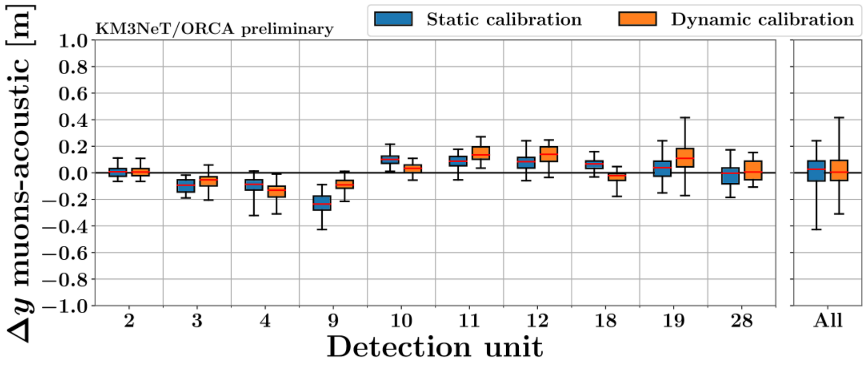

Figure 2.34: Optimal position offset in metres obtained with the muon track quality method with respect to the acoustic calibration, static and dynamic shown for each individual DU of ORCA and for all DUs. Boxes contain 50% of the DU entries. The whiskers show the minimum and maximum entry values.

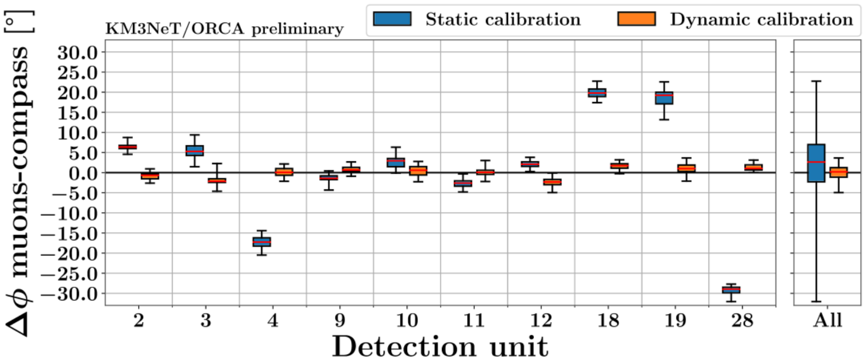

Figure 2.35: Optimal orientation offset obtained with the muon track quality method with respect to the orientation calibration from compasses, shown for each individual DU of ORCA and for all DUs. Boxes contain 50% of the DU entries. The whiskers show the minimum and maximum entry values.

Figure 2.36: A KM3NeT hydrophone connected to BM during an acoustic calibration test at CPPM.

neutrino detection. A filter frequency of > 700 Hz, is applied in KM3NeT/ARCA to reject the low frequency ambient sea-noise changing in 1/f, and flattens at about 5 kHz, therefore improving the Signal to Noise ratio in the detection of beacon pulses which frequencies are between 20 and 40 kHz. However in KM3NeT/ORCA hydrophones, no filter is applied to keep sensitivity for very low frequencies of marine mammals detection studies. They will also be crucial in the absolute orientation calibration procedure based on the acoustics study described in Chapter 4.

2.7 Time and PMT calibration

The time synchronisation of KM3NeT is crucial to achieve the precise hit position and sub-nanosecond time resolution specifications required by the physics goals of the collaboration. The delays arising at different levels of the infrastructure, by cable length, signal propagation, affect the time calibration of the KM3NeT detector elements. To reach the sub-nanosecond relative timing precision they must be resolved at different scales using appropriate calibration tools:

- inter-PMT: The relative time offset (t0) of each PMT channel is defined as the difference between its mean transit time and the one of the designated reference PMT for the DOM. The transit time in a PMT refers to the time it takes for an electron to travel from the photocathode to the anode. The distribution of the transit time is assumed to be gaussian and the standard deviation of the transit time is measured in-lab to be around 2.1 ns. This calibration aims to synchronize the individual PMT within a DOM. It is based on the light produced from the decay of ^{40}K naturally present in sea water. The knowledge on the constant salt density, the ^{40}K isotope ratio and the decay properties allows to calibrate the timing and efficiency of the PMTs using coincident hits on neighboring PMTs as in [51]. The results are independent from the sea water properties such as absorption length. The coincidence rate detected by a pair of PMTs is proportional to the product of their respective photo-detection efficiencies and a factor reflecting the coincidence rate as a function of the opening angle between the PMT axes. By using this constant radioactive background mainly from the sea water salt all the 465 pairs of PMTs of a DOM can be simultaneously fitted. Eventually the time offsets and efficiency of each PMT are determined in a dynamic calibration process as shown in Figure 2.37. The offsets and efficiencies are found to stable for months.

- inter-DOM: A White Rabbit (WR) network interface is implemented in the DU base CLB in order to synchronize the detector elements with a nanosecond accuracy. The WR protocol uses the measurement of the round-trip-time signals from the shore station to

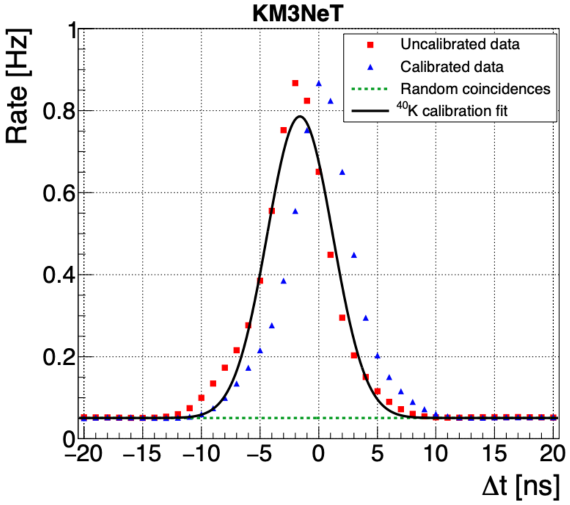

Figure 2.37: Distribution of the time differences between the hit in coincidences for a pair of nearby PMTs for uncalibrated (red) and calibrated (blue) hit times after applying the time offset. Superimposed are the calibration fit (black) and the background of random coincidences (green) with uniformly distributed time differences.

the DU bases to synchronise the CLB clock on the master clock by accounting for the propagation delays. However with this methods only the DUs are synchronized, the clock is broadcasted to the DOM but the different cable length for each DOM are not taken into account. Therefore the DOMs of a DU need to be synchronised. To that purpose a dedicated laser calibration setup in a dark room (for instance at CPPM) is used. During the calibration process a single PMT is chosen for reference in every DOM and the hit times recorded are used to measure the inter-DOM time offsets. This reference PMT has a time offset of zero with respect to the DOM in order to match the inter-DOM and intra-DOM calibrations. Those time offsets are verified in-situ by flashing LED beacons or nanobeacons installed on the DOM's upper hemisphere.

• inter-DU: Based on the study of the muon track quality (discussed previously) when shifting the DU time reference, the inter-DU time offsets are measured and reported in Figure 2.38 from [50]. Although the WR system is used to synchronize the DUs, remaining offsets are measured at the level of 5 ns for KM3NeT/ORCA and 10 ns for KM3NeT/ARCA and are corrected thanks to this method. It also illustrates that the difference between static and dynamic is small for KM3NeT/ORCA.

Once the offset are applied the inter-quartile difference values that quantify the spread-

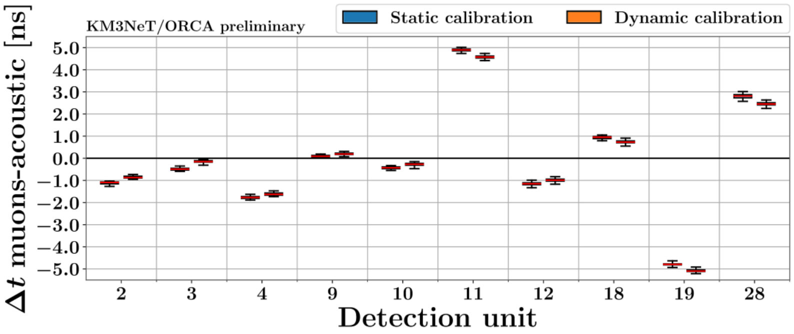

Figure 2.38: Optimal time offset obtained with the muon track quality method with respect to the orientation calibration from compasses, shown for each individual DU of ORCA and for all DUs. Boxes contain 50% of the DU entries. The whiskers show the minimum and maximum entry values.

ing of the optimal time offsets are computed. They fall within ≈ 0.1 ns for ORCA and 0.3 ns for ARCA. Therefore again consistent with the sub-nanosecond specifications to reach the envisaged angular resolution of KM3NeT.

2.8 Conclusion

The relative sub-nanosecond timing, $< 3^\circ$ orientation precision and ≈ 10 cm positioning accuracy of the detector elements match the specifications formulated by KM3NeT in [26]. It demonstrates the success of all the effort and time dedicated by the Collaboration to the calibration of the detector. However a large improvement on the knowledge of the absolute orientation, mainly of the KM3NeT/ARCA detector, is still necessary to achieve the envisaged pointing accuracy as quoted in [VHE]. Therefore motivating the work presented in the next two chapters.

Chapter 3

Cosmic ray shadows of the Moon and the Sun

This chapter reports the first observation of the Moon and the Sun shadows in the sky distribution of cosmic-ray induced muons measured with KM3NeT/ORCA. The analysed data-taking period spans from February 2020 to November 2021, when the detector had 6 Detection Units deployed at the bottom of the Mediterranean Sea. The shadows induced by the Moon and the Sun were detected at their nominal position with a statistical significance of 4.2σ and 6.2σ, and an angular resolution of $\sigma_{res} = 0.49°$ and $\sigma_{res} = 0.66°$, respectively, consistent with the prediction of 0.53° from simulations. This early result confirms the effectiveness of the detector calibration, in time, position and orientation and the accuracy of the event direction reconstruction. This also demonstrates the performance and the competitiveness of the detector in terms of pointing accuracy and angular resolution. A first study constraining the pointing accuracy of KM3NeT/ARCA in a 21-DUs configuration is also presented. In a more recent work, the evolution of the Sun shadow has been measured with data taken by KM3NeT/ORCA in the period that spans from February 2020 to August 2023 with up to 18 DUs.

3.1 Origin of the signal

Cosmic rays are blocked by nearby celestial bodies such as the Moon and the Sun. This induces a deficit in the atmospheric muon flux and in other secondary CR particles coming from the direction of these objects. This effect had been predicted by Clark in 1957 [52]. Its observation can be used to verify the pointing accuracy and angular resolution of detectors which are able to measure secondary particles from CR interactions. The Moon and the Sun shadows in CRs have been observed by multiple experiments (IceCube [53], ANTARES [54, 55], MACRO [56], L3 [57], MINOS [58], ARGO-YBJ [59], HAWC [60] and others). As a permanent bright high-energy neutrino source has yet to be found, the observation of the Moon and Sun shadows in CRs is an important calibration tool for neutrino telescopes such as KM3NeT/ORCA and helps to demonstrate their pointing accuracy and to measure their angular resolution.

3.2 Data sample

The data used in this analysis were collected between February 11, 2020, and November 18, 2021 for a total of 499.3 days. Quality cuts on the number of used hits and the likelihood of the track reconstruction were applied to remove poorly reconstructed events keeping 83% of the initial event sample. An average event density of 3000 events per square degree is measured in the vicinity of Moon and Sun. It is expected that about 640 CR events are blocked by each of the two sky objects. The position of the Moon/Sun in the sky is obtained using the *astropy* package [61] that relies on the International Celestial Reference System (ICRS) coordinates described in [62]. The latitude of 43° North of the detector and the data taking period of more than one year lead to broad zenith angle distributions of the selected events in the vicinity of Sun and Moon as shown in Figure 3.1.

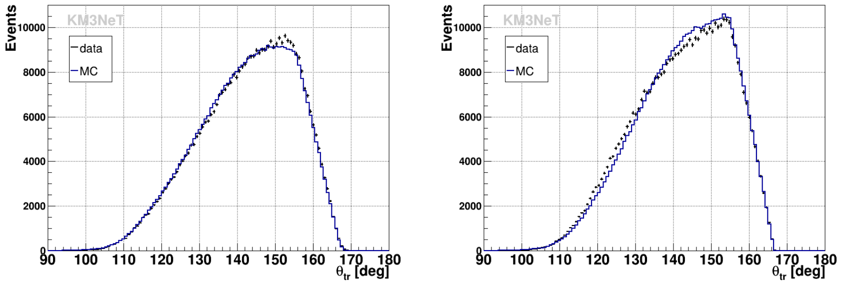

Figure 3.1: Zenith angle distribution of selected events for the Moon (left) and the Sun (right). Data (black crosses) and simulations rescaled to data (blue histograms) are shown.

Monte Carlo (MC) simulations are used to optimise the track selection as described in Section 3.5, and predict the angular resolution and amplitude of the CR deficit induced by the Moon and the Sun. Secondary muons at the KM3NeT/ORCA detector are simulated with the MUPAGE package [63] [64]. These muons are then propagated through sea water and Cherenkov photons are created within a cylindrical volume surrounding the simulated detector. Finally the detector response is simulated by producing digitized hits from photons detected by PMTs and by adding noise hits from environmental background mainly due to ^{40}K decay and bioluminescence. These are derived from real data runs in a time-dependent way following the *run-by-run* approach previously introduced by the ANTARES Collaboration [28]. The time-dependent PMT efficiencies are monitored and used in the simulation. The last two steps are done with KM3NeT custom software [65]. The resulting hit patterns are passed through the trigger and reconstruction steps using the same software that is used to process real data. The simulated track sample is about 4 times larger compared to the real data sample.

The optimisation of the track selection is performed by varying the cut on the angular error estimate from the track reconstruction to maximize the significance of the shadow signal. By requiring a more and more stringent cut a smaller but higher quality event sample is selected. The chosen value keeps 45% of the original MC sample.

3.3 Shape of the shadow

The general equation that describes the shape of the deficit to be measured is written as

$$G_i(A, \sigma_{\mathrm{res}}, x_s, y_s) = A \int_{x_p} \int_{y_p} P(x_s - x_p, y_s - y_p) \cdot \mathrm{PSF}(x_p - x_i, y_p - y_i)\, dx_p\, dy_p \qquad (3.1)$$

Here, P describes an arbitrary shape of a sky object around (x_s, y_s). The point spread function (PSF) characterises the shape and size of the response of the detector to a point source emission.

The effect of the size of the Moon/Sun on the shadow signal has been studied with a toy MC that was generated by randomly sampling true event coordinates within a square of 10° size. Then the events that have true coordinates falling within a 1° radius disk (representing the Moon/Sun) were discarded. Figure 3.2 shows the shadow effect artificially produced on the distribution of the reconstructed event coordinates. For an angular resolution above the Moon radius it is difficult to see the shadow in the event distribution therefore it is necessary to apply a statistical method to measure it. The case for KM3NeT corresponds to the left of the Figure where the Moon is three times smaller than the estimated angular resolution, and the shadow is fully blurred. When the angular resolution improves below the radius of the sky object, its contours start to be visible in the reconstructed events distribution, therefore cannot be neglected.

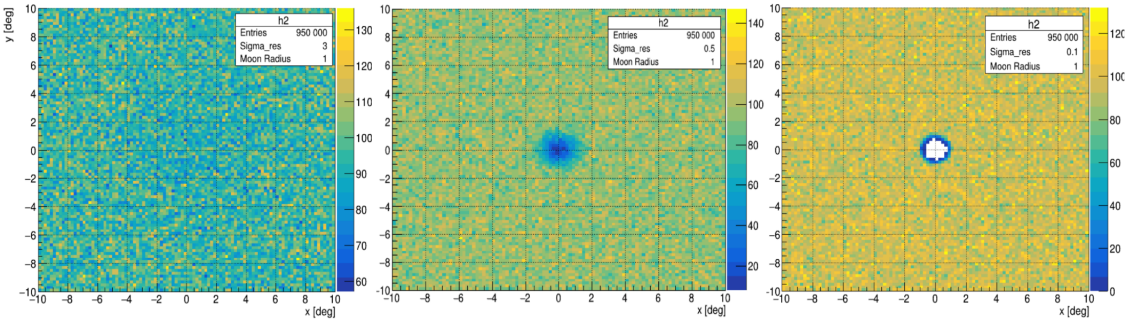

Figure 3.2: Distribution of the reconstructed toy-MC event coordinates for the case of a larger resolution than the Moon radius on the left and the case of a half the moon radius in the centre and a tenth of the moon radius on the right.

The Figure 3.3 illustrates that the compatibility between the data from the toy MC including the shadow and the model involving a PSF (gaussian) that neglects the size of the sky object, is lost when the angular resolution of the detector goes below the sky object angular radius. Therefore, as the Moon/Sun apparent angular radius is $\approx 0.26°$, more than a factor two lower than the PSF width of KM3NeT/ORCA (described in the next paragraph), the size of the sky object can safely be ignored. In the approximation of

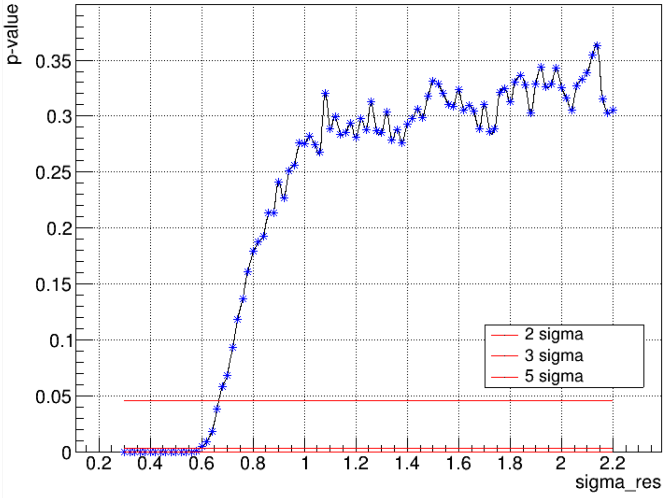

Figure 3.3: Compatibility between the PSF (gaussian here) and the toy MC data when varying the angular resolution for a fixed Moon radius of 1°.

small sky object size compared to the PSF width, G_i factorizes as

$$G_i(A, \sigma_{\text{res}}, x_s, y_s) = A \cdot \text{PSF}(x_s - x_i, y_s - y_i) \int_{x_p} \int_{y_p} P(x_s - x_p, y_s - y_p)\, dx_p\, dy_p \tag{3.2}$$

Which becomes for a circular object of radius R_s

$$G_i(A, \sigma_{\text{res}}, x_s, y_s) = A \cdot \text{PSF}(x_s - x_i, y_s - y_i) \cdot \pi R_s^2. \tag{3.3}$$

In KM3NeT/ARCA the PSF width is expected to be lower than KM3NeT/ORCA therefore it should be verified that the angular resolution remains above the Moon/Sun radius to safely ignore the size of the sky object.

The PSF of the detector has a slightly different radial shape compared to a Gaussian function (see Figure 3.4, right). The non-gaussian tail will be accounted for by fitting the shadow amplitude A. It is observed, that the PSF is identical for the data samples selected for Moon and Sun. Further, the PSF is perfectly symmetric in x and y as shown in Figure 3.4 (left).

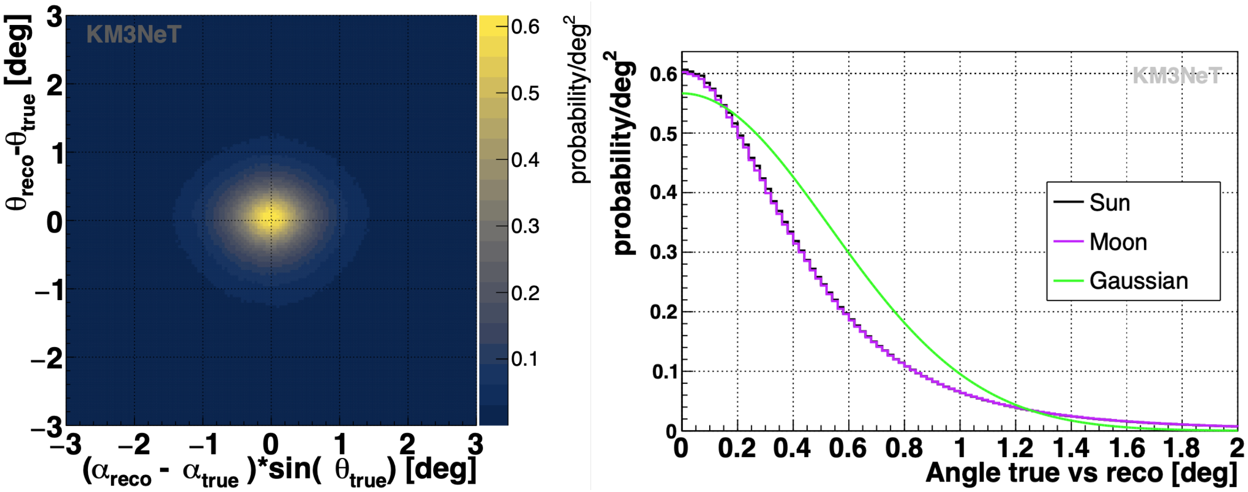

Figure 3.4: PSF from MC, *i.e.* the difference between the true muon direction and the reconstructed one in 2-dimensional angular space (up) and as function of the space angle difference (down, blue and magenta for Sun and Moon, respectively). A Gaussian PSF with $\sigma = 0.53°$ is shown in green for comparison.

In the Gaussian approximation of the PSF, which allows to fit an angular resolution

σ_{res}, G_i takes the form used in the analysis

$$G_i(A, \sigma_{res}, x_s, y_s) = A\frac{R_s^2}{2\sigma_{res}^2} \exp\Big[-\frac{(x_i - x_s)^2 + (y_i - y_s)^2}{2\sigma_{res}^2}\Big]. \tag{3.4}$$

A possible improvement could be to account for the PSF in the fit and use the full width at half maximum FWHM as a proxy for the angular resolution.

The Moon radius varies between 0.245° and 0.279° resulting in an amplitude variation of ±14% around the mean value. However our data sample covers several Moon cycles, so the average value is used. A similar statement can be made for the Sun whose apparent radius varies between 0.262° and 0.271° during the year.

3.4 Analysis method

The search for the shadow of the Moon/Sun is done in the phase space of the angular differences between the reconstructed track coordinates and the celestial object. Both a 1-dimensional and a 2-dimensional analysis have been performed. The 1-dimensional analysis uses the space angle between the direction of the Moon/Sun and the track. The 2-dimensional analysis uses two Cartesian coordinates (x, y), starting from the zenith and azimuth angles of the sky object θ_{sk}, α_{sk} and the tracks θ_{tr}, α_{tr} respectively,

$$\begin{aligned} x &= (\alpha_{sk} - \alpha_{tr}) \sin\theta_{tr} \\ y &= \theta_{sk} - \theta_{tr} \end{aligned} \tag{3.5}$$

2D maps that extend to ±6° in (x, y) have been constructed. Data are only used for times when the full ±6° field around the Moon/Sun is above the horizon. An angular range of ±6° contains the detectable shadow signal entirely and it allows for a simultaneous fit of the shadow and background parameters while analysing just a moderately-sized atmospheric muon sample. It has been verified that the results do not depend on the precise choice of the chosen angular range. A constant 0.1° binning in x and y is chosen, however results are reproduced when choosing a smaller binning. The 1D histogram contains tracks that are closer than 4° to the Moon/Sun position.

The significance of the shadowing effect of Moon/Sun is determined with a likelihood ratio test, by comparing the likelihood of a background hypothesis model H_0, with the likelihood of a signal plus background model H_1 which includes a shadowing effect. The

Poisson likelihood with the definition in Ref [66]

$$\chi^2(H) = 2\sum_{i}^{N_{bin}}[N_{i,H} - n_i + n_i \ln(n_i/N_{i,H})] \tag{3.6}$$

is used, where n_i stands for the event count in the i-th space angle bin to be compared with the expectations $N_{i,H}$ under the H_0 and H_1 hypotheses. The difference in $\Delta\chi^2_{H1/H0} = \chi^2(H_1) - \chi^2(H_0)$ values is used to determine the probability to reject the null hypothesis and to extract the significance of the observation from it. The background event distribution in azimuth is found to be uniform, while the zenith angle dependency can be conveniently parametrized with a 2^{nd} order polynomial function. This yields for the 2D maps

$$N_{i,H_0} = \rho\big[1 + a_1 y_i + a_2 y_i^2\big] \tag{3.7}$$

with ρ a constant track density per space angle and a_1, a_2 parameters which are determined during minimisation. The track density per space angle is constant due to the averaging over the complete range of zenith and azimuth positions of the sky object. For the 1D maps, each bin contains events from an almost symmetric zenith angle range above and below the Moon/Sun position resulting in a uniform exposure, *i.e.* $N_{i,H_0} = \rho$.

The event expectation in bin i for the signal plus background hypothesis H_1 is defined as

$$N_{i,H_1} = N_{i,H_0} - \rho \cdot G_i \tag{3.8}$$

where G_i defined in Section 3.3. It describes the deficit of secondary CR events due to the shadowing effects of Moon/Sun in bin i with coordinates x_i, y_i as a bi-dimensional Gaussian described by Equation 3.4 where A is the relative shadow amplitude. For $A = 1$ the number of blocked CR events correspond to $\rho\pi R_s^2$. The angular resolution of the detector for the selected sample of CR events is measured by σ_{res}, the angular width of the Gaussian shadow. The R_s, x_s, y_s parameters are the apparent angular radius of the celestial object and the relative angular position of the Moon/Sun shadow with respect to their nominal positions. For the 1D maps, shown in Section 3.6, the term $(x_i - x_s)^2 + (y_i - y_s)^2$ in Equation 7.9 is replaced by δ^2, the square of the angular distance between the track and the sky object from Equation 3.9 with V_{tr} and V_{sk} the direction vector of the track and the sky object respectively.

$$\delta = \arccos\left(V_{tr} \cdot V_{sk}\right) * 180/\pi \tag{3.9}$$

The significance of the shadow is found by fitting ρ, a_1, a_2, A and σ_{res} at $(x_s, y_s) = (0, 0)$ on the 2D or 1D event distribution respectively. Results from these fits are summarized in section 5.2. The position of the shadow is obtained by simultaneously fitting ρ, a_1, a_2, (x_s, y_s) and A, with σ_{res} fixed to its expectation value from MC. Results from these fits are found in Section 5.3.

3.5 Signal optimisation

The angular error estimate is used to optimize the sensitivity to the signal. The angular error estimate given by the reconstruction algorithm for each track is not a direct measure of the angular resolution, but an indicator for the reconstructed direction quality. It is used to select events with a better angular resolution, therefore to optimize the sensitivity to reject H0. To optimize the selection a scan over the angular error estimate is performed. The scan is done by keeping only events with a better angular error estimate than the cut value. An optimum is expected as stricter cuts remove more events so a balance between the available data sample and its angular precision is expected.

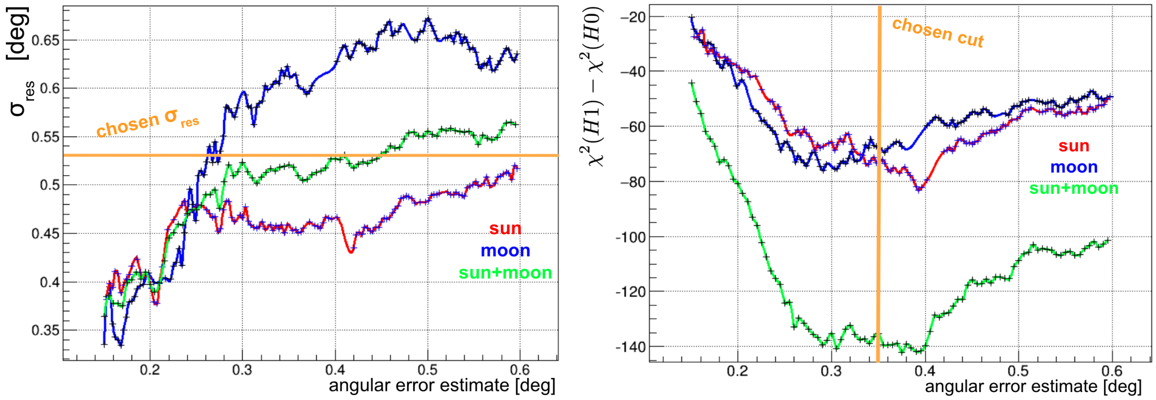

Figure 3.5: Angular error estimate cut optimisation. The width of the gaussian is shown on the left while the sensitivity to the shadow measurement is shown on the right as a function of the cut on the angular error.

The right part in Figure 3.5 illustrate the sensitivity to the shadow measurement for the Moon(blue), the Sun(red) and the Moon+Sun(green) using a cut on the angular error between 0.1° and 0.6°. The left part reports the expected angular resolution for a given cut on the angular error estimate. The chosen cut is 0.35° and the corresponding gaussian width is $\sigma_{res} = (0.53 \pm 0.04)^\circ$ and amplitude $A = 0.90 \pm 0.09$. The amplitude is expected to be below 1 due to the gaussian approximation which does not account for the non-gaussian tail in the PSF. The effect of the cut and the fraction of selected events is shown in Fig. 3.6.

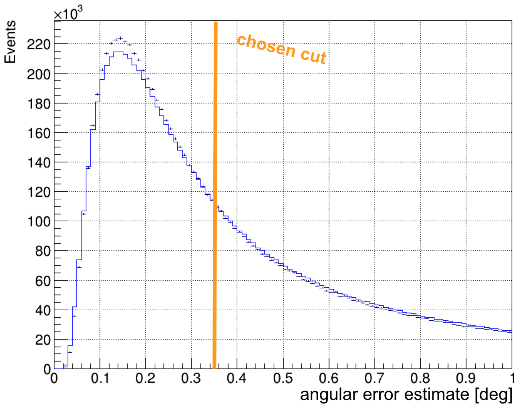

Figure 3.6: Normalised angular error estimate distribution. The blue line represents MC, and the black crosses correspond to data with errors.

45% of the events are selected with the cut and a good data/MC agreement is observed for that variable.

3.6 Background parametrisation

The down-going events from all directions are shown in Figure 3.7 in local coordinates. In addition below, the events close to the Sun and the Moon are shown. The events mostly accumulate in the direction close to vertical, where the muons have less water to cross therefore need less energy to arrive at the detector.

The background distributions in x and y are shown in Figure 3.8 for the Sun as an example. The background is entirely fitted from the data considering the deficit of event due to the shadow effect negligible. Fits of the H_0 hypothesis using a constant, and 2^{nd} order polynomial function describe the data well. Despite the detector having only 6 DUs, Earth rotation averages out any possible azimuth dependence, leaving a constant x distribution. The MC predictions are also compatible with these functions. Although slight differences are observed between data and MC in the zenith distribution, the 2^{nd} order fit to data accounts for these.

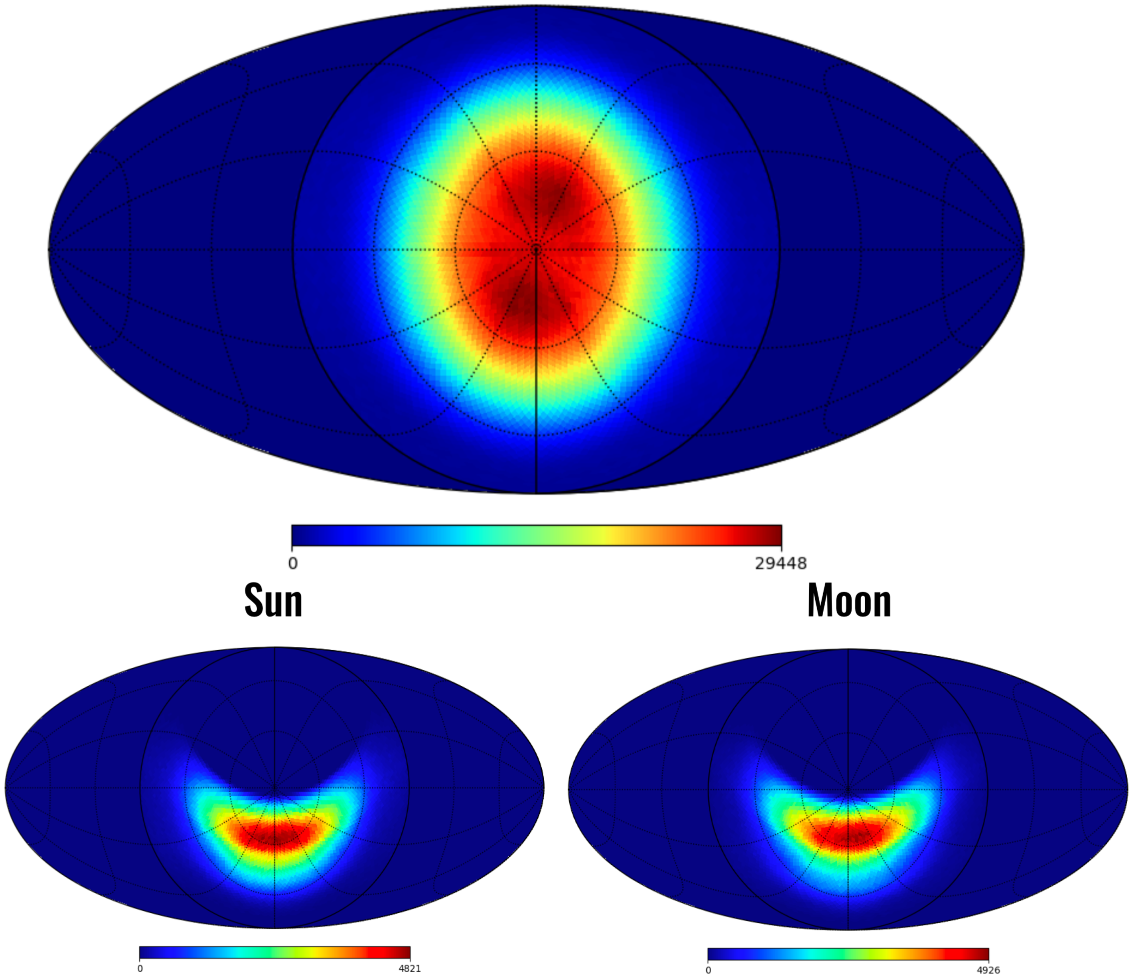

Figure 3.7: On the top the event distribution from all directions is shown in local coordinates with the vertical down-going placed in the centre of the skymap. The events with a space angle below 12° from the Moon (right) and the Sun (left) are shown below.

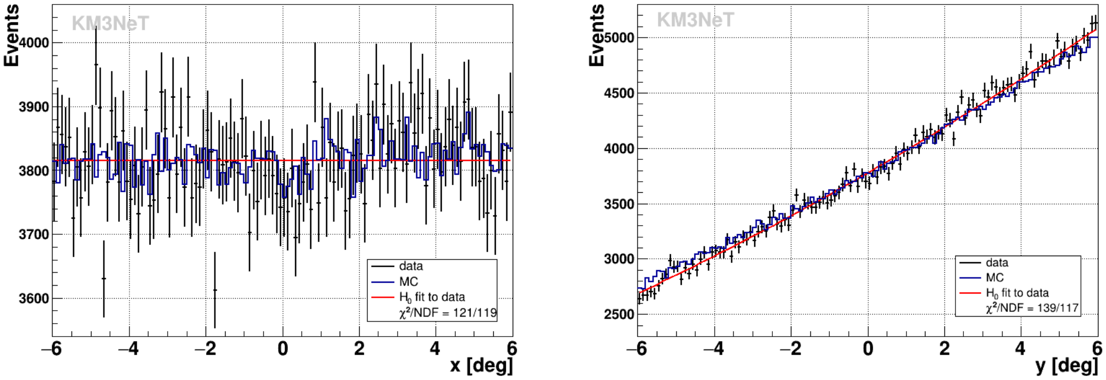

Figure 3.8: Event distribution in x and y for the Sun data sample (black crosses) compared to the polynomial fits from the H_0 hypothesis (red lines) and MC predictions rescaled to data (blue histograms)

.

A cross-check study on fake-sources in data have been performed in order to characterise the statistical fluctuations and verify the interpretation of the $\Delta\chi^2$ based on the Wilk's theorem. The analysis uses time shifted data-sets, which consist of using all events that fall in the Moon/Sun vicinity [2, 4, ... , 22] hours after the Moon/Sun was at that position. This produces comparable data-sets where no shadow is expected and the same region in zenith is scanned. It allows to quantify the expected statistical fluctuations when computing the same fit in 2D at the nominal fake Moon/Sun position. The results are shown in Figure 3.9. The low number of fake-sources does not allow to precisely measure the $\Delta\chi^2$ distribution, but it confirms that no fake-sources occurs in the same regions as the two sky objects' shadows.

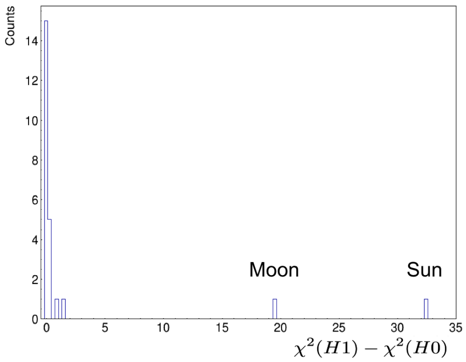

Figure 3.9: Fake-sources and sky objects $\Delta\chi^2$ distribution.

3.7 Measurement of the shadow with ORCA

The Table 3.1 report the results of the 1D and the 2D fit at the nominal position. It reflects the consistency between the expected angular resolution and amplitude with the measured ones.

Parameters	Moon 1D	Moon 2D	Sun 1D	Sun 2D
σ_{res}	$0.49° \pm 0.11°$	$0.49° \pm 0.15°$	$0.66° \pm 0.08°$	$0.65° \pm 0.13°$
A	0.69 ± 0.17	0.71 ± 0.27	1.38 ± 0.31	1.31 ± 0.34
$\Delta\chi^2_{H1/H0}$	-20.7	-21.3	-47.2	-43.0
Significance	4.2σ	4.2σ	6.5σ	6.2σ
Events/deg^2	2886	2892	3166	3161

Table 3.1: Parameters from the fits at nominal position $(x_s, y_s) = (0, 0)$

Figure 3.10 shows the 1D distributions of the event density as a function of the angular distance from the Moon/Sun. The fit results from the 1D and 2D fits at $(x_s, y_s) = (0, 0)$ are summarized in Table 3.1. The significances are derived from the $\Delta\chi^2_{H1/H0}$ with two degrees of freedom (A, σ_{res}). The values obtained for A and σ_{res} can be compared to MC expectations of $A = 0.90 \pm 0.09$ and $\sigma_{res} = (0.53 \pm 0.04)°$ for the combined Moon/Sun sample. The fitted values of σ_{res} are found compatible with the prediction from simulations. The deeper amplitude and higher significance of the Sun shadow is consistent with the effects of the particular structure of the Sun's magnetic field during the periods of low solar activity, whose dipole shape is expected to enhance the Sun shadowing effect [67].

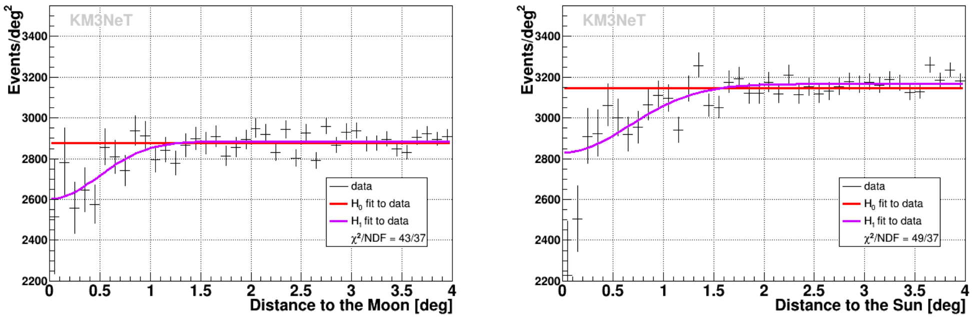

Figure 3.10: Event density as a function of the distance to the Moon on the left and the Sun on the right. Data (black crosses) are compared to the H_0 fit (red) and the H_1 fit (magenta).

3.8 Pointing accuracy of ORCA

The results from the fits of the 2D map in (x_s, y_s) with $\sigma_{res} = 0.53°$ are shown in Figure 3.11. The plot illustrates $\chi^2(H_1) - \chi^2(H_0)$ in colour coding. The image of the shadow is clearly visible.

Figure 3.12 shows the 1σ (68.3%), 2σ (95.4%), 3σ (99.7%) confidence contours for the two parameters (x_s, y_s) around the best fit point $x_s = (0.11 \pm 0.21)°$, $y_s = (0.04 \pm 0.13)°$ for the Moon and $x_s = (-0.01 \pm 0.11)°$, $y_s = (0.10 \pm 0.12)°$ for the Sun. The true position of the Moon and the Sun in Figure 3.12 are contained within the 68% contours, yielding a 84% and 67% compatibility between the nominal and the best fit positions, calculated from the corresponding $\Delta\chi^2$ with two degrees of freedom (x_s, y_s). The slightly different shapes of the contours for Moon and Sun can be entirely attributed to statistical fluctuations.

A study dedicated to constrain possible azimuth rotations of the detector has been performed. To simulate a rotation of the detector, all events' azimuth coordinate are shifted. The 2D fit is run over the shifted data-set and a $\Delta\chi^2$ is calculated. The sample is not identical to the non-shifted data-set due to migration of event from outside the fitted phase space, therefore it does not follow the Wilk's theorem requirements. However this effect is neglected and the Wilk's theorem is assumed to be valid. The Figure 3.13 illustrates the effect of the rotation of the detector in azimuth on the Sun shadow measurement. However in the Moon/Sun shadow 2D fit x_s is fitted, not the azimuth, which directly translates into the azimuth if the elevation of the Moon/Sun is zero. Both the Moon and the Sun have a non-zero elevation therefore x_s accounts for the average elevation of the sky object leading to a factor $\approx 1/2$ between the true azimuth shift and fitted x_s visible in

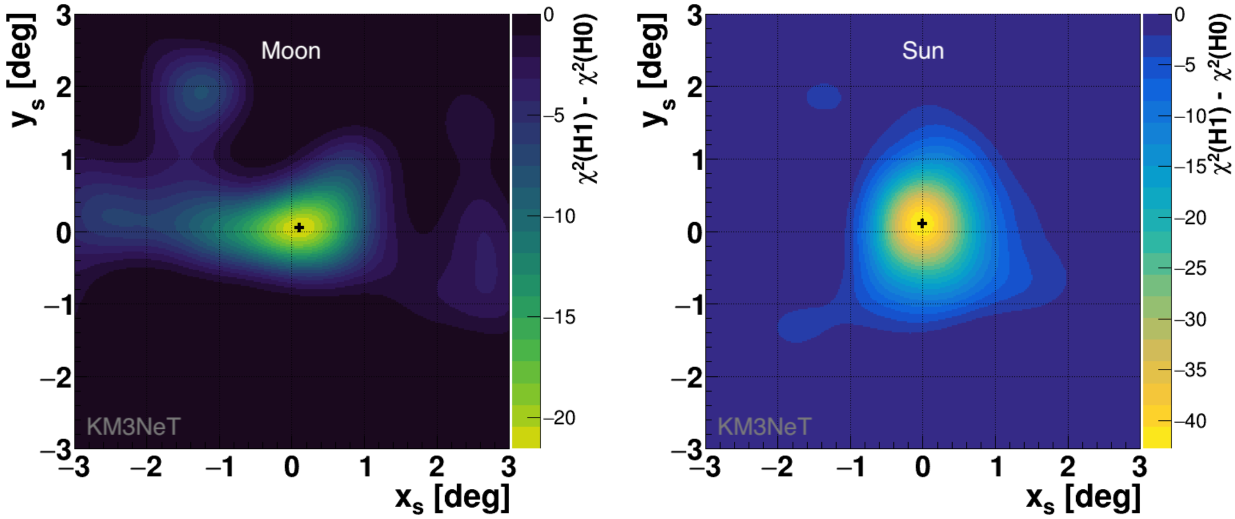

Figure 3.11: colour-coded $\Delta\chi^2_{H1/H0}$ as a function of x_s and y_s for the Moon (left) and the Sun (right).

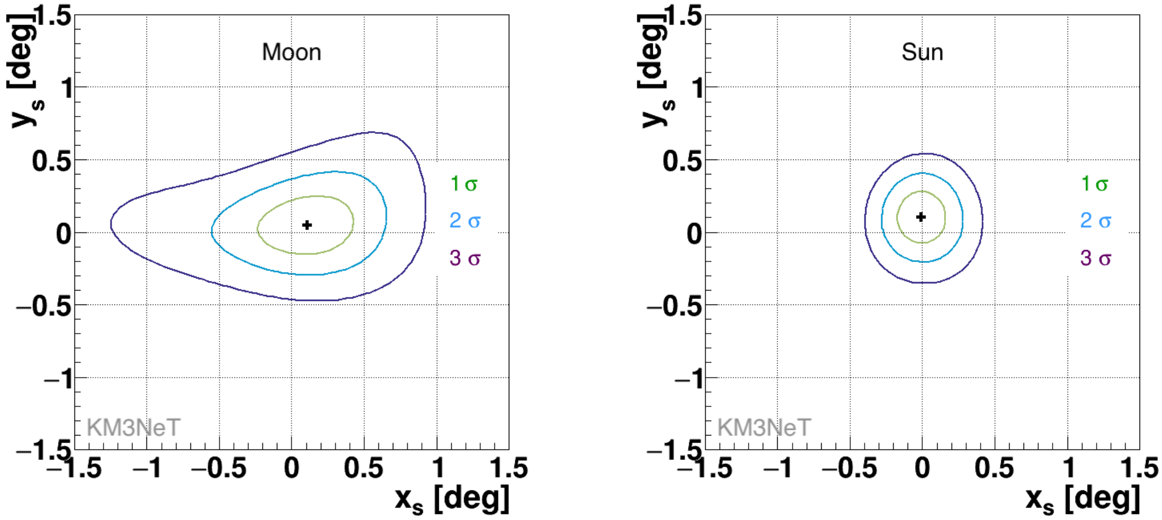

Figure 3.12: Confidence intervals derived from Figure 3.11 for the Moon (left) and the Sun (right). The black cross indicates the best fit point.

Figure 3.13 left. The right part of the Figure illustrates the exclusion of possible azimuth rotations of KM3NeT/ORCA at the 3σ confidence level larger than ±0.8°. This study on the azimuth shifts was performed before having the full ORCA6 data-set finalised, therefore a small difference is observed for the minimum position of the Sun shadow.

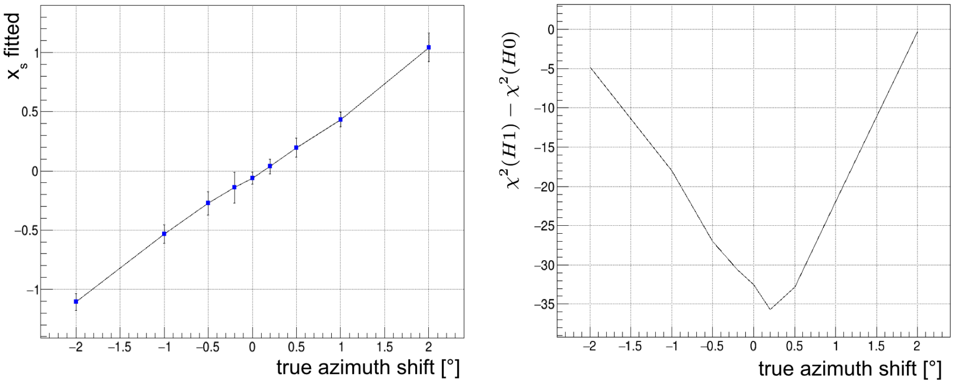

Figure 3.13: Results of the fit when adding an artificial azimuth shift to the events coordinates.

A similar analysis was performed in collaboration with Ludovic Donneger [68], whom I co-supervised, using data taken by KM3NeT/ORCA from January 2020 to August 2023 with between 6 and 18 DUs (ORCA6 to ORCA18). This study is based on more than twice the statistics used in the ORCA6 results. The average density of 14809 event per square degree for the combined Moon and Sun is almost a factor 5 larger than the previous study based on the Sun signal observed with KM3NeT/ORCA6. Figure 3.14 shows the 1σ (68.3%), 2σ (95.4%), 3σ (99.7%) confidence contours for the two parameters (x_s, y_s) around the best fit point for the Moon and the Sun combined.

The Figure 3.15 illustrates the new likelihood profile of possible azimuth rotations of KM3NeT/ORCA. The interval for allowed rotations of the detector becomes at the 3σ confidence level $[-0.15°, +0.55°]$. This results in a mild preference for a rotation of $\approx +0.3°$ in azimuth.

3.9 Pointing accuracy of ARCA

A similar analysis was performed using data taken with KM3NeT/ARCA in a 21 DUs configuration from September 2022 to June 2023 for a total exposure of 228 days, corresponding

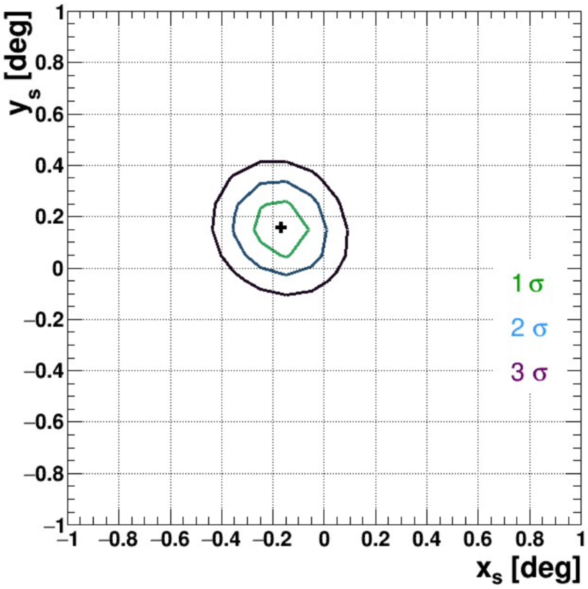

Figure 3.14: Confidence intervals for the Moon and the Sun (ORCA6 to ORCA18) combined signals. The black cross indicates the best fit point.

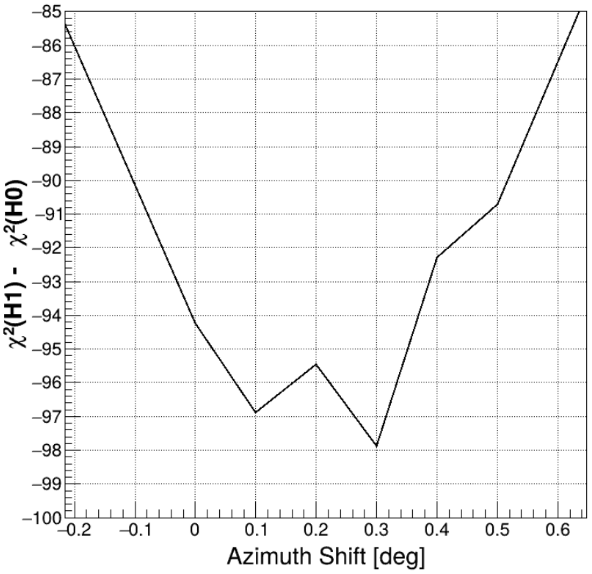

Figure 3.15: Results of the fit when adding an artificial azimuth shift to the events coordinates for the latest (ORCA6 to ORCA18) combined Moon and Sun signals.

to an average density of 1197 events per square degree for the Moon. This amounts to a third of the KM3NeT/ORCA6 statistics due to the 3.5 km depth of KM3NeT/ARCA and the steeply falling primary CR flux. The additional kilometre of water muons have to traverse reduces the observed muon rates in KM3NeT/ARCA6 one order of magnitude below KM3NeT/ORCA6 as visible in Figure 1.16. The results from the fits of the 2D map in (x_s, y_s) with $\sigma_{res} = 0.5°$ and $\sigma_{res} = 0.75°$ are shown in Figure 3.16. In the Figure the 1σ (68.3%), 2σ (95.4%), 3σ (99.7%) confidence contours for the two parameters (x_s, y_s) around the best fit point $x_s = (0.58 \pm 0.25)°$, $y_s = (-0.15 \pm 0.19)°$ for $\sigma_{res} = 0.5°$ and $x_s = (0.40 \pm 0.27)°$, $y_s = (0.09 \pm 0.31)°$ for $\sigma_{res} = 0.75°$. The true position of the Moon in both cases are contained within the 2σ contours. The pointing accuracy study suffers from the lack of statistics, therefore no deviation can be excluded with more than 3σ. However this first study demonstrates a first constrain of the absolute pointing using KM3NeT/ARCA cosmic ray Moon shadow. The Sun shadow does not help to constrain further the absolute pointing because no shadow is visible for the Sun in that time period where the solar activity is high.

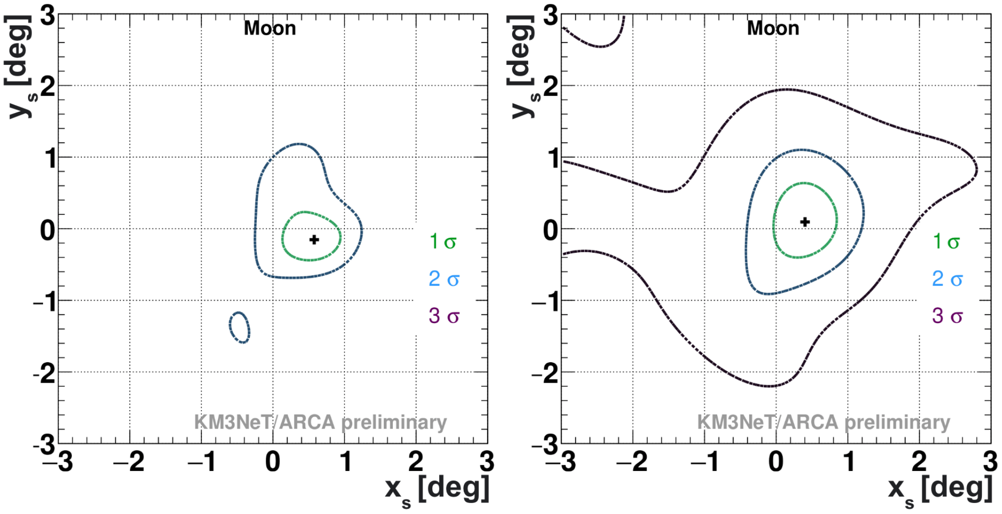

Figure 3.16: Confidence intervals for the Moon with fixed $\sigma_{res} = 0.5°$ (left) and $\sigma_{res} = 0.75°$ (right). The black cross indicates the best fit point.

3.10 Time evolution of the Sun shadow

A new analysis was performed in collaboration with Ludovic Donneger, using data taken by KM3NeT/ORCA from January 2020 to August 2023 with between 6 and 18 DUs. This study is based on more than twice the statistics used in the ORCA6 results, allowing to analyse the evolution of the Sun shadow with time.

The cumulative number of events is shown in 3.17 for the Moon and the Sun as a function of time. Small variation in the rates are visible for the Moon due to its period of rotation around the Earth, while the maximum of the Sun elevation changes with the seasons affecting the event rates.

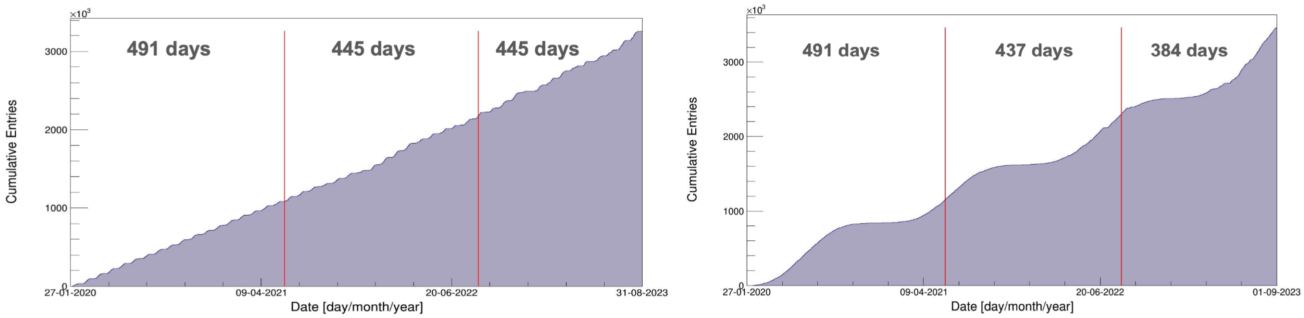

Figure 3.17: Cumulative number of events as function of time for the Moon(left) and the Sun(right). The statistics is divided into 3 periods with similar size, indicated with red bars.

The shadow's size, strength and amplitude for each time bin are measured from the 2D fit at the nominal position with fixed shadow width and reported in Table 3.2 for the Moon and the Sun. The position of the best fit in 2D are also reported, together with the number of events per square degree.

To illustrate the effect of the Sun's activity on the measurement of the cosmic ray shadow, the evolution of the sunspot number as a function of time is shown in Figure 3.18 from SpaceWeatherLive data. During the full period of the study a particularly quick increase of the sunspot number was measured.

The correlation between the sunspot number and the amplitude of the Sun shadow is shown in 3.19.

The evolution of the amplitude of the Moon shadow as a function of time is compatible with a constant. On the contrary the Sun signal decreases with time down to the level

Moon	Bin 1	Bin 2	Bin 3
A	0.66 ± 0.18	0.91 ± 0.18	0.59 ± 0.18
Significance	3.58σ	4.98σ	3.20σ
σ_{res}	fixed at 0.53		
x_s	-0.12 ± 0.20	-0.02 ± 0.13	-0.16 ± 0.16
y_s	0.18 ± 0.14	0.31 ± 0.14	-0.07 ± 0.23
Events/deg^2	2374	2412	2382

Sun	Bin 1	Bin 2	Bin 3
A	0.86 ± 0.17	0.69 ± 0.17	0.31 ± 0.18
Significance	4.82σ	3.85σ	1.73σ
σ_{res}	fixed at 0.53		
x_s	-0.18 ± 0.15	-0.13 ± 0.16	-0.94 ± 0.42
y_s	0.07 ± 0.18	0.14 ± 0.23	0.33 ± 0.20
Events/deg^2	2547	2549	2547

Table 3.2: Parameters from the fits at nominal position $(x_s, y_s) = (0, 0)$ with σ_{res} fixed, and the best fit positions.

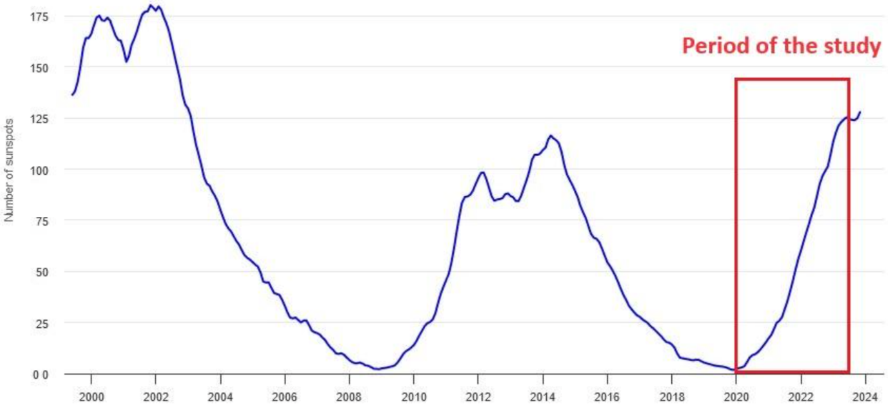

Figure 3.18: The sunspot number evolution with time between 2000 and 2024.

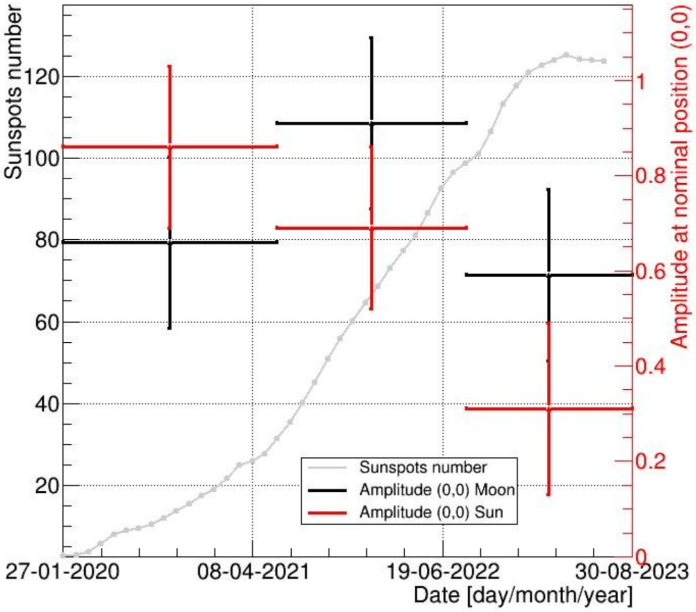

Figure 3.19: The sunspot number on the left y-axis and the amplitude on the right y-axis for three equal bins in time. The amplitude of the Moon and Sun shadows are shown with black and red crosses, respectively.

where no sun shadow is visible anymore. The rejection of the modeling of the Sun shadow amplitude with a constant instead of linear fit as function of time was calculated at ≈ 2.4 σ given the 1σ errors provided in Table 3.2.

3.11 Conclusion

The Moon and the Sun's CR shadows have been observed with a high statistical significance using data collected between February 2020 and November 2021 with 6 DUs of the KM3NeT/ORCA detector. The demonstrated sensitivity to the shadow observation with only one and half years of data taking and a yet incomplete detector reflects the good understanding of the detector positioning, orientation, time calibration [69] and reconstruction capabilities. The shadow observed in data is compatible with expectations from MC concerning the significance, angular width and amplitude, except for the Sun's amplitude, where it was found above expectations. A preliminary study of the absolute pointing of KM3NeT/ARCA using data taken with 21 DUs from September 2022 to June 2023 was shown. It does not provide evidence for mis-calibration, and more statistics is necessary to constrain precisely the absolute orientation at the 3σ level. The analysis of the new data from KM3NeT/ORCA until August 2023 with up to 18 DUs allowed to measure the evolution of the Sun and the Moon shadow with time, and observe a correlation between the amplitude of the Sun shadow and the sunspot number as in [53]. It also contributed to constrain better the absolute orientation of KM3NeT/ORCA to the level below 0.5°.

Chapter 4

Constrain the absolute pointing with acoustic signals

4.1 Motivation

The knowledge on the absolute orientation of the detector is crucial to fully exploit the astronomy potential of KM3NeT. The conversion from the local coordinates of a neutrino event into an absolute frame of reference, e.g. galactic or equatorial coordinates, comes with an uncertainty on the absolute position and orientation of the detector footprint. This uncertainty currently largely dominates the pointing accuracy of both KM3NeT/ORCA and KM3NeT/ARCA. It is illustrated in Figure 4.1 that shows the angular resolution of KM3NeT/ARCA after completion with 230 DUs, that decreases below 0.1° for ν_μ with energies above 100TeV.

Moreover KM3NeT/ARCA in its early 21 DUs configuration reaches already 0.3° for $\nu_\mu > 100$TeV. Therefore motivating studies to reduce the uncertainty on the absolute orientation below the tenth of degree. However constraining the absolute orientation is challenging because there is no standard candles for neutrino telescopes to calibrate on. Some other options to perform this calibration were explored in ANTARES and KM3NeT. The observation of the cosmic ray shadow of the Moon in ANTARES did not show evidence for mis-calibration. The measured shadow position was compatible at 2σ with the nominal position of the Moon and the allowed azimuth rotation interval at 3σ was 4° large. In addition, in ANTARES the pointing was verified using a surface array of scintillation detectors on a boat. Searching for atmospheric muon coincidences between the surface array and the detector, the latter can be calibrated cross-referencing the events with the

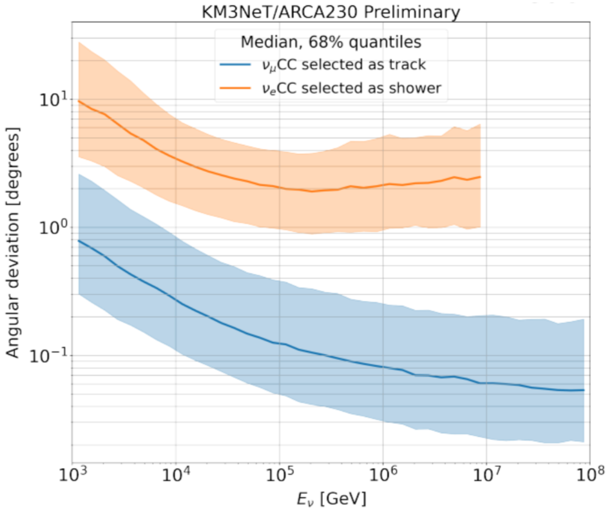

Figure 4.1: Angular resolution for a ν_μ and a ν_e using the full ARCA230 detector simulation [34].

GPS coordinates of the boat [70]. Due to the typical duration of sea campaigns, the data analysed suffered from low statistics therefore giving results compatible with the Moon shadow but not precise enough to set better constraints. Then the observation of the Moon and Sun shadow in KM3NeT/ORCA allowed to exclude with a confidence level of 3σ possible rotations in azimuth larger than ±0.8°. The acoustic study described in this Chapter is an alternative technique to improve the current knowledge on the absolute pointing with a target accuracy of <0.1°. Thanks to the precise acoustic positioning based on the long baseline RAMSES system in KM3NeT/ORCA provided by the Exail company, the post-deployment uncertainty of the anchor position on the seafloor is ∼0.5m.

4.2 Beamforming principle

The acoustic calibration technique consists of diffusing acoustic pulses from a beacon located on a boat. The pulses are detected by the hydrophones on the anchors of the DUs. as shown in Figure 4.2. Using the beamforming technique the position of the source is reconstructed in the detector reference frame. It is compared to the absolute GPS-calibrated position of the beacon in order to constrain the absolute orientation and consequently the absolute pointing accuracy of the detector.

The principle behind the beamforming technique is to search for a point in space where

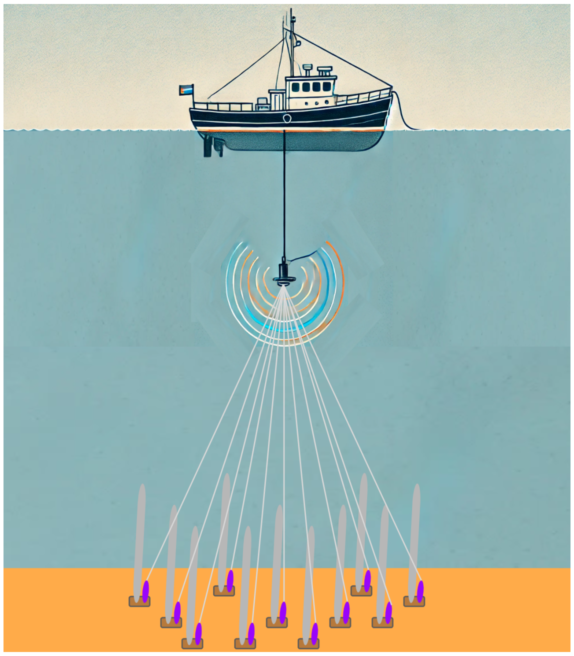

Figure 4.2: Scheme of the KM3Beam acoustic emission system.

the sum of the signals received by the hydrophones, after compensating for the propagation delays, is subject to constructive interferences. The scan is performed over a grid of points around the source GPS position. The grid is chosen to probe angles smaller than 0.1° at the distance of the beacon. The sum of the signals from all acoustic receivers is cross-correlated with the emitted signal pattern. The point where the highest cross-correlation is observed provides the best estimate of the position of the beacon. A decrease of 3 dB with respect to the maximum cross-correlation determines the resolution of the pointing [1].

The calculation of the propagation delays from the scan point to the hydrophones requires an accurate knowledge of the position of the hydrophones. This can be achieved by separately calibrating their position using a multilateration technique based on a series of measurements performed at different fixed beacon positions.

The proof of concept for KM3NeT/ORCA is described in [1] where the calibration system was simulated. However instabilities in the timing of the acoustic pulses during the sea campaign prevented the analysers from obtaining constraints on the absolute orientation. Some inconsistencies in the reconstruction of the sound velocity suggested a poor regularity in the time of emission of the pulses, with discontinuities and drifting behaviours. Fixing the timing issue of the emitted pulse patterns is one of the objectives of this work and is described in Section 4.4.

4.3 Acoustic system

The technical equipments part of the acoustic emission system are shown in Figure 4.3 and listed below:

1. The GPS Spectracom (or Boat GPS) with an antenna.
2. The Arbitrary Waveform Generator (AWG) Keysight 33600A from CPPM.
3. A PC windows with Keysight drivers and matlab installed.
4. The acoustic emitter provided by Exail.
5. The amplifier Echoes 10k provided by Exail.
6. The Hydrophone from KM3NeT and piezos.
7. An oscilloscope to verify the regularity of the emissions.

Figure 4.3: Installation and cabling of the emission system at CPPM.

The technical equipments part of the positioning system on the boat:

1. Inertial central Hydrins.
2. Boat GPS.

The structure of the emissions and the form of the received acoustic signal are described in Section 4.4. The customised pattern of the signal encoded in matlab and communicated to the AWG via a LAN connection is described in Section 4.5. The communication between the different components of the acoustic sytem is controlled by the central PC using matlab control tools and described in Section 4.6. In order to control the emission time of the acoustics pulses emitted by the AWG, they are calibrated on the GPS PPS expected to be regular at the level of a few nanoseconds. The time synchronisation is described in Section 4.7.

4.4 Emission pattern

The empirical strategy behind the emission pattern is to increase the interval between pulses in order to ensure a clear separation at reception with a moving emitter, and tag them with a given duration in order to build a direct correspondence between the received pulse with the emission time and boat position. Therefore the time interval between pulses is 5 seconds. Each emitted pulse is tagged with a given duration starting from 40 ms up to 85 ms, in order to facilitate the emission/reception time matching in the sea. No double pulses are emitted anymore as it was the case for the previous operation. In Figure 4.4 the 4 steps of the cross-correlation between the chirp pattern and the received sound signal are shown, from raw hydrophone data to the Hilbert transform after cross-correlation with every chirp pattern. Each color represents the correlation with a given chirp duration. It illustrates the emission cycle that lasts 50 seconds, and is repeated for the duration of the envisaged acoustic run.

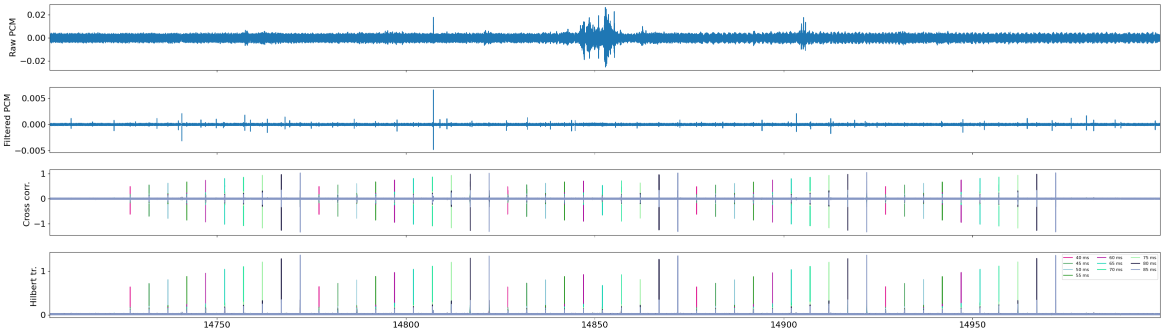

Figure 4.4: Cross-correlation as a function of time for signals propagating in the air at CPPM.

The time is discretized with a sampling frequency for the raw acoustic data of 195 312.5 Hz, corresponding to 5.12 micro-seconds per sample and a useful bandwidth of 97.5 kHz.

4.5 Pulse shape

A *chirp* is a frequency-modulated cosine wave where the frequency is varying linearly in a range between f_0 and f_1, over a designated time interval between 0 and t_1.

$$f(t) = f_0 + \alpha t; \quad \alpha = \frac{f_1 - f_0}{t_1}. \tag{4.1}$$

The chirp $v(t)$ is represented by the equation:

$$v(t) = v_0 \sin\left(2\pi\left(f_0 t + \frac{\alpha}{2}t^2\right)\right) \tag{4.2}$$

in which v_0 is the peak amplitude of the signal. The chirp is multiplied by a window function defined as

$$w(t) = e^{-\left(\frac{2t-t_1}{t_1}\right)^{100}} \tag{4.3}$$

The size of the acoustic pulses ranges between 40 ms and 85 ms. This range ensures the normalised quality factor defined as Q divided by the pulse duration, is optimal, below the threshold where it gets degraded around 100 ms as visible in Figure 4.5.

The chosen digital-to-analog conversion sampling rates of the AWG Keysight 600A is 48kHz. In order to ensure a multi-frequency signal that reduces the effect of *grating lobes* [71], the frequencies used to produce the chirp are between 5kHz and 15kHz.

4.6 Device communication

Temporal stability and time synchronization are ensured through the use of time barriers with Single Program Multiple Data (SPMD), which facilitates multi-threading in the MATLAB parpool package. For the communication with the equipment involved in the emission system, one thread is dedicated to opening the GPS port and reading the GPS data, as well as writing the times and lengths of chirps to a file for each emission. The GPS is used for the timing of the emissions and the corresponding positioning of the boat during the sea campaign. Another thread controls the opening of the AWG port and the communication with the AWG, along with recording the emission times and chirp lengths in a data file. The time barriers ensure that the AWG thread is synchronized with the reception of the PPS (Pulse Per Second) at each iteration of the emission cycle. Both the

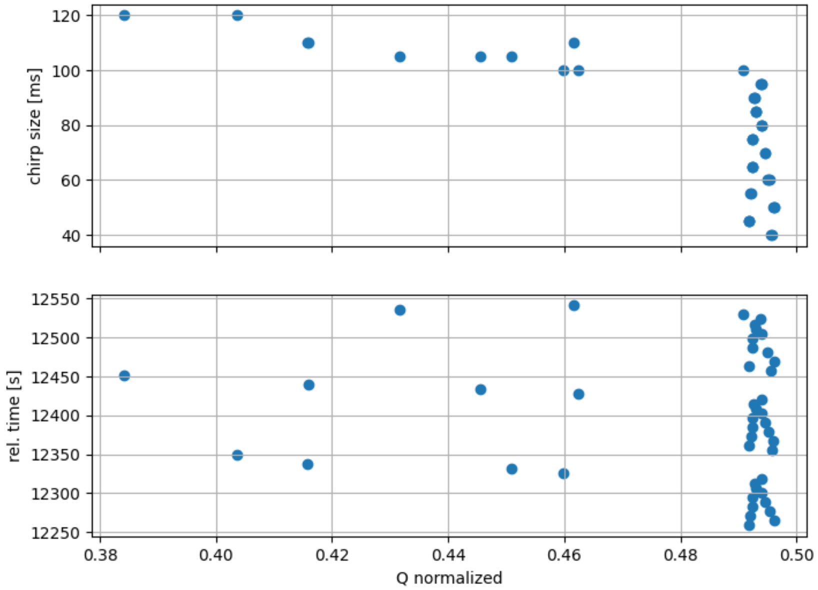

Figure 4.5: Time and chirp duration as a function of the normalised quality factor.

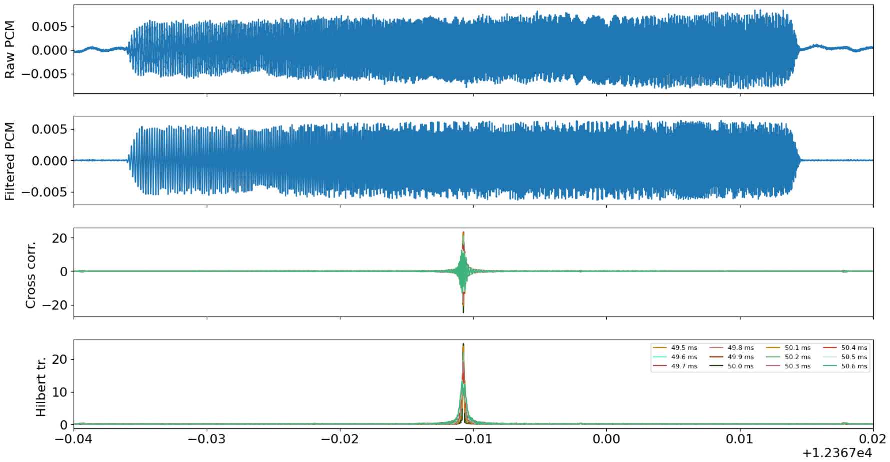

Figure 4.6: A single 50 ms pulse measured at CPPM with the signal propagating in the air.

GPS and the AWG are opened and closed once, before and after the communication is finished. This helped to stabilize the emissions and avoid repeating the instabilities encountered in the 2020 sea campaign. The chirp duration is modified and communicated to the AWG every five seconds.

4.7 Time synchronisation

The time synchronisation between the emitter and receiver and the timing regularity before the sea operation is the main difficulty of the preparation. Tests at CPPM were performed to study the time synchronisation of the acoustic emission system. The test consist of producing acoustic pulses with an Arbitrary Waveform Generator (AWG) at regular time intervals synchronised with a GPS (spectracom) pulse per second (PPS). The signal is amplified and transmitted to an acoustic emitter which will then emit the sound pulses. A KM3NeT hydrophone receives the acoustics signals, which are dated using its own time reference based on the KM3NeT GPS. To study the synchronisation, the emission/reception timing are compared, and the regularity of the emission is verified.

Some delays were measured as shown in Figure 4.7 with an oscilloscope at CPPM between the Spectracom GPS(emission) and the KM3NeT/CPPM GPS (reception). The two GPS have an intrinsic delay below 750 nano-seconds, clearly below our target time uncertainty threshold of $100\mu s$. The use of the down-front instead of the up-front of the PPS from the Spectracom GPS induces a additional delay of 20 milliseconds. This was corrected and the setup is now using the up-front time both for the emission and reception. The emission of the chirp visible in the lower right panel of Figure 4.7, starts 50 micro-seconds after the up-front of the GPS PPS.

An unpredicted delay of 4.1 milliseconds from the chirp coding was also discovered and corrected since the last sea operation. Both corrections are shown in the Figure 4.8 that represents the sub-second time of the pulses measured in every test run of the system at CPPM. No delay was found from CPPM/KEYSIGHT vs Exail AGILENT AWG exchange. In addition no drift of the absolute time from two runs (8 and 10) separated by two hours was found in the same conditions. The main absolute delay to be corrected is a constant offset of -40ms that was found in the raw data for every runs.

It should be noted that during the sea operation, the GPS system at the shore station was not responding, therefore the time synchronisation between the GPS for emission and the time of the received pulses will have to be re-calculated post sea operation. The available NTP timing was used instead for the dating of the received acoustics pulses.

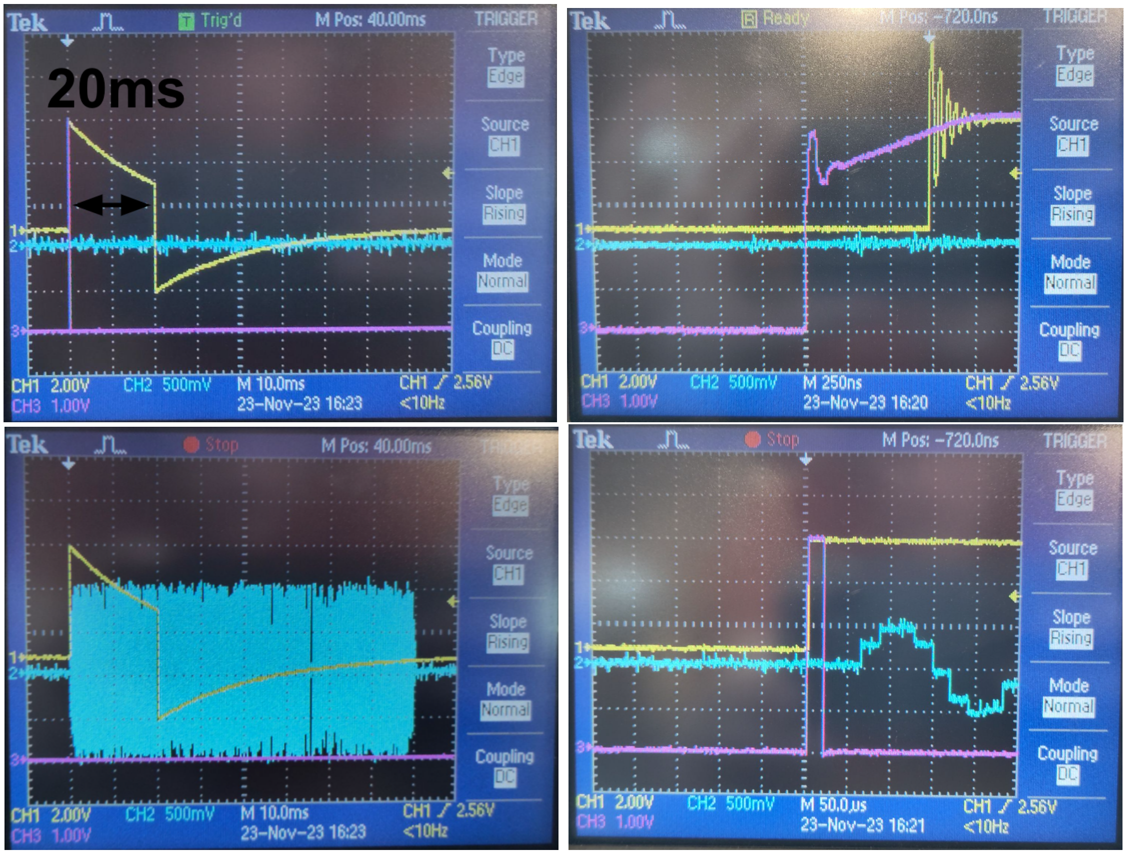

Figure 4.7: GPS PPS synchronisation with emission time. In yellow the Spectracom GPS, in purple the CPPM GPS, and in blue the emission signal from the KEYSIGHT AWG from CPPM.

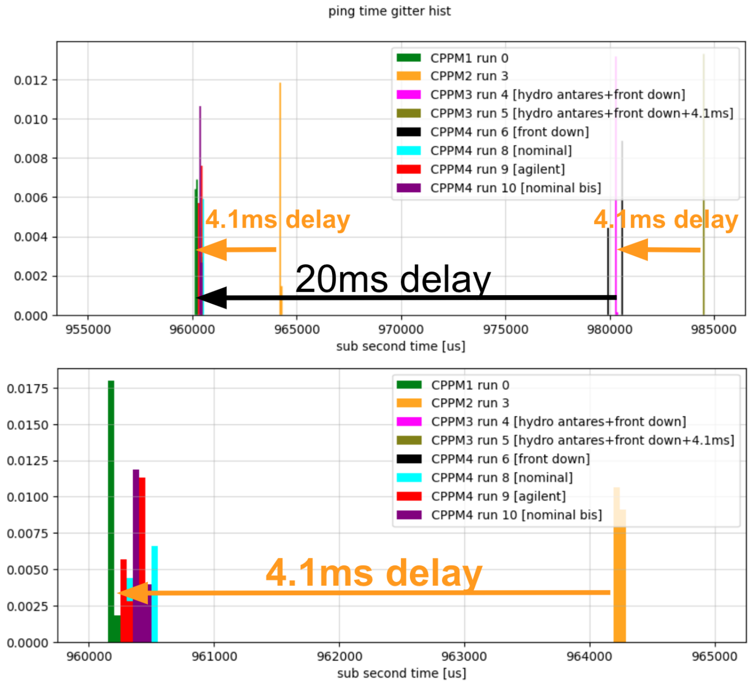

Figure 4.8: Time distribution after retrieving the seconds for the received pulses measured with a KM3NeT hydrophone using different run setup at CPPM.

4.8 Test in water

On the 13th of Febuary 2024, a final test of the system in water was performed at CPPM. The set-up of the emitter in water is shown in Figure 4.9 and the pulses as function of time with all the different pulse lengths in Figure 4.10. The signal/noise ratio in water is higher than in the air, allowing for an clear extraction of the time of arrivals. During this conclusive test, it was verified that the time difference of the measured signal is consistent with the distance between the emitter and receiver in water as shown in Figure 4.11.

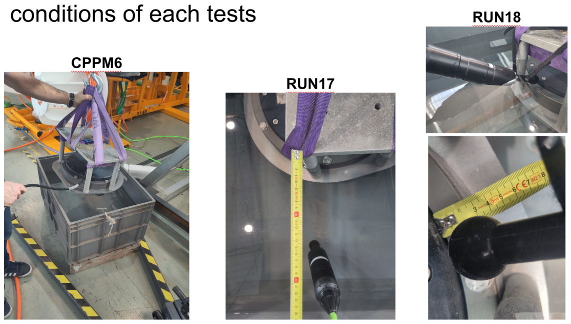

Figure 4.9: Set-up of the emitter and hydrophone in water.

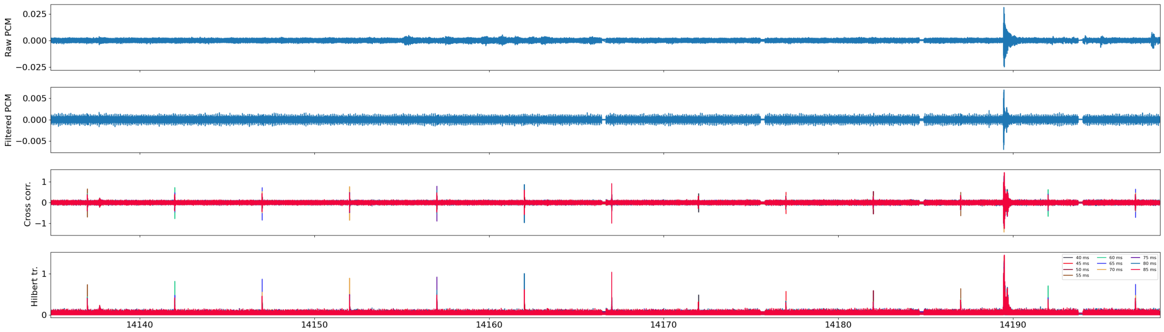

Figure 4.10: Pulses correlation at CPPM with sound propagating in the water.

The Figure 4.12 and the Figure 4.13 illustrate the jitter for every pulse measured that is contained within a +/-15 micro-seconds range. This confirms the time stability of the emission system that is compatible with the target accuracy of the *absolute pointing* study.

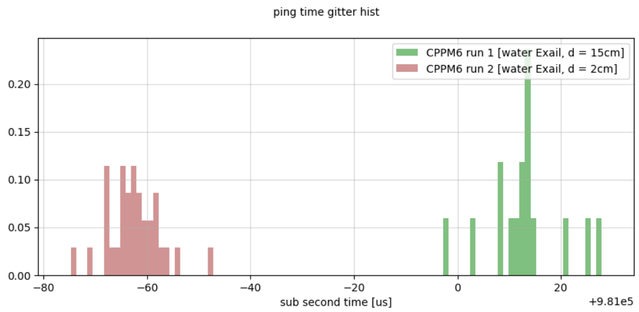

Figure 4.11: Sub second time distribution.

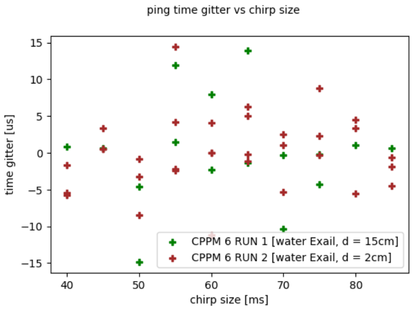

Figure 4.12: The distribution of the time jitter of the pulses as a function of the chirp size.

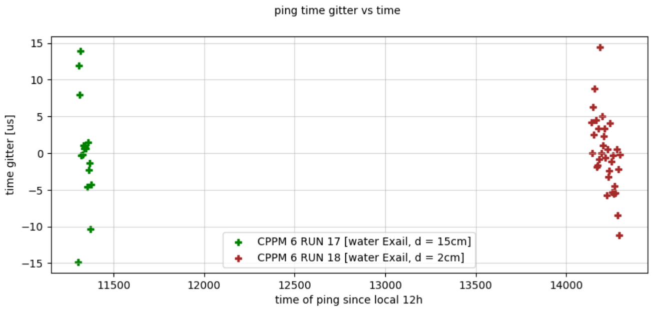

Figure 4.13: The time jitter of the pulses as a function of the absolute time since 12:00 local time in seconds.

The Figure4.14 illustrates the stable normalised quality factor for the range of chirp duration used for that operation. The border effects of the water box are likely to modify the norm of quality factor measured.

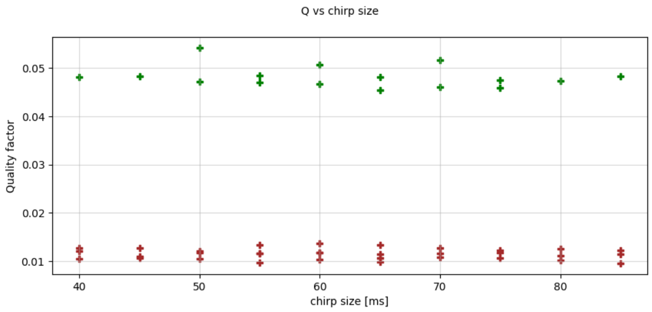

Figure 4.14: The quality factor normalised by the chirp size, as a function of the chirp size in milli-seconds.

4.9 Acoustic sea campaign

On the 9th of July 2024, a sea operation carried out with the Exail (former iXBlue) company was performed. Acoustic signals were sent from the Exail emitter immersed below the boat. A total of 11 hydrophones and 7 piezos sensors of KM3NeT/ORCA were recording data. A 10V peak to peak signal was set on the KEYSIGHT 33600A, synchronised with an up-front GPS PPS from the boat. After a static emission run above the detector, the boat followed a triangular path around the detector centre as shown in Figure4.15. The path followed the path of the previous campaign in 2020, while the emission of acoustic pulses was separated into 4 runs.

The pulses shown in Figure 4.15 for a single hydrophone confirmed that the ORCA detector successfully received the acoustics pulses, separated with 5 seconds interval. The different colours observed are consistent with the emission pattern that involves cycles of increasing pulse durations between 40 and 85 ms.

The analysis of the acoustic data from the sea campaign is currently ongoing at CPPM.

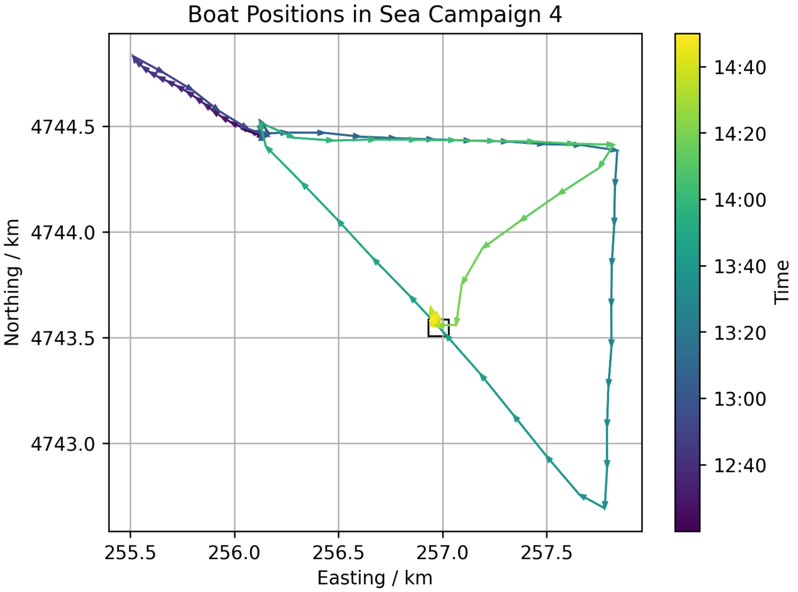

Figure 4.15: The path of the boat during the sea campaign as function time is shown. The arrow indicated the direction of motion of the boat and the black square represents the detector position on the seafloor. The graph was produced by Sharif ElMentawi at CPPM.

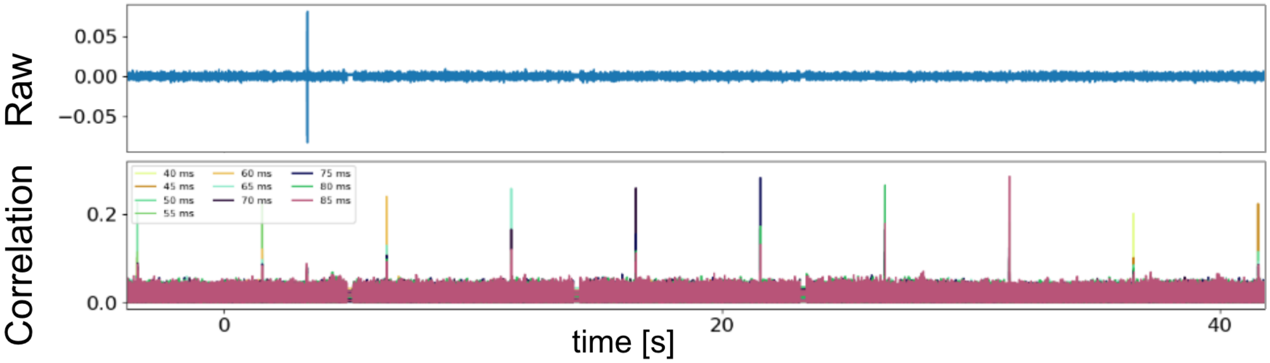

Figure 4.16: The raw acoustic data and the result of the correlation with the CHIRP template for every acoustic pulses received are shown as function of time. The colours indicate the duration of the template used for the correlation.

Chapter 5

Technical aspects of the analysis

In the context of neutrino physics, in order to measure oscillation parameters with high precision, the particle identification plays a crucial role. This chapter is reporting on the particle identification (PID) methods, on the data sample and the analysis method used in KM3NeT/ORCA. An alternative track-shower separation to identify neutrino flavours using the KM3NeT/ORCA6 data is proposed. With a particular focus on the optimisation of the alternative PID for the ν_τ appearance signal.

5.1 Background rejection

The data used in this analysis were collected between mid-February 2020, and mid-November, 2021 for a total livetime of 510 days or and 433 kton-years of exposure. In order to perform the analysis with a pure neutrino sample, events produced by atmospheric muons and optical background need to be excluded from the recorded dataset. Therefore, quality cuts on the number of used hits $>= 15$, the likelihood > 40 and the direction (up-going) of the track reconstruction were applied to remove poorly reconstructed events, remove noise events from ^{40}K decay and reduce most of the atmospheric muon background.

After this first selection, the data sample is mostly composed of atmospheric muons, and their amount can be significantly reduced by restricting the sample to events with an up-going reconstructed track direction, given that atmospheric muons from below the horizon are absorbed by the Earth. The remaining muons are the mis-reconstructed one. The selected events are classified into different subsets aiming at separating the track and shower event topologies. The definition of the classes (subsets), as well as the background-rejection criteria used for this analysis, were optimised for the measurement of neutrino oscillation parameters. These will be described in the following.

5.2 BDT particle identification

A BDT based algorithm is used in all the official oscillation analysis measurements, including the ones reported in Chapter 6 and 7. It relies on the training of a classifier on 43 different features using MC events. Those features are related to the energy, likelihood of the track/shower reconstruction, direction, hits of each reconstructed event. The trained classifier applied to a sample predicts a Track score and an Atm. muons score that determines how track-like and atmospheric-muon-like respectively an event is. In Figure 5.1 the weighted distribution of the scores and the data/MC ratio illustrates the good agreement between data and expectation for those variables.

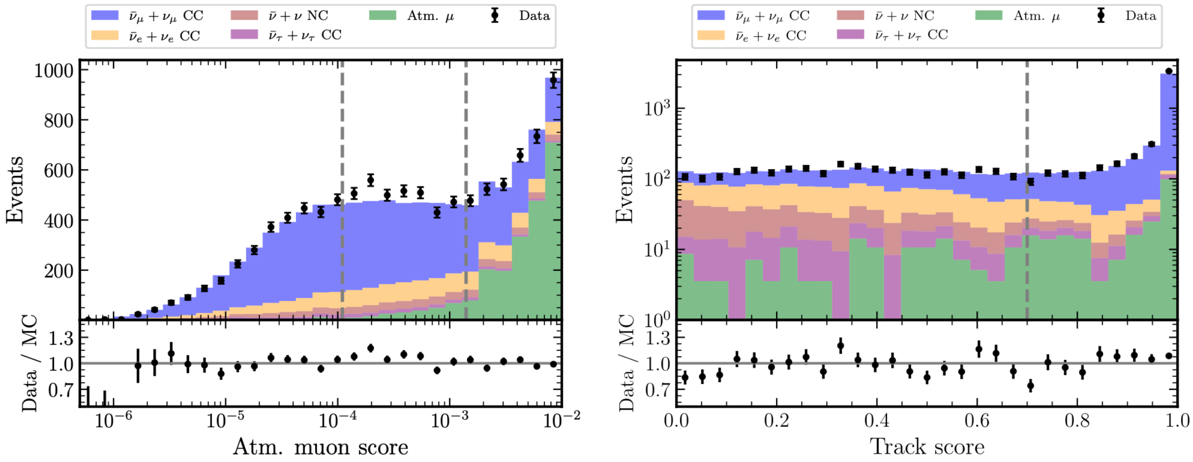

Figure 5.1: The Atmospheric muon score and Track score stacked distribution for all neutrino flavors is drawn in colors with atmospheric muons in green, $\nu_\tau + \bar{\nu_\tau}$ CC in purple, $\nu + \bar{\nu}$ NC in brown, $\nu_e + \bar{\nu_e}$ CC in orange and $\nu_\mu + \bar{\nu_\mu}$ CC in blue. The Data is shown with black dots and error bars. On the bottom part the data/MC ratio shows the agreement between the expected number of events and the collected data. The grey bands represents the cut values used to defined the classes.

To measure neutrino oscillations, a clean neutrino sample is produced by removing the atmospheric muon background using the upgoing direction of the tracks as a pre-cut and further cutting on the Atm. muon score at 1.8×10^{-3} to remove the rest of the muons as shown in Figure 5.1. With this approach, 99.98% of the background can be rejected while keeping about 60 % of the signal.

The BDT outputs are also used to separate the data into three classes. The events that have a Track score below 0.7 are classified as Showers, while the events that fall above 0.7 are further divided into 2 classes the High and Low Purity Tracks by cutting on the Atm. muon score at 1.1×10^{-4}. The cuts in the BDT scores have been optimised for performance to measure neutrino oscillation parameters [18]. Each class is defined to ensure enough statistics per class and per bin.

5.3 RGS particle identification

Several sophisticated methods are being explored to perform particle identification such as Boosted Decision Trees (BDTs), and more recently Graph or Deep Neural Networks (DNN). While these approaches show a strong potential to find the purest classification, a simple and robust alternative is proposed in this work. One of the motivation for this alternative approach is that some discontinuities in the trained function of the BDT were found, i.e small changes in the feature space produce a highly different output of the BDT. Furthermore the interpretation of the output of the network or BDT is difficult and the determination of the origin of a mismatch between simulations or between data and simulation can be opaque, therefore hard to treat or improve. This motivates the search for a transparent and simple algorithm that is robust to small changes in the feature space.

This Section will report on the performance of the alternative particle identification and its impact on the measurements obtained using an early six-lines configuration of the ORCA detector (ORCA6), with data recorded in 2020 and 2021.

5.3.1 Introduction to the Random Grid Search

The Random Grid Search (RGS) algorithm consists in a fast and transparent approach that relies on a combination of cuts in one or two dimension to separate two (or more) populations of events. The cut combinations involves a few features (typically 4 or 5) which makes the investigation on the data/MC agreement and the physical interpretation easier.

The Random Grid Search algorithm was introduced in 1995 during the search of the top quark at FermiLab [72], and is still used in multiple experiments like in the search for supersymmetry at LHC [73].

The RGS algorithm follows the general idea to search for cuts where they are likely to be useful, i.e. in the expected signal region. If a reconstructed event i between 0 and n (the size of the sample) represents a neutrino interaction, with a feature X_i associated to it, then $(X_i, >)$ defines a cut that selects all events with $X > X_i$. A combination of consecutive cuts for a given event i and three features X, Y and Z in 1D can be represented as $((X_i, >), (Y_i, <), (Z_i, <))$ and called a set of 1D cuts. The set of cuts can also be a combination of 2D cuts. In that case the set of 2D cuts takes the form $[((X_i, >), (Y_i, >)), ...]$ where the 1D and 2D cuts are schematized. In the most advanced version of the RGS a track and a shower event are selected, and the 2D cut is defined as the line equidistant to both events coordinates as shown in Figure 5.2 right.

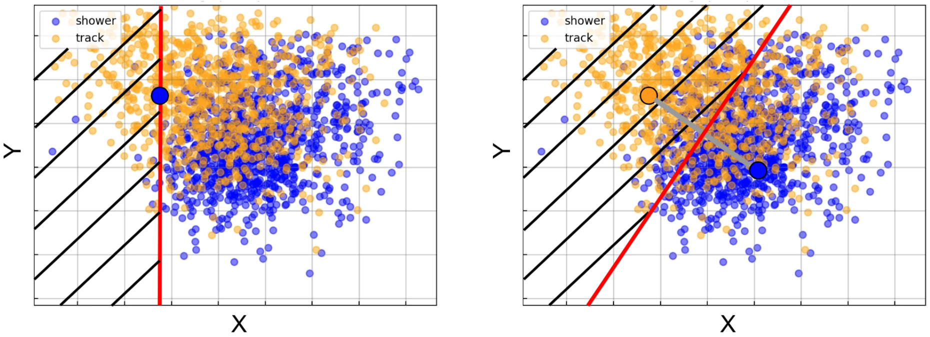

Figure 5.2: Scheme of the effect on a population of tracks and showers of a 1D cut on the left and 2D cut on the right.

When keeping track of the signal events (true positive rate) and background events (false positive rate) that passed the set of cuts, one can produce the performance graph. The RGS tests all the sets of cuts in 2D based on a fixed set of features. After comparing the best sets of cuts of many different sets of features, the best set of features is determined and fixed.

The choice of the true energy range of the sample and the weight of the events affects the RGS performance. The Figure 5.3 illustrates the true energy distribution of the events. On the left, the shape of the distribution reflects the spectral index used to generate the neutrino events. On the right, it reflects the distribution expected in data. In order to avoid potential biases arising from the arbitrary choice of the weight, when the algorithm is applied on data, the RGS will use the weighted events as shown on the right part of Figure 5.3 and the full energy range.

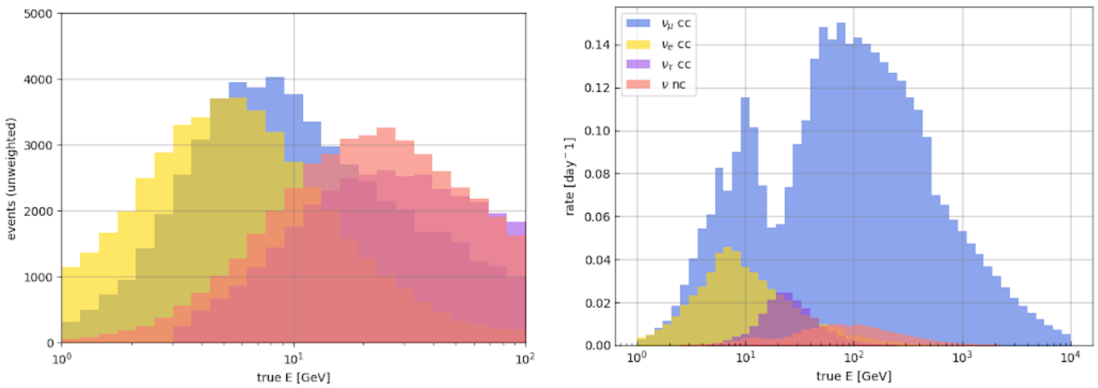

Figure 5.3: The true energy distribution is shown, with on the left the events without reweighing and on the right the correctly weighted events for each neutrino flavor and channel.

5.3.2 Ranking of features

The ranking of the features is the first step of the RGS procedure to find good discriminating cuts. The separability S(F) for the feature F is defined as

$$S(F) = 1 - \frac{\Sigma_i n_i^s(F) n_i^t(F)}{\sqrt{\Sigma_i (n_i^s(F))^2 \Sigma_i (n_i^t(F))^2}}. \tag{5.1}$$

with n_i^t and n_i^s the number of track and shower events in bin i. The distribution is divided in 20 bins and this can be generalised to n dimensions. The measure of the overlap of the 2 distribution helps to isolate a set of good separating features.

The top features pairs have the highest 2D separability equivalent to the lowest overlap between the true track and the true shower distribution. The 2D separability is shown on the left of Figure 5.4 and the left of Figure 5.5 while the correlation matrices are shown on the right. The most correlated features were removed during the process. The brightest squares in the separability maps illustrate the pairs of features that provide the best separation power. The darkest squares in the correlation matrices illustrate the features that are the most correlated. The Figure 5.4 shows the separability and the correlation for the full sample. In the RGS procedure the track class is first defined, then from the events that were not selected as tracks the RGS isolates the shower-like events. Therefore Figure 5.5 shows the 2D separability and correlation of the most powerful 9 features based on the sample of events that did not pass the track selection.

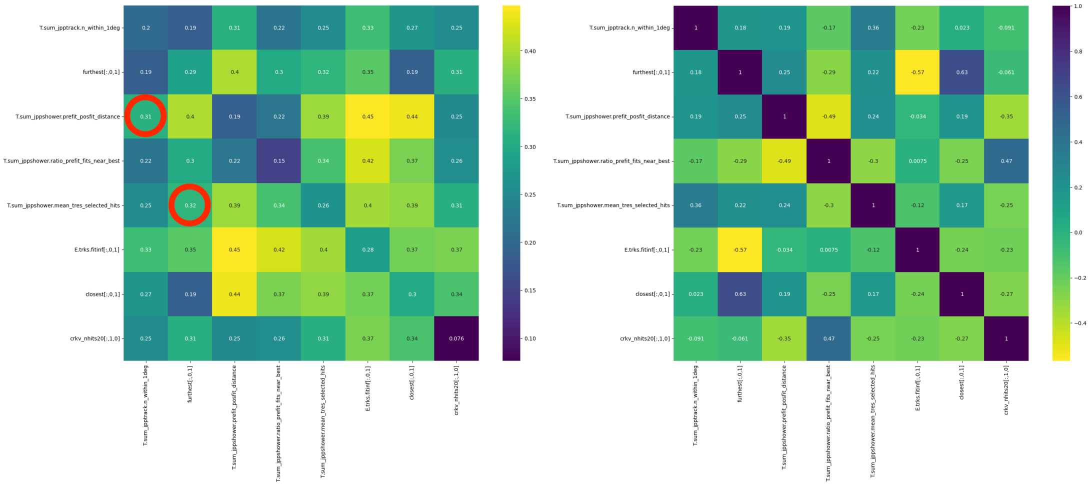

Figure 5.4: The 8 best features track vs shower 2D separability for the full sample is shown on the left and the correlation matrix on the right. The red circles indicates the feature pairs that have been selected.

Figure 5.5: The 9 best features track vs shower 2D separability on the sample after track class removal is shown on the left and the correlation matrix on the right. The red circles indicates the feature pairs that have been selected.

5.3.3 RGS performance

Several studies have been performed to reach with the RGS a high performance while using a low number of features. The side of the cut ($>$ *or* $<$) for each feature must be fixed in advance in order for the RGS to run efficiently and reduce the number of iteration from n events $\times 2^n$ features to n events $\times$ n features.

The comparison between 2D and 1D cuts, described previously, using the same features is presented in Figure 5.6 left. A better performance is found when using cuts in two dimension, therefore it was decided to use 2D combination of features from the ranking to the optimisation stage. From this stage the RGS will be using the 2D approach by cutting using the perpendicular between a random track and shower. The Figure 5.6 on the right illustrates the better separation performance when isolating the tracks from the showers than the showers from the tracks. This is due to the important overlap (low separability) between low energy tracks and all showers. Higher energy tracks are easier to isolate therefore the performance for isolating tracks in general is better.

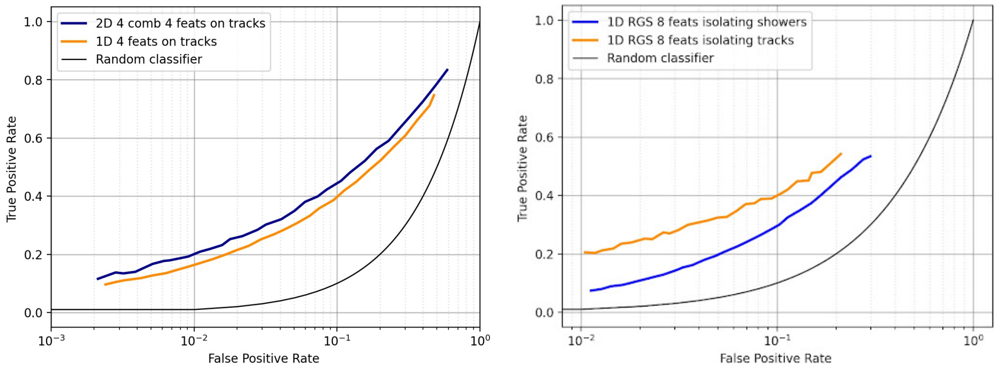

Figure 5.6: The RGS performance using 2D vs 1D cuts on 4 identical features in the energy range 10-20 GeV is shown on the left. The random classifier performance is shown for comparison. The RGS track vs shower isolation performance between 10-20 GeV is shown on the right. The tracks are considered as signal for the orange case and the showers are considered as signal in the blue case.

The Figure 5.7 on the left illustrates that the RGS is not meant to use a very high number of features. Depending on the region of the purity that is chosen, a total number of 4-5 features is typically enough in the context of track-shower separation. The Figure 5.7 on the right shows the performance when using different sampling e.g. different number of random events to cut on before selecting the best one. It illustrates that the algorithm is

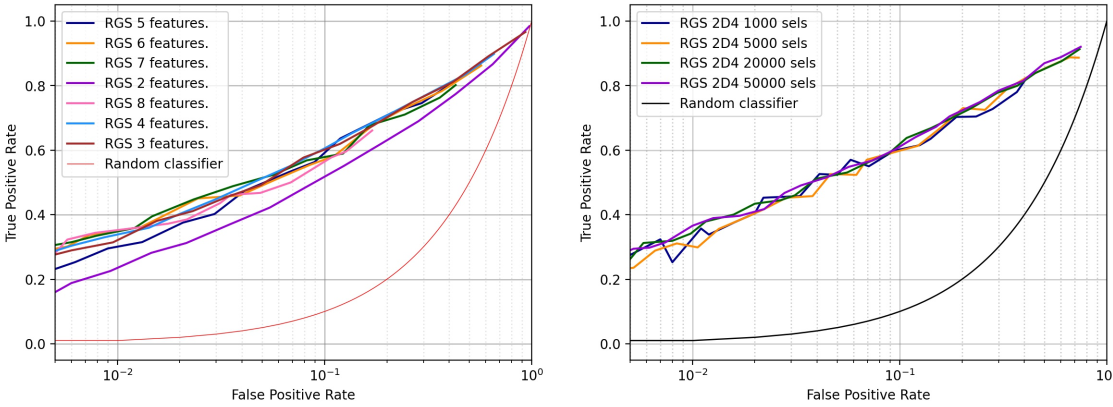

Figure 5.7: The RGS performance is shown on the left when using n features from the top ranked features. The RGS performance when using a different number of random events to cut on is shown on the right.

quick to find good cuts, and it's unnecessary to sample 1M events to find an efficient set of cuts. Around 10 thousand events will be used in the final RGS procedure taking a few minutes to compute.

The procedure to find the best set of features and the best set of cuts consist first in testing all sets of 2, 3 or 4 combined 2D cuts when selecting features within a list of 8 features. Then compute the performance curve, and compare the Pareto front (top points in the ROC curve), for each set of 2D cuts. This allows to find and fix the best set of cuts and features.

5.3.4 Sensitivity optimisation

Once the best set of features is fixed, the goal is to optimize in order to find the best cu values which would give the highest sensitivity for a given study. In this work the purpose is to increase the sensitivity to the ν_τ appearance described in Chapter 6. It was found that the best classes division for ν_τ appearance observation was into 3 classes: tracks, middles and showers without separating in this approach the track class into 2 as it is described in Section 5.2 and in [74]. In fact this has no effect on the ν_τ appearance sensitivity because ν_τ are observed mainly as an excess in the shower class. In this approach the events that have an Atm. muon score below 3×10^{-3} are kept. In Figure 5.8 the track isolation cut and the shower isolation cut optimisation are shown. The chosen cuts on the Pareto front give the best sensitivity to the tau appearance while conserving a reasonable number of events per bin. The shower isolation cut is found in the sample after removing all events classified as tracks during the previous cut combination.

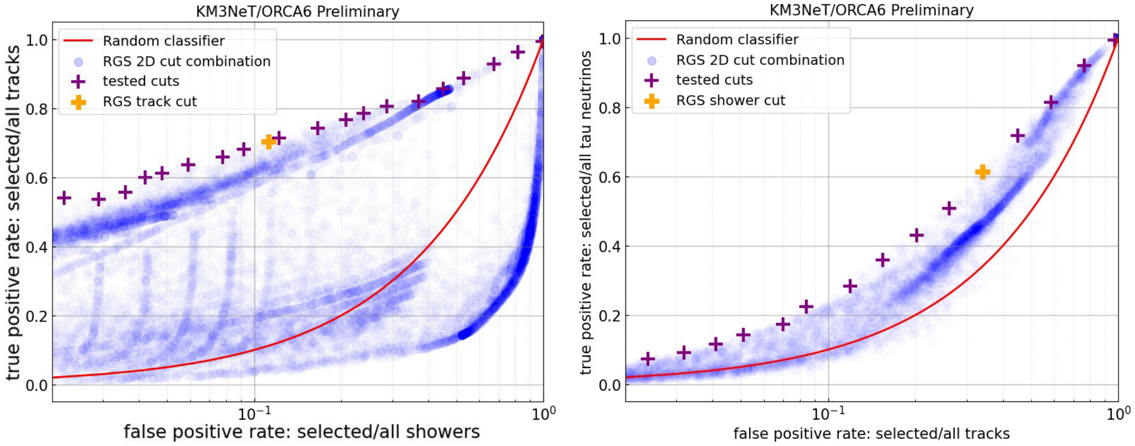

Figure 5.8: Efficiency and purity of each of the RGS sets of cuts. These are shown with blue dots, while the tested cut values for optimisation are shown with purple crosses. The orange cross represents the chosen value for the RGS cut for track isolation on the left and shower isolation after tracks removal on the right. The cuts were optimised for the sensitivity to ν_τ appearance. A random classifier is shown with a red line for comparison.

The comparison of the RGS and BDT performance to isolate tracks is shown in Figure 5.9. The absolute performance of the RGS is a few percents lower than the BDT.

The 2D RGS approach is summarized in Figure 5.10 where the red lines represents the 2D cuts that are used to separate tracks from showers. The line's equation is calculated to be perpendicular to the line passing by a track and a shower selected randomly by the RGS algorithm. The asymmetry in bin i is defined as

$$A_i = \frac{n^i_{shower} - n^i_{track}}{\sqrt{n^i_{shower} + n^i_{track}}} \tag{5.2}$$

with n_{shower} (n_{track}) the number of true showers (true tracks) in the bin.

In Figure 5.11 the red lines represents the optimised 2D combination A & B that define the RGS track class. The mixed+showers region is further divided in two classes thanks to the intersection of the 2D combination C & D & F written in Table 5.1.

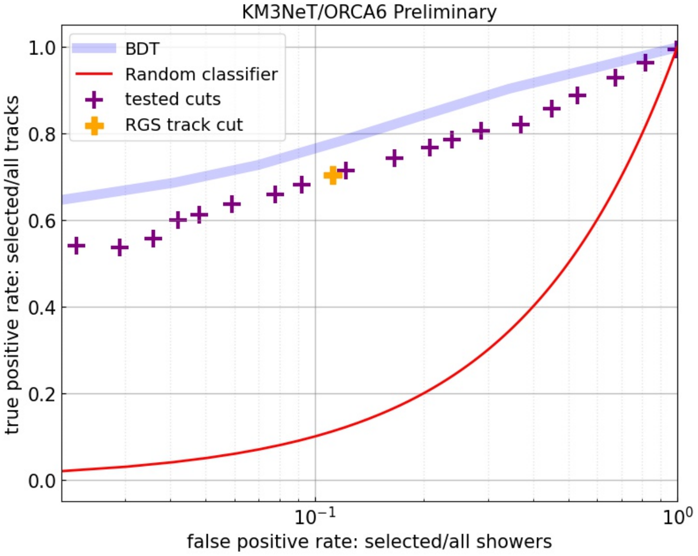

Figure 5.9: Performance of the RGS for isolating tracks in efficiency and purity compared to the BDT classifier in blue.

<table>
<tr><th colspan="6">2D combination $Z = y - (ax + b)$</th></tr>
<tr><th colspan="6">RGS track class definition: $A\&B$</th></tr>
<tr><th>pars.</th><th>feature x</th><th>feature y</th><th>coeff a</th><th>coeff b</th><th>cut dir.</th></tr>
<tr><td>comb. A</td><td>f1</td><td>f3</td><td>-0.2356</td><td>+ 1.9124</td><td>$Z > 0$</td></tr>
<tr><td>comb. B</td><td>f2</td><td>f5</td><td>-5.0702</td><td>+125.6146</td><td>$Z > 0$</td></tr>
<tr><td colspan="6">RGS shower class definition:$(\bar{A} or \bar{B})$ & $(C\&D\&F)$</td></tr>
<tr><td>comb. C</td><td>f3</td><td>f2</td><td>-0.0101</td><td>+71.1553</td><td>$Z < 0$</td></tr>
<tr><td>comb. D</td><td>f3</td><td>f5</td><td>-3.0422</td><td>+7.4538</td><td>$Z < 0$</td></tr>
<tr><td>comb. E</td><td>f5</td><td>f4</td><td>-0.3291</td><td>+2.503</td><td>$Z < 0$</td></tr>
</table>

Table 5.1: Coefficients of RGS cut combination for Tracks and Showers classes definition. The features are described in Chapter 2.

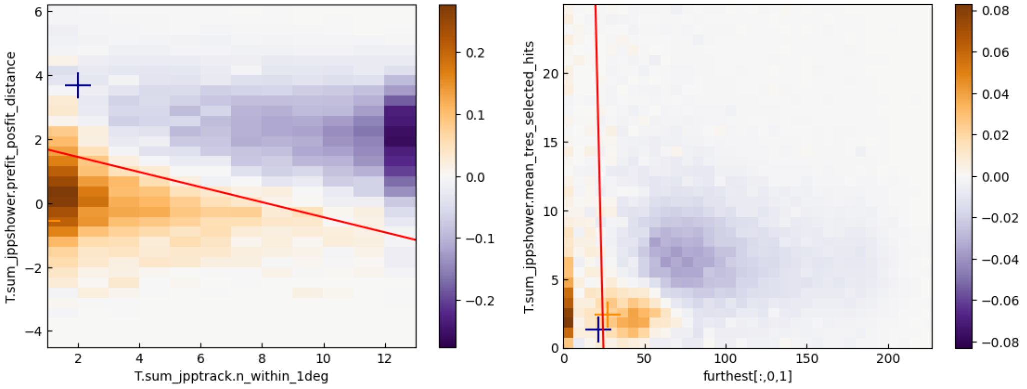

(a) The two combinations of cuts correspond to the isolation of tracks from the initial sample based on the 2D combination A & B in Table 5.1.

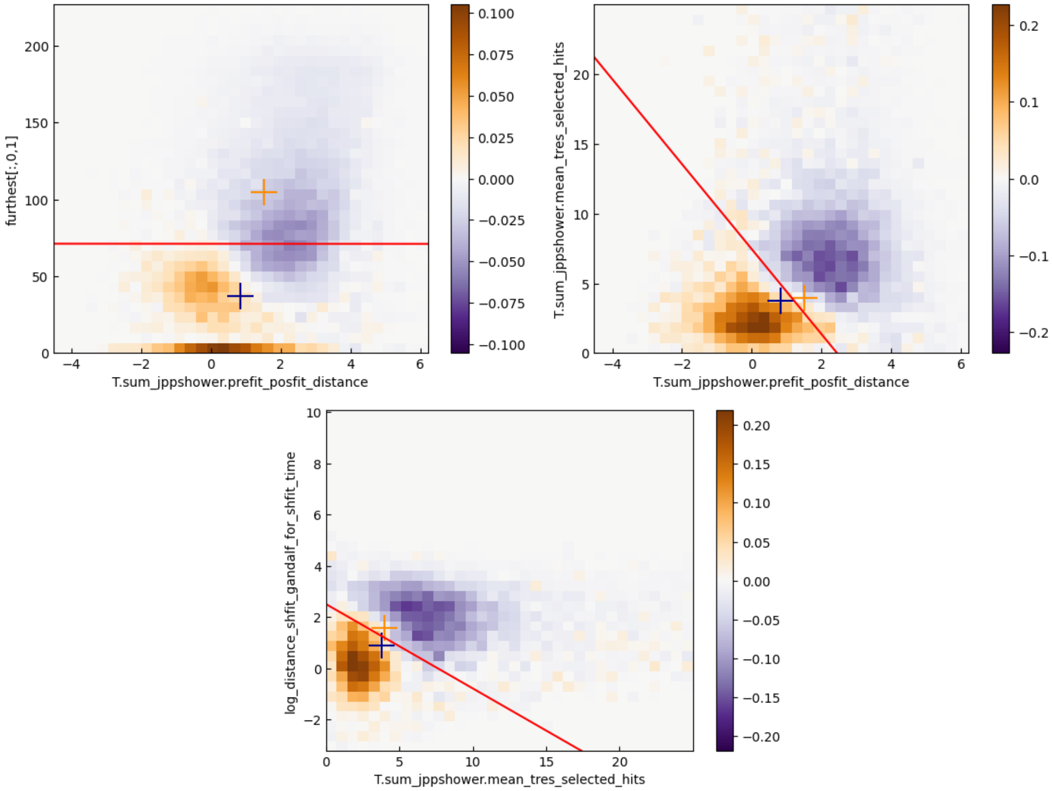

(b) The three combinations of cuts correspond to the isolation of showers (2D combination C & D & F in Table 5.1) from the sample after removing the selected tracks.

Figure 5.10: The color scale indicates the significance of the track-shower asymmetry as defined in Figure 5.11, the blue region is enhanced in tracks while the orange region is enhanced in showers.

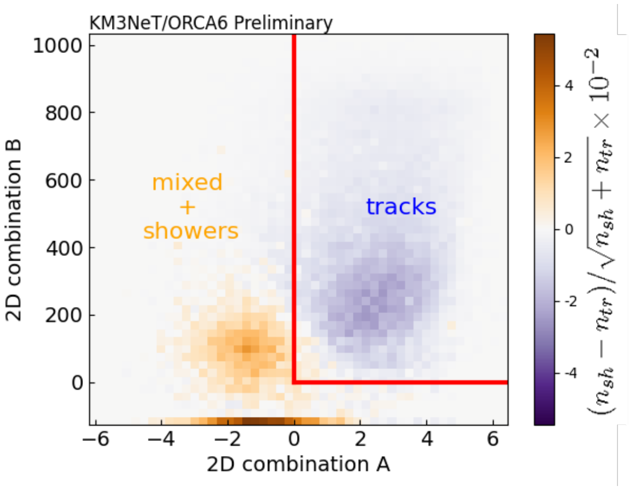

Figure 5.11: Significance of the track-shower asymmetry, with n_{sh} and n_{tr} the number of showers and tracks in each bin respectively. The blue region is enhanced in tracks while the orange region is enhanced in showers. Red lines are used to define the separation between the Tracks class and the Showers+Mixed classes by the RGS cuts defined in Table 5.1 and correspond to the orange crosses shown on the left of Figure 5.8.

In the data/MC comparison shown in Figure 5.12 for the 5 features involved in the RGS cuts, the events corresponding to all MC flavors are weighted, this allows to appreciate the good understanding of the data for each parameter that is used in the RGS class separation. For most bins the data/MC ratios are contained in a ±20% band around 1. The peak at 0 in the parameter showing the distance to the furthest Cherenkov hit correspond to events for which no hit passes the Cherenkov distance and time conditions.

The Table 5.2 compares the event distribution per classes for the two particle identification methods. The middles and showers classes are less populated but the purity of the Showers is enhanced because the contamination of Tracks is lower.

The flavour distribution of the events in the different classes is shown in Figure 5.13. This allows to appreciate the strong differences between the two methods, and the low contamination of the RGS Showers class. The classes however are not equally populated in the RGS case.

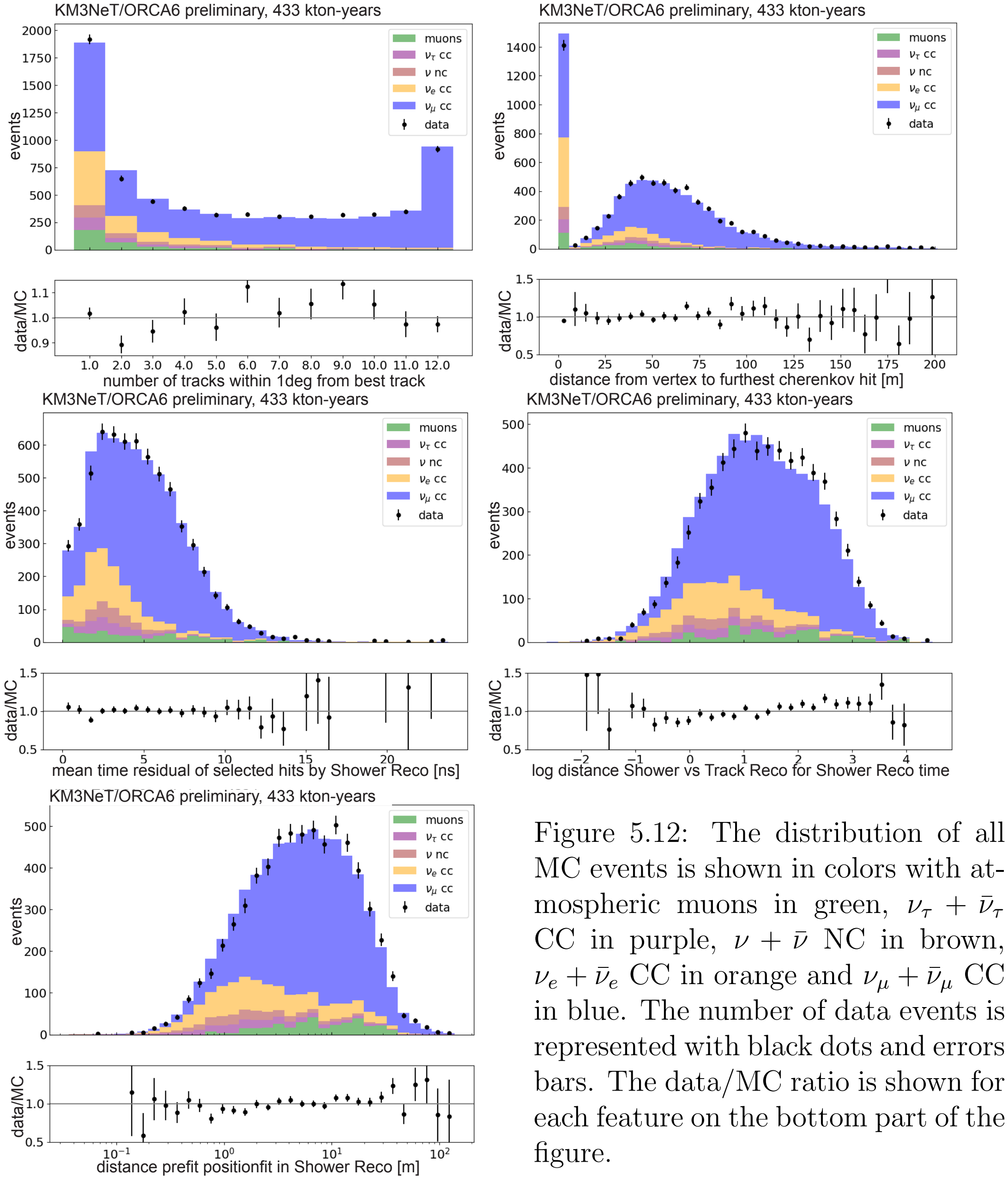

Figure 5.12: The distribution of all MC events is shown in colors with atmospheric muons in green, $\nu_\tau + \bar{\nu}_\tau$ CC in purple, $\nu + \bar{\nu}$ NC in brown, $\nu_e + \bar{\nu}_e$ CC in orange and $\nu_\mu + \bar{\nu}_\mu$ CC in blue. The number of data events is represented with black dots and errors bars. The data/MC ratio is shown for each feature on the bottom part of the figure.

RGS	**Tracks**	**Middles**	**Showers**	**Total**
All	3186.9	1561.4	1342.3	6090.6
ν NC	33.1	152.2	208.58	393.9
ν_e CC	71.8	359.0	520.3	951.1
ν_μ CC	3224.1	1043.5	582.6	4850.3
ν_τ CC	33.6	73.1	115.2	222.1
Atm. muons	102.3	60.3	27.1	189.7
BDT	**HP Tracks**	**LP Tracks**	**Showers**	**Total**
All	1869.6	2001.1	1958.9	5829.6
ν NC	12.6	21.9	291.0	325.5
ν_e CC	50.9	85.0	607.0	742.9
ν_μ CC	1778.5	1787.9	906.2	4472.7
ν_τ CC	20.4	18.8	132.6	171.8
Atm. muons	7.1	87.5	22.1	116.7
Data	1868	2002	1958	5828

Table 5.2: Event distribution per classes corresponding to the best fit to data in the standard oscillation model using the BDT, and the nominal asimov set for the RGS.

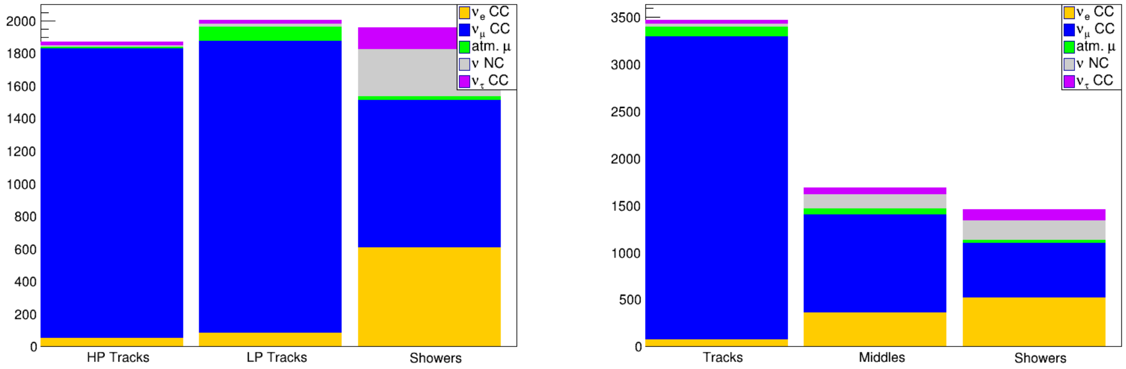

Figure 5.13: A stacked histogram of the distribution of flavours in the 3 classes defined with the BDT on the left and RGS on the right.

5.3.5 Sensitivity results

The RGS cuts presented in this work were optimised to define classes in order to have the highest possible sensitivity to ν_τ appearance described in Chapter 6. For each of the 3 classes defined previously the oscillation parameters are fitted in the 2D space of the reconstructed zenith angle and the reconstructed energy. The fit is accounting for various systematic effects reported in [75]. The ν_τ normalisation is unconstrained in this study. The sensitivity to tau appearance is shown in Figure 5.14. The comparison is made between the two separation methods discussed in this work, in the CC-only case where the ν_τ normalisation affects only the events rates in the charged current interaction channel and in the CC+NC case where the ν_τ normalisation affects event rates in both interaction channels. The sensitivity using both separation methods is similar, and indicates that the no ν_τ hypothesis could be significantly rejected with this data set if data matches expectations.

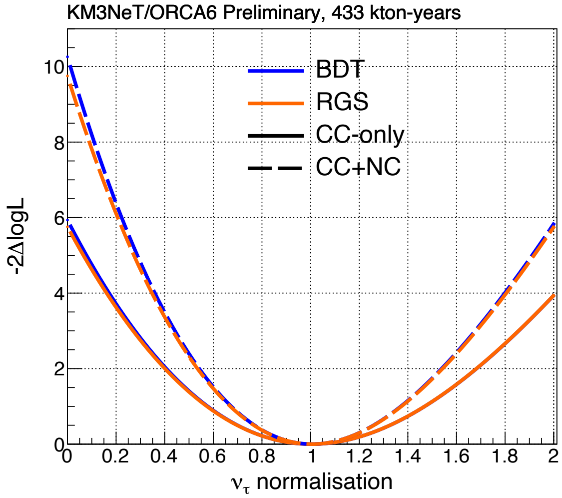

Figure 5.14: Sensitivity to ν_τ normalisation corresponding to the ICRC23 433 kton-years data sample when using RGS (in orange) and BDT (in blue) methods for particle identification of tracks and showers. The full line represents the ν_τ normalisation affecting CC-only and the dotted line both CC+NC events.

Figure 5.15 contains the reconstructed L/E distribution which combines the two main observables, the reconstructed zenith angle and the reconstructed energy of the neutrinos.

The L/E distribution offers a good visibility of the oscillation dip in both the Tracks and Showers classes. The Shower reconstruction is used for the Showers and Mixed classes and the Track reconstruction is used for the Tracks class from RGS and the Low/High Purity Tracks as well. The BDT classification is used on the left plots and the RGS classification for the right plots. The top histograms show the BDT High Purity Tracks class/RGS Tracks class while the lower ones show the Showers class for both. The left histograms reveals the result of the fit with different hypothesis, free ν_τ normalisation, fixed to 0 for the no-τ hypothesis and fixed to 1 for the nominal ν_τ hypothesis. The best fit lies in the middle of the two hypothesis 0 and 1. On the other side one can appreciate the L/E range between the 2 hypothesis when using the RGS classification without showing the best fit. Data point are shown in blacks only for the official result, where the oscillation gap is clearly visible. More data will be needed to measure significantly the tau appearance, while high ν_τ normalisation are already rejected by the measurement from KM3NeT [76].

When applying the RGS classification a better overall agreement is found with the model when fitting data with standard oscillation parameters. A log-likelihood of 465 (490) for 434 (424) number of degrees of freedom is found for the RGS (BDT) particle identification classes. This confirms that the choice of the method used for particle identification has a strong impact on the measurements, and simple/transparent methods can lead to a robust modeling of the data.

5.3.6 Conclusion

This work highlights the potential for a new particle identification method that relies on a few features and gives a similar sensitivity to ν_τ appearance as the BDT classification. The good understanding of our data was demonstrated in the different comparisons between data and MC for the features involved in both methods (RGS and BDT). However due to the faster implementation of the algorithm and the better performance, the BDT method was selected for all KM3NeT/ORCA6 results. Many new possibilities for particle identification will arise as the detector grows. One of them is the direct identification of ν_τ CC in the Showers class.

5.4 Analysis method

The BDT classifier described in Section 5.2 is used to defined the Showers, High and Low Purity Tracks class. Events classified as tracks (showers) with reconstructed energies above

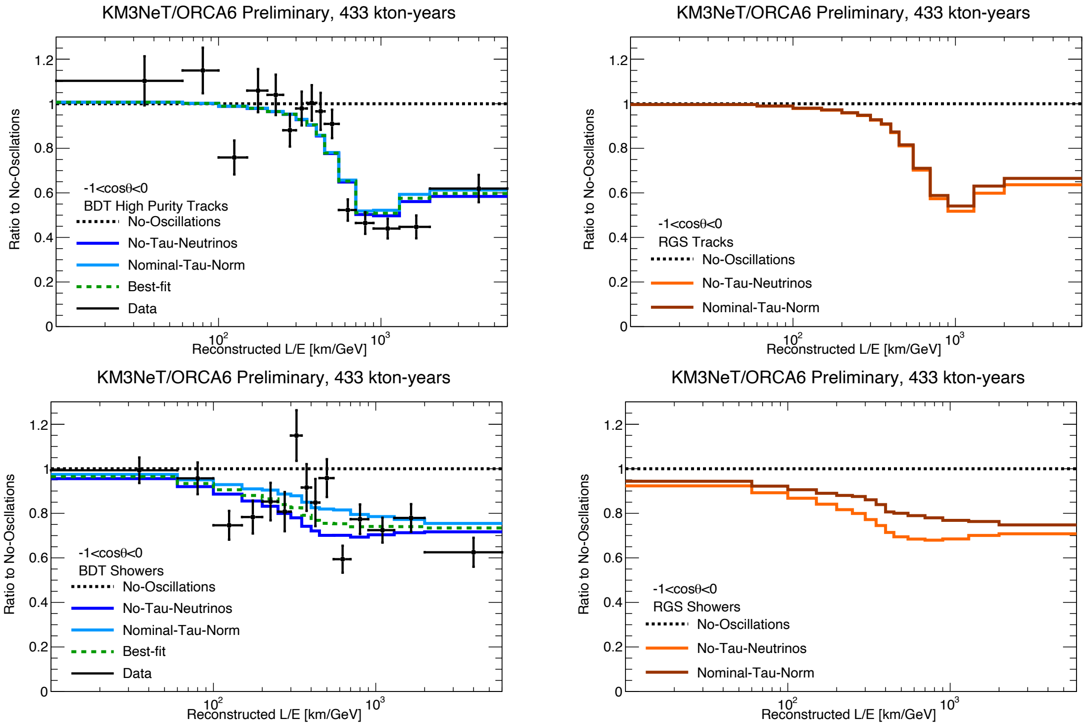

Figure 5.15: The L/E distributions of data and MC for different hypotheses are shown. The L/E using BDT classification is shown on the left side and the RGS classification on the right side. On the top the BDT High Purity Tracks class/RGS Tracks class is represented while on the lower part the BDT/RGS Showers classes are shown. On the left histograms the result of the fit with free ν_τ normalisation is drawn in green, the no-τ hypothesis in blue and nominal ν_τ normalisation hypothesis in cyan. In the right part the no-τ and nominal ν_τ normalisation hypothesis are drawn in orange and brown respectively.

100 GeV (1 TeV) are excluded in order to prevent contributions from events with energies higher than what has been simulated.

The resulting dataset contains 5828 events, distributed in the aforementioned classes as shown in Table 5.3. Additionally, the composition of a reference model that best describes the observed dataset, assuming that $S_\tau = 1$ (see Table 5.4), is also presented in Table 5.3. According to this model, a total of 185 CC tau neutrino and antineutrino interactions are expected. The majority of these (77% CC) are selected in the shower class because the tau leptons produced in ν_τ CC interactions decay into electrons or hadrons with a total branching ratio of about 83%. The remaining fraction of tau neutrino interactions is evenly distributed between the High Purity Tracks and the Low Purity Tracks.

The parameter of interest (PoI) is measured by fitting a model to the observed event distribution. The event distribution predicted by the model depends on the PoI, as well as on several nuisance parameters ϵ that account for systematic uncertainties.

Neutrino oscillation probabilities depend on the ratio between the path length L of the neutrino from its production to its detection, and the energy of the neutrino E. The energy is obtained from the event reconstruction algorithm by fitting the observed signals in the PMTs to the expected signal for a given track or shower reconstructed position and direction. The path length L is instead proportional to the cosine of the reconstructed zenith direction. For each of the classes introduced in Section 7.2, the two-dimensional distribution of the reconstructed energy as a function of the cosine of the zenith angle θ is built. Ten equally-spaced bins are used for $\cos\theta$, in the range [-1, 0] (where $\cos\theta = -1$ corresponds to vertically up-going neutrinos). For the reconstructed energy, 15 bins between 2 GeV and 1 TeV are used. The binning is performed on the logarithmic scale and optimised such that the expected number of events in each bin is at least 2. The distribution of the events from data are shown in Figure 5.16.

The distribution of the events from data compared to MC best fit from standard oscillation fit and no-oscillation fit are shown in Figure 5.17.

The different models introduced in Section 6.1 are fitted to the data through the minimisation of a negative log-likelihood function $-2\log\mathcal{L}$ defined as:

$$-2\log\mathcal{L} = -2\sum_{c}\sum_{ij}\left(n_{ij}^{\text{model}} - n_{ij}^{\text{data}} + n_{ij}^{\text{data}}\log\left(\frac{n_{ij}^{\text{data}}}{n_{ij}^{\text{model}}}\right)\right) + \sum_{\epsilon}\left(\frac{\epsilon_{\text{exp}} - \epsilon_{\text{obs}}}{\sigma_\epsilon}\right)^2 \tag{5.3}$$

The minimisation is based on the MINUIT library and the uncertainties on the fitted values, i.e. the reported post-fit uncertainties, are estimated from the likelihood profiles.

Event Type	Showers	High Purity Tracks	Low Purity Tracks
ν_e CC + $\bar{\nu}_e$ CC	603	51	85
ν_μ CC + $\bar{\nu}_\mu$ CC	902	1777	1786
ν_τ CC + $\bar{\nu}_\tau$ CC	143	22	20
ν NC + $\bar{\nu}$ NC	289	13	22
atmospheric $\mu + \bar{\mu}$	22	7	89
Total MC	1959	1870	2002
Total Data	1958	1868	2002

Table 5.3: Number of events and composition for the three PID classes for a fit to the observed data, under the assumption that CC tau neutrino cross section scale factor $S_\tau = 1$. The observed number of events is reported in the last row.

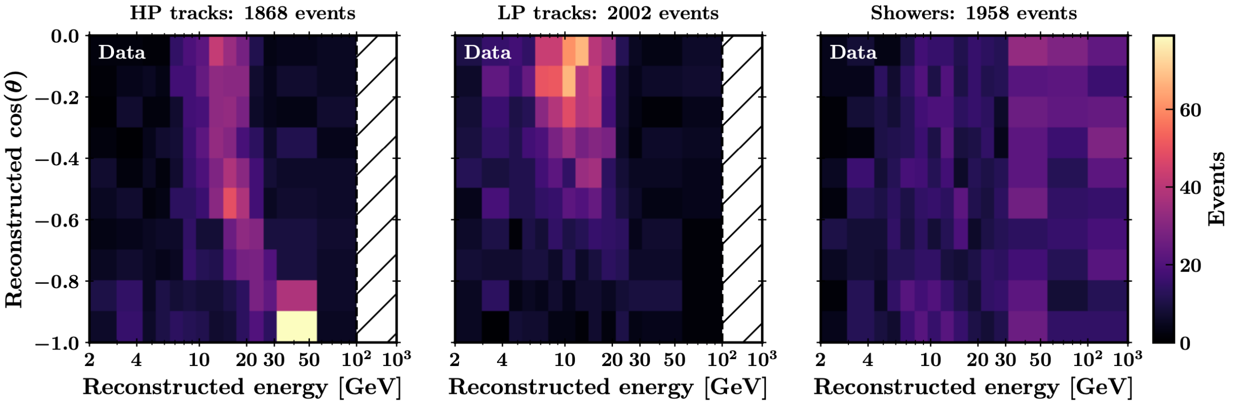

Figure 5.16: Data distribution for each class as function of the reconstructed energy and zenith angle.

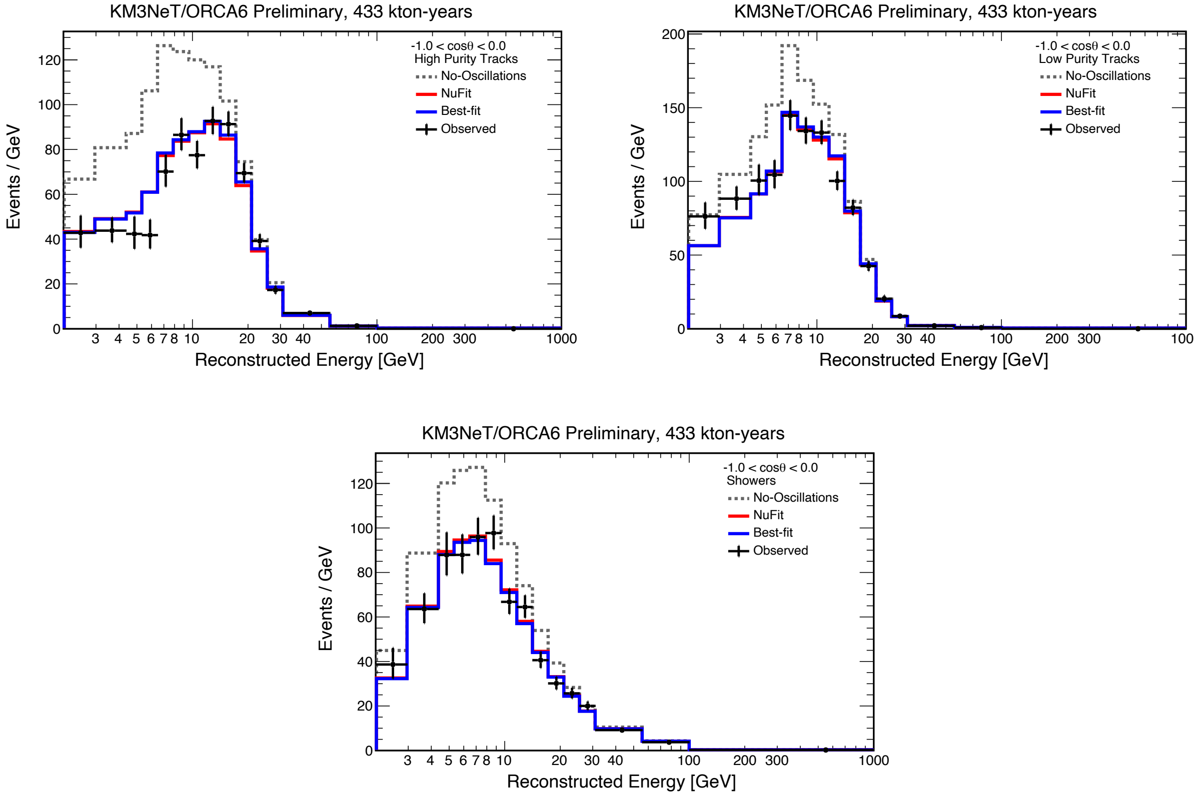

Figure 5.17: The reconstructed energy distributions of data and MC for different hypotheses are shown, compared to the no-oscillation hypothesis. On the top left the High Purity Tracks class, on the top right the Low Purity Tracks class is represented while on the lowest part the Shower class is shown. The result of the fit with fixed oscillation parameters to nominal values is in red, the best fit with standard oscillation parameters in blue and data point are in black with the corresponding error bars.

The first sum runs over all classes c and each bin ij of the aforementioned two-dimensional histograms, computing the Poisson likelihood of observing a number of events in data, n^{data}, given a model with an expectation of n^{model}. The second sum of Equation 5.3 runs instead over the nuisance parameters ϵ for which constraints have been set by other experiments. This knowledge is taken into account by fitting the systematic uncertainties ϵ with a Gaussian prior σ_ϵ in order to prevent the fit from converging at values far away from the expectation of the corresponding parameter ϵ_{exp}.

These also include the oscillation parameters. The analysis is, however, only sensitive to Δm^2_{31} and θ_{23} which are left free in the fit, while the other oscillation parameters are fixed to the NuFit v5.0 reference values [77]. Uncertainties on the shape of the atmospheric neutrino flux are modelled by the spectral index and the deviation from the predicted ratios between horizontal and vertically up-going neutrinos $\nu_{\text{hor}}/\nu_{\text{ver}}$. Additionally, the deviation from the predicted ratios between neutrinos and antineutrinos $\nu_\mu/\bar{\nu}_\mu$, $\nu_e/\bar{\nu}_e$, as well as the deviation from the predicted flavour ratios ν_μ/ν_e address the uncertainties in the flavour composition of the atmospheric neutrino flux. All systematic uncertainties related to the atmospheric neutrino flux are fitted with different priors based on [78]. A nuisance parameter S_{NC} is introduced to account for uncertainties in the all-flavour neutral current interaction cross section. The parameter of interest for the cross section measurement, S_τ, is also a nuisance parameter in the standard fit.

An additional nuisance parameter (High-energy Light Simulation) addresses the differences between the light simulation codes that have been used in the simulation of low- and high-energy neutrinos, while the Energy Scale combines several uncertainties associated with the detector such as PMT efficiencies and water properties adapted from [79]. Finally, four normalisation nuisance parameters are considered: Overall Normalisation, Track Normalisation (concerning High Purity Tracks), Shower Normalisation and Muon Normalisation (concerning the atmospheric muons), allowing for a scaling of the corresponding event numbers.

The nuisance parameter central values ϵ_{exp} and priors σ_ϵ are summarised in Table 5.4 and also described in [74], a short naming convention is also introduced for each systematics in parenthesis in the table, those will be used in the results section of Chapter 7.

The fit is started from several initial values to avoid convergence into local minima. In particular, starting values in both octants of θ_{23} and for both mass orderings are used. Additionally, it was found that using two different starting values for the Energy Scale (above and below the central value of 1) makes the minimisation procedure more robust.

The sensitivity to tau appearance is estimated by profiling the log-likelihood ratio

$$LLR = -2\Delta \log \mathcal{L} = \min_\epsilon\left(-2\log \mathcal{L}\right) - \min_{n_\tau,\epsilon}\left(-2\log \mathcal{L}\right) \tag{5.4}$$

Parameter	Central value ± prior
θ_{23} [°]	49.2 (49.3)
$\Delta m^2_{31} \times 10^{-3}[\mathrm{GeV}]^2$	2.517 (-2.424)
Spectral Index (δ_γ)	0.00 ± 0.3
$\nu_{\mathrm{hor}}/\nu_{\mathrm{ver}}$ (δ_γ)	0.00 ± 2%
$\nu_\mu/\bar{\nu}_\mu$ ($s_{\mu\bar{\mu}}$)	0.00 ± 5%
$\nu_e/\bar{\nu}_e$ ($s_{e\bar{e}}$)	0.00 ± 7%
ν_μ/ν_e ($s_{\mu e}$)	0.00 ± 2%
S_{NC} (f_{NC})	1.00 ± 20%
Energy Scale (E_s)	1.00 ± 9%
High-energy Light Simulation (f_{HE})	1.00 ± 50%
Overall Normalisation (f_{all})	1.00
HP Track Normalisation (f_{HPT})	1.00
Shower Normalisation (f_{S})	1.00
Muon Normalisation (f_μ)	1.00
S_τ	Depending on analysis

Table 5.4: All nuisance parameters and their treatment in the fit are shown. For the oscillation parameters θ_{23} and Δm^2_{31}, the values for normal (inverted) ordering are given.

where the first term represents the likelihood evaluated at the best-fit values of the nuisance parameters and a fixed value for n_τ, and the second term represents the likelihood evaluated at the best-fit values for the nuisance parameters as well as for n_τ. The LLR is therefore evaluated for different values of n_τ in order to calculate the sensitivity and confidence intervals.

According to Wilks' theorem [80], the test statistic $-2\Delta\log\mathcal{L}$ approaches a χ^2 distribution with one degree of freedom. Under this assumption, sensitivity/confidence intervals in units of σ are given by $\sqrt{LLR}$, corresponding to horizontal lines in the $-2\Delta\log\mathcal{L}$ profile curve. However, Wilks' theorem is not valid near physical boundaries of the parameter of interest such as $S_\tau = 0$. Therefore, the confidence intervals are additionally evaluated following a modified Feldman-Cousins (FC) correction as in [81]. In this, pseudo datasets with different values of the PoI are generated where the remaining model parameters are set to the nominal values. A pseudo dataset consists of a two-dimensional event distribution in the energy-$\cos\theta$ plane, where Poissonian fluctuations are added to the bin contents in order to account for statistical fluctuations. Due to limitations in computing resources, the FC correction has been calculated for 6 values of the PoI, and confidence levels have been interpolated from the obtained results. For each PoI value, 1000 pseudo datasets have been generated, and for each pseudo dataset two fits have been performed: first with PoI free, and second with PoI fixed to the true value of the pseudo dataset. For every pseudo dataset, the prior ϵ_{exp} from Equation 5.3 is randomised by drawing it from a Gaussian distribution with mean ϵ_{CV} and width σ_ϵ from Table 5.4. The remaining fitting procedure follows the same approach as described for data. The test statistic is given by Equation 5.3 and the 68% (90%) confidence level C_{68} (C_{90}), is calculated as the 68% (90%) quantile of the $-2\Delta\log\mathcal{L}$ distribution:

$$\omega = \int_{-\infty}^{C_\omega} -2\Delta\log\mathcal{L}$$

The uncertainty on the limits is obtained by exploiting a bootstrapping technique [82] in which the $-2\Delta\log\mathcal{L}$ distribution is resampled 10000 times from the original/observed distribution, each time giving a value of C_ω. The reported limit and uncertainty are given by the mean and standard deviation of the C_ω distribution, respectively.

Chapter 6

Tau neutrino appearance and cross section

Solar [83, 84], reactor [85, 86, 87, 88], and atmospheric [11, 89, 90] experiments mostly exploited the ν_e, $\bar{\nu}_e$, and ν_μ disappearance channels, whereas the high-statistics in the ν_e and $\bar{\nu}_e$ appearance channels have been investigated in long-baseline accelerator experiments [91, 92]. On the contrary, the detection and study of ν_τ neutrinos is intrinsically challenging. There are no known sources of ν_τ easily exploitable. Their existence was suggested in 1977 [93], while their first experimental observation was reported only in 2000 [94]. Due to the high mass of the τ-lepton, the $\nu_\tau$charged-current (CC) interactions have an energy threshold of about 3.5 GeV. Compared to the other flavours the cross section is suppressed close to that energy threshold and zero below as described in Chapter 1. Therefore, in contrast with the current few-percent precision on the PMNS matrix elements in the electron and muon rows [95], the τ-row remains the least constrained, essentially due to a lack of ν_τ statistics. Moreover, the current knowledge of the CC tau neutrino interactions intrinsically limits the achievable precision in oscillation experiments. Hence, exploring the ν_τ-appearance channel becomes valuable to further constrain the ν_τ CC cross section.

This work explores atmospheric tau neutrinos with KM3NeT/ORCA. Atmospheric neutrino oscillation in the [1, 100] GeV energy range are observed in different oscillation channels. The $\nu_\mu \to \nu_e$ appearance channel is used to probe the neutrino mass ordering by studying the $\nu/\bar{\nu}$ asymmetric effect of resonant oscillation in the Earth's mantle due to the matter effect [96]. The ν_μ-disappearance is the dominant channel and contributes to a precise measurement of the atmospheric oscillation parameters Δm^2_{31} and θ_{23}. Additionally, thanks to its high accessible statistics compared to other next-generation experiments [79, 96], KM3NeT/ORCA has a competitive sensitivity to the ν_τ-appearance channel.

This work reports the first exploration of the ν_τ detection in an intermediate KM3NeT/ ORCA geometry, corresponding to 5% of the nominal volume (KM3NeT/ORCA6), which collected data in the period 2020-2022.

6.1 From the $\nu_\tau$normalisation to the ν_τ CC cross section measurement

Due to the very short τ lepton lifetime, an event-by-event ν_τ identification in KM3NeT/ ORCA is currently not possible. Nevertheless, the tau neutrino appearance can be quantified on a statistical basis. The ν_τ-normalisation n_τ [97, 98, 99] is defined as the ratio between the observed and expected number of CC tau neutrinos that appear after the oscillations. When accounting for the charged-current ν_τ only, n_τ can be expressed as a scaling factor of the ν_τ CC cross section; therefore, its measurement allows to directly constrain the ν_τ CC cross section.

The rate of detected charged current ν_τ events can be expressed as

$$N_\tau = \int_E \int_{\cos(\theta)} \sigma_\tau^{meas} \big\{ \Phi_e P_{e\tau} + \Phi_\mu P_{\mu\tau} \big\} k_N \times \epsilon \times dE \times d\cos(\theta), \tag{6.1}$$

with σ_τ^{meas} the measured ν_τ cross section, k_N the number of target nucleons in the detector volume, ϵ the detector efficiency, the $P_{\alpha\tau}$ probabilities defined in Chapter 1 and Φ_α the atmospheric neutrino flux, for flavour α, computed from the Honda model [100]. The measured ν_τ cross section σ_τ^{meas} is related to the theoretical expectation value σ_τ^{th} from GENIE [101]. In [97] the ν_τ-normalisation corresponds to a scale factor for the measured cross section. In this case, it is referred to as S_τ, and the measured cross section can be defined as

$$\sigma_\tau^{\mathrm{meas}}(E_\nu) = S_\tau \times \sigma_\tau^{\mathrm{th}}(E_\nu); \tag{6.2}$$

therefore S_τ is equivalent to a normalisation of the number of charged current tau neutrino events. The theoretical uncertainties above 10 GeV as mentioned in Chapter1 are below 7%. In the DIS regime, additional form factors F4 and F5 have a significant impact on the cross section as described in [102].

6.2 ν_τ CC cross section measurement

The analysis procedures described in Section 5.4 have been applied to fit each of the models described in Section 6.1 to the data set described in Section 7.2. The results are summarised in Tables 6.1 and 7.9, which respectively show the best-fit values for the parameters of interest of each model, and the best-fit values for the nuisance parameters.

Model	PoI	N_{ν_τ} CC	N_ν NC
S_τ	$0.48^{+0.49}_{-0.33}$	92^{+94}_{-64}	340^{+76}_{-76}

Table 6.1: Measured ν_τ-normalisation S_τ and corresponding number N_{ν_τ} CC of charged current tau and N_ν NC of neutral current neutrino. The 1σ uncertainties for S_τ are obtained with the FC approach described in Section 5.4.

The parameter of interest S_τ when measuring the ν_τ CC cross section. The parameter S_τ and the corresponding 1σ uncertainty were measured to be $0.48^{+0.49}_{-0.33}$. The best fit corresponds to a total number of 92 observed ν_τ CC interactions. The profiled log-likelihood for S_τ in Figure 6.1 allows to visualise the best-fit value as well as 68% and 90% confidence intervals and the FC correction.

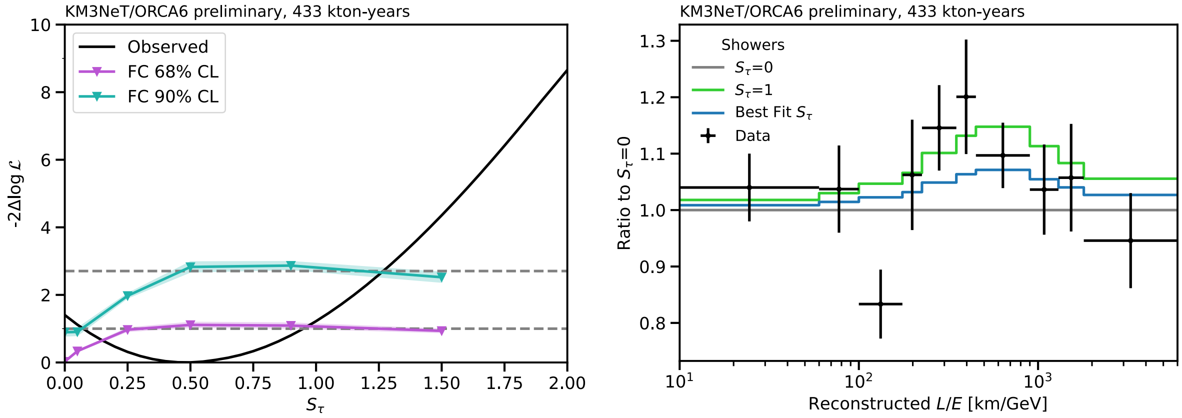

Figure 6.1: **Left:** Measured log-likelihood profile for the model probing the ν_τ CC cross section. The 68% (purple) and 90% (blue) interval from FC approach are also shown. **Right:** Measured L/E distribution for the shower class with best-fit model and a model with nominal ν_τ-normalisation S_τ with respect to no tau-appearance.

Systematic uncertainty	S_τ $\pm 1\sigma$
θ_{23}	$45.6^{+3.63}_{-3.69}$
Δm^2_{31} $[10^{-3}\,\mathrm{GeV}^2]$	$2.15^{+0.29}_{-0.28}$
Spectral Index	$-0.02^{+0.03}_{-0.03}$
$\nu_{\mathrm{hor}}/\nu_{\mathrm{ver}}$	$-0.002^{+0.02}_{-0.02}$
$\nu_\mu/\bar{\nu}_\mu$	$-0.003^{+0.05}_{-0.05}$
$\nu_e/\bar{\nu}_e$	$0.006^{+0.07}_{-0.07}$
ν_μ/ν_e	$-0.004^{+0.02}_{-0.02}$
S_{NC}	$0.89^{+0.20}_{-0.20}$
Energy Scale	$0.98^{+0.11}_{-0.08}$
High-energy Light Simulation	$1.50^{+0.33}_{-0.30}$
Overall Normalisation	$1.09^{+0.17}_{-0.11}$
Track Normalisation	$0.91^{+0.04}_{-0.04}$
Shower Normalisation	$0.92^{+0.06}_{-0.06}$
Muon Normalisation	$0.48^{+0.40}_{-0.36}$
S_τ	PoI

Table 6.2: All systematic uncertainties and their best-fit values along with their 1σ post-fit uncertainties.

The dashed lines indicate the 68% and 90% confidence levels (CLs) according to Wilks' theorem whereas the colored lines represent the CLs from the FC correction with their corresponding 1σ uncertainty derived from bootstrapping. As expected, the CLs from Wilks and FC mostly deviate from each other for low values of S_τ, i.e. close to the boundary. Above $S_\tau = 0.25$ (0.50) the difference for the 68% (90%) CL is negligible. Overall, the corrected 68% CL is found to be [0.15, 0.96]. The p-value, i.e. the fraction of pseudo datasets for which $-2\Delta\log\mathcal{L}$ is larger than the observed one, for $S_\tau = 0$ is $(5.9 \pm 0.8)\%$. The L/E distribution is shown on the right side of Figure 6.1. The ratio for the observed data compared to the best-fit model and a model with $S_\tau = 1$ to a model with the extreme case $S_\tau = 0$ is presented. The distribution is shown for the shower class, where the most sensitivity to tau appearance is found.

The measured tau neutrino cross section is related to the theoretical expectation following Equation 6.2. In Figure 6.2, the energy-dependant theoretical expectation from [101] is scaled using the best-fit value $S_\tau = (0.48^{+0.49}_{-0.33})$, while the median of the ν_τ CC true energy distribution E_{ν_τ} is at 20.3 GeV between 12.3 and 35.9 GeV at 68% CL. The corresponding theoretical expectation is $\sigma_\tau^{\text{th}}(E_{\nu_\tau}) = 5.29 \times 10^{-38}\text{cm}^2$; hence, the measured cross section is $\sigma_\tau^{\text{meas}}(E_{\nu_\tau}) = (2.5^{+2.6}_{-1.8}) \times 10^{-38}\text{cm}^2$. The averaging of the neutrino and antineutrino cross section is done following

$$\begin{aligned}\langle\sigma_{\nu_\tau}\rangle &= r_\nu \sigma_{\nu\tau} + (1-r_\nu)\sigma_{\bar{\nu}_\tau}\\ r_\nu &= X_\nu/(X_\nu + \epsilon X_{\bar{\nu}})\\ X_\nu = \int dE \int d\theta & \left[\Phi_\mu P_{\mu\tau} + \Phi_e P_{e\tau}\right]\sigma_{\nu_\tau}.\end{aligned}$$

The neutrino fraction is found as $r_\nu = 71\%$. While ϵ accounts for potential differences in the reconstruction efficiencies between neutrino and antineutrino events due to their non-identical interaction inelasticities. However it is found that the invisible neutrino from tau decay fully compensates for the presumed inelasticity effect and $\epsilon = 1.0$ is found.

The effect of the nuisance parameters on the fit result of S_τ is presented in Figure 6.3. In this, each blue bar represents the impact of a nuisance parameter on S_τ. Each bar is calculated by performing two fits: one in which the nuisance parameter is fixed to the best-fit value from Table 7.9 plus its 1σ post-fit uncertainty given by the MINOS error, and one in which it is fixed to the best-fit value minus its uncertainty. Each fit yields a new fitted value for S_τ denoted as S_τ^{shift}, which allows to calculate the impact as $\left(S_\tau^{\text{shift}} - S_\tau^{\text{bf}}\right)/\sigma_{S_\tau}$, where S_τ^{bf} is the best-fit value of S_τ, and σ_{S_τ} its 1σ error. This plot also shows the pulls

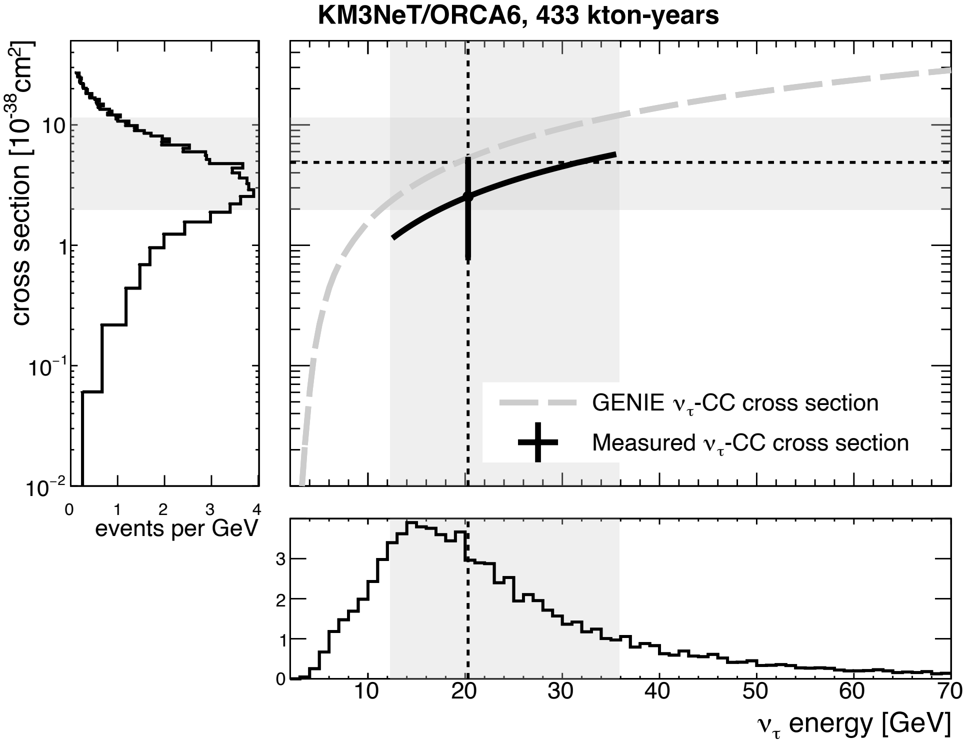

Figure 6.2: Measurement of the charged-current tau neutrino cross section in black, compared to the $\nu_\tau/\bar{\nu_\tau}$ averaged theoretical expectation in gray as a function of the energy. The light gray bands represent the 68% range of the distributions.

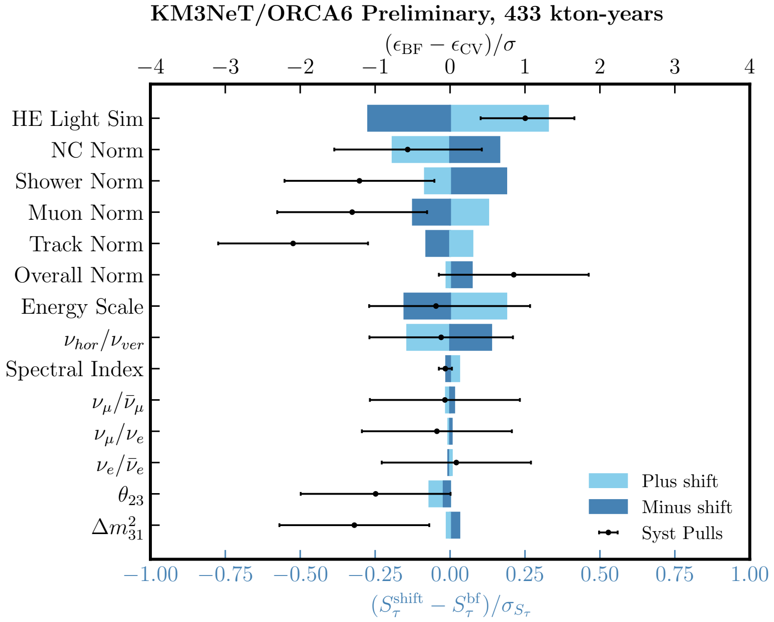

Figure 6.3: Impact (blue bars, lower x-axis) and pulls (black markers, upper x-axis) of the systematic uncertainties considered in the model probing the ν_τ CC cross section.

for each nuisance parameter (black markers), which are defined as the difference between the best-fit value ϵ_{BF} and the expected value ϵ_{CV} of the corresponding parameter, divided by its uncertainty $\left(\epsilon_{\mathrm{BF}} - \epsilon_{\mathrm{CV}}\right)/\sigma$. If available, σ is given by the pre-fit uncertainty (see table 5.4), and the error bars represent the ratio of the post-fit and pre-fit uncertainties $\sigma_{\epsilon}^{\mathrm{post-fit}}/\sigma_{\epsilon}^{\mathrm{pre-fit}}$. For the parameters that are fitted without constraints, σ is given by the post-fit uncertainty and the error bars are set to 1.

The High-energy Light Simulation and the S_{NC} normalisation are the nuisance parameters with the largest impact on S_{τ}. The Energy Scale, i.e. the detector uncertainties, has a non-negligible impact. Regarding the atmospheric neutrino flux parameters, only the ratio between up- and horizontally-going neutrinos has a sizable influence, whereas especially the three composition ratios do not affect the S_{τ} measurement significantly. Systematic uncertainties that are fitted without constraints have larger pulls, as expected. Among the systematic uncertainties that are fitted with a prior, only High-energy Light Simulation and S_{NC} show large pulls. Except for the spectral index, for which the post-fit uncertainty is significantly reduced compared to the pre-fit one, all constraints are close to 1.

6.3 Comparison with other experiments and conclusion

The ν_τ-normalisation has been measured and used for constraining CC tau neutrino cross section by exploring KM3NeT/ORCA data. A data sample of 433 kton-years exposure collected with 5% of the nominal instrumented volume, corresponding to 6 operational DUs, has been used for these analyses.

The approach assumes that the the neutrino mixing matrix is unitary consequently, possible deviations of the ν_τ-normalisation from 1 correspond to a scaling of the ν_τ CC event rate appearing from the oscillated atmospheric neutrino flux. This method was already used by other experiments, exploring the ν_τ-appearance channel in the oscillation of neutrinos either from the ν_μ CNGS beam (as in OPERA [98]) or from the atmosphere (as in Super-Kamiokande [97] and IceCube [99]). Nonetheless, the comparison among previously reported measurements must account for the detection of neutrinos at different energies and interacting in different media.

As in the other atmospheric neutrino experiments, Super-Kamiokande and IceCube, the KM3NeT/ORCA6 analysis is performed on a statistical basis, due to the impossibility of directly tagging ν_τ and $\bar{\nu}_\tau$, and focuses on ν_τ at the maximum appearance around 25 GeV. In the KM3NeT/ORCA6 event sample, 92 ν_τ CC are observed. The ν_τ-normalisation is fitted while keeping the θ_{23} angle and the Δm^2_{31} mass splitting parameters free as well. Both normal and inverted ordering hypotheses are tested. In this way, the ν_τ-normalisation is measured at $0.48^{+0.49}_{-0.33}$. The significance of not observing ν_τ CC ($S_\tau = 0$) is at 1.2σ level. The up to date overview of the ν_τ CC normalisation measurements at 68% CL, including KM3NeT/ORCA6 result, is reported in Figure 6.4. None of the reported results show any statistical evidence of a deviation of the ν_τ-normalisation from 1. In the case of OPERA [103], the very low statistic of a sample of a few neutrino candidates is balanced by event-by-event reconstruction. Super-Kamiokande performed a combined fit of their maximum statistics (corresponding to ≈15 years of data taking), explicitly assuming the normal order hypothesis for neutrino mass splitting. In the IceCube analyses, instead, the ν_τ-normalisation is fitted with fixing the solar oscillation parameters, while θ_{13} is treated as systematic uncertainty with 20% prior; a profile to both the normal and the inverted ordering is performed while fixing the δ_{CP}-phase to 0. Although at least a factor of 10 in the ν_τ CC statistics, the reported precision is comparable with all the other measurements. Nevertheless, KM3NeT/ORCA competitiveness in the field is confirmed despite the small dimensions of its current geometry; remarkably comparable precision with previous measurements of the ν_τ-normalisation is already reached. The reported result is expected to

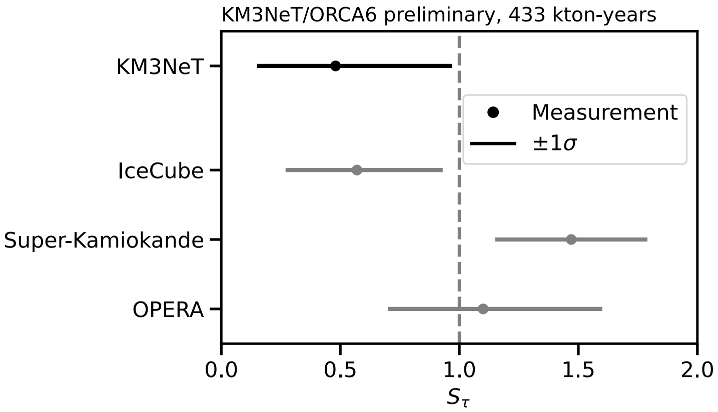

Figure 6.4: Comparison of S_τ measurement of KM3NeT/ORCA6 with previous results on ν_τ CC cross section normalisation reported by OPERA [98], Super-Kamiokande [97], and IceCube [99] experiments.

be improved in the near future thanks to larger statistics and improved knowledge on the systematics.

The ν_τ-normalisation S_τ can be interpreted as a scale factor of the ν_τ CC cross section, allowing to constrain its measurement. Up to now, the knowledge on the neutrino interactions is still one of the main sources of systematics in neutrino oscillation experiments, and measurements of the ν_τ CC cross section have been reported only by a few experiments. Hence, exploiting the energy range and interaction medium diversity accessible in the different experiments as well as the different impact of systematic effects and uncertainties is an additional motivation for pursuing it. Therefore, the KM3NeT/ORCA measurement allows for further containing the current knowledge of the ν_τ CC cross section. In order to measure it in KM3NeT/ORCA data, the theoretical ν_τ cross section is calculated at the median of the ν_τ energy distribution, 20.3 GeV. In the case of OPERA [103], the accessible neutrino energy range is restricted below 20 GeV and ν_τ CC interactions take place in the lead-based target. On the contrary, in experiments exploiting the ν_τ-appearance channel from the atmospheric neutrino oscillation, the separation between ν_τ and $\bar{\nu}_\tau$ cannot explicitly be taken into account. The KM3NeT/ORCA6 measurement of the ν_τ CC cross section is found to be $\sigma_{meas} = (2.5^{+2.6}_{-1.8})\times 10^{-38}\text{cm}^2$; still dominated by statistical uncertainties, no robust deviations from the GENIE simulation expectation is observed. For a better comparison highlighting the difference among the aforementioned experiments, a summary of the reported measurements of the ν_τ CC cross section and the corresponding statistics is reported in Table 6.3.

experiment	interaction medium	energy [Gev]	n. of observed ν_τ section	ν_τ CC cross [nucleon$^{-1}\times 10^{-38}$ cm^2]
OPERA [103]	lead	$\leq$20	10	$2.46^{+2.4}_{-2.0}$
SK [104]	water	15^{+25}_{-8}	338.1 ± 72.7	0.94 ± 0.20
KM3NeT/ORCA6 (this work)	water	$20.3^{+15.6}_{-8}$	92^{+92}_{-64}	$2.5^{+2.6}_{-1.8}$

Table 6.3: Summary of the reported measurements of the ν_τ CC cross section and the corresponding statistics; the measurement from OPERA [103] has been converted in the same units as Super-Kamiokande and KM3NeT/ORCA6 by dividing by the number of nucleons, given the target composition.

With more statistics the KM3NeT/ORCA measurement of the CC tau neutrino cross section will improve in precision and explore a larger ν_τ energy range. This will help in our understanding of the tau neutrino cross section structure functions, affected by the large tau lepton mass, with respect to the muon and electron neutrino.

Chapter 7

Search for Non Unitary Neutrino Mixing

The oscillation of neutrinos has been measured in various channels since its experimental confirmation in 1998 [11]. However, the constrains on the oscillation probabilities are still too weak to probe the unitarity of the 3×3 neutrino mixing matrix U. This is most striking in the third column [99] where the uncertainty on the unitarity of U is the largest. The unique sensitivity of KM3NeT/ORCA to the non-unitarity is due to the strong matter effects that atmospheric neutrinos encounter when propagating through the earth density layers. This Chapter will present the first observation where the low scale non-unitarity is directly evaluated on earth-crossing atmospheric neutrinos.

7.1 Theoretical framework

The mechanisms to generate the neutrino mass were described in Chapter 1. If neutrinos are Majorana and masses are generated within the seesaw mechanism, the new mass states could be explored in the entire energy range. The new neutrino states are sometimes also named Heavy Neutral Leptons (HNLs).

One can distinguish two regimes of mass ranges for the HNLs. If the HNL masses are too heavy to be kinematically produced at the neutrino production site, the regime is called high-scale [105]. For neutrino production in cosmic ray showers the high-scale regime applies when the HNL cannot be produced in pion decay, i.e. for $m_{i>3} > m_\pi - m_\mu \approx 40$ MeV, with m_π and m_μ the mass of the pion and the muon, respectively. In the high-scale scenario, only the Majorana mass term is allowed and the flavor states are non-orthogonal

$$\langle\nu_\beta|\nu_\alpha\rangle = \frac{(\mathrm{UU}^\dagger)_{\beta\alpha}}{\sqrt{(\mathrm{UU}^\dagger)_{\alpha\alpha}(\mathrm{UU}^\dagger)_{\beta\beta}}} \neq \delta_{\beta\alpha} \tag{7.1}$$

with $\alpha, \beta = e, \mu, \tau$. This leads to zero distance oscillations $P_{\beta\alpha}(L = 0) \neq 0$ among the three active neutrino states [106]. A re-normalisation of the mixing matrix has to be applied as

$$\overline{U}_{\alpha i} \equiv \frac{U_{\alpha i}}{\sqrt{(UU^\dagger)_{\alpha\alpha}}}. \tag{7.2}$$

in order to ensure the completeness of the flavor state space [105]. The high-scale scenario induces modifications of the W and Z couplings that impact precision electroweak observables, leading to stringent limits [107]. This scenario causes a departure from unitarity of the mixing matrix with effects proportional to $(\mathrm{UU}^\dagger)_{\beta\alpha}$ for $\alpha \neq \beta$. Therefore impossible to distinguish from the unitarity case when only $(\mathrm{UU}^\dagger)_{\alpha\alpha} \neq 0$. Even with non-unitary neutrino mixing the probability remains unitary $\sum_\beta P_{\beta\alpha}(x) = 1$ thanks to the completeness of the flavor states basis.

In the low-scale realisation of the seesaw scheme were the new masses involved are within experimental reach, like the inverse or linear seesaw [108], the neutrino mixing matrix is given by a $n \times n$ $(n > 3)$ unitary matrix. To ensure that the neutrino production spectrum is not significantly affected by the presence of a new neutrino mass state, the width of the decaying particle into a new mass neutrino must not be $\approx 10\%$ smaller than the decay rate into an active neutrino. If the neutrinos are produced via pion decays this maximum mass is ≈ 15 MeV [109]. In that scenario the new states are kinematically accessible and participate to neutrino oscillations. The flavor state space is complete and orthogonal since the mixing matrix is unitary, therefore no re-normalisation is applied like in the high-scale scenario. However the sum of the observable probabilities $\sum_\beta P_{\beta\alpha}(x) \neq 1$ with $\alpha, \beta = e, \mu, \tau$ due to the contribution of new neutrino mass states in the oscillations. Hence a very-short distance oscillations effect will give rise to a *probability leaking term* in the model which accounts only for the averaged-out oscillations [106].

The non-unitary neutrino mixing (NUNM) is useful to probe the case of any number of new mass states, including the possibility of 3 heavy neutrinos $\nu_{1b}, \nu_{2b}, \nu_{3b}$ as partners of the SM neutrinos $\nu_{1a}, \nu_{2a}, \nu_{3a}$, that naturally arise in the canonical type-1 seesaw model.

The full neutrino mixing matrix $\mathrm{U} = \mathrm{U}^{n\times n}$ described by Eq. 7.3 is unitary. The non-unitary matrix N corresponds to the upper left 3×3 component of U.

$$U = \begin{pmatrix} N & S \\ W & T \end{pmatrix} = \begin{pmatrix} N^{3\times 3} & S^{3\times(n-3)} \\ W^{(n-3)\times 3} & T^{(n-3)\times(n-3)} \end{pmatrix}. \tag{7.3}$$

It can be decomposed in a product of $n(n-1)/2$ rotations, with the Pontecorvo–Maki –Nakagawa–Sakata (PMNS) neutrino mixing matrix $\mathrm{U}_{\mathrm{PMNS}} = (R_{23} \cdot R_{13} \cdot R_{12})^{3\times 3}$ as in Eq. 7.4. The rotations R_{ij} of angle θ_{ij}, also contain a CP-violating phase δ_{ij} if $j - i > 1$. When the rotations R_{ij} are applied in this specific order, the non-unitary part of U is lower triangular.

$$U = R_{n-1\,n} \cdot R_{n-2\,n} \cdots R_{3\,n} \cdot R_{2\,n} \cdot R_{1\,n} \cdots R_{2\,3} \cdot R_{1\,3} \cdot R_{1\,2}. \tag{7.4}$$

From this observation, the general structure of the non unitarity parametrisation is constructed $I + \alpha = (UU_{\mathrm{PMNS}}^{-1})^{3\times 3}$. The lower triangular matrix α is defined as

$$\alpha = \begin{pmatrix} \alpha_{11} & 0 & 0 \\ |\alpha_{21}|e^{i\phi_{21}} & \alpha_{22} & 0 \\ |\alpha_{31}|e^{i\phi_{31}} & |\alpha_{32}|e^{i\phi_{32}} & \alpha_{33} \end{pmatrix}. \tag{7.5}$$

involving 9 new parameters in addition to the SM mixing angles and phases with real diagonal parameters and complex non-diagonal ones. This lower triangular formalism was first introduced by Okubo in 1962 [110], used by [111, 112, 113, 114], and tested on data in [115]. The non-unitary matrix α applied to the unitary mixing matrix U_{PMNS} gives the non-unitary matrix N,

$$N = (I + \alpha)\, U_{\mathrm{PMNS}}. \tag{7.6}$$

This model avoids the computationally intensive parametrisation of these effects with a $n \times n$ unitary mixing matrix in a sterile neutrino model with the number of corresponding angles and phases that grows as fast as n^2. As part of this work, the model was implemented in the publicly available OscProb software [18] (in commit *9afa5c4* Feb 23, 2024), used to calculate the neutrino oscillation probabilities in KM3NeT. The complete matter potential V and the mass splitting matrix Δ are defined in Eq. 7.7 with $V_{CC} = \sqrt{2}G_F n_e$ and $V_{NC} = -\frac{1}{\sqrt{2}}G_F n_n$, where n_e and n_n are the electron and neutron number density, respectively. The $n \times n$ matrices are defined with $\mathrm{V}^{n\times n} = \mathrm{diag}\{\mathrm{V}, 0, \ldots, 0\}$ and $\Delta^{n\times n} = \mathrm{diag}\{\Delta, \Delta m^2_{41}, \ldots, \Delta m^2_{n1}\}$.

$$\Delta = \frac{1}{2E}\begin{bmatrix} 0 & 0 & 0 \\ 0 & \Delta m^2_{21} & 0 \\ 0 & 0 & \Delta m^2_{31} \end{bmatrix} \quad V = \begin{bmatrix} V_{CC} + V_{NC} & 0 & 0 \\ 0 & V_{NC} & 0 \\ 0 & 0 & V_{NC} \end{bmatrix} \tag{7.7}$$

In the mass scale regime considered in this work, the new neutrino masses are several order of magnitudes above the active neutrino masses [116]. In that case, the model is not sensitive to the details of the sterile sector, in particular, oscillation effects due to the $\mathrm{m}_{i>3} \gg \sqrt{\Delta \mathrm{m}^2_{\mathrm{atm}}}$ are averaged out. Under that approximation the Hamiltonian in matter in the mass basis $\mathrm{H}_m^{n\times n}$, can be truncated in Eq. 7.8 as discussed in [115].

$$H_m^{n\times n} = \Delta^{n\times n} + U^\dagger V^{n\times n} U \longrightarrow H_m^{3\times 3} = \Delta + N^\dagger V N \tag{7.8}$$

In the tilde basis defined in Eq. 7.9, the Hamiltonian $\widetilde{\mathrm{H}}$ is written in a similar way as the standard Hamiltonian in matter in the flavour basis $\widetilde{H}_{\mathrm{PMNS}} = U_{\mathrm{PMNS}} \Delta U^\dagger_{\mathrm{PMNS}} + V$. However in the case of NUNM the matter potential is affected by the non-unitary factor (I+α), therefore the neutron-induced matter potential V_{NC} is relevant. It can't be ignored like in the unitarity case where the NC matter potential affecting all flavours is equivalent to an absolute phase shift in the evolution of the neutrino state.

$$\widetilde{H} = U_{\mathrm{PMNS}} H_m^{3\times 3} U^\dagger_{\mathrm{PMNS}} = U_{\mathrm{PMNS}} \Delta U^\dagger_{\mathrm{PMNS}} + (I+\alpha)^\dagger V (I+\alpha). \tag{7.9}$$

The calculation of the probability after propagation of the neutrino state and after the eigensystem have been solved, is affected by the non unitary factor $(I+\alpha)$ that can't simply move inside the exponential because it is non-unitary. Eq. 7.10 describes the oscillation probability to observe flavour γ from initial flavour β after propagation of a distance L in a fixed density in the presence of unitarity violation (super-script α).

$$P^\alpha_{\gamma\beta} = S^2_{\beta\gamma} = \left| \left((I+\alpha) e^{-i\widetilde{H}L} (I+\alpha)^\dagger \right)_{\beta\gamma} \right|^2 . \tag{7.10}$$

In the case of varying density with non-unitary mixing [105], the probability propagation is more complex. The Eq 7.11 ensures that the non-unitarity transformation applies only once before and after the propagation of the neutrino state. It should not depend on the numbers of density layers.

$$S(x) = (NN^\dagger) T \prod_{a=1}^{n} (NN^\dagger)^{-1} S_a(x) \tag{7.11}$$

The index of the density layer a is between 1 and n and T is the space ordering of the matrix multiplication. The Eq 7.12 is an example given for the case of two density layers of size L.

$$S(2L) = S_2(L)(NN^\dagger)^{-1}S_1(L) = (I+\alpha)e^{-i(\widetilde{H}_2+\widetilde{H}_1)L}(I+\alpha)^\dagger \tag{7.12}$$

The current constraints given in Table 7.1 are based on non-observation of very short distance oscillations [117, 118] and constraints from light sterile neutrino search [119]. The most weakly constrained individual parameter is α_{33}. The muon disappearance being the main channel of KM3NeT/ORCA, it will be more sensitive to α_{22}, α_{32} and α_{33} than α_{31}, α_{11} and α_{21}. Hence the work will be concentrated on studying α_{22}, α_{32} and α_{33} effects individually and in pairs.

Present Bounds [107]
$\alpha_{33} > 0.10$
$\alpha_{22} > 0.022$
$\alpha_{11} > 0.024$
$\|\alpha_{32}\| < 0.012$
$\|\alpha_{31}\| < 0.069$
$\|\alpha_{21}\| < 0.025$

Table 7.1: Current bounds at the 2σ CL derived in [107], for individual low scale NUNM parameters.

To understand the effect of the non-unitary parameter α_{33} one can consider the case study of non zero α_{33} and $V_{NC} = 0$. However in most of the results shown in this work $V_{NC} \neq 0$ unless stated otherwise. In that case (where $V_{NC} = 0$) the α_{33} effect is a reduction of the ν_τ appearance. This case compares to the CC+NC approach followed in [99], where the ν_τ normalisation modifies both the rates of CC ν_τ and the ν_τ contribution to NC events. Hence, the modified probability for a neutrino of initial flavor δ to remain active is defined as

$$P^\alpha_\delta = P_{\delta e} + P_{\delta\mu} + (1+\alpha_{33})^2 P_{\delta\tau}. \tag{7.13}$$

The modified CC ν_τ and NC event rates are given by N^α_τ and N^α_{NC}, respectively, and defined as $N^\alpha_\tau = (1+\alpha_{33})^2 N_\tau$ and by

$$N^\alpha_{NC} = \int_E \int_{\cos(\theta)} \sigma_{NC} \Big\{ \Phi_e[P^\alpha_e] + \Phi_\mu[P^\alpha_\mu] \Big\} k_N \times \epsilon \times dE \times d\cos\theta. \tag{7.14}$$

However when accounting for the full matter effects, including the V_{NC} potential, the relation with ν_τ appearance is broken and α_{33} affects also the muon appearance and disappearance.

This non-unitarity test in the low-scale scenario can be translated into a 1-sterile neutrino case study based on

$$\cos(\Theta_{34})^2 = (1 + \alpha_{33})^2 \tag{7.15}$$

under the hypothesis of $\Delta m^2_{41} \gg \frac{E}{L}$, $\theta_{14} = \theta_{24} = 0$. The mapping to light sterile neutrino is valid only for individual parameters, as soon two or more NUNM parameters are used in the fit the correspondence is broken. The Figure 7.1 illustrates the effect of α_{33} **with and without** V_{NC} compared to the effect of θ_{34}. It shows how the inclusion of the neutral current potential modifies the non-unitarity effect from only the tau appearance channel to the muon disappearance channel as well. The latter currently drives the sensitivity of KM3NeT/ORCA to α_{33} due to the high statistics and high purity of the track sample.

In addition, the Figure 7.2 illustrates the effect of the single parameter α_{33} or α_{22} or α_{32} non-zero. The amplitude in the muon disappearance and the tau appearance channel is suppressed in the case of non-zero α_{22} and α_{33}, with a heavier effect of α_{22} in the muon disappearance channel strongly enhanced by the earth matter effects which gives most sensitivity in KM3NeT/ORCA. The effect of non-zero α_{32} is a shift of the maximum of the oscillation probability in both channels.

The Figure 7.3 contains a 2D oscillogram that illustrates the comparison between the non-unitarity and unitarity case in the muon disappearance channel on the left and the tau appearance channel on the right. It highlights the complex effect of non-unitarity below 10 GeV due to matter even in the case of a single parameter non-zero.

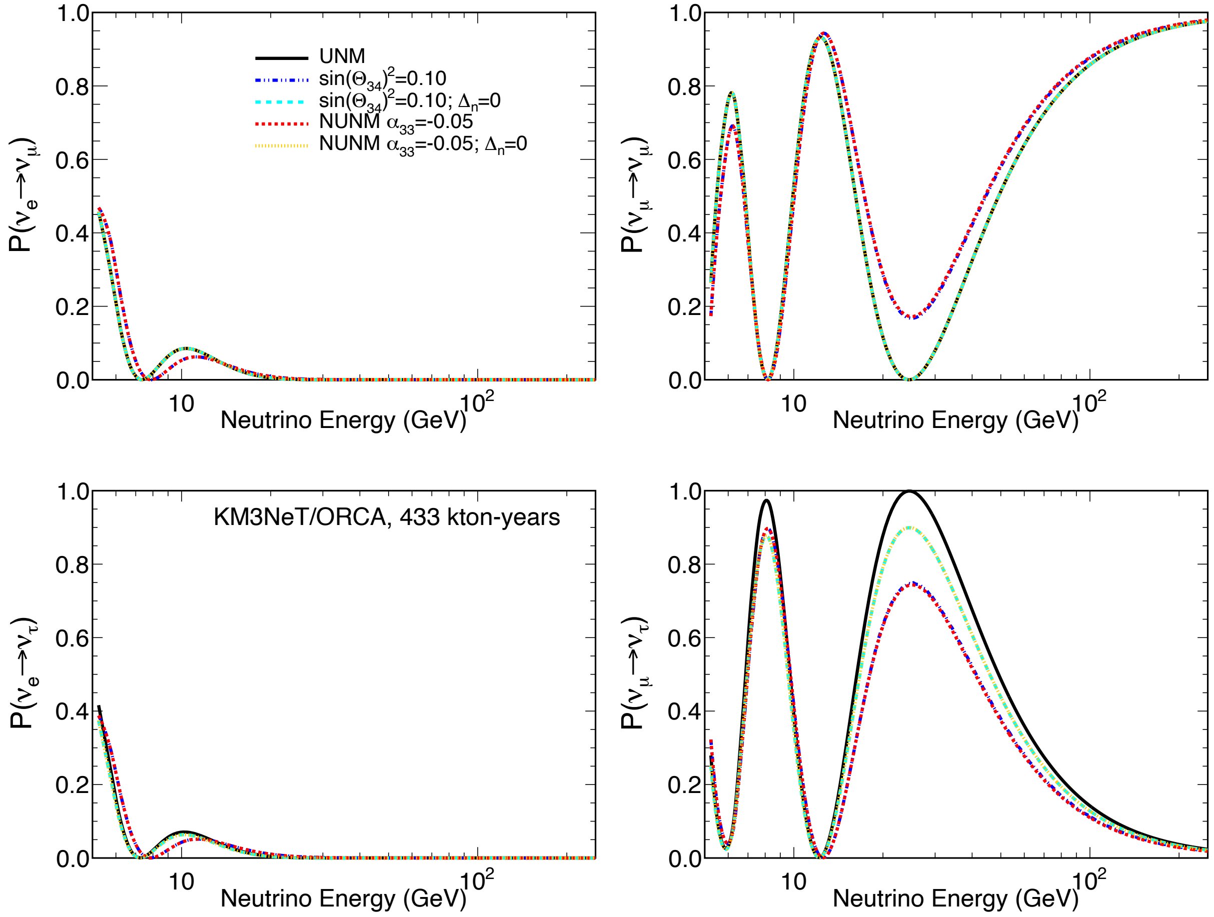

Figure 7.1: The oscillation probability for vertically up-going neutrinos as function of neutrino energy for a fixed sterile mixing angle θ_{34}, the corresponding non unitary parameter α_{33} with $\Delta m_{41} = 10eV^2$ and $\sin(2\theta_{23}) = 1$.

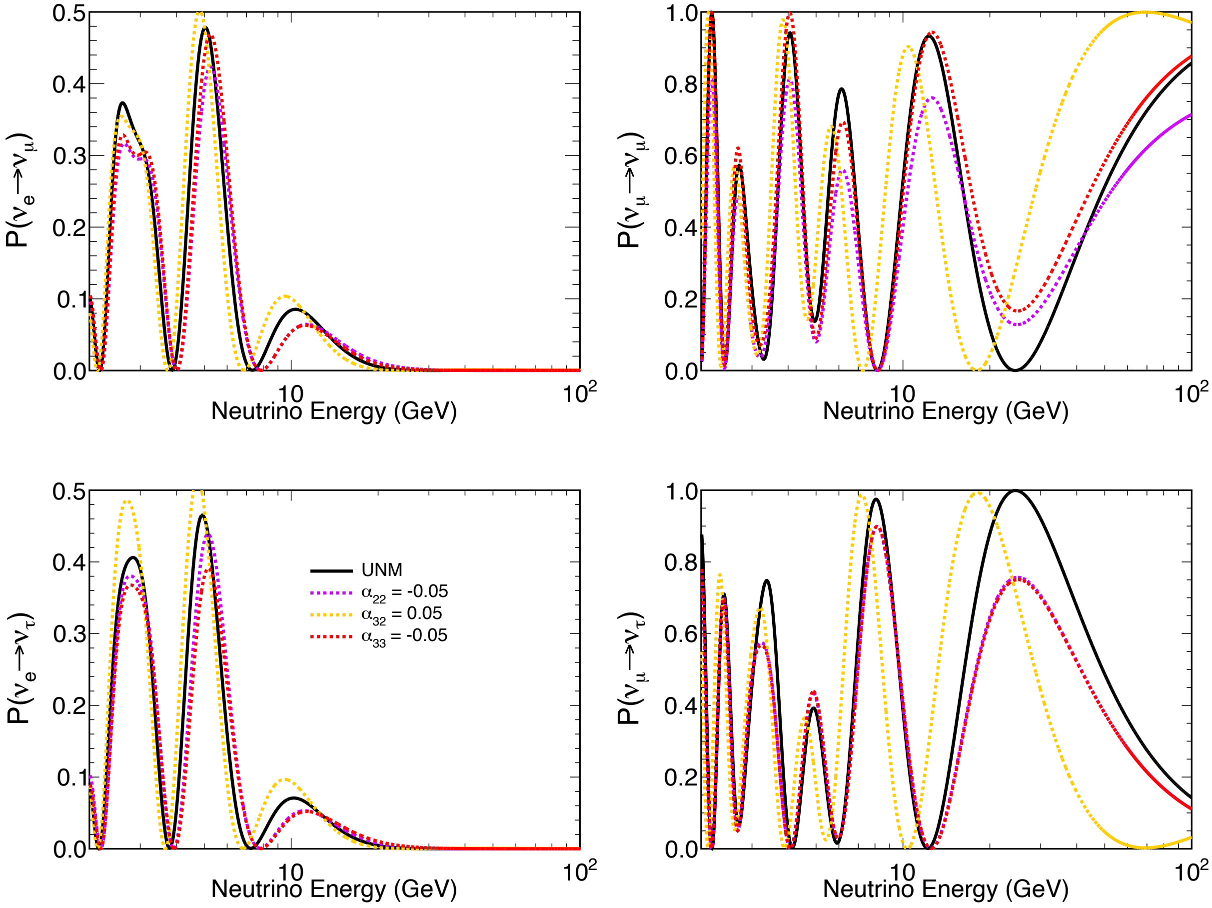

Figure 7.2: The oscillation probability for vertically up-going neutrinos as function of neutrino energy the non unitary parameter α_{22} (purple), α_{33} (red) and α_{32} (orange).

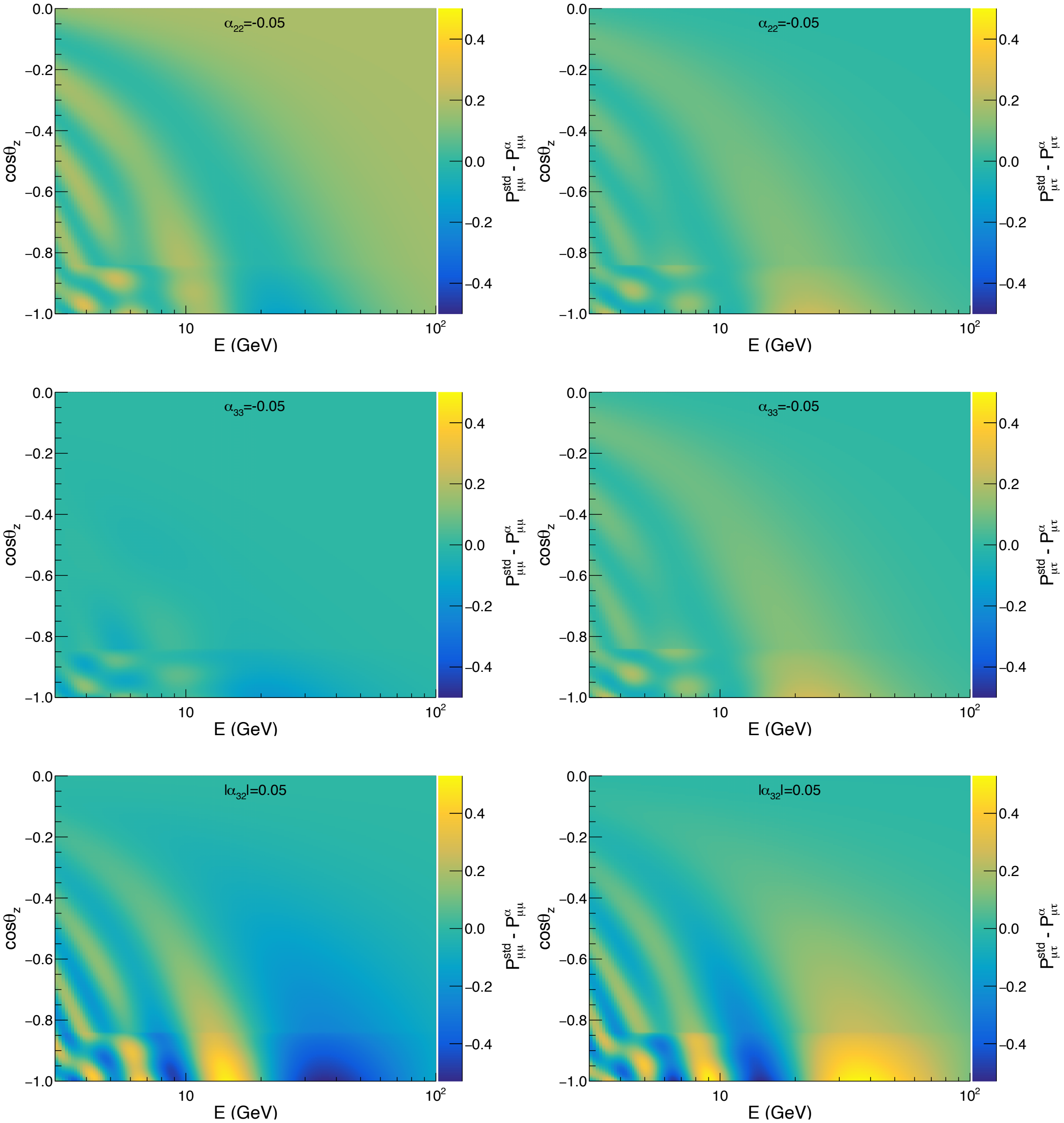

Figure 7.3: The oscillation probability for up-going neutrinos as function of neutrino energy for $\alpha_{22} = -0.05$ (top), $\alpha_{33} = -0.05$(middle), or $|\alpha_{32}| = 0.05$(bottom). The comparison between NUNM and unitarity case in the muon disappearance channel is shown on the left and in the tau appearance channel on the right.

7.2 Pseudo data

The 433 kton-years MC and data sample used in this analysis are described in Chapter 5. In addition a pseudo data set was generated from the MC expectation histograms with the oscillation parameter at nominal values (NuFIT5.0) by incorporating Poisson fluctuations in every bin used in the fit. The pseudo dataset contains in total 5787 events, distributed in the HP Tracks, LP Tracks and Showers classes. Table 7.2 shows the composition of the pseudo dataset that represents the event distribution after fitting the NUNM model to the pseudo-data. While the Figure 7.4 shows the flavour composition of the classes for the best fit.

Event Type	Showers	High Purity Tracks	Low Purity Tracks
ν_e CC + $\bar{\nu}_e$ CC	740	59	89
ν_μ CC + $\bar{\nu}_\mu$ CC	837	1648	1478
ν_τ CC + $\bar{\nu}_\tau$ CC	159	24	20
ν NC + $\bar{\nu}$ NC	325	15	24
atmospheric $\mu + \bar{\mu}$	70	22	276
Total MC	2132	1769	1888
Total Data	2131	1770	1886

Table 7.2: Expected number and composition for the three PID classes for the best fit to the pseudo-data generated from nominal oscillation parameter values.

7.3 Sensitivity on Monte Carlo

The sensitivity to NUNM is evaluated on the asimov set, comparing the χ^2 between the fit with 1 or 2 NUNM parameters non zero and the fit assuming the unitarity hypothesis.

7.3.1 Sensitivity to individual NUNM parameters

The LLR profiles on Monte Carlo for the 3 diagonal α_{ii} and the absolute value of the 3 non-diagonal one α_{ij} are shown in Figure7.5. Both ordering are fitted while the true NO is assumed. Only in the case of α_{32} the difference in sensitivity between IO and NO is

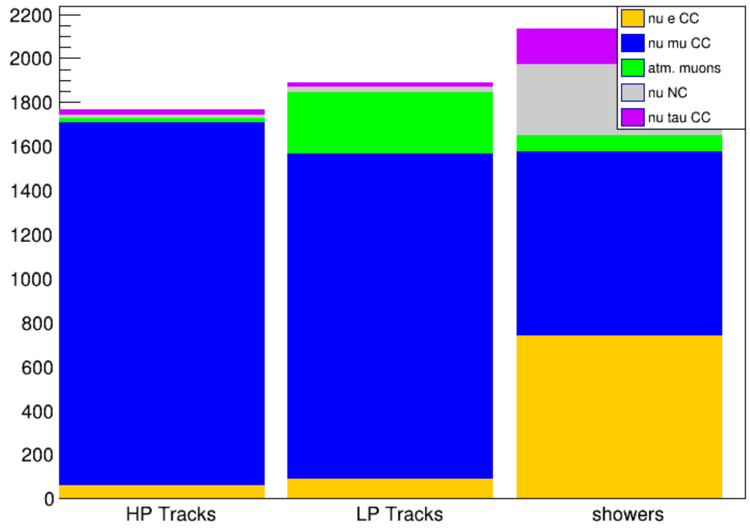

Figure 7.4: Distribution of the neutrino flavours per classes after the the NUNM fit on pseudo data.

significant. The nominal value is always $\alpha_{ij} = 0$ from the definition of α in Section 7.1, therefore the profile reach LLR = 0 at $\alpha_{ij} = 0$. KM3NeT/ORCA is mainly sensitive to α_{22}, α_{33} and $|\alpha_{32}|$.

The sensitivity to α_{22} is higher than α_{33} as expected from the probability versus energy comparison shown in Figure 7.2, because α_{22} has a greater impact on the ν_μ disappearance channel.

The high-scale non-unitarity described in Section 7.1 and in [105] is evaluated on MC only and the sensitivity LLR in 1D are reported in Figure7.6. The LLR profiles for the 3 non-diagonal α_{ij} are shown. Both ordering are fitted while the true is NO and the lowest χ^2 is kept. The nominal value is always $\alpha_{ij} = 0$ from the definition of α in Section 7.1, therefore the profile reach $LLR = 0$ at $\alpha_{ij} = 0$. The profiles look similar to the low-scale however they are not identical. The diagonal parameters do not impact the probabilities when considered alone. They have a visible impact only when combined with a non-diagonal one.

The potential limits from the sensitivity study that could be set by KM3NeT on the low-scale NUNM parameters are reported in Table 7.3 from [107]. The currently least constrained parameter is α_{33}, and data from KM3NeT/ORCA could contribute constraining it

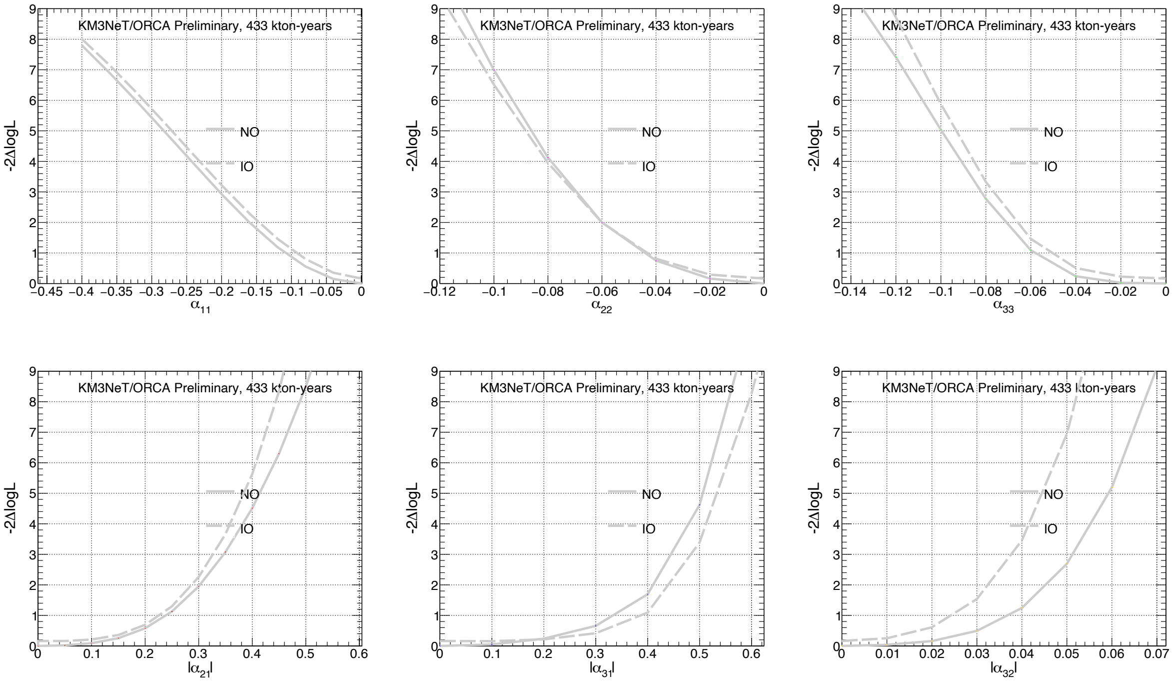

Figure 7.5: The 3 σ sensitivity range in the LLR profiles are shown for the low scale NUNM for the two orderings, NO and IO, with a full and dashed gray line, respectively. On the top the 3 diagonal parameters of the α matrix and on the bottom the 3 absolute value of the non-diagonal parameters of the α matrix are scanned.

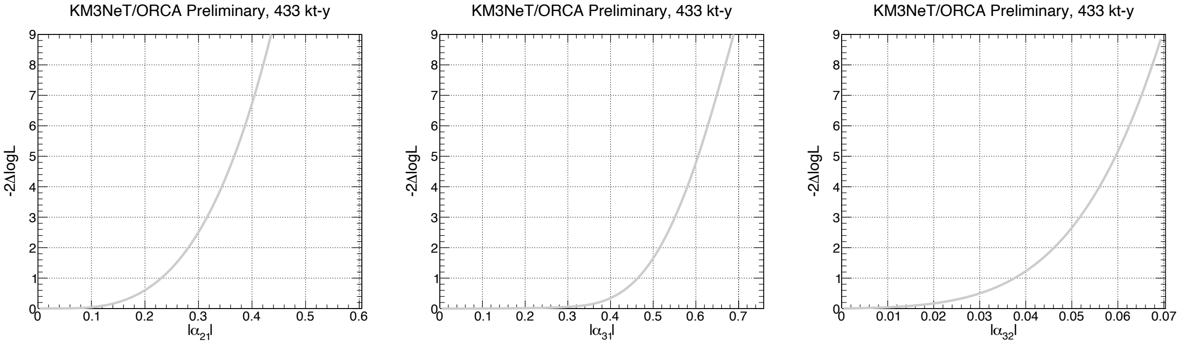

Figure 7.6: The 3 σ sensitivity range from the NUNM high-scale scenario defined in Section 7.1. The LLR is shown with a full a gray line marginalised over the ordering.

further. The present bounds are derived from non-observation of very-short distance oscillation and light sterile neutrino search [119] while the only direct measurement of NUNM parameters are based on data from T2K+NOvA [115] mainly focused on α_{21} and α_{22}.

NUNM par. at 2σ CL	Present Bounds [107]	T2K+NOvA [115] NO(IO)	KM3NeT/ORCA [Sens.] NO(IO)
$\alpha_{33} >$	-0.1	-(-)	-0.09(-0.09)
$\alpha_{22} >$	-0.022	-0.06(-0.06)	-0.08(-0.08)
$\alpha_{11} >$	-0.024	-(-)	-0.24(-0.24)
$\|\alpha_{32}\| <$	0.012	-(-)	0.05(0.04)
$\|\alpha_{31}\| <$	0.069	-(-)	0.48(0.52)
$\|\alpha_{21}\| <$	0.025	0.12(0.13)	0.38(0.33)

Table 7.3: Comparison of sensitivity limits on NUNM parameters with current bounds at the 2σ CL from [107].

The following studies will focus on α_{22}, α_{33} and $|\alpha_{32}|$ as they are the non-unitarity parameters that KM3NeT/ORCA is the most sensitive to.

7.3.2 Sensitivity to pairs of NUNM parameters

The sensitivity contours at the 90% confidence level in 2D are shown in Figure 7.7 for the three parameters, α_{22}, α_{33} and $|\alpha_{32}|$ by testing NO and IO, while the rest of the NUNM parameters are fixed to zero. A correlation is visible in the α_{22}, α_{33} 2D plane as expected from the oscillation probabilities study, where the non-unitarity effect show some degeneracies between the two parameters. Therefore the effect could in future iteration of the analysis be parameterised by a single parameter $\alpha_x = \alpha_{22} = \alpha_{33}$.

7.4 Results on pseudo-data

The pseudo-data is useful to get an intuition of the sensitivity of the current data statistics to a given model, by looking at the error bars in each bin. With increasing statistics the errors shrink and the H0 hypothesis is rejected with a higher significance.

The L/E distributions of the pseudo-data and model for different hypothesis are shown in Figure 7.8, divided by the no-oscillation hypothesis. A 3σ deviation of $\alpha_{33} = -0.13$ to

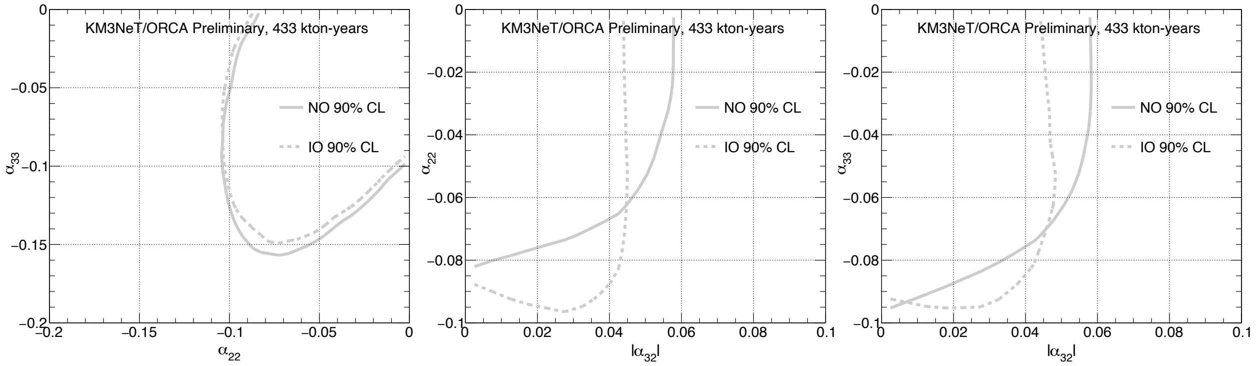

Figure 7.7: The 90% confidence level contours are shown for the two orderings, NO and IO with a gray full and dashed line, respectively. On the left the 2 low diagonal parameters of the α matrix are shown, α_{22} vs $|\alpha_{32}|$ in the middle and α_{33} vs $|\alpha_{32}|$ on the right.

nominal is also shown to illustrate the region in L/E where the sensitivity to this parameter appears. In this case the oscillation dip will be reduced, and most sensitivity will be in the HP track class due to matter effects. Some sensitivity will also come from the LP Tracks and Showers.

Then, fits were performed on the same pseudo-data with one parameter free at a time. The effect of the fits are fully compatible with nominal.

The LLR is between the fit using the model with a fixed value of α_{ij} and the best-fit with the corresponding α_{ij} parameter free in the physical region. The LLR profiles from the fit marginalised over the orderings on the pseudo-data are shown in Figure 7.9. All profiles show a compatibility with 0 below the level of 1.4 σ.

As a second step a fit on pseudo-data is run with α_{22}, α_{33}, $|\alpha_{32}|$ and the corresponding phase ϕ_{32} free. The pulls of the nuisance parameters are reported in Table 7.9 with the corresponding 1σ errors from the MINOS procedure. They are also consistent with their central values as expected. The measured parameters at the best fit point are reported in the Table 7.8 with the corresponding 1σ post-fit errors from the MINOS procedure, all consistent with 0. The fit is run with α_{22}, α_{33}, $|\alpha_{32}|$ and the corresponding phase ϕ_{32} free. All values from the fit are consistent with the unitarity hyposthesis as expected.

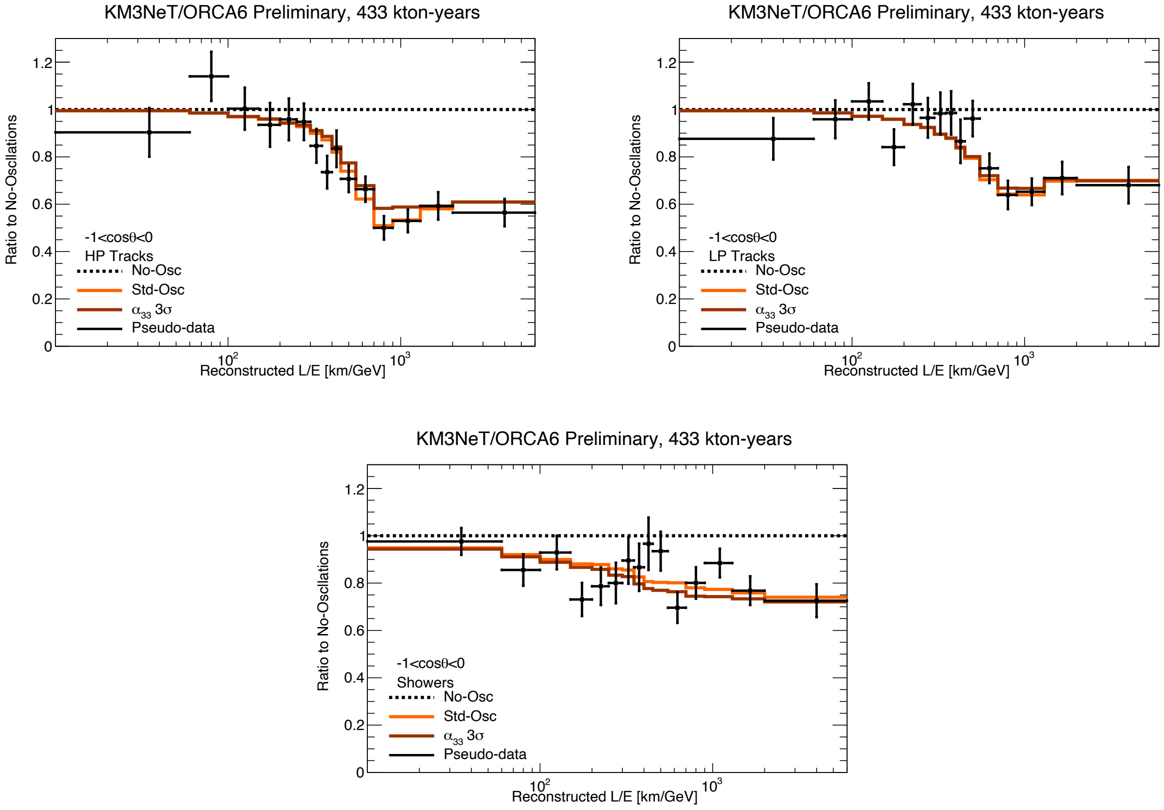

Figure 7.8: The L/E distributions of pseudo-data and MC for different hypotheses are shown, divided by the no-oscillation hypothesis. On the top left the High Purity Tracks class, on the top right the Low Purity Tracks class is represented while on the lowest part the Shower class is shown. The result of the fit with fixed oscillation parameters to nominal values is in orange, α_{33} fixed 3σ away from nominal is in brown and pseudo-data point is in black with the corresponding error bars.

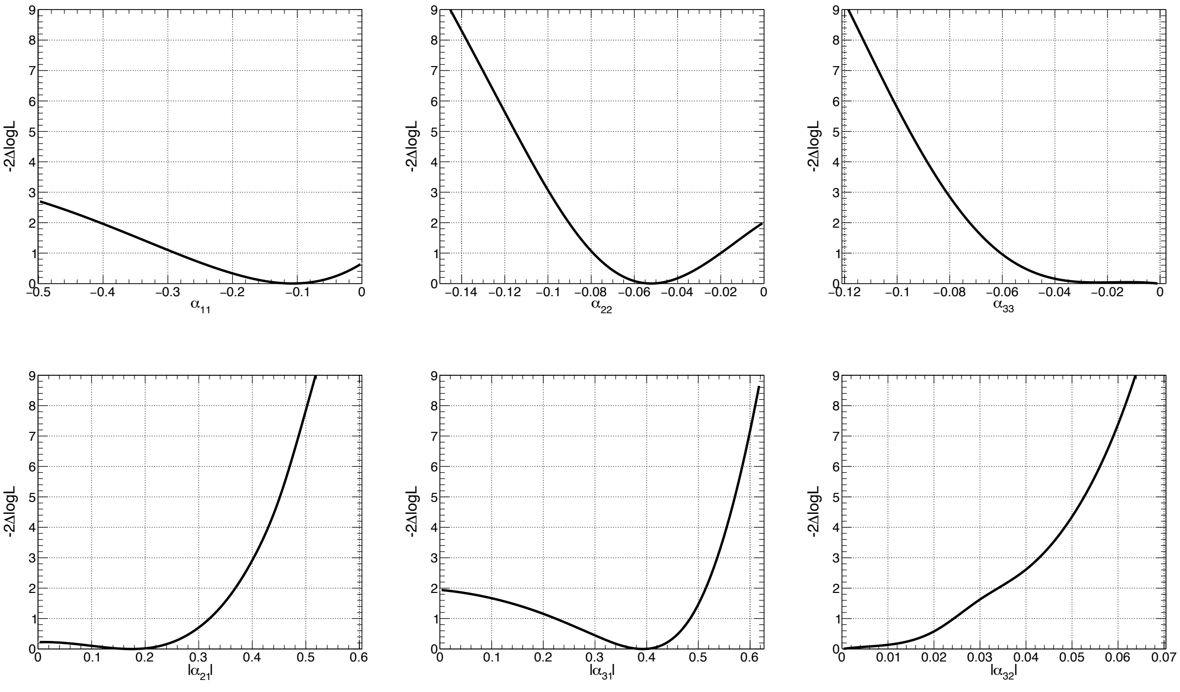

Figure 7.9: The LLR profiles from pseudo-data are marginalised over the ordering. On the top the 3 diagonal parameters of the α matrix and on the bottom the 3 absolute value of the non-diagonal ones are scanned.

Systematic uncertainty	BF $\pm 1\sigma$
θ_{23}	$44.8^{+7.6}_{-6.7}$
Δm^2_{31} [10^{-3} GeV^2]	$-1.99^{+0.24}_{-0.28}$
Spectral Index	$0.04^{+0.03}_{-0.03}$
$\nu_{\text{hor}}/\nu_{\text{ver}}$	$-0.002^{+0.01}_{-0.02}$
$\nu_\mu/\bar{\nu}_\mu$	$-0.007^{+0.04}_{-0.05}$
$\nu_e/\bar{\nu}_e$	$-0.004^{+0.07}_{-0.07}$
ν_μ/ν_e	$-0.001^{+0.02}_{-0.07}$
High-energy Light Sim.	$1.04^{+0.28}_{-0.26}$
Energy Scale	$0.99^{+0.09}_{-0.07}$
Overall Norm.	$1.03^{+0.19}_{-0.16}$
Track Norm.	$1.03^{+0.05}_{-0.04}$
Shower Norm.	$1.05^{+0.09}_{-0.08}$
Muon Norm.	$1.76^{+0.67}_{-0.51}$
S_{NC}	$1.04^{+0.29}_{-0.19}$
S_τ	$1.08^{+0.19}_{-0.18}$

Table 7.4: All systematic uncertainties for pseudo-data and their best fit values along with their post-fit 1σ uncertainties given by the MINOS errors.

Measured NUNM parameters	Best fit $\pm 1\sigma$
α_{22}	$-0.07^{+0.05}_{-0.05}$
α_{33}	$-0.02^{+0.05}_{-0.05}$
$\|\alpha_{32}\|$	$0.01^{+0.03}_{-0.01}$
$\phi_{32}[^\circ]$	-53

Table 7.5: Results for pseudo-data and their best fit values along with their 1σ uncertainties given by the MINOS errors.

7.5 Study of the systematics on pseudo-data

The study of the impact of the nuisance parameters on the pseudo-data is shown in Figure 7.10. The significance of the impact of the nuisance parameters on the parameter of interest written on the bottom axis is shown in colored bars, with σ_α calculated as the 1σ post-fit uncertainty on the parameter of interest. The pulls of the nuisance parameters are shown in black with the error σ calculated as the ratio between the post-fit and pre-fit uncertainties. The pre-fit uncertainty is defined as the prior previously reported for the nuisance parameters that were constrained, and is set to 1 for the unconstrained ones. The pre-fit uncertainty reflects the knowledge on the nuisance parameter before the fit. The post-fit uncertainty is the 1σ error on the corresponding nuisance parameter, computed from the profile after the fit. The impact of the nuisance parameters on α_{33} are small compared to α_{11} or α_{21}. The impact of the normalisations on α_{22} and α_{11} is the largest effect. Except for the muon norm that reaches up to 2.5σ the pulls are within 2σ from their central values in all cases. The effect of fixing a single systematic on the 2D contours for the main 2D combination of the parameters of interest is shown in Figure 7.11. The impact is bigger in the α_{22} vs α_{33} space, where the overall normalisation and the shower normalisation have a sizeable effect. The CC tau normalisation is also having an impact on the α_{22} vs α_{32} contours. Except for those, the effect of the systematics on the sensitivity is limited in the 2D plane as well.

The correlation between the nuisance parameters in the case of free α_{33} is shown in Figure 7.12. A small anti-correlation is visible between α_{33} and θ_{23} or Δm_{31} that is also visible in the Figure7.10. In other words some of the NUNM parameter α_{33} effect is equivalent to a smaller θ_{23} mixing.

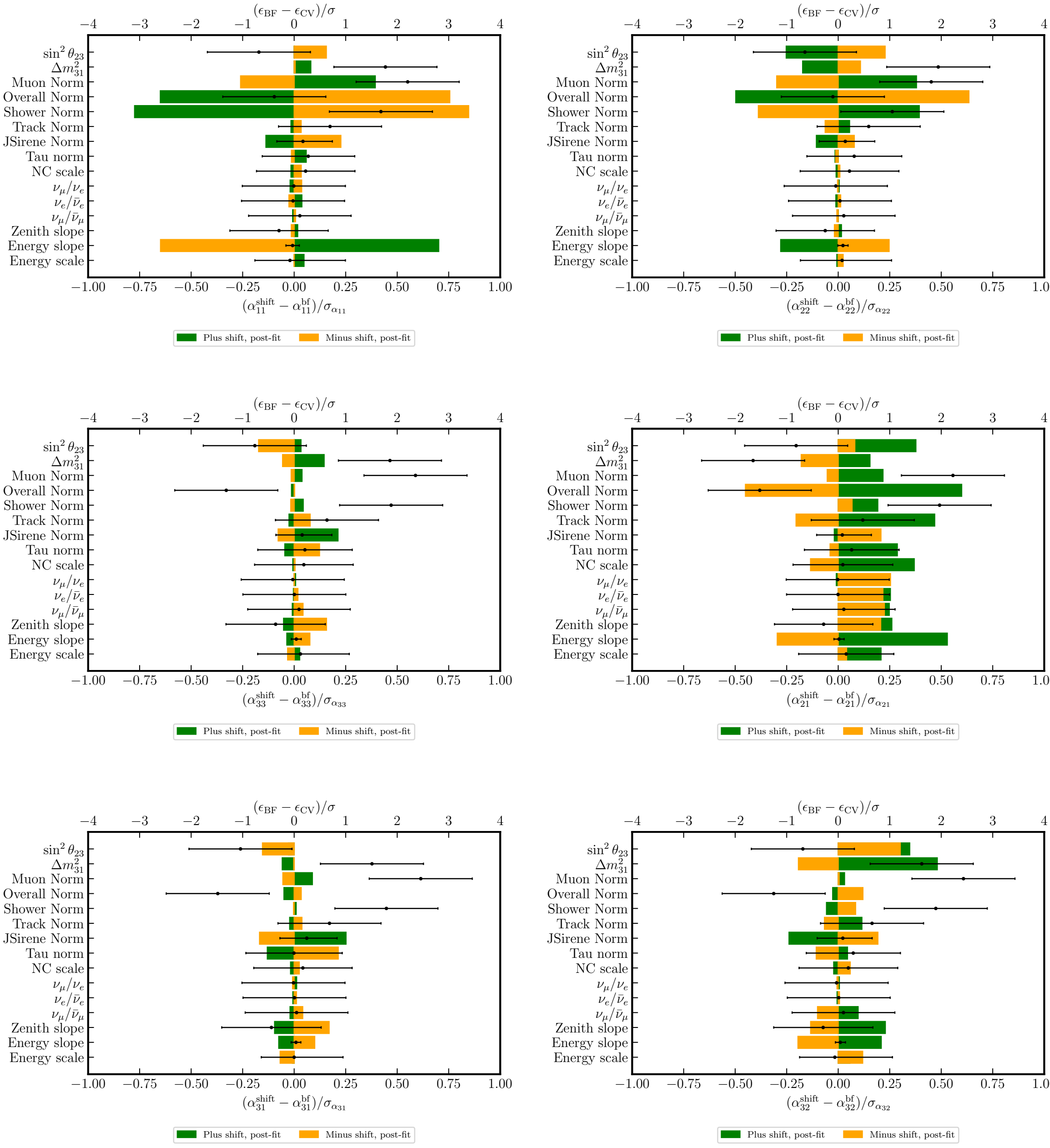

Figure 7.10: The significance on pseudo-data of the impact of the nuisance parameters on the parameter of interest written on the bottom axis is shown in colored bars. The pulls of the nuisance parameters are shown in blacks with the errors calculated as the ratio between the post-fit and pre-fit uncertainties.

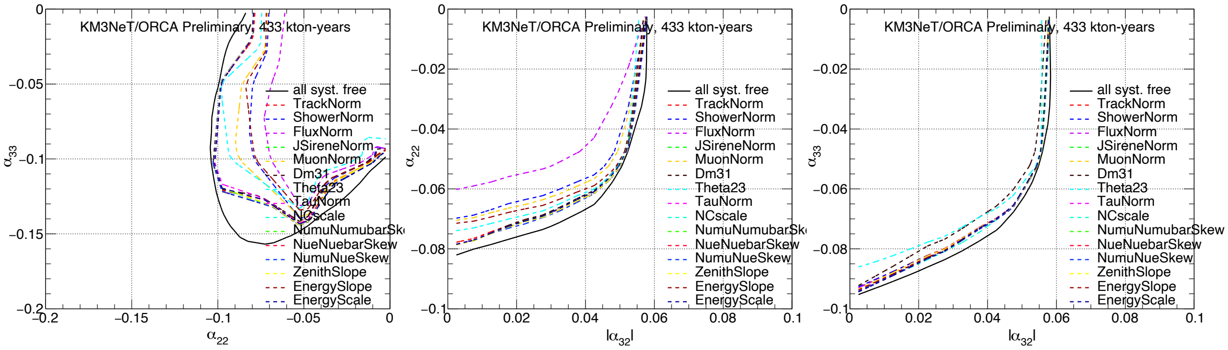

Figure 7.11: Impact of each single systematics on the sensitivity 90% CL contours for 2D combination of the three main parameters α_{22}, α_{33} and α_{32}.

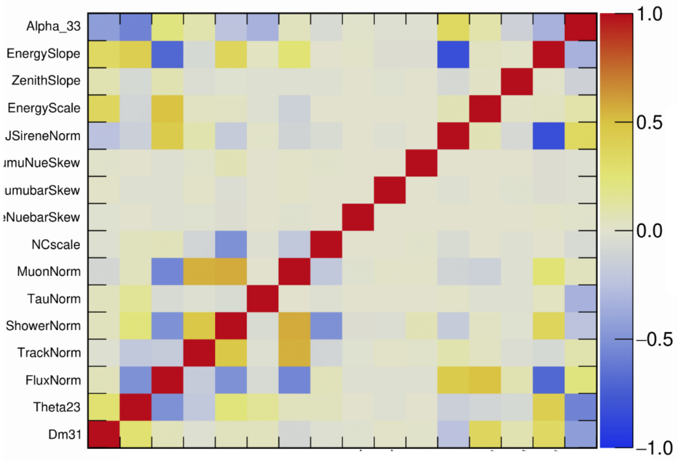

Figure 7.12: The correlation matrix of the parameters involved when fitting the Asimov set is shown including a free parameter α_{33}.

7.6 Results on data

The analysis procedures described in Chapter 5, have been applied to fit the model described in Section 7.1 to the data set described in Chapter 5.

7.6.1 Measurement of $(1+\alpha_{33})^2$ in the $V_{NC}=0$ case

The effect of $(1+\alpha_{33})^2$ described in Equation 7.15 when ignoring NC matter potential ($V_{NC}=0$), sometimes referred to as H-earth scenario because it is equivalent to $n_n=0$, is a possible reduction of the ν_τ appearance, affecting both CC and NC ν_τ events as described in Equation 7.13. Therefore in that specific case which does not account for all matter effects, $(1+\alpha_{33})^2$ is equivalent to a ν_τ normalisation. The α_{33} measurement including all matter effects is reported in the next Section. The measurement of $(1+\alpha_{33})^2$ has been performed using two different models. First, the CC tau neutrino cross section scale factor S_τ is included as a nuisance parameter and fitted with a prior of 20% as for the recent measurement of the atmospheric oscillation parameters with KM3NeT/ORCA6 [74]. In addition, the special case of $S_\tau=1$ is considered in order to compare to the results reported by the IceCube Collaboration [99]. The best-fit value for α_{33}^2 when S_τ is treated as a nuisance parameter is $0.69^{+0.41}_{-0.33}$ ($0.68^{+0.36}_{-0.32}$, for $S_\tau=1$), corresponding to 131 ν_τ CC interactions. The profiled log-likelihood ratio is presented in Figure 7.13 showing that the difference between both models is marginal at the best-fit and mostly visible for larger values of the non-unitarity parameter α_{33}^2. Due to the high computational cost, the FC correction is only applied for the case where S_τ is fitted. As for the measurement of S_τ, the FC CL is significantly reduced compared to the Wilks one for low values of α_{33}^2. Since the best fit value of α_{33}^2 is higher than for S_τ, the correction mostly affects higher confidence intervals. The FC correction for the 68% (90%) CL is [0.32, 1.12] ([0.21, 1.50]) and the p-value for $\alpha_{33}^2=0$, i.e. no tau appearance is 0.01.

Both models agree with unitarity, i.e. $(1+\alpha_{33})^2=1$ within a 1σ level (0.60 σ and 0.78 σ), while no tau-appearance is disfavoured with a 2.1σ significance in both cases. This is also shown in Figure 7.13 right, which presents the observed L/E distribution compared to that of the best fit and models with $(1+\alpha_{33})^2=0$ and $(1+\alpha_{33})^2=1$ for the case that includes S_τ as a nuisance parameter. In this case, the excess in data compared to no tau-appearance is more prominent than in the case of measuring S_τ since the signal includes the neutral current tau neutrino interactions. Hence, the difference between models with $\alpha_{33}^2>0$ and the no tau-appearance model is larger, leading to a better rejection power of the latter, also seen in Figure 7.13.

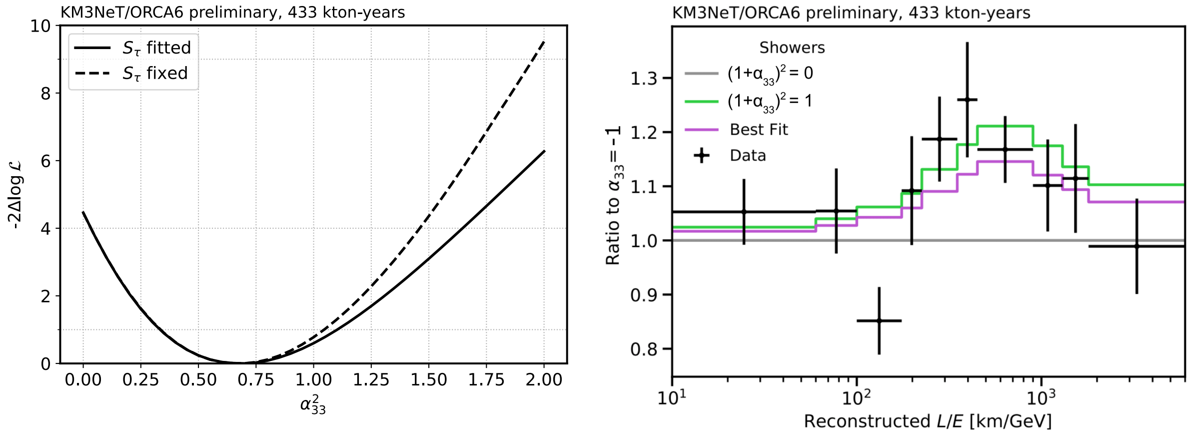

Figure 7.13: Assuming $V_{NC} = 0$: **Left:** Measured log-likelihood profile for the models probing non-unitarity. **Right:** Measured L/E distribution for the shower class with best-fit model and a model with nominal tau normalisation $(1 + \alpha_{33})^2 = 1$ with respect to no tau-appearance for the model including S_τ as a nuisance parameter.

The differences between the best-fit values for $(1 + \alpha_{33})^2$ as well as for the nuisance parameters are negligible for both models. This is due to the fact that the fitted value of S_τ is 0.99 which is close to the nominal value. Therefore, impacts and pulls are presented in Figure 7.17 only for the case including S_τ.

Since the fitted value of S_τ is close to the expectation, the pull for this parameter is small. However, this parameter has the largest impact on $(1 + \alpha_{33})^2$ since it is correlated with S_τ. Fixing S_τ $\pm 1\sigma$ leads to a shift of $(1 + \alpha_{33})^2$ by about $\pm\frac{1}{3}\sigma$.

Overall, the pulls of the nuisance parameters are compatible with what is obtained from the dedicated measurement of S_τ, except for the Energy Scale which has the opposite sign. Similarly to what observed for S_τ, the normalisations have the largest impact. However, the most important ones are HE Light Simulation, Shower Normalisation, and Overall Normalisation whereas the impact of the NC Normalisation S_{NC} is reduced. The two flux shape systematics have comparable effects on the fit results for $(1 + \alpha_{33})^2$, while the composition ratio uncertainties are still negligible.

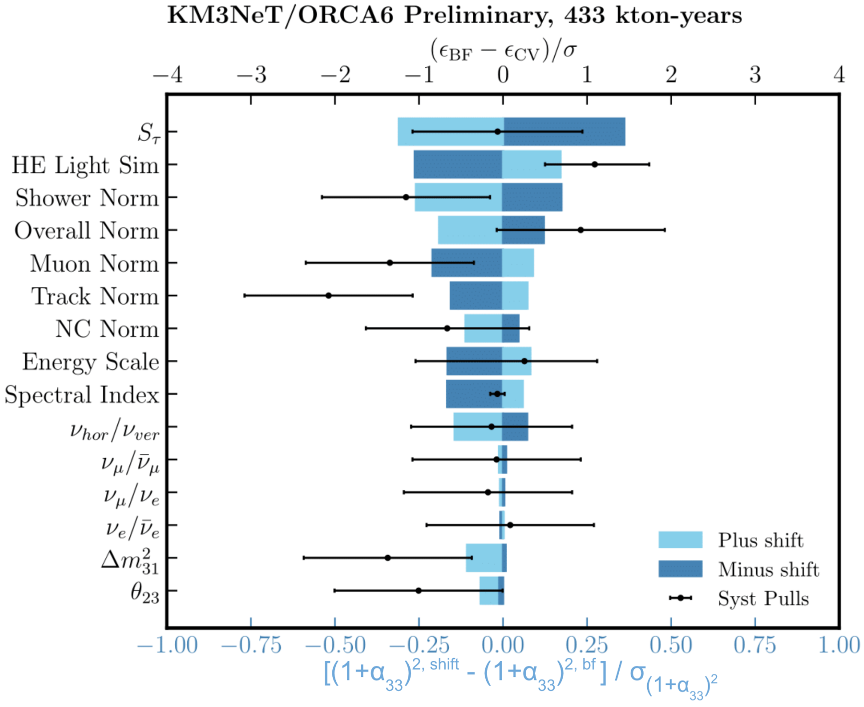

Figure 7.14: Impact (blue bars, lower x-axis) and pulls (black markers, upper x-axis) of the systematic uncertainties considered in the models probing non-unitarity assuming $V_{NC} = 0$

7.6.2 Measurements of individual NUNM parameters with full matter effects

The measured LLR profiles for the 3 diagonal α_{ii} and the absolute value of the 3 non-diagonal one α_{ij} are shown in Figure 7.15. The profiles are compared to the current bounds from [107] at the 2σ CL. The α_{33} limit is improved by the KM3NeT/ORCA measurement. Due to statistical fluctuations, the data prefers beyond maximal mixing in θ_{23} therefore the rejection of $\alpha_{33} < 0$ is enhanced. The data prefers a non-zero value for $\alpha_{22} = -0.04$ with a non-significant rejection of the nominal case at the level of 1.4 σ. The α_{11} fit prefers the non-physical region, therefore the KM3NeT/ORCA rejection is enhanced in the physical region $\alpha_{11} \leq 0$. The other parameters are close the nominal expectation.

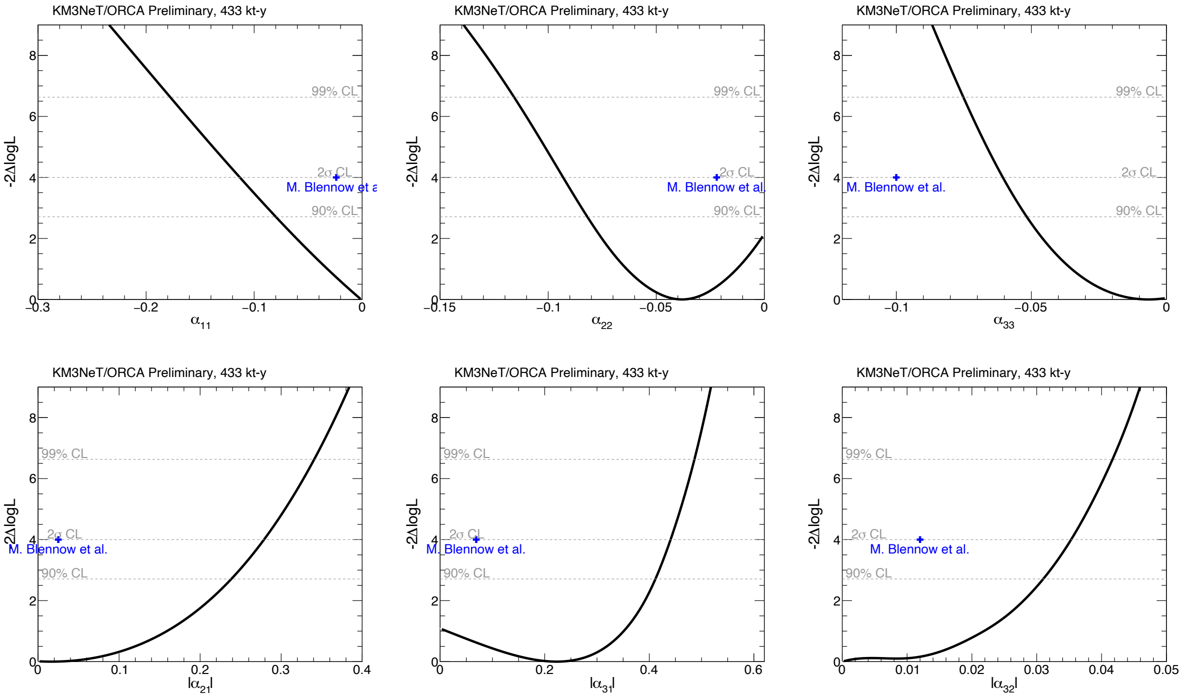

Figure 7.15: The measured 3 σ range in the LLR are shown for the two orderings. On the top the 3 diagonal parameters of the α matrix and on the bottom the 3 absolute value of the non-diagonal ones are scanned.

As the limit on α_{33} was improved by a factor 2 the result of the fit are given for that specific case in more details, including Feldman-Cousin (FC) corrections. This work was performed in collaboration with Nicole Geisselbrecht at ECAP and Chiara Lastoria in LPC Caen. The result for α_{33} only are summarised in Table 7.6, which respectively show the best-fit values for the parameters of interest, and the best-fit values for the nuisance parameters.

For the measurement of α_{33} only, the tau neutrino cross section scale factor S_τ is included as a nuisance parameter and assigned a 20% uncertainty. The best-fit value is $0.99^{+0.03}_{-0.02}$ corresponding to 170^{+35}_{-33} ν_τ CC and a total of 325^{+76}_{-76} NC events. The profiled log-likelihood ratio is presented in Figure 7.16. On the left hand side, it is compared to a model with $V_{\rm NC} = 0$ and $S_\tau = 1$ for which the best-fit value is $0.83^{+0.20}_{-0.25}$. The latter result can be compared to the results published by the IceCube collaboration [99] following the physics interpretation from Section 7.1, where the CC+NC tau normalisation corresponds to α_{33}^2 with $V_{\rm NC} = 0$. The difference in the sensitivities for both models originates from the fact that when $V_{\rm NC} = 0$, α_{33} affects only the tau appearance probability, as shown in Figure 7.1. If on the other hand $V_{\rm NC} \neq 0$, α_{33} additionally affects other oscillation channels including ν_μ disappearance leading to better constraints.

The FC correction is shown on the right side of Figure 7.16. Due to the high computational cost, it is only applied for the case where S_τ is fitted and $V_{\rm NC}$ is included. The results are similar to Wilks' theorem except for values of α_{33} that are close to 0, which suggests that there is a physical boundary. In fact, $\alpha_{33} > 0$ is an unphysical region for which the sum of oscillation probabilities would exceed 1. Overall, the 68% confidence interval is almost unaffected whereas the 2σ confidence interval is slightly reduced and is found to be [-0.05, 0.04]. The best fit is consistent with unitarity, i.e. $\alpha_{33} = 0$ (p-value of

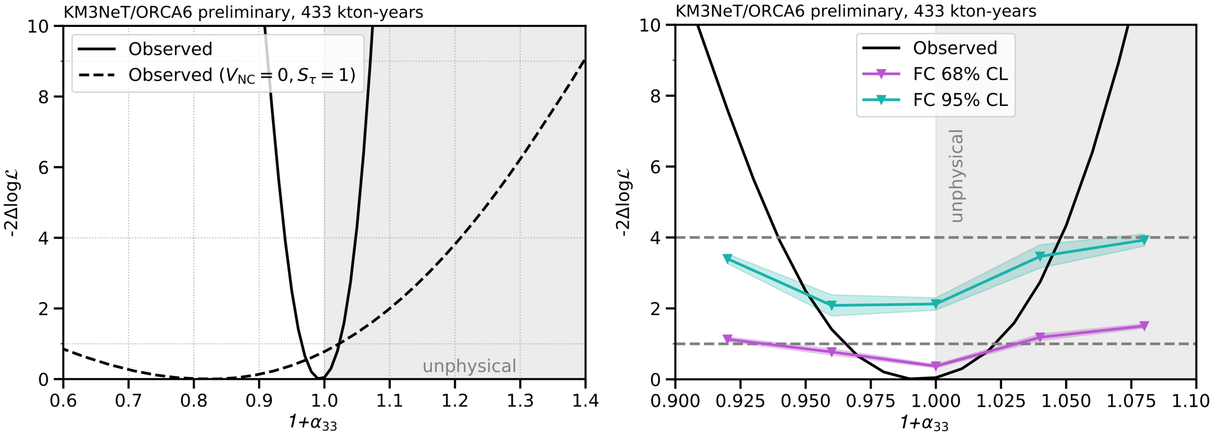

Figure 7.16: Measured log-likelihood profile for the model probing non-unitarity. **Left:** Comparison with a model with $V_{\rm NC} = 0$ and $S_\tau = 1$. **Right:** FC correction.

Systematic uncertainty	α_{33} $\epsilon \pm 1\sigma$
θ_{23}	$45.8^{+3.80}_{-3.82}$
Δm^2_{31} $[10^{-3}\,\mathrm{GeV}^2]$	$2.18^{+0.19}_{-0.35}$
δ_γ	$-0.02^{+0.03}_{-0.03}$
δ_θ	$-0.005^{+0.02}_{-0.02}$
$s_{\mu\bar{\mu}}$	$-0.004^{+0.05}_{-0.05}$
$s_{e\bar{e}}$	$0.006^{+0.07}_{-0.07}$
$s_{\mu e}$	$-0.004^{+0.02}_{-0.02}$
f_{NC}	$0.86^{+0.20}_{-0.20}$
E_s	$1.03^{+0.11}_{-0.08}$
f_{HE}	$1.59^{+0.33}_{-0.30}$
f_{all}	$1.11^{+0.17}_{-0.11}$
f_{HPT}	$0.92^{+0.04}_{-0.04}$
f_{S}	$0.92^{+0.06}_{-0.06}$
f_μ	$0.51^{+0.40}_{-0.36}$
S_τ	$0.92^{+0.19}_{-0.18}$

Table 7.6: All systematic uncertainties and their best-fit values along with their 1σ post-fit uncertainties.

$68.01 \pm 1.51\%$), also when neglecting the V_{NC} potential and fixing the ν_τ CC cross section (0.6 σ according to Wilks' theorem).

Impacts and pulls for the measurement of α_{33} are presented in Figure 7.17. Overall, the pulls of the nuisance parameters are comparable with what is obtained from the measurement of S_τ, except for E_s which has the opposite sign and a larger pull for Δm^2_{31}. The nuisance parameter with the largest impact on α_{33} is clearly θ_{23}. This can be explained by the fact that both parameters affect the ν_μ disappearance. Additionally, α_{33} has an influence on the tau appearance channel which can partly be compensated by S_τ leading to a non-negligible impact of this parameter. Apart from Δm^2_{31} and f_{S}, the remaining nuisance parameters don't have a major impact on the result.

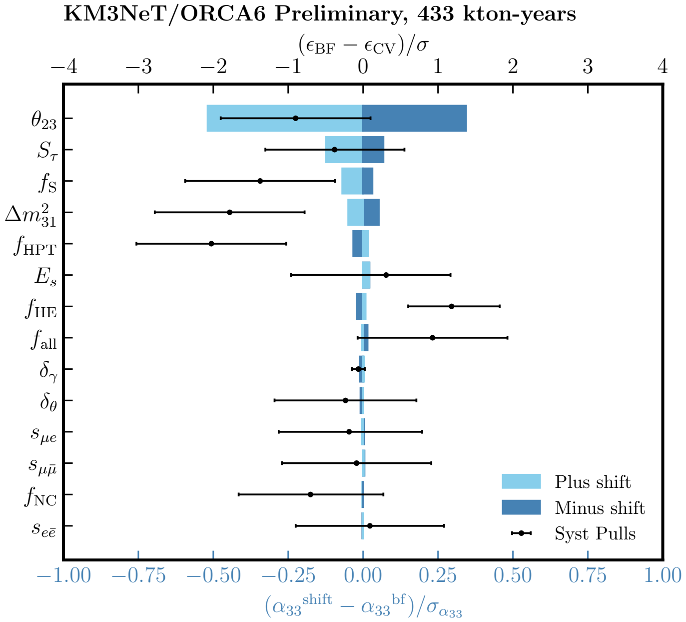

Figure 7.17: Impact (blue bars, lower x-axis) and pulls (black markers, upper x-axis) of the systematic uncertainties considered in the models probing non-unitarity.

The observed limits from KM3NeT/ORCA on the NUNM parameters are reported in Table 7.7. The present bound are derived from non-observation of very-short distance oscillation and light sterile neutrino search in [107].

NUNM par.	Present Bounds	KM3NeT/ORCA Data
$\alpha_{33} >$	-0.1	-0.05 (w. FC)
$\alpha_{22} >$	-0.022	-0.09
$\alpha_{11} >$	-0.024	-0.11
$\lvert\alpha_{32}\rvert <$	0.012	0.03
$\lvert\alpha_{31}\rvert <$	0.069	0.44
$\lvert\alpha_{21}\rvert <$	0.025	0.28

Table 7.7: Comparison of KM3NeT/ORCA limits on NUNM parameters with current bounds at 2σ CL from [107].

7.6.3 Measurements of pairs of NUNM parameters

The measured contours at the 90% confidence level are shown in Figure 7.18 for 2D combinations of the parameters α_{22} and α_{33} with $|\alpha_{32}|$, by testing NO and IO, while the rest of the NUNM parameters are fixed to zero. The contours agree with the unitarity hypothesis at the level of ≈ 2 units in $2\Delta \ln \mathcal{L}$.

The fit in Figure 7.19 with α_{22} and α_{33} free finds a minimum 8.3 units in $2\Delta \ln \mathcal{L}$ away from the unitarity scenario at coordinates (0,0). As observed in the sensitivity study a correlation between the two diagonal parameters is observed. Therefore a projection in the orthogonal plane of α_{22} and α_{33} is shown in Figure 7.20. It illustrates the correlation between the parameters and the deviation that appears strictly in the sum $\alpha_{22}+\alpha_{33}$. Later it should be possible to use a single parameter to test the same effect $\alpha_x = \alpha_{22} = \alpha_{33}$. It is currently the only measurement of low-scale non-unitarity from earth-crossing neutrinos with more than one parameter free.

The following results report on the investigation performed on the best fit with α_{22} and α_{33} free. The measured values of the physics parameters are given in the Table 7.8.

The systematics Table 7.9 is providing the information on the fit (α_{22} and α_{33} free)

Measured NUNM parameters	Best fit $\pm 1\sigma$
α_{22}	$-0.11^{+0.03}_{-0.03}$
α_{33}	$-0.12^{+0.05}_{-0.05}$

Table 7.8: Data best fit values along with their 1σ uncertainties.

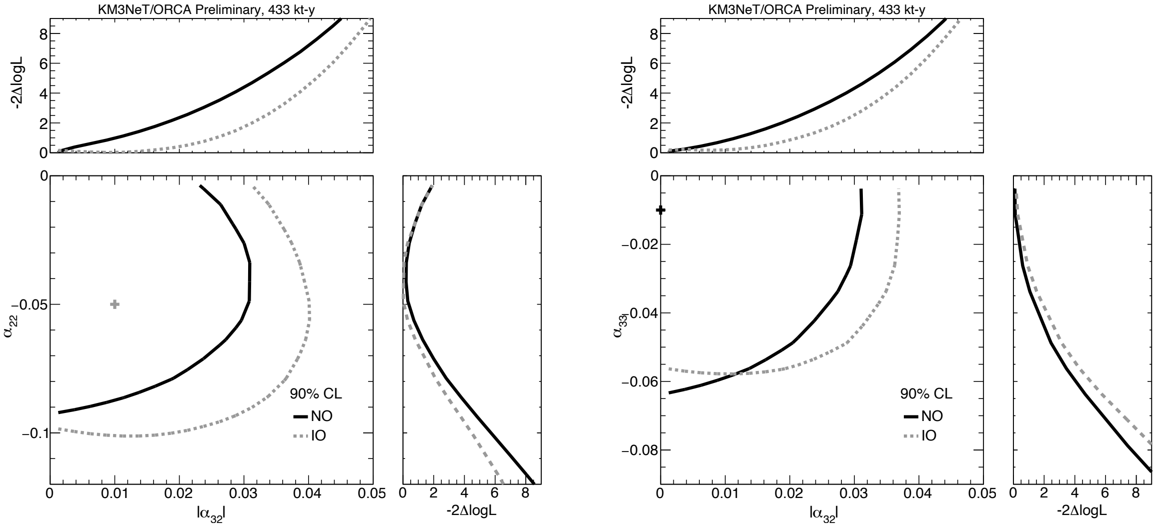

Figure 7.18: The 90% confidence level contours are shown for the two orderings, NO and IO with a gray full and dashed line, respectively. On the left α_{22} vs $|\alpha_{32}|$ contours are shown and α_{33} vs $|\alpha_{32}|$ on the right. The cross indicates the BF point, the color of the cross indicate NO/IO.

result for all systematics involved with the 1σ error obtained from the LLR profile. An observed correlation with the overall normalisation is discussed in Appendix A.

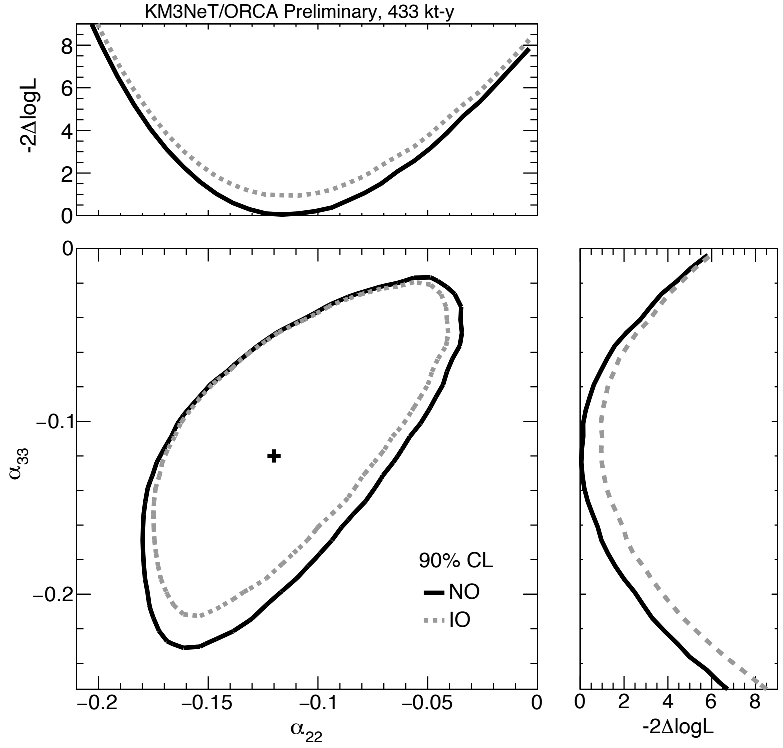

Figure 7.19: The 90% confidence level contours are shown for the two orderings, NO and IO with a gray full and dashed line, respectively. The 2 diagonal parameters α_{22} and α_{33} are combined in the fit. The cross indicates the BF point, the color of the cross indicate NO/IO.

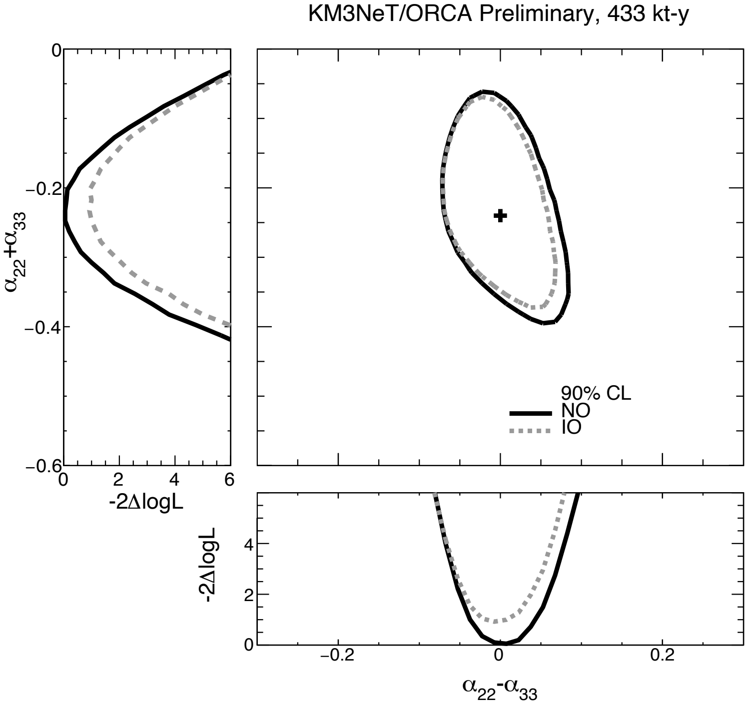

Figure 7.20: The 90% confidence level contours are shown for the two orderings, NO and IO with a gray full and dashed line, respectively. The combination of the 2 orthogonal parameters α_{22} + α_{33} and α_{22} - α_{33} is used for the fit.

Systematic uncertainty	BF $\pm 1\sigma$
θ_{23}	$46.2^{+4.85}_{-5.06}$
Δm^2_{31} [$10^{-3}\,\mathrm{GeV}^2$]	$2.06^{+0.25}_{-0.25}$
Spectral Index	$0.01^{+0.03}_{-0.03}$
$\nu_{\mathrm{hor}}/\nu_{\mathrm{ver}}$	$0.004^{+0.02}_{-0.02}$
$\nu_\mu/\bar{\nu}_\mu$	$0.0007^{+0.05}_{-0.05}$
$\nu_e/\bar{\nu}_e$	$0.002^{+0.07}_{-0.07}$
ν_μ/ν_e	$-0.002^{+0.02}_{-0.02}$
High-energy Light Sim.	$1.54^{+0.32}_{-0.29}$
Energy Scale	$0.98^{+0.11}_{-0.08}$
Overall Norm.	$1.47^{+0.23}_{-0.20}$
Track Norm.	$0.91^{+0.04}_{-0.04}$
Shower Norm.	$0.80^{+0.06}_{-0.06}$
Muon Norm.	$0.14^{+0.31}_{-0.14}$
S_{NC}	$0.91^{+0.19}_{-0.19}$
S_τ	$0.99^{+0.19}_{-0.19}$

Table 7.9: All systematic uncertainties for data and their best fit (with α_{22} and α_{33} free) values along with their post-fit 1σ uncertainties given by the profiles.

7.6.4 FC study with the (α_{22}, α_{33}) pair

The distribution of the $-2\Delta\ln\mathcal{L}$ in Figure 7.21 is based on 1000 pseudo-experiment generated by applying Poisson fluctuations to every bins from the Asimov set without NUNM signal. The systematics' central values are fluctuated according to a gaussian with the size of the gaussian prior used in the fit. The difference in likelihood between the fit with $(\alpha_{22}, \alpha_{33})$ free and $(\alpha_{22}, \alpha_{33}) = (0, 0)$ fixed is shown in order to compute the significance from the FC method and verify the validity of the wilks' theorem. The blue histogram shows the PEs distribution, while the full blue vertical line is the 2σ significance if the wilks' theorem is valid and in dotted blue the 2σ from the FC method. The wilks' theorem in that case appears to be conservative and the black line that represents the $-2\Delta\ln\mathcal{L} = 8.3$ observed in data with 9 out of 1000 PEs falling above the observed $-2\Delta\ln\mathcal{L}$ therefore giving a significance of 2.6σ and a p-value of 0.9%.

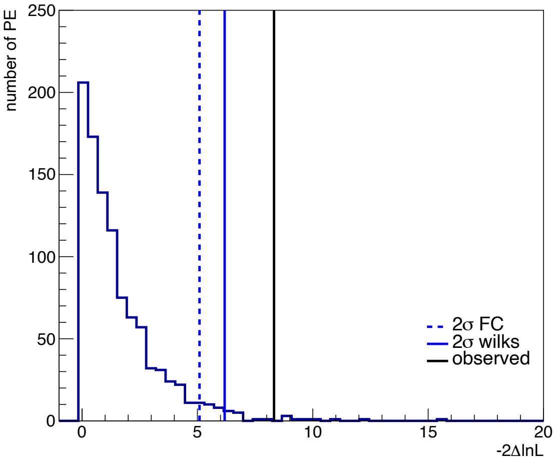

Figure 7.21: The distribution of the $-2\Delta\ln\mathcal{L}$ when using 1000 pseudo-experiment and fit with the UNM and NUNM hypothesis. The blue histogram shows the PEs distribution, the full blue vertical line is the 2σ significance if the wilks' theorem is valid and in dotted blue the 2σ from the FC method. The black line represents the $-2\Delta\ln\mathcal{L}$ obtained in data.

The Figure 7.22 illustrates the comparison for all PEs between the fitted α and the true value at 0 chosen in the Asimov set. It shows how likely it is to get the observed value in data when fluctuating the bin content. It confirms that the values obtained in Data are unlikely to be statistical fluctuations but it is not fully rejected.

In addition the Figure 7.23 illustrates the distribution for all PEs of the fitted sum and difference of the α_{22} and α_{33} compared to the true value. Only the sum is significantly

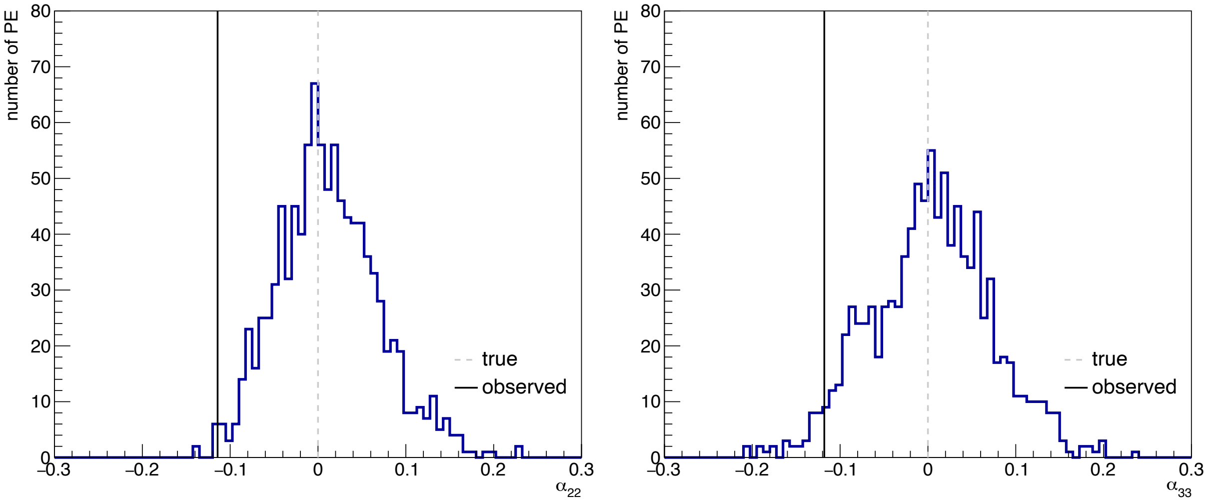

Figure 7.22: The comparison for all PEs between the fitted α_{22} on the left, α_{33} on the right, and the true value in dotted gray. The black line represents the value observed in data.

deviating from the expected fitted values around zero. It appear again that the two diagonal parameters are correlated.

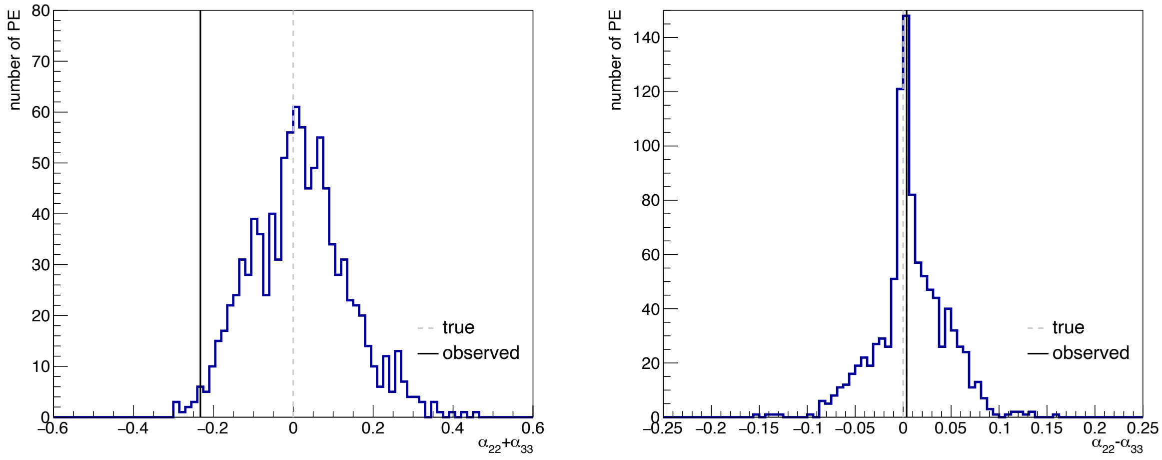

Figure 7.23: The comparison for all PEs between the fitted sum (left) and difference (right) between α_{22} and α_{33} with respect to the true value in dotted gray. The black line represents the value observed in data.

7.7 Conclusion

The work on the 2 years of stable data taken with 5% of the full instrumented volume in the KM3NeT/ORCA6 configuration permitted a robust understanding of the data and simulations. It led to the precise measurement of the oscillation parameters with competitive precision. It allows to perform searches that further test the neutrino oscillations and the hypothesis of unitarity, to improve the knowledge on the generation of the neutrino mass. The NUNM model is implemented in [18] and was tested in order to precisely reproduce the effect of the 1-sterile neutrino model. The fit was tested on pseudo-data, the 1σ uncertainties of the measured parameters were reported and the impact of the nuisance parameters evaluated. The sensitivity of KM3NeT/ORCA6 to the NUNM parameters has been measured and compared to the current bounds. New limits found from the fit to the data were set, and improved the current bound on α_{33} by a factor 2 as $\alpha_{33} > -0.05$. Furthermore the 90% CL contours were provided for the combination of α_{22} with α_{33}, α_{22} with α_{32}, and α_{33} with α_{32}. It was found in the case of α_{22} and α_{33} free, the unitarity is being rejected with a p-value of 0.9%, however an increased statistics is required to make a significant statement on the unitarity rejection. The study of the correlation of the parameters could lead to consider the orthogonal phase space in future studies. Last but not least, it represents the first direct search for low scale non-unitary neutrino mixing using earth-crossing atmospheric neutrino data, which involves both the NC and CC potential in the matter effects.

Conclusion

This dissertation has reported an alternative particle identification technique, an analysis of the tau neutrino appearance and non-unitary neutrino mixing, and assessed the absolute orientation of KM3NeT using two different methods.

Advancements in the detector calibration, through two different methods employed to constrain KM3NeT's absolute orientation, were reported. The continuous efforts of the collaboration on the calibration, which reflects the understanding of the detector, is essential to align with the broad physics reach of KM3NeT. The knowledge of the detector absolute orientation has improved down to $[-0.15^\circ, +0.55^\circ]$ at 3σ CL in azimuth rotations thanks to the study of the Moon and Sun cosmic ray shadows that were observed both with high significance using KM3NeT/ORCA data. An acoustic study, based on the detection with KM3NeT/ORCA of acoustic pulses emitted from a boat, that aims at improving the detector's pointing accuracy to the sub-degree level, using the beamforming principle, was also reported. These measurements have reduced the systematic uncertainties associated with the pointing capabilities of KM3NeT which will support its goal of contributing to the global network of multi-messenger astronomy.

This work reported the first observation of the tau neutrino appearance with the KM3NeT/ORCA detector. The data corresponding to an exposure of 433 kt-years, was taken with an early six DUs configuration operating from January 2020 to November 2021. The data was analysed following a binned likelihood method. Different particle identification algorithms were described and their performance was compared. The ν_τ normalisation (called S_τ) affecting the CC tau neutrino event rates was measured as $0.48^{+0.49}_{-0.33}$. This translated into a measured cross section of $\sigma_\tau^{\mathrm{meas}}(E_{\nu_\tau}) = (2.5^{+2.6}_{-1.8}) \times 10^{-38}\mathrm{cm}^2$ for a median tau neutrino energy of $20.3^{+15.6}_{-8.0}$ GeV. This opens the door to new prospects in the study of tau neutrinos with KM3NeT/ORCA. In particular adding new cross section measurements in the tau neutrino energy range, when statistics will be sufficient, will allow to study the structure functions of the tau neutrino cross section and compare to other neutrino flavours.

Through the successful implementation of the non-unitary neutrino mixing model and analysis framework, the effect of non-unitarity as a parametrised deviation of the standard 3-flavour oscillation probabilities has been studied. The analyses performed in this work have demonstrated the capability of KM3NeT/ORCA to probe these potential deviations, particularly in regions of the parameter space that remain largely unexplored. Limits from atmospheric neutrino data have been set by KM3NeT/ORCA for individual diagonal parameters α_{11}, α_{22}, α_{33} and non-diagonal $|\alpha_{21}|$, $|\alpha_{31}|$, $|\alpha_{32}|$. The limit on α_{33} has improved the current bound by a factor 2, to the level of -0.05 at the 2σ CL. In addition pairs of parameters have been fitted together for the first time. A deviation for the sum of α_{22} and α_{33} has been measured with a p-value 0.9% (including Feldman Cousin correction) with respect to the unitary case $\alpha_{22} = \alpha_{33} = 0$.

In conclusion, the outcomes of this thesis highlight the impressive capabilities of KM3NeT, not only as a neutrino telescope but as a precision instrument for measuring fundamental neutrino properties and testing the Standard Model.

APPENDICES

Appendix A

Additional studies for the (α_{22}, α_{33}) pair

To understand the effect of the NUNM parameters at the best fit point, an Asimov set was prepared with a NUNM signal introduced and the systematics values corresponding to the best fit with α_{22} and α_{33} free. The Figure A.1 allowed to demonstrate that the χ^2 or likelihood is distributed among the three classes with 1.9 in the HP Tracks, 3.1 in the LP Tracks and 2.3 units in the Showers. The horizontal region is mainly contributing to the likelihood, which is expected as it is the region where most events are located.

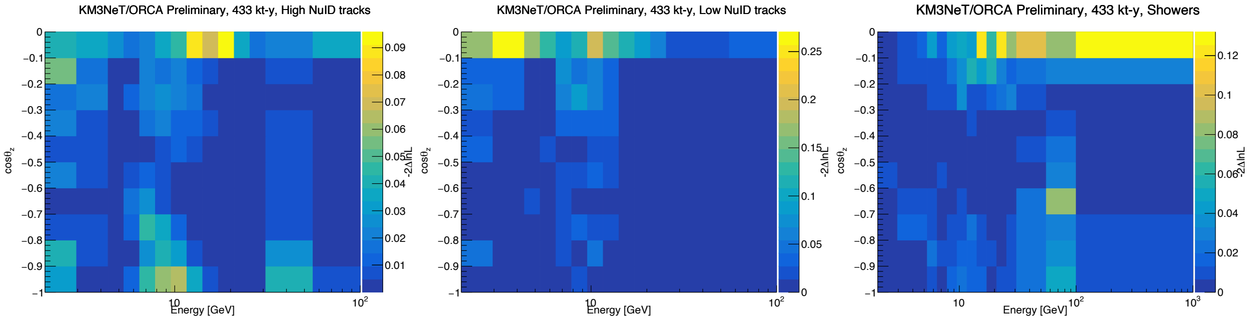

Figure A.1: Simulation of a signal with α_{22} and α_{33} at the best fit values reported for the fit of the data. The events per bin in the reconstructed 2D space are shown.

The Figure A.2 illustrates the difference in $2\ln\mathcal{L}$ between the unitarity and the non-unitarity fit with α_{22} and α_{33} free on Data. Due to the heavy fluctuations, the signal is more difficult to visualize and no conclusion can be drawn, even though the main differences are observed in the same regions as shown in Figure A.1 for the Asimov set.

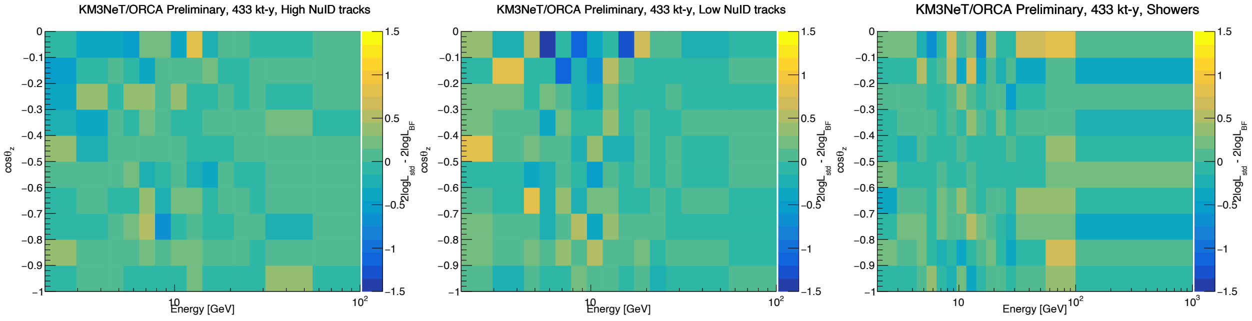

Figure A.2: Observed signal with α_{22} and α_{33} free in the fit of the data. The events per bin in the reconstructed 2D space are shown.

The L/E distribution in the Figure A.3 illustrates the difference between the unitarity and the NUNM scenario with α_{22} and α_{33} free at the best fit. The difference between the two is small and it is even more difficult in the 1D space to identify a clear pattern.

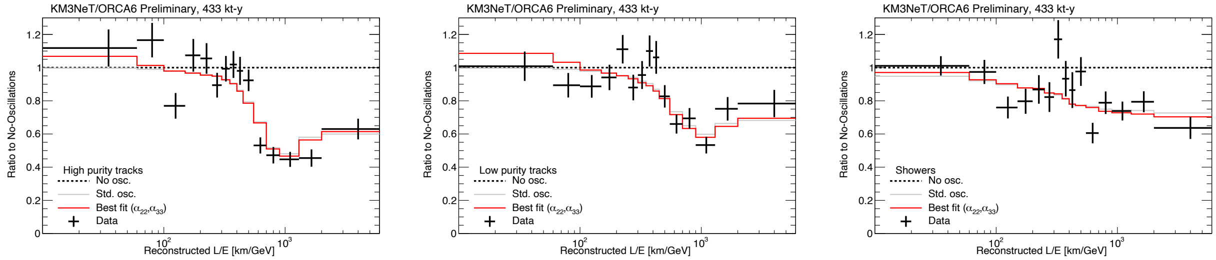

Figure A.3: The L/E distributions of Data and MC for different hypotheses are shown, divided by the unitarity hypothesis. On the left the High Purity Tracks class, in the middle the Low Purity Tracks class is represented while on the right part the Shower class is shown. The result of the fit with fixed oscillation parameters to nominal values is in gray, the best fit with α_{22} and α_{33} free is in red and the Data is in black with the corresponding error bars.

The L/E distribution in the Figure A.4 allows to observe the ratio between the best unitarity and NUNM scenario with α_{22} and α_{33} free compared to Data. It appears that in 1D with the current statistics the error bar are compatible with the nominal scenario.

However the distribution here is the projection of a 2D phase space therefore averaging some of the effect.

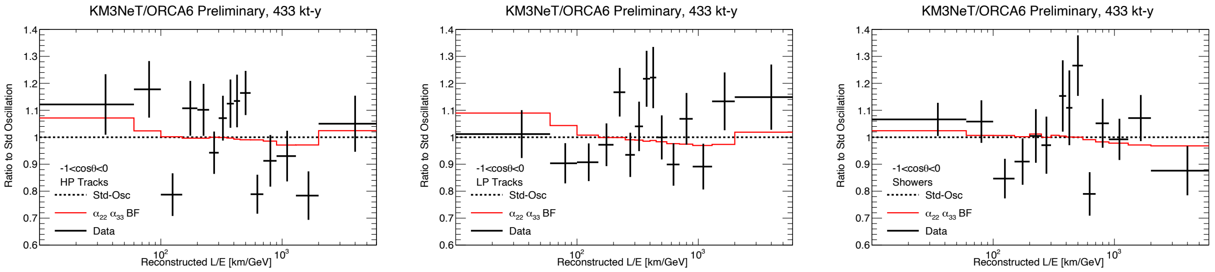

Figure A.4: The L/E distributions of Data and MC for different hypotheses are shown, divided by the no-oscillation hypothesis. On the left the High Purity Tracks class, in the middle the Low Purity Tracks class is represented while on the right part the Shower class is shown. The result of the fit with fixed oscillation parameters to nominal values is a dotted line, the best fit with α_{22} and α_{33} free is in red and the Data is in black with the corresponding error bars.

In addition the Figure A.5 is showing the pulls for all systematics involved with respect to the 1σ post-fit uncertainty. It shows how far from the expectation value before the fit the observed values was. And the impact of the systematic on the parameter of interest when shifting the systematic by 1σ from the best fit value. This allows to determine the order of importance of the systematics depending on the impact on the measurement. The overall norm is correlated to the α_{22} and α_{33} parameters. Although the effect of α_{22} and α_{33} is complex due to matter, at first order it could be compensated by a higher overall norm. In fact in Figure A.5 the overall norm is pulled further than the standard oscillation case in the opposite direction to α_{22} and α_{33}. This does not explain the important improvement in χ^2 observed, however future studies could implement a prior on the normalisations in order to prevent possible related issues.

The oscillation probability as function of the energy is shown in the Figure A.6 for the best fit point, it includes the comparison with the case where a overall normalisation of 1.47 is applied to the best fit probabilities. It shows that the best fit effect is heavily modifying the probability but some is compensated by the overall normalisation which moves freely in the fit. Although at lower energy the effect is more complex than a simple scaling.

Moreover a comparison between unitarity and NUNM for the oscillation probability as a function of the energy and $cos(\theta)$ is shown in the Figure A.7. The NUNM is included at the best fit with α_{22} and α_{33} free. At low energies the non-unitarity modifies the effect of the matter potential.

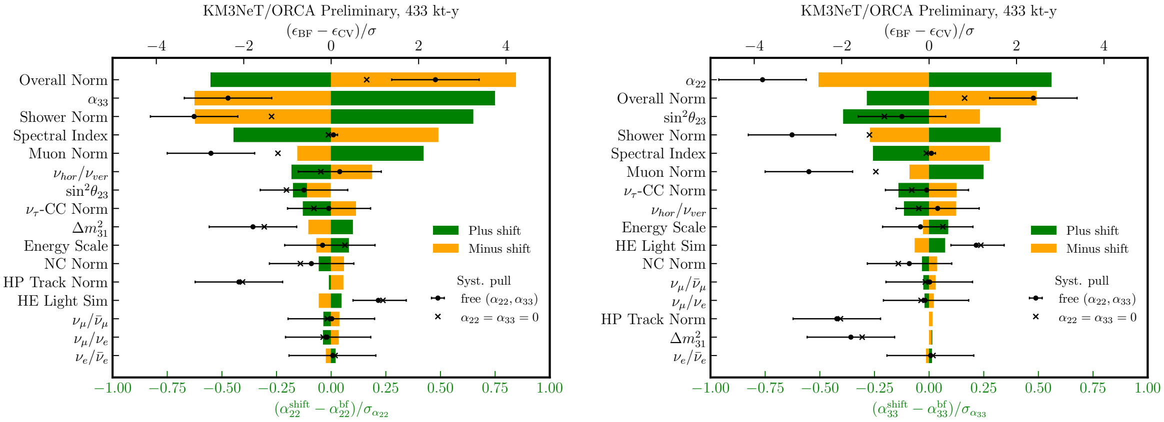

Figure A.5: The significance of the impact of the nuisance parameters on the parameter of interest written on the bottom axis is shown in colored bars. The pulls of the nuisance parameters are shown in blacks with the errors calculated as the ratio between the post-fit and pre-fit uncertainties. The dots are the result from the NUNM fit and the crosses represent the unitarity case.

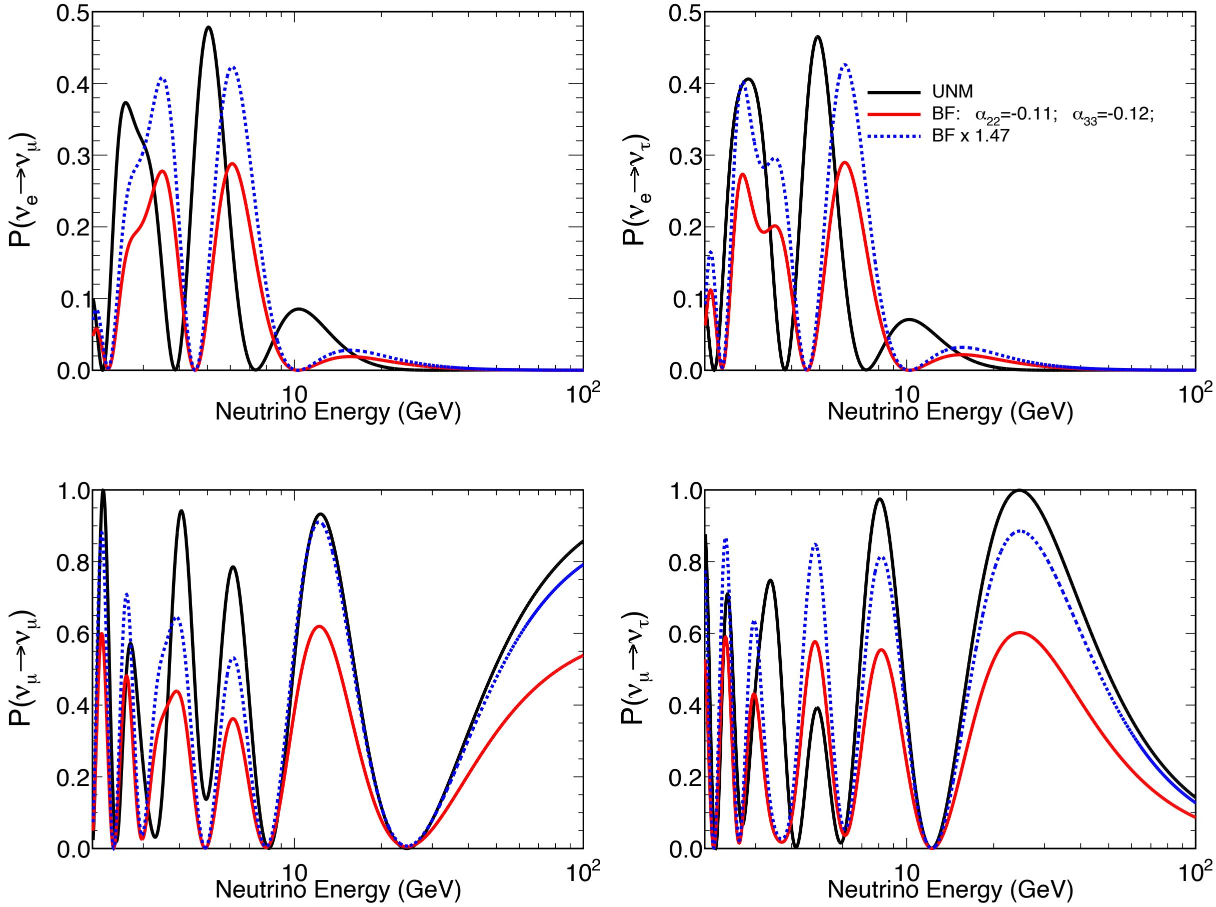

Figure A.6: The oscillation probability for vertically up-going neutrinos as function of the neutrino energy are shown for α_{22} and α_{33} at the best fit. It is compared to the $V_{NC} = 0$ (or $n_n = 0$) case.

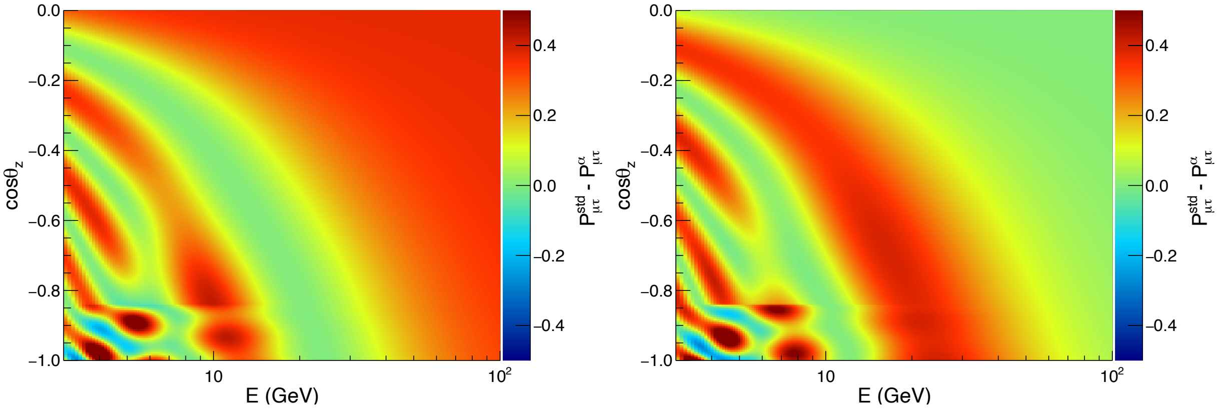

Figure A.7: The oscillation probability for up-going neutrinos as function of neutrino energy is shown for the best fit. The comparison between NUNM and unitarity case in the muon disappearance channel is shown on the left and in the tau appearance channel on the right.

References

[1] M. Lincetto, *Development of multi-messenger real-time analyses for the KM3NeT neutrino telescope*, Ph.D. thesis, Aix-Marseille University, 2020.

[2] F. Reines and C.L. Cowan, *The neutrino*, *Nature* **178** (1956) 446.

[3] S. Bilenky, *Introduction to the Physics of Massive and Mixed Neutrinos*, vol. 947, Springer (2018), 10.1007/978-3-319-74802-3.

[4] C.S. Wu, E. Ambler, R.W. Hayward, D.D. Hoppes and R.P. Hudson, *Experimental test of parity conservation in beta decay*, *Phys. Rev.* **105** (1957) 1413.

[5] P.W. Higgs, *Broken Symmetries and the Masses of Gauge Bosons*, *Phys. Rev. Lett.* **13** (1964) 508.

[6] J.A. Formaggio and G.P. Zeller, *From eV to EeV: Neutrino Cross Sections Across Energy Scales*, *Rev. Mod. Phys.* **84** (2012) 1307 [`1305.7513`].

[7] S. Hallmann, *Sensitivity to atmospheric tau-neutrino appearance and all-flavour search for neutrinos from the Fermi Bubbles with the deep-sea telescopes KM3NeT/ORCA and ANTARES*, Ph.D. thesis, Erlangen-Nürnberg University, 2021.

[8] KM3NeT collaboration, *gSeaGen: The KM3NeT GENIE-based code for neutrino telescopes*, *Comput. Phys. Commun.* **256** (2020) 107477 [`2003.14040`].

[9] T. Kozynets, T. Stuttard and D.J. Koskinen, *Deep Inelastic Scattering Cross Section Uncertainties in Tau Neutrino Appearance Measurements*, `2409.01258`.

[10] ALEPH collaboration, *Determination of the Number of Light Neutrino Species*, *Phys. Lett. B* **231** (1989) 519.

[11] F.Y. et al., *Evidence for oscillation of atmospheric neutrinos*, *Phys. Rev. Lett.* **81** (1998) 1562.

[12] B. Pontecorvo, *Inverse beta processes and nonconservation of lepton charge*, *Zh. Eksp. Teor. Fiz.* **34** (1957) 247.

[13] KATRIN collaboration, *Direct neutrino-mass measurement based on 259 days of KATRIN data*, `2406.13516`.

[14] DESI collaboration, *DESI 2024 VI: Cosmological Constraints from the Measurements of Baryon Acoustic Oscillations*, `2404.03002`.

[15] S. Gariazzo, *Neutrino masses in cosmology*, in *21st Lomonosov Conference on Elementary Particle Physics*, 1, 2024 [`2401.11976`].

[16] A.V. Borisov and A.P. Isaev, *Neutrino Mass in Effective Field Theory*, *Phys. Part. Nucl.* **55** (2024) 634 [`2312.17714`].

[17] S. Weinberg, *Phenomenological Lagrangians*, *Physica A* **96** (1979) 327.

[18] J.A.B. Coelho, *https://github.com/joaoabcoelho/oscprob*, .

[19] A.M. Dziewonski and D.L. Anderson, *Preliminary reference earth model*, *Phys. Earth Planet. Interiors* **25** (1981) 297.

[20] E. Akhmedov, *Quantum mechanics aspects and subtleties of neutrino oscillations*, in *International Conference on History of the Neutrino: 1930-2018*, 1, 2019 [`1901.05232`].

[21] M.C. Gonzalez-Garcia, M. Maltoni and T. Schwetz, *NuFIT: Three-Flavour Global Analyses of Neutrino Oscillation Experiments*, *Universe* **7** (2021) 459 [`2111.03086`].

[22] E. Vitagliano, I. Tamborra and G. Raffelt, *Grand Unified Neutrino Spectrum at Earth: Sources and Spectral Components*, *Rev. Mod. Phys.* **92** (2020) 45006 [`1910.11878`].

[23] J. Mulder and R. Bruijn, *Seasonal variation of the atmopsheric muon flux in the KM3NeT detectors*, *PoS* **ICRC2023** (2023) 355.

[24] M. Honda, M. Sajjad Athar, T. Kajita, K. Kasahara and S. Midorikawa, *Atmospheric neutrino flux calculation using the NRLMSISE-00 atmospheric model*, *Phys. Rev. D* **92** (2015) 023004 [`1502.03916`].

[25] KM3NeT collaboration, *Measurement of the atmospheric muon neutrino flux with KM3NeT/ORCA6*, *PoS* **ICRC2023** (2023) 1093.

[26] KM3NeT collaboration, *Letter of intent for KM3NeT 2.0*, *J. Phys. G* **43** (2016) 084001 [`1601.07459`].

[27] M. Ageron et al., *Dependence of atmospheric muon flux on seawater depth measured with the first KM3NeT detection units: The KM3NeT Collaboration*, *Eur. Phys. J. C* **80** (2020) 99.

[28] A. Albert et al., *Monte Carlo simulations for the ANTARES underwater neutrino telescope*, *J. C. A. P.* **2021** (2021) 064.

[29] R. Abbasi et al., *Lateral distribution of muons in IceCube cosmic ray events*, *Phys. Rev. D* **87** (2013) 012005.

[30] A. Romanov, *Cosmic ray studies with the KM3NeT neutrino telescope*, Ph.D. thesis, Genoa U., 2023. 10.15167/romanov-andrey.

[31] Pierre Auger collaboration, *Cosmic-ray anisotropies in right ascension measured by the Pierre Auger Observatory*, *Astrophys. J.* **891** (2020) 142 [`2002.06172`].

[32] KM3NeT collaboration, *Atmospheric muons measured with the KM3NeT detectors in comparison with updated numeric predictions*, *Eur. Phys. J. C* **84** (2024) 696 [`2403.11946`].

[33] KM3NeT collaboration, *Implementation and first results of the KM3NeT real-time core-collapse supernova neutrino search*, *Eur. Phys. J. C* **82** (2022) 317 [`2109.05890`].

[34] S. Aiello et al., *Astronomy potential of KM3NeT/ARCA*, `2402.08363`.

[35] KM3NeT collaboration, *The KM3NeT multi-PMT optical module*, *JINST* **17** (2022) P07038 [`2203.10048`].

[36] J.S. Watt, *Light pulses in the night sky associated with extensive cosmic ray air showers.*, Ph.D. thesis, 1956.

[37] J.V. Jelley, *Cerenkov radiation and its applications*, *British Journal of Applied Physics* **6** (1955) 227.

[38] NEMO collaboration, *Deep seawater inherent optical properties in the Southern Ionian Sea*, *Astropart. Phys.* **27** (2007) 1 [`astro-ph/0603701`].

[39] ANTARES collaboration, *Transmission of light in deep sea water at the site of the ANTARES Neutrino Telescope*, *Astropart. Phys.* **23** (2005) 131 [`astro-ph/0412126`].

[40] M. Ackermann et al., *Optical properties of deep glacial ice at the South Pole*, *J. Geophys. Res.* **111** (2006) D13203.

[41] B. O Fearraigh, *Following the light - Novel event reconstruction techniques for neutrino oscillation analyses in KM3NeT/ORCA*, Ph.D. thesis, Amsterdam U., 2024.

[42] A. Domi, *Shower Reconstruction and Sterile Neutrino Analysis with KM3NeT/ORCA and ANTARES*, Ph.D. thesis, Aix-Marseille U., Genoa U., 2019. 10.15167/domi-alba.

[43] Y. Becherini, A. Margiotta, M. Sioli and M. Spurio, *A Parameterisation of single and multiple muons in the deep water or ice*, *Astropart. Phys.* **25** (2006) 1 [`hep-ph/0507228`].

[44] C. Forti, H. Bilokon, B. d'Ettore Piazzoli, T.K. Gaisser, L. Satta and T. Stanev, *Simulation of atmospheric cascades and deep underground muons*, *Phys. Rev. D* **42** (1990) 3668.

[45] G. Giacomelli and A. Margiotta, *The MACRO Experiment at Gran Sasso*, in *Charles Peck Fest*, 7, 2007 [`0707.1691`].

[46] GEANT4 collaboration, *GEANT4–a simulation toolkit*, *Nucl. Instrum. Meth. A* **506** (2003) 250.

[47] M. de Jong, *Multi-dimensional interpolations in c++*, 2019.

[48] C. Gatius Oliver, F. Bretaudeau, M. De Jong and L. Martin, *Dynamical position and orientation calibration of the KM3NeT telescope*, *PoS* **ICRC2023** (2023) 1033.

[49] KM3NeT collaboration, *Acoustic positioning system for KM3NeT*, *PoS* **ICRC2015** (2016) 1169.

[50] L. Bailly-Salins, *Time, position and orientation calibration using atmospheric muons in KM3NeT*, *PoS* **ICRC2023** (2023) 218.

[51] KM3NeT collaboration, *The prototype detection unit of the KM3NeT detector*, *Eur. Phys. J. C* **76** (2016) 54 [`1510.01561`].

[52] G.W. Clark, *Arrival Directions of Cosmic-Ray Air Showers from the Northern Sky*, *Phys. Rev. D* **108** (1957) 450.

[53] M. Aartsen et al., *Measurements of the time-dependent cosmic-ray Sun shadow with seven years of IceCube data: Comparison with the Solar cycle and magnetic field models*, *Phys. Rev. D* **103** (2021) 042005.

[54] A. Albert et al., *The cosmic ray shadow of the Moon observed with the ANTARES neutrino telescope*, *The Eur. Phys. J. C* **78** (2018) 1006.

[55] A. Albert et al., *Observation of the cosmic ray shadow of the Sun with the ANTARES neutrino telescope*, *Phys. Rev. D* **102** (2020) 122007.

[56] M. Ambrosio et al., *Moon and Sun shadowing effect in the MACRO detector*, *Astrop. Phys.* **20** (2003) 145.

[57] P. Achard et al., *Measurement of the shadowing of high-energy cosmic rays by the Moon: A search for TeV-energy antiprotons*, *Astrop. Phys.* **23** (2005) 411.

[58] P. Adamson et al., *Observation in the MINOS far detector of the shadowing of cosmic rays by the sun and moon*, *Astrop. Phys.* **34** (2011) 457.

[59] B. Bartoli et al., *Observation of the cosmic ray moon shadowing effect with the ARGO-YBJ experiment*, *Phys. Rev. D* **84** (2011) 022003.

[60] A.U. Abeysekara et al., *The hawc gamma-ray observatory: Observations of cosmic rays*, *Proc. 33rd ICRC, Rio de Janeiro, Brazil* (2013) .

[61] A.M. Price-Whelan et al., *The Astropy Project: Building an Open-science Project and Status of the v2.0 Core Package*, *Astron. J.* **156** (2018) 123.

[62] F. Arias, P. Charlot, M. Feissel and J. Lestrade, *The extragalactic reference system of the International Earth Rotation Service, ICRS*, *Astron. and Astrop.* **303** (1995) 604.

[63] G. Carminati, M. Bazzotti, A. Margiotta and M. Spurio, *Atmospheric MUons from PArametric formulas: a fast GEnerator for neutrino telescopes (MUPAGE)*, *Comput. Phys. Com.* **179** (2008) 915.

[64] Y. Becherini, A. Margiotta, M. Sioli and M. Spurio, *A parameterisation of single and multiple muons in the deep water or ice*, *Astropart. P.* **25** (2006) 1.

[65] K. Melis, A. Heijboer, M. De Jong et al., *KM3NeT/ARCA Event Reconstruction Algorithms*, *Proc. 35th ICRC* (2017) 950.

[66] S. Baker and R.D. Cousins, *Clarification of the use of CHI-square and likelihood functions in fits to histograms*, *Nucl. Instr. Meth.* **221** (1984) 437.

[67] Becker Tjus, J., Desiati, P., Döpper, N., Fichtner, H., Kleimann, J., Kroll, M. et al., *Cosmic-ray propagation around the sun: investigating the influence of the solar magnetic field on the cosmic-ray sun shadow*, *A.&A.* **633** (2020) A83.

[68] L. Donneger, *Measurement of the Moon and Sun shadows in cosmic rays with the data taken by the KM3NeT/ORCA detector between 2020 and 2023*, Tech. Rep. , Centre de Physique des Particules de Marseille (Apr., 2024).

[69] R. Coniglione, A. Creusot, I. Di Palma, D. Guderian, J. Hofestaedt, G. Riccobene et al., *KM3NeT Time Calibration*, *Proc. 36th ICRC* **ICRC2019** (2019) 868.

[70] M. Sanguineti, *Pointing accuracy of the ANTARES detector: Moon shadow and surface array analysis*, *PoS* **ICRC2017** (2017) 1053.

[71] T.L. Szabo, *Chapter 7 - array beamforming*, in *Diagnostic Ultrasound Imaging: Inside Out (Second Edition)*, T.L. Szabo, ed., (Boston), pp. 209–255, Academic Press (2014), DOI.

[72] CDF Collaboration collaboration, *Observation of top quark production in $\overline{p}p$ collisions with the collider detector at fermilab*, *Phys. Rev. Lett.* **74** (1995) 2626.

[73] P.C. Bhat, H.B. Prosper, S. Sekmen and C. Stewart, *Optimizing event selection with the random grid search*, *Comp. Phys. Com.* **228** (2018) 245.

[74] KM3NeT collaboration, *Measurement of neutrino oscillation parameters with the first six detection units of KM3NeT/ORCA*, *JHEP* **10** (2024) 206 [`2408.07015`].

[75] V. Carretero, *Measuring atmospheric neutrino oscillations with km3net/orca6*, *PoS(ICRC2023)996* (2023) .

[76] N. Geisselbrecht, *Measuring atmospheric tau neutrino appeanrance with km3net/orca6*, *PoS(ICRC2023)1107* (2023) .

[77] I. Esteban, M. Gonzalez-Garcia, M. Maltoni, T. Schwetz and A. Zhou, *The fate of hints: updated global analysis of three-flavor neutrino oscillations*, *Journal of High Energy Physics* **2020** (2020) .

[78] G.D. Barr, S. Robbins, T.K. Gaisser and T. Stanev, *Uncertainties in atmospheric neutrino fluxes*, *Physical Review D* **74** (2006) .

[79] KM3NeT collaboration, *Letter of intent for KM3NeT 2.0*, *J. Phys. G* **43** (2016) 084001 [`1601.07459`].

[80] S.S. Wilks, *The Large-Sample Distribution of the Likelihood Ratio for Testing Composite Hypotheses*, *Annals Math. Statist.* **9** (1938) 60.

[81] G.J. Feldman and R.D. Cousins, *Unified approach to the classical statistical analysis of small signals*, *Phys. Rev. D* **57** (1998) 3873.

[82] B. Efron, *Bootstrap methods: Another look at the jackknife*, in *Breakthroughs in Statistics: Methodology and Distribution*, S. Kotz and N.L. Johnson, eds., (New York, NY), pp. 569–593, Springer New York (1992), DOI.

[83] SNO collaboration, *Measurement of the rate of $\nu_e + d \to p + p + e^-$ interactions produced by ^8B solar neutrinos at the Sudbury Neutrino Observatory*, *Phys. Rev. Lett.* **87** (2001) 071301 [`nucl-ex/0106015`].

[84] SNO collaboration, *Direct evidence for neutrino flavor transformation from neutral current interactions in the Sudbury Neutrino Observatory*, *Phys. Rev. Lett.* **89** (2002) 011301 [`nucl-ex/0204008`].

[85] Daya Bay collaboration, *Observation of electron-antineutrino disappearance at daya bay, Phys. Rev. Lett, 108:171803* (2012) .

[86] Daya Bay collaboration, *Improved measurement of electron antineutrino disappearance at daya bay, Chinese Phys., C37:011001* (2013) .

[87] Double Chooz collaboration, *Indication of reactor $\bar{\nu}_e$ disappearance in the double chooz experiment, Phys. Rev. Lett., 108:131801* (2012) .

[88] RENO collaboration, *Observation of reactor electron antineutrinos disappearance in the reno experiment, Phys. Rev. Lett.* ***108**:191802* (2012) .

[89] K.A. et al. (Super-Kamiokande Collaboration), *Search for differences in oscillation parameters for atmospheric neutrinos and antineutrinos at super-kamiokande*, *Phys. Rev. Lett.* **107** (2011) .

[90] M.G.A. et al., *Neutrino oscillation studies with icecube-deepcore*, *Nuclear Physics, Section B* **908** (2016) 161.

[91] NOvA collaboration, *Expanding neutrino oscillation parameter measurements in NOvA using a Bayesian approach*, `2311.07835`.

[92] T2K collaboration, *Measurements of neutrino oscillation parameters from the T2K experiment using* 3.6×10^{21} *protons on target*, *Eur. Phys. J. C* **83** (2023) 782 [`2303.03222`].

[93] G.A. et al., *Must the new heavy lepton have it's own neutrino?*, *Phys. Lett. B 67 463–466* (1977) .

[94] DONUT collaboration, *Observation of tau neutrino interactions*, *Phys. Lett. B* **504** (2001) 218 [`hep-ex/0012035`].

[95] I. Esteban, M. Gonzalez-Garcia, M. Maltoni, T. Schwetz and A. Zhou, *The fate of hints: updated global analysis of three-flavor neutrino oscillations*, *Journal of High Energy Physics* **2020** (2020) .

[96] KM3NeT collaboration, *Determining the neutrino mass ordering and oscillation parameters with KM3NeT/ORCA*, *Eur. Phys. J. C* **82** (2022) 26 [`2103.09885`].

[97] L.Z. et al., *Measurement of the tau neutrino cross section in atmospheric neutrino oscillations with super-kamiokande*, *Physical Review D* **98** (2018) .

[98] A.N. et al., *Discovery of tau neutrino appearance in the cngs neutrino beam with the opera experiment*, *Physical Review Letters* **115** (2015) .

[99] A.M. et al, *Measurement of atmospheric tau neutrino appearance with icecube deepcore*, *Physical Review D* **99** (2019) .

[100] M. Honda, M.S. Athar, T. Kajita, K. Kasahara and S. Midorikawa, *Atmospheric neutrino flux calculation using the nrlmsise-00 atmospheric model*, *Phys. Rev. D* **92** (2015) 023004.

[101] C. Andreopoulos, C. Barry, S. Dytman, H. Gallagher, T. Golan, R. Hatcher et al., *The genie neutrino monte carlo generator: Physics and user manual*, 2015.

[102] S. Alekhin et al., *A facility to Search for Hidden Particles at the CERN SPS: the SHiP physics case*, *Rept. Prog. Phys.* **79** (2016) 124201 [`1504.04855`].

[103] A.N. et al., *Final results of the opera experiment on ν_τ appearance in the cngs neutrino beam*, *Physical Review Letters* **120** (2018) .

[104] L.Z. et al., *Measurement of the tau neutrino cross section in atmospheric neutrino oscillations with super-kamiokande*, *Physical Review D* **98** (2018) .

[105] C.S. Fong, *Theoretical Aspect of Nonunitarity in Neutrino Oscillation*, `2301.12960`.

[106] C.S. Fong, H. Minakata and H. Nunokawa, *Non-unitary evolution of neutrinos in matter and the leptonic unitarity test*, *Journal of High Energy Physics* **2019** (2019) .

[107] M. Blennow, P. Coloma, E. Fernandez-Martinez, J. Hernandez-Garcia and J. Lopez-Pavon, *Non-Unitarity, sterile neutrinos, and Non-Standard neutrino Interactions*, *JHEP* **04** (2017) 153 [`1609.08637`].

[108] M. Malinský, T. Ohlsson, Z.-z. Xing and H. Zhang, *Non-unitary neutrino mixing and cp violation in the minimal inverse seesaw model*, *Physics Letters B* **679** (2009) 242–248.

[109] P.B. Denton and J. Gehrlein, *New oscillation and scattering constraints on the tau row matrix elements without assuming unitarity*, *JHEP* **06** (2022) 135 [`2109.14575`].

[110] S. Okubo, *Note on Unitary Symmetry in Strong Interaction. II Excited States of Baryons*, *Prog. Theor. Phys.* **28** (1962) 24.

[111] S. Parke and M. Ross-Lonergan, *Unitarity and the three flavor neutrino mixing matrix*, *Physical Review D* **93** (2016) .

[112] F. Escrihuela, D. Forero, O. Miranda, M. Tórtola and J. Valle, *On the description of nonunitary neutrino mixing*, *Physical Review D* **92** (2015) .

[113] A.S.K. et al., *Model-independent constraints on non-unitary neutrino mixing from high-precision long-baseline experiments*, *Journal of High Energy Physics* **2022** (2022) .

[114] S. Sahoo, S. Das, A. Kumar and S.K. Agarwalla, *Constraining non-unitary neutrino mixing using matter effects in atmospheric neutrinos at ino-ical*, 2023.

[115] L.S. Miranda, P. Pasquini, U. Rahaman and S. Razzaque, *Searching for non-unitary neutrino oscillations in the present t2k and novνa data*, 2021.

[116] H. Hettmansperger, M. Lindner and W. Rodejohann, *Phenomenological consequences of sub-leading terms in see-saw formulas*, *Journal of High Energy Physics* **2011** (2011) .

[117] P.e.a. Astier, *Search for →e oscillations in the nomad experiment*, *Physics Letters B* **570** (2003) 19–31.

[118] E. Radicioni, *Results from the chorus experiment at cern*, *Nuclear Physics B - Proceedings Supplements* **85** (2000) 95.

[119] SUPER-KAMIOKANDE collaboration, *Limits on sterile neutrino mixing using atmospheric neutrinos in Super-Kamiokande*, *Phys. Rev. D* **91** (2015) 052019 [`1410.2008`].